Department of Civil, Construction and Environmental Engineering
UNIVERSITY OF NAPLES FEDERICO II

Doctorate in Civil Systems Engineering (XXXVIII Cycle)

Regionalization of Flow Duration Curves In Southern Peninsular Italy

Ph.D. coordinator:

Prof. Ing. Andrea Papola

Tutors:

Prof. Ing. Giuseppe Del Giudice

Prof.Ing. Cristiana Di Cristo

Co-Tutor:

Ing. Roberta Padulano

Ph.D. student:

Fatemeh Moradi

Summary

List of Figures

List of Tables

Acknowledgments

First and foremost, I would like to express my deepest and most sincere gratitude to my supervisor, Professor Giuseppe Del Giudice. His exceptional guidance, continuous support, and invaluable feedback have been fundamental throughout the development of this thesis. His scientific rigor, intellectual generosity, and constant encouragement have not only shaped the quality of this work, but have also contributed profoundly to my personal, professional, and academic growth. I am especially grateful for his patience in guiding me through complex concepts, and for the trust he has placed in me, which has allowed me to face challenges with greater confidence and determination.

I also wish to extend my heartfelt thanks to Dr. Roberta Padulano, whose presence has been a constant source of support and reassurance during this journey. Her kindness, empathy, and availability have made a significant difference in the most demanding moments of this work. She has always been ready to listen, to help, and to encourage me, and I deeply appreciate the way she has believed in my efforts and valued my progress. Her supportive attitude and her sincere appreciation of my work have given me strength, motivation, and hope, especially when doubts or fatigue seemed overwhelming.

My profound gratitude goes to my family, who represent the solid foundation upon which all of my achievements are built. To my parents, I owe more than words can say. Their unconditional love, sacrifices, and constant encouragement have accompanied me in every phase of my life. They have believed in me even when I struggled to believe in myself, and their example of perseverance, integrity, and generosity has guided me through difficulties and inspired me to keep moving forward. To my brothers, I am sincerely thankful for their support, understanding, and reassuring presence. Even in silence, their closeness has been a source of comfort and stability, reminding me that I was never alone in this journey.

A very special and deeply personal thank you goes to my soulmate, Arash. Your presence in my life has been a continuous source of strength, serenity, and inspiration. Throughout the years of study and research, and especially during the preparation of this thesis, you have stood by my side with unwavering patience, love, and understanding. You have shared with me moments of joy and enthusiasm, but also nights of stress, worry, and exhaustion. You have listened to my doubts, encouraged my dreams, and reminded me of my abilities when I felt overwhelmed. This achievement is not only mine; it is ours. Your faith in me has helped me to move forward, to believe in my path, and to see meaning even in the most challenging days. For all of this, and for the countless small and big gestures of love that cannot be fully expressed in words, I am infinitely grateful.

Finally, I would like to recall the spirit of Rumi, the famous Iranian poet, whose words accompany and illuminate the inner journey behind every academic path. He reminds us that “what you seek is seeking you,” and that through love, patience, and perseverance, every difficulty can become a step toward deeper understanding. In this sense, this thesis is not only an academic result, but also a part of my personal journey toward growth, awareness, and inner light.

Introduction

Prediction of streamflow characteristics in ungauged basins is a central challenge in hydrology, particularly in regions with sparse or fragmented monitoring networks. In such contexts, regionalization methods provide a practical solution by transferring hydrological information from gauged to ungauged sites through empirical relationships between streamflow indices and measurable catchment descriptors.

A key tool in this process is the Flow Duration Curve (FDC), which condenses the variability of streamflow regimes into a single statistical representation, capturing flows from high extremes to persistent low values. However, the application of conventional FDCs in Mediterranean catchments is particularly complex. These basins are strongly influenced by seasonal rainfall, prolonged summer droughts, and intermittent streamflow regimes, which generate long sequences of zero-flow days. In such contexts, traditional FDCs must be reconstructed to distinguish between zero-flow and non-zero-flow components, ensuring that both flow intermittency and discharge magnitude are properly represented. This methodological adjustment is essential in southern Italy, where climatic gradients, geomorphological complexity, heterogeneous geology, and discontinuous records make regionalization both challenging and necessary.

This thesis addresses these challenges by developing a statistical framework for the regionalization of FDC parameters across a study domain that represents nearly one-fifth of southern Italy. The focus is placed on three indices that capture complementary aspects of flow regimes. The first is the mean of the log-normal distribution (μ), which represents the central tendency of normalized flows and reflects the internal structure of the flow regime relative to the mean discharge. The second is the mean non-zero discharge (Q_{nz}), which characterizes the average flow magnitude during periods when water is present. The third is the duration of non-zero flow (τ), which quantifies hydrological persistence and continuity. In addition to these FDC-based indices, the Baseflow Index (*BFI*) is included as a complementary measure, offering insight into subsurface contributions to streamflow. Importantly, this study is the first to incorporate a permeability map of the region into the regionalization framework, thereby improving the representation of geological controls on runoff generation and groundwater–surface water interactions.

The methodology integrates exploratory correlation analysis, stepwise regression in both linear and log-transformed space, jackknife cross-validation, and outlier detection. Particular emphasis is placed on balancing statistical performance with hydrological interpretability, avoiding models that are statistically efficient but physically implausible. Furthermore, the framework explicitly tests the sensitivity of regionalization outcomes to streamflow record length, thereby assessing the reliability of models derived from shorter or incomplete data series.

1. Flow Duration Curves (FDCs): Concepts, Applications, and Literature Review

This chapter provides an overview of flow duration curves (FDCs), explaining their role in representing streamflow variability, their construction methods, and their main applications in hydrology. It also reviews existing approaches discussed in the literature and outlines the contribution of this study to advancing FDC regionalization in southern Italy.

1.1 Definition of Flow Duration Curve

The flow duration curve (FDC) is a cumulative frequency graph that represents the percentage of time a specific discharge is equalled or surpassed within a defined period. It serves as one of the most informative tools for illustrating a stream's flow behaviour across its entire discharge range, regardless of the chronological sequence of flows, and can be interpreted as a relationship between flow magnitude and frequency (Smakhtin, 2001).

In its conventional form, this graph does not have a probabilistic interpretation because streamflow values are temporally correlated and strongly influenced by seasonal conditions. As a result, the probability that the discharge on a given day will exceed a specified threshold depends not only on the flows of preceding days but also on the time of year (Mosley & McKerchar, 1993). Nevertheless, the FDC is frequently interpreted as the complement of the cumulative distribution function for the streamflow observed at a given site, an expedient interpretation in which temporal dependencies and autocorrelation are not modeled explicitly.

1.2. Construction Methods of FDCs

Two principal procedures are used to build flow-duration curves: the period-of-record FDC method and the calendar-year method that yields annual FDCs (AFDCs).

1.2.1 Period-of-Record Method

Empirically, in the period-of-record approach, discharges are ordered from largest to smallest, grouped into discharge classes, and the frequency of observations in each class is counted. Cumulative class frequencies are then converted to percentages of the total number of time steps over the record, and the lower bound of each discharge class is plotted against its associated percentage point (Searcy, 1959).

An alternative formulation defines the FDC as the complement of the cumulative distribution function (CDF) computed over the entire period of record. In line with this definition, Vogel & Fennessey (1994) proposed several nonparametric estimators. In practice, the observed daily discharges are ranked in descending order, and exceedance probabilities are estimated using plotting positions, such as the Weibull formula: $p = \frac{i}{n+1}$, where i is the rank and n is the sample size. The resulting curve plots flow quantiles against their exceedance percentages, providing a holistic view of long-term flow behavior.

Figure 1.1 provides a schematic FDC—constructed for demonstration purposes—relating discharge (m³/s) to exceedance probability (%). The blue curve demonstrates the typical shape of an FDC: steep initial decline from peak flows (exceeding 1200 m³/s at very low probabilities, representing rare flood events) to sustained baseflows (leveling off around 10–20 m³/s at high probabilities, indicating consistent low-flow conditions supported by groundwater or perennial sources). This visualization captures the full variability across the record without separating by years, offering a compact summary for applications like water resource management or hydropower assessment. The inset provides an alternative view by converting probabilities to cumulative days (spanning 0 to 1095 days, equivalent to about 3 years), showing how long certain discharge levels are maintained or exceeded over time.

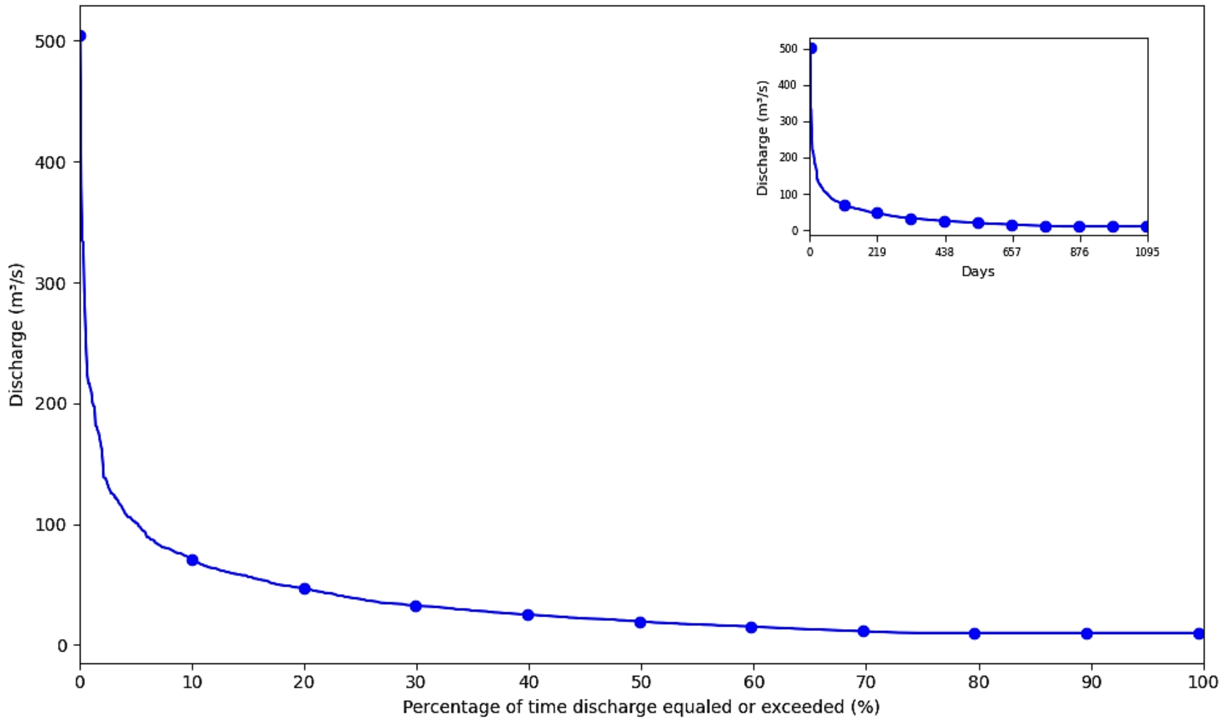

Figure 1.1: Period-of-record FDC plotting discharge versus exceedance probability, constructed using nonparametric estimators like the Weibull plotting position. Inset: Discharge versus cumulative days exceeded, highlighting flow durations over approximately 3 years.

1.2.2 Annual AFDCs

The annual-based construction, introduced by LeBoutillier & Waylen (1993), applies the same ranking procedure separately to each year of record. For a fixed exceedance probability *p*, the corresponding annual flow values (ordinates) are then summarized across years using measures of central tendency, such as the mean or median, to capture interannual variability in the AFDCs at each probability level. This year-by-year framework inherently facilitates uncertainty analysis, as a single period-of-record FDC masks the sampling variability of specific quantiles (Figure 1.2). Nonparametric confidence intervals can thus be derived by treating the *n* annual values at each *p* as a sample, from which intervals at a desired level (e.g., 95%) are constructed around the central estimate.

To illustrate the concept, Figure 1.2 shows individual FDCs for four specific years (2001 in orange, 2002 in red, 2003 in green, and 2004 in blue). Each curve plots discharge (in m^3/s) against exceedance probability (in %), demonstrating how flow varies within each year—from high discharges at low exceedance probabilities (rare, high-flow events) to low discharges at high probabilities (common, low-flow conditions). The inset graph provides a time-based view, plotting discharge against the number of days in the year, highlighting the duration of flows above certain levels. This per-year visualization reveals interannual differences, such as the steeper decline in

2001 compared to later years, which could indicate varying hydrological conditions like wetter or drier periods.

Figure 1.3 depicts AFDCs aggregated across multiple years, using a logarithmic scale for discharge to better capture the wide range of flow values. The red lines represent empirical AFDCs (individual year curves), the solid blue line shows the median AFDC (central tendency across years), and the lighter blue bands or lines indicate percentile AFDCs (capturing variability). Annotations highlight key exceedance probabilities, such as p=0.95 and p=0.05. This plot explains how the annual-based approach summarizes variability: the median curve provides a typical FDC, while percentiles offer confidence intervals, allowing for uncertainty assessment in hydrological planning, such as reservoir design or environmental flow requirements.

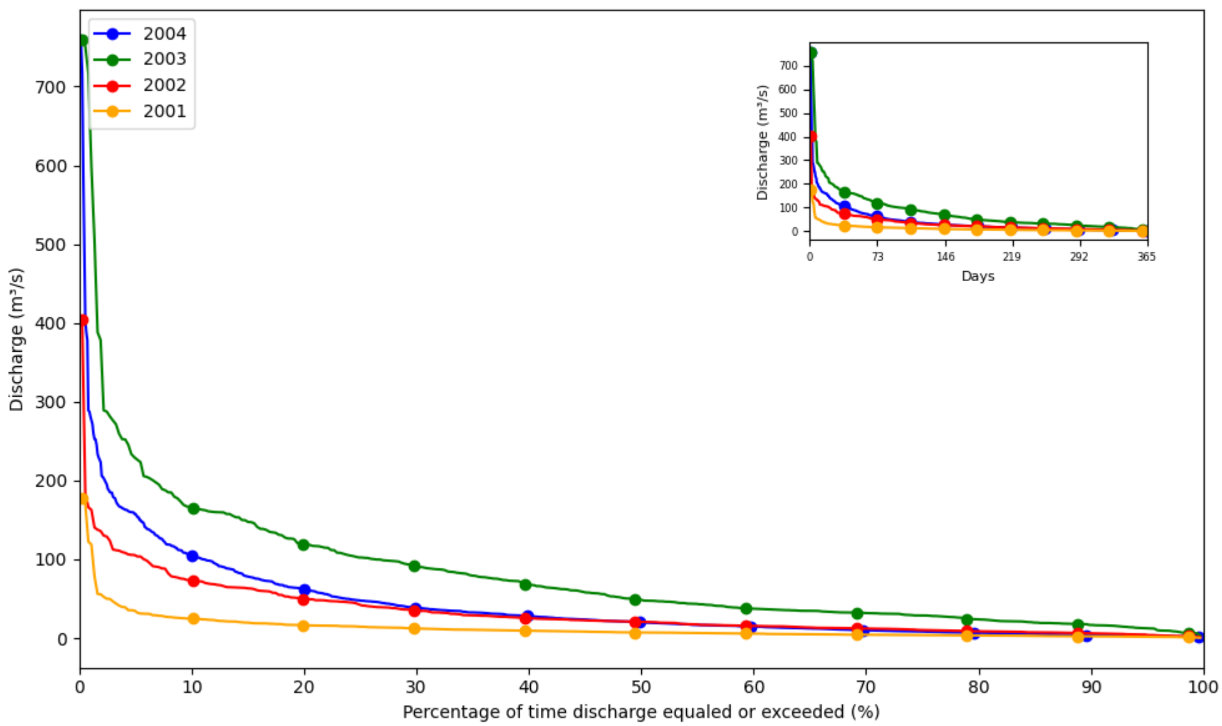

Figure 1.2: FDCs for individual years 2001–2004, illustrating year-to-year variability in river discharge versus exceedance probability. Inset: Cumulative discharge duration in days.

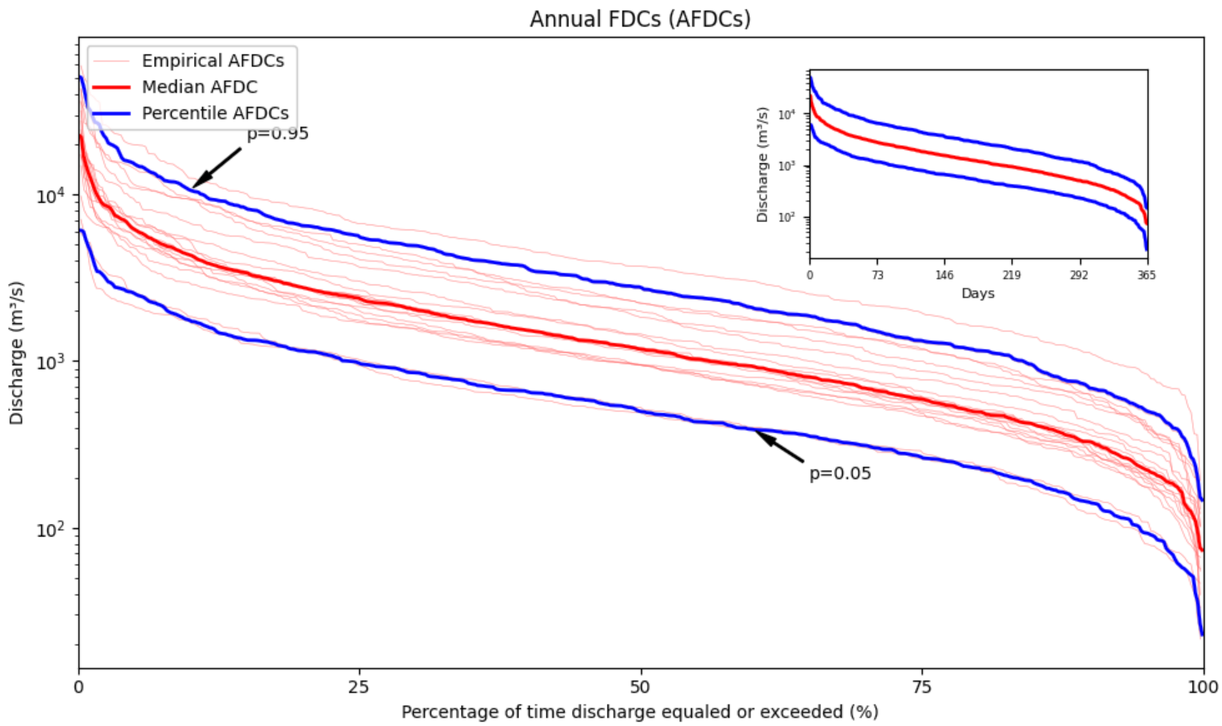

Figure 1.3: AFDCs showing empirical data (red), median AFDC (blue), and percentile-based variability (light blue), with annotations for key exceedance probabilities (p=0.95 and p=0.05).

1.2.3. Comparative Interpretation: Period-of-Record FDC vs AFDC

The period-of-record flow-duration curve (FDC) summarizes the full range of observed discharges over an entire historical dataset. It is commonly used for tasks such as filling data gaps, extending daily streamflow series, and—when combined with regional models, generating daily flows at ungauged sites. However, its interpretation depends heavily on the specific record used: an empirical FDC from a finite sample simply shows the proportion of days in that record when a given discharge was exceeded. It should not be confused with the probability distribution of independent "annual" flows. Longer records can reduce sampling errors and improve quantile estimates, but unlike traditional flood or low-flow frequency analyses, the probabilistic interpretation of a period-of-record FDC remains tied to the observation period.

In contrast, annual flow-duration curves (AFDCs) are designed to describe hydrologic conditions in wet, typical, and dry years. They enable the creation of confidence intervals around a representative curve (e.g., the median annual curve) and allow return periods to be assigned to specific annual curves. The median AFDC is particularly robust, as it resists distortion from isolated floods or droughts while preserving the typical magnitude-frequency structure of daily streamflow. Since their reintroduction, AFDCs have proven valuable in various hydrologic and ecohydrologic applications. They have been used to anticipate hydropower production (Mohor et al., 2015), to assess regional similarity among streams under differing flow regimes (Patil & Stieglitz, 2011), and to describe variability in baseflow conditions (Hamel et al., 2015). They also support comparisons of streamflow regimes across catchments (Hrachowitz et al., 2009) and before–after evaluations of land-use change (Kinoshita & Hogue, 2015); in ecological assessments, related AFDC metrics have been applied to quantify delays in fish passage (Lang, 2005). Collectively, the ensemble of AFDCs summarizes how within-year flow patterns vary from year to year, whereas the period-of-record FDC provides a single, time-aggregated portrait of overall site conditions.

1.3. Flow Regime Classification

1.3.1 Exceedance-Probability Zones

FDC is a fundamental tool in hydrology for characterizing streamflow regimes and informing water resource management, flood analysis, and environmental flow assessments. According to the United States Environmental Protection Agency, an FDC is typically partitioned into five exceedance-probability zones to describe distinct hydrological conditions: high flow (0–10%), moist conditions (10–40%), mid-range flow (40–60%), dry conditions (60–90%), and low flow (90–100%). These zones, as illustrated in Figure 1.4, provide a framework for interpreting streamflow variability (Ranatunga et al., 2016).

High-Flow Zone (0–10% Exceedance)

The high-flow zone, corresponding to the 0–10% exceedance probability, represents the highest streamflow rates that occur least frequently, typically associated with flood events or extreme runoff conditions. These flows are driven by intense precipitation, snowmelt, or a combination of both. This zone is critical for flood risk assessment, infrastructure design, and floodplain management. For example, Vogel and Fennessey (1995) highlight the importance of the high-flow zone in determining flood frequency and magnitude, emphasizing its role in probabilistic flood modeling.
m

Moist Conditions (10–40% Exceedance)

The moist conditions zone (10–40% exceedance) reflects periods of above-average streamflow, often associated with seasonal rainfall or moderate runoff events (Yokoo & Sivapalan, 2011).
This zone is indicative of wetter-than-normal conditions and is crucial for understanding water availability for irrigation, hydropower, and ecological needs. Studies such as,(Searcy, 1959)emphasize the utility of this zone in assessing sustainable water yields for reservoir management.

Mid-Range Flow (40–60% Exceedance, Q_{50})

The mid-range flow zone (40–60% exceedance) encompasses the median flow, commonly referred to as Q_{50}, which represents the flow rate that is equaled or exceeded 50% of the time. Q_{50} is a key metric for characterizing typical streamflow conditions and serves as a benchmark for comparing flow regimes across different watersheds. It is widely used in environmental flow assessments and water quality studies, as it reflects the central tendency of a river's flow behavior. (Castellarin, Galeati, et al., 2004) discuss the application of Q_{50} in regional flow-duration curve estimation, highlighting its role in hydrological modeling.

Dry Conditions (60–90% Exceedance)

The dry conditions zone (60–90% exceedance) corresponds to below-average flows, often occurring during periods of limited precipitation or drought. This zone is critical for assessing water scarcity, planning water supply systems, and evaluating ecological impacts during low-flow periods(Botter et al., 2008).

Low-Flow Zone (90–100% Exceedance)

The low-flow zone (90–100% exceedance) represents the lowest streamflow rates, which are equaled or exceeded most of the time. These flows, often referred to as baseflow, are sustained by groundwater contributions and are critical for maintaining aquatic ecosystems during dry periods. Baseflow is strongly influenced by the geological characteristics of a watershed, such as aquifer permeability, soil type, and bedrock structure. For example, Longobardi & Villani (2013) demonstrate that watersheds with high-permeability substrates have higher baseflows compared to those with low-permeability substrates.

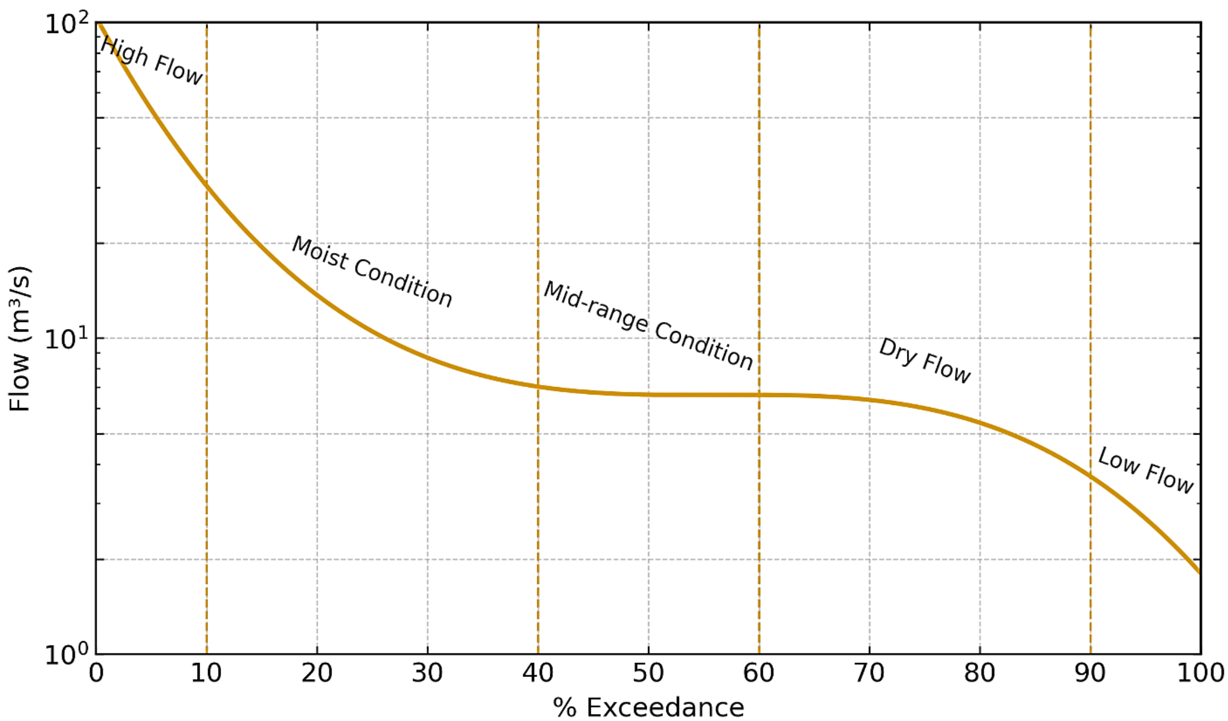

Figure 1.4: Schematic representation of a FDC divided into five hydrological zones based on exceedance probability, illustrating distinct flow regimes: high flow (0–10%), moist conditions (10–40%), mid-range conditions (40–60%), dry flow (60–90%), and low flow (90–100%). (Ranatunga et al., 2016)

1.3.2 Interpretation of FDC Shapes

The shape of FDC is a key hydrological tool that captures storage characteristics of a catchment's streamflow regime. FDCs can be categorized into three main classes: steep (or flashy), moderate, and flat (or mild), as originally outlined by Searcy (1959). Figure 1.5 illustrates four schematic examples of FDC shapes, each plotted with dimensionless flow (normalized discharge) on the y-axis against duration (percentage of time) on the x-axis, highlighting variations in streamflow regimes.

Moderate FDCs exhibit a more gradual decline in flow across the duration axis. These curves typically correspond to catchments where both direct runoff and groundwater contributions are present, resulting in a more balanced flow regime with reduced variability**.** Panel (a) represents this type of response, indicating streams with predominantly fluvial regimes that experience only brief and infrequent dry periods.

Flat or mild FDCs**,** on the other hand, show a gentle and nearly horizontal slope, signifying stable and sustained flow conditions throughout the year. This behavior is characteristic of catchments with significant groundwater storage, low topographic gradients, or regulated flow regimes. In such systems, baseflow dominates, and flow rarely, if ever, ceases. This is clearly depicted in panel (b)**,** which illustrates streams with permanent flow maintained by perennial storage sources.

Steep or flashy FDCs are characterized by a rapid decline from high to low flows, indicating that streamflow is predominantly driven by short-lived, high-intensity precipitation events with minimal buffering from groundwater or surface storage. Such curves often approach or reach zero flow for a significant portion of the time, particularly in arid or steep catchments. In the illustrative figure, this behavior is exemplified by panel (c)**,** which represents highly torrential streams with extended dry periods. Similarly, panel (d) depicts streams with flashy characteristics but without complete cessation of flow, indicating the presence of some residual baseflow that prevents the discharge from reaching zero.

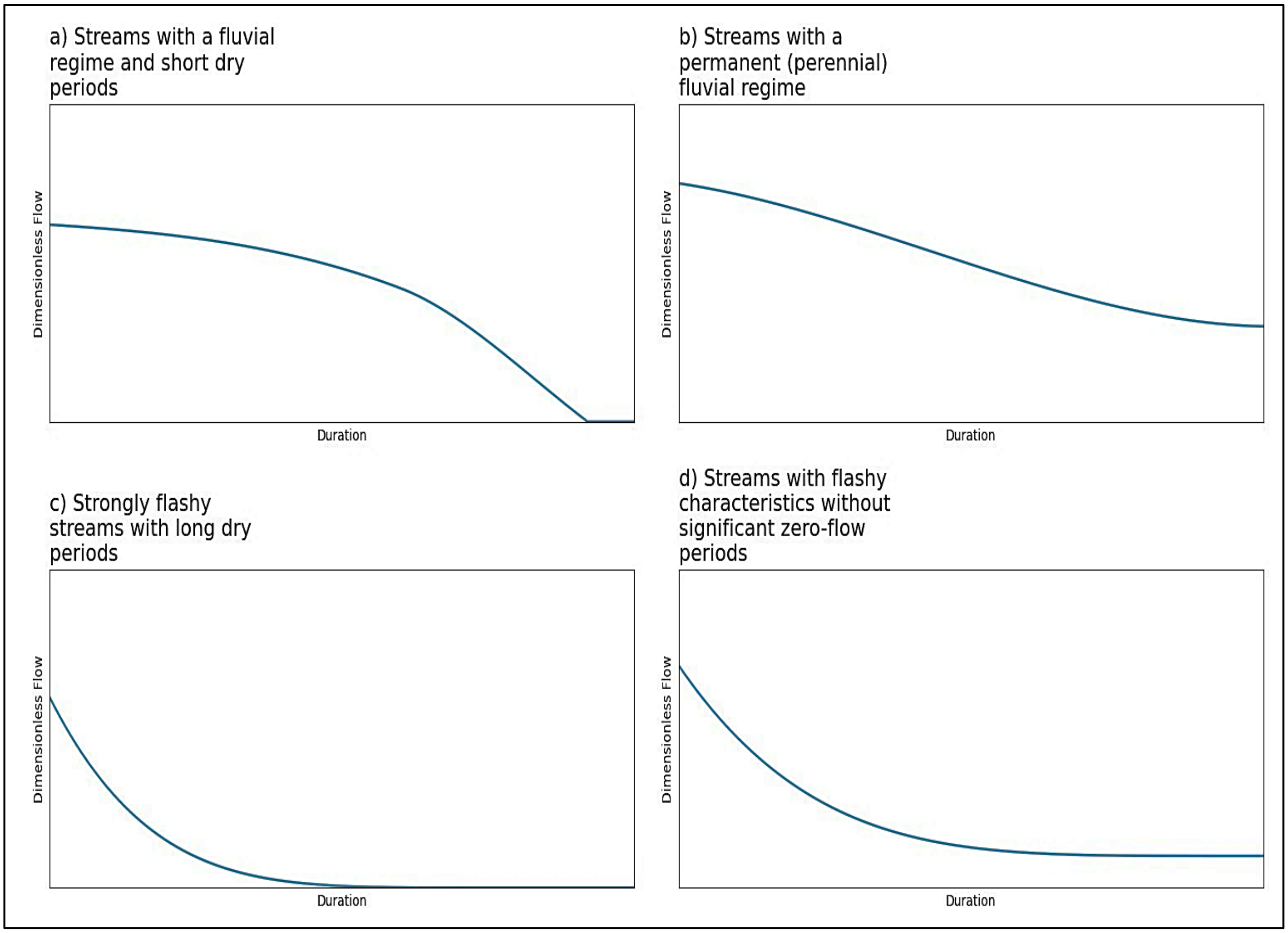

Figure 1.5: Schematic representations of FDC shapes for different streamflow regimes

1.4. FDCs Applications

FDCs have been applied across a wide spectrum of water-related disciplines, reflecting their versatility in addressing both practical and scientific challenges. These applications can be broadly categorized into engineering design, environmental management, hydrological modeling, and interdisciplinary analyses.

In engineering design**,** FDCs are fundamental to the planning and operation of hydraulic infrastructures. Within hydropower development, they quantify flow availability, thereby supporting the estimation of energy generation potential and the optimization of turbine sizing (Basso & Botter, 2012; Müller et al., 2014). Similarly, they guide the design of water supply networks, irrigation schemes, and wastewater treatment facilities by providing robust estimates of flow exceedance probabilities(Darshana et al., 2012; Hanafi et al., 2012).
In environmental management**,** FDCs serve as essential tools for monitoring water quality, assessing stream pollution, and managing reservoir sedimentation (Jang et al., 2021). They are particularly valuable in low-flow hydrology, where they help define minimum flow thresholds necessary to sustain aquatic ecosystems and comply with regulatory mandates in industrialized

contexts (Claps & Fiorentino, 1997). Furthermore, FDCs support environmental flow assessments by ensuring that residual streamflows are sufficient to maintain ecological integrity (Smakhtin & Batchelor, 2005;Ceola et al.,2018).

In hydrological modeling**,** FDCs are indispensable for characterizing streamflow variability, sediment transport capacity, and channel erosion potential (Powell et al., 2016). They are widely used in the calibration and validation of rainfall–runoff models, enhancing their ability to accurately represent catchment-scale hydrological processes (Westerberg et al., 2011;Vrugt & Sadegh, 2013). In ungauged basins, FDCs underpin regionalization approaches that transfer information from hydrologically similar catchments, thereby enabling reliable streamflow prediction in data-scarce environments(Archfield et al., 2013; Choubin et al., 2019).

Moreover, FDCs have found increasing relevance in interdisciplinary research**.** Within climate change impact assessment, they provide a framework to evaluate how alterations in climate and land use reshape streamflow regimes, adaptation and mitigation strategies (Brown et al., 2013; Müller & Thompson, 2016). In urban hydrology, FDCs are applied to analyze stormwater dynamics under varying rainfall intensities, thereby supporting flood risk management and urban resilience planning (Petrucci et al., 2014). Their utility extends further to drought risk assessment (Kjeldsen et al., 2000), snowmelt-driven runoff analysis (Kim & Kaluarachchi, 2014), and groundwater recharge estimation (Arnold et al., 2000). In ecological applications, FDCs contribute to watershed and forest management, wetland conservation, and assessments of hydrological recovery following wildfires (Acreman, 2005; Creed et al., 2008).

1.5. Regionalization of FDCs

Castellarin, Galeati, et al. (2004) classified FDC regionalization methods into two broad categories: statistical and non-statistical approaches. Statistical methods assume that the shape of FDCs can be represented by a theoretical probability distribution function. The parameters of the chosen distribution are estimated at gauged sites and then related to physiographic and climatic descriptors of the catchments through regional regression models. Non-statistical methods, in contrast, are divided into parametric and graphical approaches. Parametric approaches fit analytical equations directly to observed FDCs, providing transferable mathematical expressions. Graphical approaches replace analytical relationships with standardized FDC representations of regional validity. These are obtained by normalizing observed curves and pooling them across hydrologically homogeneous basins, yielding regional templates applicable to ungauged sites.

1.5.1 Statistical Approaches

Statistical approaches to FDC regionalization are grounded in probability theory, representing the FDC as the complement of a cumulative distribution function (CDF) fitted to observed streamflow data. In these methods, a suitable probability distribution is selected to capture the empirical relationship between discharge magnitude and exceedance probability over a specified range of flows. Once a parent distribution is identified, its parameters are estimated at gauged sites, typically by minimizing the deviation between the observed exceedance probabilities and those predicted by the fitted distribution. The choice of probability distribution and the range of percentiles used for fitting can significantly influence the quality of representation, as different regions and flow regimes exhibit distinct statistical characteristics.

A key difficulty in statistical hydrology is the identification of a probability distribution capable of capturing the full range of streamflow variability, from infrequent flood peaks to prolonged periods of low flow. Over time, a broad spectrum of candidate distributions has been explored, spanning

from relatively simple two-parameter formulations to more complex models incorporating up to five parameters. Frequently investigated examples include the Gumbel, Pearson Type III, log-normal, generalized Pareto (GP), Kappa (KAP), and mixed log-normal distributions(Tasker, 1987; Kroll & Vogel, 2002; Kumar et al., 2004; Shabri & JeMain, 2010; Liu et al., 2016; Kjeldsen et al., 2017; Blum et al., 2017;O'Shea et al., 2023).
From a statistical perspective, the choice of parent distribution is critical because it governs the ability to reproduce the observed shape of the FDC and to extrapolate reliably into unobserved flow ranges. Different studies have proposed alternative probability models. For example, LeBoutillier & Waylen (1993) demonstrated that a five-parameter mixed lognormal distribution outperformed simpler alternatives, specifically, the two- and three-parameter lognormal, Gamma, and generalized extreme value (GEV) distributions, when modelling mean annual FDCs for four Canadian rivers. Claps & Fiorentino (1997) employed a two-parameter lognormal distribution to fit AFDCs in 14 basins in southern Italy, deriving regional models from normally distributed annual parameters. Singh et al. (2001) developed a statistical regional model in the Himalayan region using the normal frequency distribution applied to normalized 10-day streamflow series.
Li et al. (2010) found that the three-parameter lognormal distribution provided an adequate fit to FDC in southeastern Australia. In Italy, both the four-parameter kappa distribution (KAP) and its special case, the generalized Pareto distribution (GPA), have been widely applied in the studies (Castellarin et al., 2007; Mendicino & Senatore, 2013), while same approaches have been reported for the northeastern United States(Vogel & Fennessey, 1994). However, the statistical fitting of these models is not without challenges. Archfield (2009) noted that both KAP and GPA can exhibit unrealistic lower bounds in the fitted distribution, potentially yielding negative flows when generating synthetic series, an issue that undermines physical plausibility. This is a typical problem in fitting parametric distribution when the tail behavior is poorly constrained by data or when the functional form imposes inappropriate asymptotic limits. Such issues are particularly relevant when the fitted distribution is used for stochastic generation of daily flows, as even a small proportion of negative values can distort subsequent hydrological analyses.
Several studies (LeBoutillier & Waylen, 1993; Castellarin, Vogel, et al., 2004; Archfield, 2009) consistently indicate that representing the empirical FDC often requires relatively complex models with at least four parameters, which offer the flexibility to capture skewness, kurtosis, and asymmetry in both high- and low-flow regimes. While this added complexity can improve goodness-of-fit across the entire probability range, it also increases parameter uncertainty and the potential for overfitting, particularly when short or noisy records are used. For this reason, some researchers have proposed focusing on a subset of the FDC, low- to median-flow, thereby reducing the influence of extreme high flows and allowing simpler models to perform adequately (Costa et al., 2014).
Selecting an appropriate distribution to represent streamflow variability requires balancing flexibility with parsimony. While multi-parameter distributions such as Burr or Kappa provide considerable flexibility, they often suffer from identifiability issues and strong parameter correlations, which limit their regional applicability. By contrast, the log-normal distribution offers a parsimonious and robust alternative: with only two parameters, it can capture the essential features of FDCs. Empirical evidence from southern Italy (Claps & Fiorentino, 1997; Longobardi & Villani, 2013) has shown that the log-normal distribution can reproduce FDCs with high accuracy, while maintaining the advantages of simplicity and practicality. Log-normal distribution effectively captures the positively skewed nature of streamflow data, where low flows are frequent and high flows are rare, making it a staple in probabilistic FDC modeling. This aligns well with

regionalization efforts, where parameterizing the distribution (e.g., mean and variance of log-transformed flows) facilitates transferring models from gauged to ungauged sites via regression or clustering based on physical, geomorphological, and climatic parameters of the catchment.

1.5.2 Non-Statistical Approaches

Regional estimation of FDCs can be broadly categorized into parametric and graphical approaches, each with distinct methodological foundations. Parametric approaches avoid assuming an underlying probability distribution for streamflow and instead directly relate discharges at specific durations (or exceedance probabilities) to physiographic and climatic descriptors of the catchment. The relationships can be expressed through a variety of mathematical forms linear, polynomial, exponential, or power-law chosen according to the hydrological setting and the predictive performance of the model.

Quimpo et al. (1983) applied a two-parameter exponential equation to represent daily FDCs in the Philippines, with the scaling parameter Q estimated from drainage area and the shape parameter mapped spatially across the archipelago. Mimikou & Kaemaki (1985) employed a third-order polynomial to model monthly FDCs in north-western Greece, where coefficients were predicted from mean annual precipitation, drainage area, hypsometric fall, and main channel length. Braud et al. (2013) proposed a three-parameter formulation for the lower portion of daily FDCs in southern-central Italy, linking curve shape and offset parameters to physical basin properties such as imperviousness, size, and slope. Yu et al. (2002) adopted a quantile-based approach in Taiwan, estimating discharges at selected exceedance probabilities (p=10, 20...90%) from physiographic and climatic indices including catchment area, mean basin elevation, slope, and precipitation, and reconstructing the FDC without invoking any theoretical probability distribution. Similarly, Castellarin et al. (2004) developed regional regression models for different quantiles (Q_{30}, Q_{70}, Q_{90}, and Q_{95}), relating them to elevation, drainage area, mean annual precipitation, and main channel length. Mendicino & Senatore (2013) introduced a power-law regression linking the Q_{10} discharge to precipitation and catchment area, highlighting the ability of simple scaling laws to capture the regional variability of specific flow percentiles.

Ganora et al. (2009) focused on the shape component of the FDC, representing it through normalized long-term curves. For regionalization, they adopted a graphical approach in which the dimensionless FDC is considered in its entirety, and pairwise dissimilarities between curves are quantified using a predefined metric. These dissimilarities were then related to variations in catchment descriptors, enabling the grouping of hydrologically similar catchments and the derivation of regional dimensionless FDCs as the average curve for each group.

1.6. The Index Flow Model

1.6.1 Conceptual Framework

The Index Flow Model conceptualizes the FDC as the product of two distinct components: a scale factor and a dimensionless curve that characterizes its shape. The scale factor, typically represented by a characteristic discharge such as the mean annual flow, governs the overall magnitude of the curve, while the dimensionless component captures the normalized shape independently of scale. This decomposition allows the curve's form to be established at a regional level—within hydrologically homogeneous areas—while the magnitude can be locally estimated through physiographic and climatic descriptors. Consequently, the complete FDC for a given site is reconstructed by multiplying the regionally defined shape by the locally derived index flow, making the method particularly suitable for regionalization studies and for predicting flow regimes in ungauged basins. From a methodological perspective, index flow models can be broadly regarded as semi-statistical approaches.

Building on this framework,Castellarin, Vogel, et al. (2004) further formalized the model by representing each daily discharge as the product of two independent stochastic components: the annual flow (AF), which encapsulates the hydrological magnitude of a given year, and the dimensionless within-year share (X^0), which describes the intra-annual distributional shape. Probability distributions are fitted separately to the AF series, often with a log–logistic distribution—and to the X^0 values standardized by their year-specific AF, (using four parameters distribution including the generalized extreme value GEV, generalized logistic GLO and generalized Pareto GPA distributions). Under the assumption of independence, inter-annual variability affects only the magnitude but not the intra-annual pattern, thereby eliminating the need for explicit time-series modelling and removing persistence or seasonality effects. The long-term FDC is then obtained as the probabilistic mixture of the AF and X^0 distributions, while inter-annual variability of annual FDCs can be summarised through percentile envelopes (e.g., 10th, 50th, 90th) or duration curves of variability derived from cross-year dispersion.

A particular challenge in applying the index flow model arises in arid and semi-arid climates, where zero-flow observations are common. In such intermittent or ephemeral river systems, prolonged dry periods often result in extended sequences of no discharge, which complicates statistical modelling. If continuous probability distributions are fitted directly to datasets containing zeros, they may generate physically meaningless negative flows unless an explicit lower bound at zero is imposed (Smakhtin, 2001). While this constraint ensures physical consistency, it simultaneously reduces the flexibility of the distribution to represent the full variability of flows. Consequently, the development of robust regional models in these hydrological settings requires not only careful treatment of zero-flow occurrences, but also an appropriate methodological framework that can reconcile the discontinuity between zero and non-zero states while retaining sufficient descriptive power to capture the dynamics of non-zero flows.

1.6.2 Treatment of Zero-Flow Conditions

The treatment of zero flows constitutes a fundamental element in the development of regional models for catchments with a finite probability of ephemeral behaviour. As emphasized by Haan (1977), three principal strategies have been proposed for incorporating zero values into frequency analysis. The first approach consists of adding a small constant to all observations. While this technique preserves the presence of zero events, it does not overcome the inherent discontinuity between the zero and non-zero states, with the result that continuous probability distributions remain inadequate to fully represent the data. The second approach involves analyzing only the non-zero values and subsequently adjusting the results to reflect the full record. Although applied in practice, this method has been criticized as biased (Haan, 1977), since it disregards the information carried by genuine zero events, which are particularly relevant in arid and semi-arid climates. The third and most rigorous approach is based on the theorem of total probability. In this framework, the hydrological regime is represented by two complementary components: the probability of observing a non-zero flow, and the conditional distribution of flows given that they are non-zero(Jennings & Benson, 1969). By combining these two components, the full flow regime can be reconstructed as a weighted mixture of zero and non-zero states.

Compared with the alternative strategies, the application of the theorem of total probability offers a more robust and hydrologically meaningful solution, as it explicitly integrates the frequency of zero flows into the statistical model rather than obscuring or discarding them. This characteristic is of particular importance in ephemeral rivers, where extended dry periods constitute a natural feature of the flow regime and cannot be adequately captured by methods that treat zeros as artefacts. Consequently, in the context of the present study, this approach was adopted as the most appropriate means of representing the dual behaviour of ephemeral catchments, thereby ensuring consistency in the subsequent regionalization process that seeks to integrate both perennial and ephemeral systems within a unified modelling framework.

Croker et al. (2003) applied the total probability theorem (Haan, 1977) in combination with a log–linear regression model linking mean annual rainfall to estimate FDCs for gauged sites. This method enabled the identification of the cease-to-flow point, expressed as the intermittency ratio—the proportion of zero-flow days relative to the total number of days in the observation period. Building on this concept, (Post (2004); Shao et al. (2009); Costa et al. (2014)) integrated mean flow values and basin descriptors into modelling frameworks that simultaneously incorporated the cease-to-flow point and the slope of the FDC. Similarly, (Viola et al. (2011); Rianna et al. (2011, 2013)) investigated the interplay between hydrological indices, catchment characteristics, and FDC metrics, with the aim of improving the representation of flow regimes in intermittently flowing rivers.

Rianna et al. (2011) applied the index-flow model in combination with the law of total probability to analyze catchments in Italy. Their methodology, based on normalized long-term flow-duration curves, disregarded interannual variability as well as the persistence and seasonality of the series. The parameters of the normal distribution, along with the scale and shape parameters of the Generalized Extreme Value (GEV) distribution, were estimated through equations dependent on geomorphological descriptors. The framework explicitly considered only non-zero flows for the derivation of the conditional distribution, while the total-probability theorem was employed to quantify the cease-to-flow condition, expressed as the proportion of time the river remains dry. Their analysis demonstrated that the parameters defining the shape of the normalized long-term FDC are strongly controlled by the permeability of the catchment substrate and the mean basin elevation. This indicates that the FDC shape primarily reflects physical factors associated with infiltration capacity and topographic setting. The cease-to-flow condition was also shown to depend on catchment permeability and drainage area: more permeable basins and larger contributing areas generally experience fewer zero-flow days. In contrast, the scale factor of the index-flow model was found to be governed predominantly by the drainage area, underscoring the role of basin size as the main determinant of overall discharge magnitude.

Building upon this,(Mendicino & Senatore, 2013) extended the methodology by integrating the index-flow model with the law of total probability, assigning distinct statistical distributions to both the normalized daily streamflow series (X') and the annual flow (AF). For X', they tested a two-parameter log-logistic distribution and a four-parameter kappa distribution, while in an alternative configuration they coupled a cubic-root-transformed normal distribution for AF with a three-parameter generalized Pareto (GPA) distribution for X'. Their analysis, conducted in Calabria, explicitly addressed the intermittent regimes typical of southern Italian catchments, where zero-flow conditions are common. They noted that assuming a constant cease-to-flow parameter hinders the ability to capture interannual variability, limiting the construction of confidence intervals based on annual FDC percentiles. Their regression analysis further revealed that FDC shape parameters were mainly related to geological attributes, perenniality indices, and

elevation differences, while the parameters associated with AF were strongly influenced by total annual precipitation and drainage area.
Their analysis involved regressing the parameters obtained from the fitted statistical distributions against catchment descriptors. The results showed that the parameters describing the shape of the normalized FDC were primarily related to geological characteristics of the catchment, perenniality indices, and elevation differences. In contrast, the parameters associated with the annual flow (AF) exhibited strong relationships with total annual precipitation and drainage area.

1.7. Contributions of the Present Study

In light of the prevailing literature, the present thesis advances the regionalization of FDCs in Italy by overcoming methodological and geographical limitations that characterized earlier research. Previous investigations were generally confined to relatively small spatial domains or to catchments with limited hydrological variability. By contrast, this study extends the regionalization framework to a substantially broader and more diverse territory, encompassing the regions of Campania, Calabria, Basilicata, Puglia and parts of Lazio and Molise (as seen in figure1.6). This area integrates a wide range of hydro-climatic settings, from Mediterranean coastal basins to upstream montane systems, thus providing a unique opportunity to evaluate the robustness of the index-flow model under markedly heterogeneous environmental conditions. To the best of the author's knowledge, this constitutes one of the most comprehensive efforts to date in the regionalization of FDCs in Italy, with particular emphasis on the southern regions, and significantly strengthens the understanding of intermittent Mediterranean catchments.
A key innovation of this work lies in the explicit incorporation of geological information. Earlier Italian studies relied largely on empirical or proxy indicators to capture the influence of lithology on runoff processes and low-flow dynamics. While useful for exploratory analyses, such surrogates provided only approximate representations of geological variability. In contrast, this thesis introduces the use of digitized geological maps, processed within a Geographic Information System (GIS), as an integral component of regionalization. This approach allows a more detailed characterization of lithological features—particularly substrate permeability—and their role in modulating FDC parameters, thereby yielding a refined understanding of baseflow persistence and low-flow mechanisms.
Methodologically, the thesis departs from earlier approaches that relied heavily on multi-parameter probabilistic distributions to describe FDC scale and shape. Instead, it develops a semi-statistical index-flow model in which the dimensionless FDC shape is parsimoniously parameterized using the log-normal distribution, chosen for its demonstrated capacity to reproduce normalized long-term FDCs with few parameters. The scale component, in turn, is estimated through regression models linking it to key physiographic and climatic descriptors. This twofold strategy, statistical for the non-dimensional curve and deterministic for the scaling factor, achieves a balance between parsimony and hydrological realism, enhancing predictive reliability at ungauged sites.
Taken together, these elements underscore both the originality and scholarly relevance of the study. It represents a pioneering attempt to regionalize FDCs across a large and hydro-climatically diverse sector of Southern Italy, where intermittent Mediterranean regimes are widespread; it is the first Italian application to integrate GIS-derived geological datasets together with detailed land-cover information; and it provides one of the most comprehensive assessments to date of how permeability, climatic gradients and catchment characteristics jointly shape FDC behaviour under intermittent conditions. Collectively, these contributions mark a significant advance over prior Italian research and situate the study firmly within the international discourse on FDC

regionalization, offering methodological insights of broad applicability to ungauged basins worldwide.

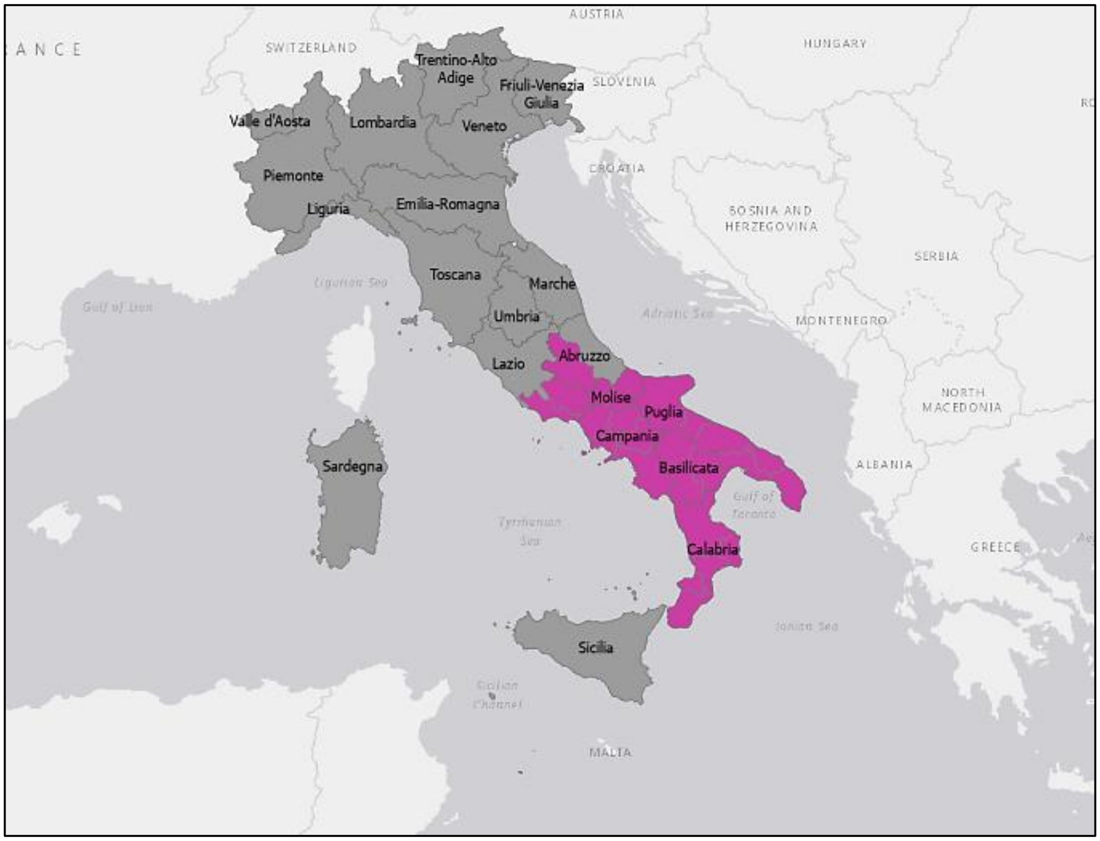

Figure 1.6: Study area in southern Italy

2. Data Collection and Preprocessing

Chapter 2 introduces the data used in the study and the steps taken to prepare it for analysis. It outlines the digitization of historical hydrological records, the challenges of ensuring accuracy, and the validation procedures applied to create a consistent dataset. It also describes the treatment of discharge and precipitation data, the estimation of baseflow indices, and the criteria for selecting reliable gauging stations. The outcome is a curated dataset that provides a solid foundation for the construction and regionalization of Flow Duration Curves (FDCs).

2.1 Digitization of Validated Hydrological Records

2.1.1 Overview of Source: Annali Idrologici

The systematic documentation of Italy's hydro-meteorological data, including measurements such as river flow and precipitation, has been preserved in the Hydrological Yearbooks published by the National Hydrological and Mareographic Service (Servizio Idrografico e Mareografico Nazionale, SIMN) since the early 20th century. These yearbooks represent a comprehensive archive of national hydrological records, providing data on daily and monthly river discharge as well as precipitation totals. An example of these records, taken from one page of the Annali Idrologici, is shown in Figure 2.1. This historical dataset is essential for analyzing Italy's hydrological patterns and supporting effective water resource management.

2.1.2 Regional Scope and Data Scarcity in Southern Italy

In southern Italy, data scarcity has long impeded hydrological research and management efforts. Previous studies aimed at recovering historical hydro-meteorological data were limited in scope, often focusing on small geographical areas or restricted time periods, such as specific years or sub-regions within a single province (Franchini & Suppo, 1996; Ganora et al., 2009; Viola et al., 2011; Longobardi & Villani, 2013; Mendicino & Senatore, 2013; Castellarin, 2014; Pumo et al., 2014). Although valuable, these efforts did not meet the broader need for comprehensive, region-wide datasets. The present study represents a significant advancement, as it is the first known comprehensive effort at this scale to digitize and consolidate historical hydro-meteorological data from ISPRA regional offices for Napoli (covering Campania and adjacent areas including marginal parts of Lazio and Molise), Catanzaro (covering Calabria and southern portions of Basilicata), and Bari (covering Puglia and the remaining eastern portions of Basilicata). The study area covers approximately 20% of Italy and spans diverse hydrological regimes, from Mediterranean climates with seasonal rainfall to mountainous catchments with complex river systems. This unprecedented regional scope sets the current work apart from prior research, offering a more holistic dataset for southern Italy.

2.1.3 Challenges of Manual Transcription

The digitization process encountered substantial challenges due to the age and condition of the yearbooks. Many records, some over a century old, are degraded, showing faded ink, brittle pages, and inconsistent formatting. Daily discharge data, which include river flow rates for each day, were especially susceptible to errors during manual transcription. The large volume of data points—365 measurements per year for each gauging station—combined with difficulties in interpreting faded or smudged numbers, increased the risk of transcription errors. Variations in table layouts, outdated typefaces, and occasional handwritten annotations further complicated the extraction process that hinder accurate digitization (as illustrated in Figure 2.1).

To address these issues, a mixed approach was adopted. While OCR software was applied as an initial step for some stations, its effectiveness was limited by the poor quality of many yearbooks. Consequently, the majority of the records were transcribed manually to ensure accuracy and consistency.

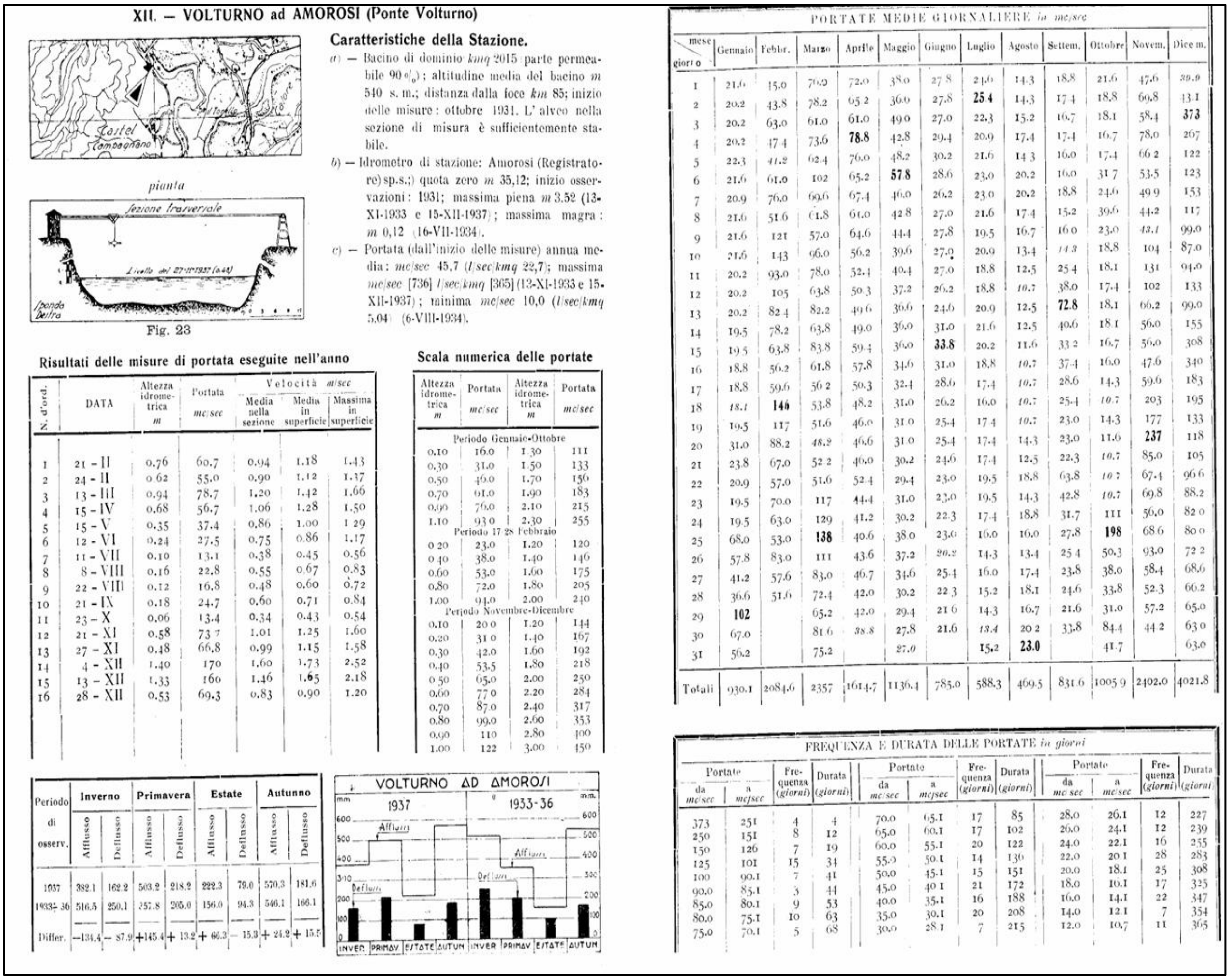

Figure 2.1: Example page from the Annali Idrologici *showing daily discharge records.*

2.1.4 Validation Protocols for Daily Discharge Records

To guarantee the accuracy and consistency of the digitized dataset, rigorous validation protocols were applied. Data were cross-referenced with available secondary sources. A key validation step involved comparing daily discharge data with summary tables that report mean, minimum, and maximum monthly discharge values derived from historical records. For instance, a table might indicate that a river in Calabria had a mean discharge of 10 m^3/s, a minimum of 5 m^3/s, and a maximum of 15 m^3/s for January 1960. To validate the daily data, the mean of the daily discharge values for each month was computed and compared to the reported monthly mean.

The resulting digital archive constitutes a homogeneous and accessible resource that preserves Italy's historical hydrological records and facilitates modern analytical applications. It forms the foundation for the regionalization of FDCs. The digitized dataset not only improves the understanding of hydrological processes in southern Italy but also provides a model for preserving and utilizing Italy's hydrological heritage, thereby supporting sustainable water management practices across the studied regions.

2.1.5 Statistical Characterization of Daily Discharge and Annual Precipitation

To support the hydrological analysis across the study area, daily discharge and annual precipitation data were systematically extracted from the digitized Annali Idrologici records. These two variables were selected for their fundamental role in characterizing hydro-climatic behavior and were obtained for each of the validated gauging stations.

Daily Discharge

For each station, daily discharge values were processed to compute a set of ten quantiles (Q_5 to Q_{90}), providing a condensed but comprehensive representation of flow conditions across the full spectrum of observed values. These quantiles summarize discharge variability without requiring assumptions about data distribution or temporal structure.

The results indicate substantial variation across the study area. Mean discharge values range from 1.59 m³/s at Q_5 to 18.34 m³/s at Q_{90}, while maximum values span from 30.5 m³/s (Q_5) to 182.0 m³/s (Q_{90}). Minimum values are consistently equal to 0.00 m³/s up to Q_{40}, which confirms the presence of intermittent rivers within the monitored network (Table 2.1).

Median values increase steadily, from 0.20 m³/s at Q_5 to 6.06 m³/s at Q_{90}**,** and the standard deviation also grows with increasing quantile level—from 4.35 m³/s (Q_5) to 33.63 m³/s (Q_{90})—reflecting greater dispersion at lower flow conditions. This statistical summary confirms the presence of a wide range of discharge conditions across the monitored stations, highlighting notable differences in hydrological behavior throughout the region.

Table 2.1: Descriptive Statistics of Daily Discharge Quantiles (Q_5–Q_{90})

Statistic	Q_5	Q_{10}	Q_{20}	Q_{30}	Q_{40}	Q_{50}	Q_{60}	Q_{70}	Q_{80}	Q_{90}
Minimum	0.00	0.00	0.00	0.00	0.00	0.02	0.04	0.07	0.13	0.25
Maximum	30.5	34.0	41.3	49.0	54.9	64.9	76.0	92.0	117.0	182.0
Mean	1.59	1.97	2.66	3.38	4.22	5.34	6.74	8.66	11.74	18.34
Median	0.20	0.29	0.42	0.63	0.91	1.34	1.65	2.32	3.12	6.06
Std. Dev.	4.35	5.12	6.55	7.95	9.41	11.34	13.61	16.75	21.96	33.63

Annual Precipitation

Annual precipitation data were extracted for the same stations and time periods as the discharge records. The values were used to compute the mean annual precipitation (*MAP*) at each site, offering a summary of long-term rainfall conditions.
The *MAP* across all stations ranges from below 600 mm/year to above 1800 mm/year, indicating considerable spatial variability. The distribution of these values is illustrated in Figure 2.2, which shows a bimodal distribution where the highest frequency (14 stations) occurs in the 600-700 mm/year bin, followed by a second peak (12 stations) in the 1100-1200 mm/year bin, with frequencies gradually declining toward the lower (<600 mm/year) and higher (>1600 mm/year) extremes.

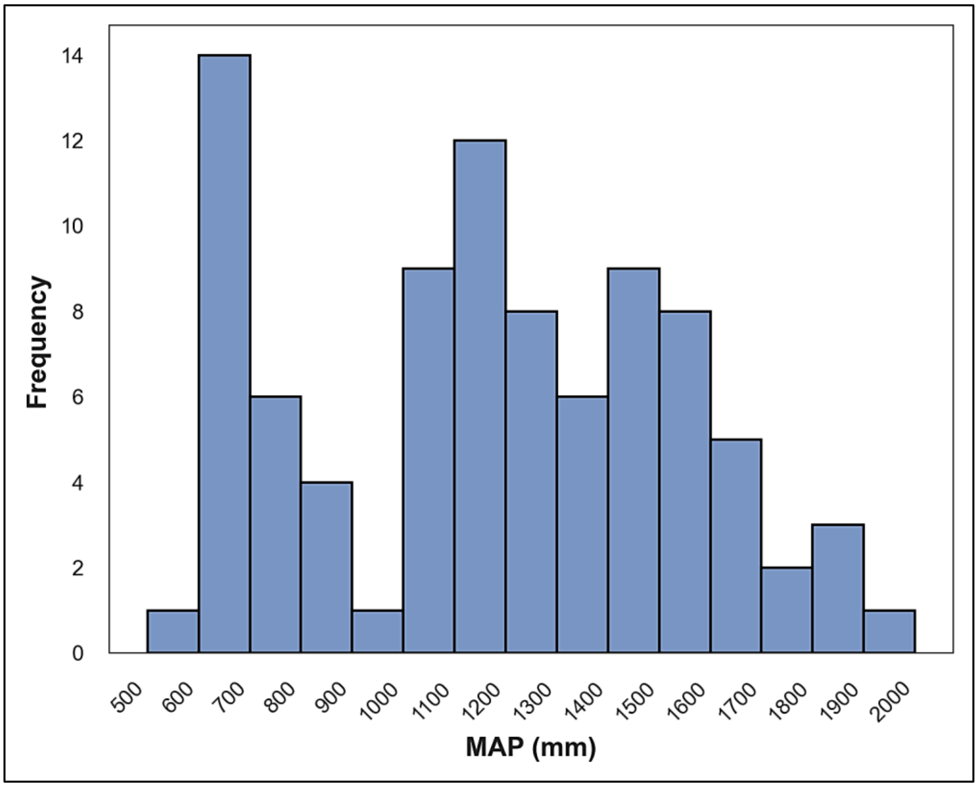

Figure 2.2: Histogram of Mean Annual Precipitation (MAP)

Together, the discharge quantiles and precipitation values offer a consistent and quantitative framework for characterizing the hydro-climatic variability observed across the region, providing essential input for subsequent analyses.

2.2 Validation and Selection of Gauging Stations

The validation of hydrological datasets constitutes a foundational step in ensuring the accuracy, internal consistency, and analytical reliability of flow-based assessments, particularly within the framework of Flow Duration Curve (FDC) regionalization. As FDCs serve as essential tools in characterizing hydrological regimes and supporting sustainable water resource management, any

deficiencies in the underlying data can propagate significant errors in model calibration, regional extrapolation, and hydrological interpretation (Castellarin, Galeati, et al., 2004).
This study utilizes historical daily discharge data from 127 gauging stations distributed across three regions in southern Italy: Napoli (1925–1994), Bari (1950–1996), and Catanzaro (1950–1984). Table 2.2 catalogues the 127 gauging stations used in this study across southern Italy—Bari (B, n = 23), Catanzaro (C, n = 51), and Napoli (N, n = 53). Record lengths are highly heterogeneous, ranging from 1 to 70 years, with frequent discontinuities (non-consecutive year blocks).
Although these datasets span extensive time periods and are invaluable for long-term hydrological analysis, they are characterized by various inconsistencies, stemming from irregular monitoring schedules, infrastructural changes, and operational interruptions over the decades of data collection. Moreover, several stations present specific limitations that compromise their direct applicability to FDC construction, including short or fragmented records, and anthropogenic alterations such as dam regulation. This chapter systematically identifies and analyzes the six principal categories of limitations observed across the dataset. Each issue is critically examined in terms of its technical implications for data quality, its potential to introduce bias in FDC derivation, and the rationale for either excluding or correcting affected records. The goal is to develop a curated, high-integrity dataset capable of accurately reflecting the natural hydrological variability within the study regions.

Table 2.2: Summary of 127 gauging stations in southern Italy.

No.	Station's Code	Station Name	Number of recorded years	Year Ranges
1	B1	Ofanto a Samuele di Cafiero	43	1952-1994
2	B2	Celone a Ponte Foggia .S. Severo	41	1954, 1956-1995
3	B3	Cervaro ad Incoronata	41	1952-1986, 1988-1992, 1994
4	B4	Salsola a Ponte Foggia .S. Severo	40	1952-1954, 1959-1983, 1985-1996
5	B5	Arcidiaconata a Ponte Rappola-Lavello	40	1952-1955, 1957-1987, 1990-1994
6	B6	Ofanto a Monteverde	39	1956-1994
7	B7	Ofanto a Cairano	31	1963-1992, 1994
8	B8	Vulgano a Ponte Troia Lucera	27	1967-1986, 1988-1994
9	B9	Carapelle a Carapelle	26	1954-1978, 1980
10	B10	Celone a Vincenzo	25	1967-1973, 1975-1980, 1982-1984, 1987-1988, 1990-1996
11	B11	Salsola a Casanova	23	1967-1972, 1974-1988, 1990-1991
12	B12	Atella a Ponte sotte Atella2	22	1973-1994
13	B13	Triolo a Ponte Lucera Torremaggiore	22	1967-1984, 1988-1991
14	B14	Lapilleso a Ponte S	22	1973-1994
15	B15	Venosa a Ponte Ferroviaro	21	1973-1993
16	B16	Atella a Ponte sotte Atella1	21	1952-1972
17	B17	Canale S.Maria a Ponte Lucera Torremaggiore	20	1967-1976, 1978-1984, 1986, 1988, 1996
18	B18	Venosa a Ponte S.Angelo	17	1952-1953, 1956-1959, 1961-1971
19	B19	Casanova a Ponte Lucera Motta1	15	1973-1982, 1988, 1990-1991, 1995-1996
20	B20	Locone a Ponte Brandi	12	1971-1972, 1974-1983
21	B21	Carapelle a Ponte Vecchio Ordona	10	1986-1988, 1990-1996
22	B22	Candelaro a STRADA DI Bonifica	7	1967-1973

23	B23	Casanova a Ponte Lucera Motta2	6	1967-1972
24	C1	Ancinale a Razzona	32	1952-1982, 1984
25	C2	Sinni a Pizzutello	28	1952-1968, 1970-1980
26	C3	Alli a Orso	29	1952-1980
27	C4	Lese a Schiena Dasino	27	1953-1958, 1960-1980
28	C5	Corase a Grascio	26	1952-1971, 1975-1980
29	C6	Sinni a Valsinni	25	1952-1976
30	C7	Coscile a Camerata	24	1960-1969, 1971-1984
31	C8	Alaco a Pirrella	24	1954-1972, 1974-1975, 1979-1981
32	C9	Garga a Torre Garga	20	1952-1971
33	C10	Lao a Pie di Borgo	19	1954, 1957-1965, 1967, 1972-1975, 1981-1984
34	C11	Agri a Le Tempe	20	1952-1971
35	C12	Bradano a Tavole Palatine	20	1952-1971
36	C13	Basento a Gallipoli	19	1952-1966, 1968-1971
37	C14	Alaco a Mammone	20	1961-1980
38	C15	Bradano a Ponte Colonna	19	1952-1953, 1955-1971
39	C16	Annunziata a Straorino	19	1953-1971
40	C17	Basento a Menza	19	1952-1969, 1971
41	C18	Tacina a Rivioto	18	1952-1953, 1956-1971
42	C19	Carti a Conca	18	1952-1966, 1969-1971
43	C20	Duverso a Giorgia	18	1953-1958, 1960-1971
44	C21	Noce a La Calda	17	1952-1955, 1957-1960, 1962-1969, 1971
45	C22	Amato a Marino	17	1952-1953, 1957-1971
46	C23	Melito a Olivelia	17	1962-1972, 1974, 1976-1980
47	C24	Trionto a Difesa	16	1964-1979
48	C25	Agri a Grumento	17	1961-1977
49	C26	Basento a Ponte pignola2	15	1952-1966
50	C27	Vasi a Scifa	13	1953-1965
51	C28	Assi a Botteria	12	1959-1962, 1964-1971
52	C29	Ancinale a Spadola	12	1968-1970, 1972-1980
53	C30	Colognati a Pizzuto	12	1960-1971
54	C31	Amato a Licciardi	12	1960-1971
55	C32	Careri a Bosco	12	1960-1971
56	C33	Agri a Tarangelo	11	1952-1962
57	C34	Esaro a La Musica	10	1952, 1960-1966, 1968-1969
58	C35	Raganello a Terzeria	11	1960-1962, 1964-1971
59	C36	Esaro a Cameli	10	1962-1971
60	C37	Metrano a Carmine	10	1956-1957, 1959-1960, 1962-1967
61	C38	Savuto a Ponte Savuto	10	1960-1968, 1971
62	C39	Metrano a Castagnara1	9	1959-1967
63	C40	Noce a Le Fornaci	9	1952, 1954-1955, 1958-1960, 1962, 1964-1965
64	C41	Mesima a Sbarretta	8	1961-1968
65	C42	Tacina a Serrarossa	8	1960-1967
66	C43	Coriglianeto a Coriglinao	7	1960-1965, 1971
67	C44	Calabro a Puzzara	6	1961-1965, 1971
68	C45	Basento a Ponte Vito	6	1953-1958
69	C46	Petrace a Gonia	5	1961-1964, 1966
70	C47	Basento a Ponte Pignola1	5	1967-1971
71	C48	Sauro a Acinello	5	1962-1966
72	C49	Metrano a Castagnara2	4	1968-1971
73	C50	Alli a Polimieri	3	1969-1971
74	C51	Noce a Monte Castrocucco	2	1971-1972
75	N1	Tanagro a Polla (Molino Maltempo)	70	1924-1931, 1933-1994
76	N2	Calore Irpino a Montella	60	1931, 1933-1942, 1945-1991, 1993-1994
77	N3	Sele ad Albanella	59	1929-1942, 1946-1949, 1951-1971, 1973-1985, 1988-1994
78	N4	Volturno Cancello Arnone 1	53	1931-1936, 1938-1942, 1950-1956, 1958-1976, 1979-1994
79	N5	Calore Lucano a Persano	53	1924-1942, 1957-1967, 1969-1984, 1987-1993
80	N6	Volturno ad Amorosi 1	52	1933-1942, 1950-1982, 1984-1988, 1991-1994
81	N7	Fibreno a Broccostella1	48	1924-1942, 1959-1987
82	N8	Sele a Contursi	47	1933-1940, 1951-1962, 1964-1968, 1970-1976, 1978-1979, 1981-1987, 1989-1994

83	N9	Liri a Sora	42	1929-1942, 1948-1975
84	N10	Calore Irpino a Apice	39	1933-1942, 1946-1973, 1993
85	N11	Torano a Piedimonte	36	1927-1931, 1933-1963
86	N12	Volturno ad Amorosi 2	35	1957-1982, 1984-1988, 1991-1994
87	N13	Alento a Casalvelino	33	1959-1983, 1985-1986, 1988, 1990-1994
88	N14	Rio Mollo a Settignano	29	1965-1993
89	N15	Volturno Cancello Arnone 2	28	1965-1976, 1979-1994
90	N16	Sarno a S.Valentino Torio	28	1958-1979, 1981-1983, 1985, 1991, 1994
91	N17	Liri a Isola Liri1	27	1930-1942, 1949-1962
92	N18	Sacco a Ceccano	28	1959-1980, 1986-1990, 1994
93	N19	Melfa a Picinisco (Ponte Ascanio)1	26	1925-1942, 1946-1953
94	N20	Calore Irpino a Solopaca	25	1965-1974, 1976-1986, 1988-1990, 1994
95	N21	Tammaro a Pago Veiano	25	1957-1977, 1985, 1992-1994
96	N22	Melfa ad Atina	24	1924-1942, 1949-1953
97	N23	Rapido a S.Elia Fiumerapido	23	1957-1979
98	N24	Melfa a Picinisco (Ponte Ascanio)2	22	1965-1982, 1990-1992, 1994
99	N25	Tammaro a Paduli	22	1955-1968, 1970-1973, 1984, 1986-1987, 1994
100	N26	Volturno di Ponte Annibale	19	1924-1942
101	N27	Sele a Persano	19	1924-1941, 1994
102	N28	Cosa a Ceccano	17	1959-1975
103	N29	Giovenco a Pescina1	16	1960-1975
104	N30	Giovenco a Pescina2	15	1976-1990
105	N31	Liri a Castronuovo	14	1926-1928, 1932-1942
106	N32	Bussento a Caselle In Pittari1	14	1955-1968
107	N33	Tusciano ad Olevano Tusciano	14	1957-1970
108	N34	Garigliano al Ponte Ambrogio	13	1930-1942
109	N35	Fucino	12	1929-1940
110	N36	Sorgenti Gari a Cassino	11	1965-1975
111	N37	Liri a Isola Liri2	10	1985-1994
112	N38	Liri a S.Apollinare	10	1933-1941, 1994
113	N39	Garigliano a Suio	10	1933-1942
114	N40	Tanagro a Contursi	10	1933-1942
115	N41	Savio a Gallo	8	1957-1964
116	N42	Calore Irpino a Melizzano	7	1936-1942
117	N43	Platano a Romagnano	7	1936-1942
118	N44	Carpino a Carpinone	7	1957-1963
119	N45	Bussento a Sicili	6	1952-1957
120	N46	Fibreno a Broccostella2	5	1990-1994
121	N47	Rio Chiaro a Cardito	4	1954-1957
122	N48	Irno a Pellezzano	4	1957-1960
123	N49	Bussento a Caselle In Pittari2	3	1952-1954
124	N50	Rio Schiavondaro	1	1994
125	N51	Ufita Ad Apice Scalo	1	1994
126	N52	Sabato a Ceppaloni	1	1994
127	N53	Calore Benevento	1	1994

2.2.1 Insufficient Record Length

Accurate regionalization of FDCs requires datasets that span sufficient temporal durations to encompass a wide range of hydrological conditions, including interannual variability, seasonal dynamics, and extreme events. Short-duration records are typically inadequate for this purpose, as they fail to capture the full spectrum of flow variability and often lead to biased statistical representations of flow characteristics (Sivakumar, 2000).

To ensure statistical robustness and mitigate sampling uncertainty, a minimum criterion of five consecutive years of discharge records is selected. Stations not meeting this criterion were considered insufficiently representative for regionalization and were therefore excluded from further analysis.
From the original set of 127 stations, nine were identified with record lengths shorter than five years:

- Rio Schiavondaro
- Ufita ad Apice Scalo
- Sabato a Ceppaloni
- Calore a Benevento
- Noce a Monte Castrocucco
- Alli a Polimieri
- Bussento a Caselle In Pittari 2
- Rio Chiaro a Cardito
- Irno a Pellezzano

The exclusion of these stations prevents the introduction of statistical artifacts and enhances the reliability of the resulting regionalization framework.

2.2.2 Stations Located at Spring Outlets

Hydrometric stations situated at natural spring outlets introduce a unique set of challenges in hydrological modeling. Unlike typical riverine stations that reflect a combination of surface runoff and baseflow contributions, spring-fed systems are predominantly sustained by groundwater discharge. As a result, these systems tend to exhibit low flow variability, subdued responses to precipitation events, and relatively stable discharge regimes throughout the year (Kresic, 2010).
In the context of FDC construction, such behavior leads to an overrepresentation of baseflow conditions and underrepresentation of peak flow events, which can distort the statistical structure of the curve. Since the objective of this study is to regionalize stream patterns that reflect catchment-scale hydrological processes, stations dominated by spring discharge were deemed unrepresentative and were excluded from the analysis.
The following spring-dominated stations were identified and removed:

- Torano a Piedimonte
- Sarno a S. Valentino Torio
- Melfa a Picinisco 1
- Sorgenti Gari a Cassino
- Fibreno a Broccostella 1
- Fibreno a Broccostella 2

2.2.3 Duplicate Stations with Identical Characteristics

In several cases, the dataset contained multiple entries for stations with identical names and nearly identical catchment characteristics, including area, mean elevation, and maximum elevation. Such duplication suggests either data entry errors or unintentional redundancy in the national archive. If not addressed, these overlaps can result in double-counting, introduce artificial weighting in spatial analyses, and compromise the uniqueness of station-based inferences.
To ensure the integrity of the dataset, each duplicate pair was carefully evaluated. The version with the more complete and continuous record was retained, while the duplicate with shorter or fragmented data was excluded.

Examples of such duplicates include:
Volturno ad Amorosi 1 (retained), Volturno ad Amorosi 2 (excluded)
Volturno a Cancello Arnone 1 (retained), Volturno a Cancello Arnone 2 (excluded)

2.2.4 Duplicate Names with Divergent Catchment Descriptors

A related issue was the presence of stations sharing identical names and similar elevation features but reporting different catchment areas. These inconsistencies may arise from administrative naming conventions or confusion in station labelling, and they complicate the spatial matching of hydrological and physiographic data.
Given the importance of catchment descriptors (e.g., area, slope, land cover) in hydrological modeling, such mismatches must be resolved. For each duplicate name, the station with the more robust and complete dataset was retained, provided that it could be reliably associated with a specific catchment polygon.
The following stations were addressed under this criterion:

- Basento a Ponte Pignola 1 (5 years, excluded), 2 (15 years, retained)
- Atella a Ponte Sotto Atella 1 (21 years, excluded), 2 (22 years ,retained)
- Casanova a Ponte Lucera Motta 1 (15 years, retained), 2 (6 years, excluded)
- Giovenco a Pescina 1 (15 years, excluded), 2 (16 years, retained)
- Metrano a Castagnara 1 (9 years, retained), 2 (4 years, excluded)

2.2.5 Impact of Dam Regulation on Discharge Records

The presence of dams and other large hydraulic structures significantly alters the natural flow regime of downstream stations. These anthropogenic influences include attenuation of flood peaks, stabilization of low flows, and shifts in seasonal timing of discharge. Such modifications are driven by operational objectives such as irrigation, hydropower, and flood control, and result in flow records that no longer reflect natural hydrological variability (Marcinkowski & Grygoruk, 2017; Mailhot et al., 2018).
To identify and manage these influences, a comprehensive multi-criteria validation framework was employed, integrating the following components:

Geospatial Analysis: Geographic Information System (GIS) tools were used to delineate each dam's contributing area and to determine the spatial relationship between the dam and downstream gauging stations. The delineation process involved treating the dam as the pour point and calculating the corresponding upstream catchment area. Catchment-area estimation methods are fully presented in Chapter 4; in this section some information is anticipated.

Hydraulic Control Ratio (HCR): A key metric introduced in this study, the *HCR* is defined as the ratio between the upstream drainage area controlled by the dam and the total catchment area of the gauging station ($HCR = A_{regulated}/A_{catchment}$; $0 \leq HCR \leq 1$). Catchment-area estimation methods are fully presented in Chapter 4; in this section those areas are only anticipated to introduce and apply *HCR*. While existing literature does not prescribe a universally accepted threshold for *HCR*, this study adopts a threshold of $HCR \geq 0.33$ as a screening criterion to identify stations potentially affected by dam regulation. This decision is based on empirical observations of FDC shifts across the analyzed stations, wherein stations with *HCR* values above this threshold consistently exhibit measurable hydrological alterations following dam construction.

Temporal Analysis**:** Dam construction dates were extracted from the official Italian database of large dams[1]. The relationship between the dam's commissioning date and the discharge record period was assessed to classify stations into those with: (a) only pre-dam records, (b) only post-dam records, and (c) mixed records spanning both periods.

Hydrological Validation via FDC Analysis: To determine the degree of regulation, FDCs were constructed separately for the pre- and post-dam periods for each station with mixed records. Alterations in the FDC shapes such as peak flow attenuation, flattening of mid-range flows, or modification of baseflow regimes—were used as diagnostic indicators of artificial regulation.

Table 2.3 summarizes the main characteristics of 17 gauging stations influenced by upstream dam regulation, including catchment and dam areas, the hydrological control ratio (*HCR*), dam construction years, and the duration of available pre- and post-dam discharge records. Based on these attributes, the stations were grouped according to the availability and quality of unaffected flow data.

Seven stations—Alaco a Mammone, Alaco a Pirrella, Esaro a La Musica, Locone a Ponte Brandi, Metrano a Castagnara, Platano a Romagnano, and Tanagro a Contursi—were fully retained for analysis, as they include at least five years of discharge data prior to dam construction and are unaffected by regulation. In contrast, Bradano a Tavole Palatine was excluded from the analysis due to the complete absence of pre-dam records, rendering it unsuitable for evaluating natural flow conditions.

The remaining nine stations—Alento a Casalvelino, Alli a Orso, Basento a Gallipoli, Bussento a Sicili, Sava a Gallo, Sinni a Pizzutello, Sinni a Valsinni, Tammaro a Paduli, and Tammaro a Pago Veiano—include mixed pre- and post-dam data, with at least five years of pre-regulation records. These stations were retained for further evaluation through Flow Duration Curve (FDC) analysis to assess the extent of dam-induced alteration. The decision to retain or exclude individual segments of their data is discussed in the following section based on visual and statistical comparison of pre- and post-dam flow regimes.

[1] (https://dgdighe.mit.gov.it/)

Table 2.3: Summary of Stations Influenced by Dam Regulation

Station Name	Catchment Area (km^2)	Dam Name	HCR	Construction Year	Time Period	Pre-Dam Years	Post-Dam Years
Alaco a Mammone	14.4	Mammone Alaco	0.96	1985	1961-1980	20	0
Alaco a Pirrella	37.3	Mammone Alaco	0.37	1985	1951-1980	24	0
Alento a Casalvelino	279.9	Piano Della Rocca	0.36	1984	1959-1994	25	8
Alli a Orso	45.5	Passante	0.66	1971	1951-1981	19	10
Basento a Gallipoli	853.3	Camastra	0.4	1962	1952-1971	10	9
Bradano a Tavole Palatine	2308.4	San Giuliano	0.47	1950	1951-1971	0	20
Bussento a Sicili	229	Contrada Sabetta	0.5	1957	1952-1957	5	1
Esaro a La Musica	530.1	Farneto Del Principe	0.46	1972	1951-1969	10	0
Locone a Ponte Brandi	227.1	Monte Melillo	0.98	1980	1971-1983	12	0
Metrano a CastagnaraI	20.5	Castagnara Metrano	0.79	1981	1959-1967	9	0
Platano a Romagnano	604.5	Conza	0.42	1974	1936-1942	7	0
Sava a Gallo	14.9	Gallo	0.87	1963	1957-1964	6	2
Sinni a Pizzutello	235	Masseria Nicodemo	0.51	1967	1951-1981	15	13
Sinni a Valsinni	1138.4	Monte Cotugno	0.7	1972	1951-1976	20	5
Tammaro a Paduli	668.9	Campolattaro	0.38	1981	1955-1994	18	4
Tammaro a Pago Veiano	551.4	Campolattaro	0.46	1981	1957-1994	21	4
Tanagro a Contursi	329.7	Conza	0.77	1974	1933-1942	10	0

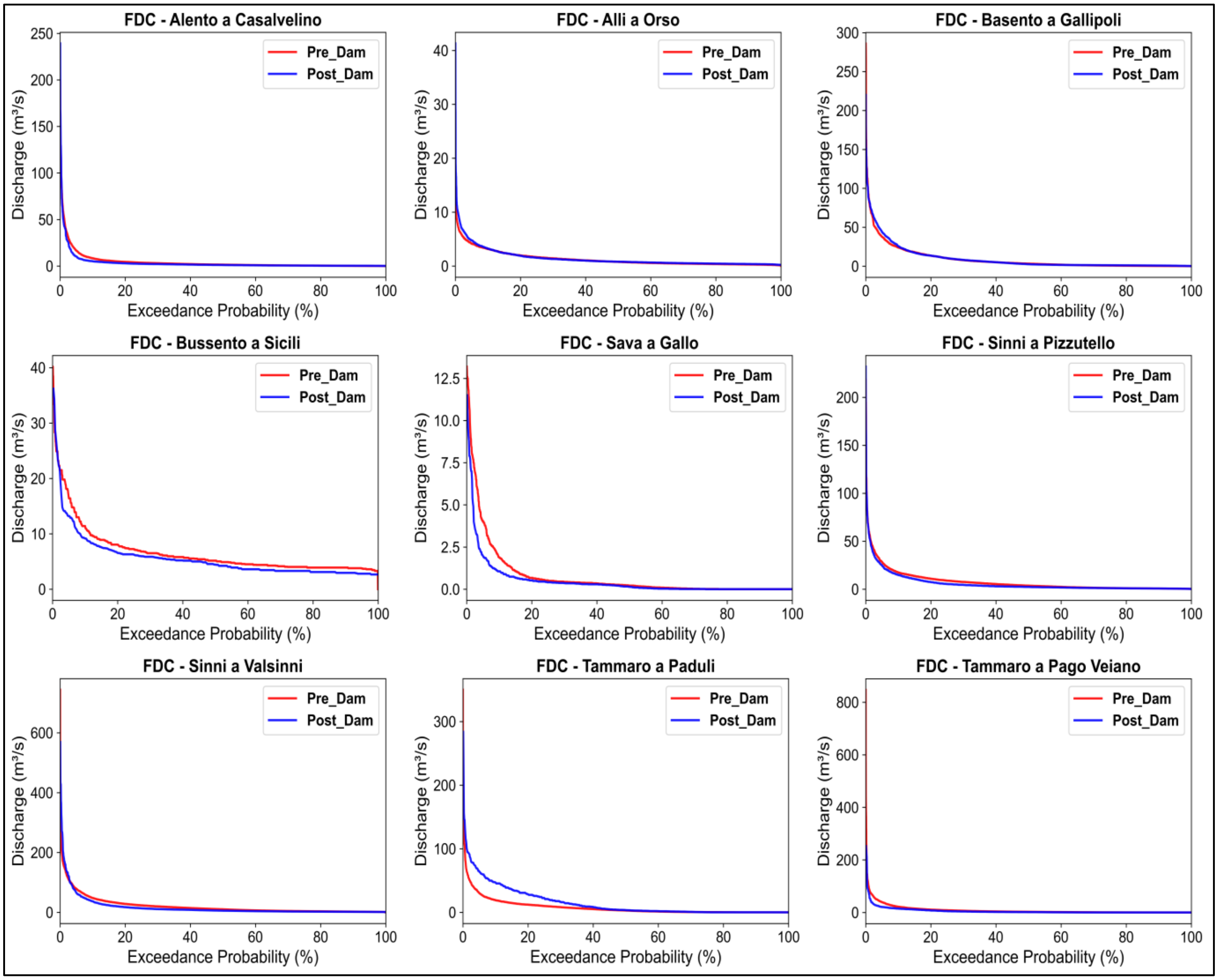

Figure 2.3: FDCs Before and After Dam Construction

The comparison of Flow Duration Curves (FDCs) before and after dam construction provides critical insight into how upstream regulation alters the natural hydrological regime. Figure 2.3 illustrates the FDCs of nine representative stations with discharge records spanning both pre- and post-dam periods. At first glance, many of the curves exhibit only modest visual differences, which could suggest that dam construction has had limited impact on the overall flow distribution. However, a more detailed quantitative analysis reveals that the changes, while sometimes subtle in appearance, are hydrologically significant (Table 2.4.a, b).

Table 2.4.a: Comparison between pre- and post-dam construction FDCs for a selection of relevant points

Station Name	**Alento a Casalvelino**		**Alli a Orso**		**Basento a Gallipoli**		**Bussento a Sicili**		**Sava a Gallo**	
Exceedance Probability	Pre_Dam	Post_Dam	Pre_Dam	Post_Dam	Pre_Dam	Post_Dam	Pre_Dam	Post_Dam	Pre_Dam	Post_Dam
1%	57.19	49.59	7.06	9.45	86.94	84.72	26.37	27.58	9.92	7.83
2%	36.84	28.75	5.77	7.01	64.79	68.75	22.3	22.14	7.7	4.97
5%	16.5	10.22	4.21	4.78	37.84	44.4	16.51	13.2	4	1.97
10%	8.37	5.12	3.16	3.25	23.9	25.8	11.4	9.17	1.88	1.06
15%	5.8	3.78	2.44	2.39	17.8	17.4	8.9	7.56	1.06	0.68
20%	4.46	2.93	1.96	1.89	13.5	13.64	8.02	6.55	0.67	0.52
25%	3.56	2.34	1.64	1.53	10.2	10.3	7.22	6.24	0.52	0.41
30%	3.08	2.13	1.44	1.31	7.8	8	6.5	5.85	0.43	0.36
35%	2.54	1.84	1.21	1.15	6.23	6.54	6.08	5.4	0.38	0.32
40%	2.11	1.55	1.04	1	5.09	5.06	5.8	5.18	0.34	0.29
45%	1.71	1.35	0.9	0.88	4.06	3.74	5.41	5	0.28	0.23
50%	1.48	1.12	0.78	0.8	3.27	2.54	5.15	4.44	0.21	0.14
55%	1.22	0.98	0.67	0.73	2.56	2	4.76	3.9	0.15	0.07
60%	0.98	0.81	0.57	0.65	1.89	1.63	4.5	3.6	0.09	0.03
65%	0.8	0.65	0.51	0.58	1.34	1.41	4.38	3.45	0.05	0.02
70%	0.65	0.6	0.45	0.53	1.04	1.28	4.14	3.3	0.02	0.01
75%	0.52	0.47	0.41	0.49	0.76	1.17	4.02	3.3	0.01	0
80%	0.44	0.38	0.37	0.44	0.58	1.05	3.9	3.1	0	0
85%	0.3	0.31	0.33	0.41	0.41	0.9	3.9	3.1	0	0
90%	0.2	0.3	0.29	0.37	0.3	0.75	3.9	2.95	0	0
95%	0.1	0.26	0.24	0.34	0.18	0.55	3.75	2.8	0	0
96%	0.1	0.23	0.22	0.32	0.16	0.45	3.68	2.8	0	0
97%	0.09	0.2	0.22	0.31	0.15	0.41	3.6	2.8	0	0
98%	0.08	0.19	0.2	0.28	0.11	0.35	3.59	2.66	0	0
99%	0.05	0.14	0.17	0.24	0.09	0.26	3.3	2.66	0	0

Table 2.4.b: Comparison between pre- and post-dam construction FDCs for a selection of relevant points

Station Name	**Sinni a Pizzutello**		**Sinni a Valsinni**		**Tammaro a Paduli**		**Tammaro a Pago Veiano**	
Exceedance Probability	**Pre_Dam**	**Post_Dam**	**Pre_Dam**	**Post_Dam**	**Pre_Dam**	**Post_Dam**	**Pre_Dam**	**Post_Dam**
1%	60.14	57.4	161	195.2	69.44	110.84	93.02	71.06
2%	45.63	41.4	125	138	50.9	91.22	67.51	37.72
5%	28.4	24.85	78.53	64.88	30.42	64.32	39.46	20.82
10%	17.5	14.8	48	36.66	19.1	46.88	21.74	14.82
15%	13.8	10.6	35.6	23.5	14.7	35.94	15	11.26
20%	10.9	7.4	28	17.34	12.1	28.23	10.8	7.61
25%	8.92	5.39	23.28	13.5	9.95	22.42	8.46	5.08
30%	7.54	4.5	19.8	10.9	8.2	16.36	6.5	3.78
35%	6.5	3.7	16.9	9.27	6.5	12	4.88	2.74
40%	5.4	2.95	14.3	8.24	5.14	8.49	3.88	2.16
45%	4.46	2.7	12.2	6.8	3.8	4.8	2.98	1.7
50%	3.66	2.37	10.2	5.55	2.82	3.46	2.42	1.39
55%	3.02	2.02	8	4.75	1.9	2.52	1.86	1.09
60%	2.44	1.76	6.49	3.94	1.26	1.87	1.48	0.65
65%	1.84	1.48	5.37	3.48	0.77	1.3	1.17	0.35
70%	1.45	1.29	4.5	2.84	0.5	0.73	0.8	0.19
75%	1.2	1.09	3.88	2.58	0.32	0.21	0.52	0.11
80%	0.97	0.93	3.4	2.32	0.22	0.09	0.38	0.06
85%	0.87	0.79	2.78	2.04	0.12	0.08	0.24	0.04
90%	0.73	0.72	2.25	1.8	0.07	0.07	0.08	0.03
95%	0.55	0.56	1.8	1.49	0.04	0.06	0.01	0
96%	0.52	0.55	1.7	1.44	0.03	0.05	0	0
97%	0.48	0.5	1.62	1.33	0.02	0.04	0	0
98%	0.46	0.44	1.5	1.27	0.01	0.02	0	0
99%	0.4	0.39	1.35	1.22	0.01	0.01	0	0

Table 2.4(a,b) summarizes the exceedance probabilities and corresponding discharges before and after dam construction. For example, at Alento a Casalvelino (*HCR* = 0.36), high flows are attenuated while low flows are enhanced. The discharge at 1% exceedance drops from 57.2 to 49.6 m^3/s (−13.3%), indicating reduced flood peaks, while at 99% exceedance, the flow increases from 0.05 to 0.14 m^3/s (+180%), suggesting regulated baseflow support. Similarly, Sava a Gallo (*HCR* = 0.87) demonstrates strong regulation across the entire FDC. At 5% exceedance, the discharge declines from 4.0 to 1.97 m^3/s (−50.8%), and beyond 75%, flows approach zero, confirming that the stream is nearly fully controlled with little or no flow release. In contrast, Alli a Orso (*HCR* = 0.66) displays a general increase across the FDC: from 7.06 to 9.45 m^3/s (+33.8%) at 1% exceedance and from 0.29 to 0.37 m^3/s (+27.6%) at 90% exceedance, indicating that managed releases have increased flow availability. Tammaro a Paduli (*HCR* = 0.38) also shows a substantial post-dam increase in flow: from 9.95 to 22.4 m^3/s (+125%) at 25% exceedance.

Other stations exhibit a clear suppression of both high and low flows. For example, Tammaro a Pago Veiano (*HCR* = 0.46) shows reductions from 39.5 to 20.8 m^3/s (−47.3%) at 5% exceedance and from 0.24 to 0.04 m^3/s (−83%) at 85%, with flows disappearing completely beyond 96% exceedance. Although in some stations—such as Basento a Gallipoli or Sinni a Pizzutello—the visual shift in FDCs appears limited, the numerical analysis demonstrates that even moderate *HCR*

values (0.4–0.6) can result in flow changes of 20–50% at key percentiles. These seemingly minor shifts can substantially affect hydrological modeling outcomes.
The dam inventory (Table 2.4.a, b) further supports this reasoning. Several stations (e.g., Sinni a Pizzutello, Alento a Casalvelino, Alli a Orso) have long records spanning both pre- and post-dam periods. If post-dam records are included in analyses aimed at characterizing natural flow regimes, the results become inherently biased by anthropogenic interventions. Therefore, despite the absence of dramatic visual discrepancies in some FDC maps, the evidence supports a methodologically sound decision to exclude post-dam data from natural flow assessments. The exclusion helps maintain the integrity of hydrological analyses and ensures that results reflect the natural, unregulated behavior of the river systems.

2.2.6 Stations Outside the Soil Map Boundaries

Incorporating soil data—particularly information on permeability—is essential for the robust regionalization of FDCs, as it directly influences how rainfall is partitioned between infiltration and surface runoff. Soil permeability plays a critical role in determining baseflow contributions and the overall discharge regime, thereby shaping the hydrological behavior of a catchment (Adongo, 2022). Consequently, the availability of spatially consistent soil data is fundamental to developing reliable relationships between catchment descriptors and FDC metrics.
However, a key limitation arises when gauging stations fall outside the boundaries of the available soil permeability maps. In such cases, the absence of data precludes the integration of soil-related variables into the regionalization framework. This can introduce inconsistencies in predictive modeling and reduce the interpretability of the results.
To ensure consistency and data integrity, stations lacking soil permeability information were excluded from further analysis. The soil dataset employed in this study is based on the detailed hydrogeological mapping provided byAllocca et al. (2007), which serves as the primary reference for permeability classification across the study area.
The following stations were identified as falling outside the mapped soil boundaries:

- Liri a Sora
- Rio Mollo a Settignano
- Liri a Isola Liri 1
- Liri a Isola Liri 2
- Sacco a Ceccano
- Melfa ad Atina
- Rapido a S. Elia Fiumerapido
- Melfa a Picinisco (Ponte Ascanio) 2
- Cosa a Ceccano
- Liri a Castronuovo
- Garigliano al Ponte Ambrogio
- Fucino
- Liri a S. Apollinare
- Garigliano a Sui
- Giovenco a Pescina2

Due to the absence of reliable soil data, these stations were excluded from the regionalization process. This limitation underscores the need for expanding and refining hydrogeological datasets in southern Italy to enhance future hydrological modeling efforts.

The rigorous validation of discharge datasets resulted in the exclusion or partial retention of several gauging stations based on criteria such as data completeness, natural flow representativeness, and independence from anthropogenic alterations—particularly dam regulation. After applying all quality control steps, including minimum record length, removal of spring-dominated and duplicate stations, exclusion of post-dam periods, and filtering based on soil data availability, a total of 89 stations were retained for FDC construction and regionalization analysis.

Table 2.5 illustrates the final selection of these 89 validated stations across the study area. This curated network forms the analytical basis for the development of spatial models, ensuring that the resulting FDC parameters reflect unaltered, natural hydrological behavior. Similarly, Figure 2.4 displays the spatial distribution of the 127 gauging stations initially collected from ISPRA (Istituto Superiore per la Protezione e la Ricerca Ambientale) regional offices of Napoli (covering Campania and adjoining areas such as parts of Lazio and Molise), Catanzaro (covering Calabria and portions of Basilicata), and Bari (covering Puglia and the remaining parts of Basilicata). Of these, 89 validated stations were retained for the analysis (highlighted in yellow), while 38 stations were excluded (in pink) following quality control and validation procedures. The network is densely arranged along the Apennine chain and its river valleys in Campania, Basilicata, and Calabria, reflecting the influence of varied climatological and topographic conditions that drive runoff generation and orographic effects in these upland catchments. Stations are strategically placed along valley corridors and at basin outlets, effectively capturing headwater contributions and the gradual shifts in flow regimes from mountainous interiors to coastal lowlands. In contrast, Puglia, with its gentler terrain, fragmented drainage network, and Adriatic foreland setting, features a sparser station distribution, aligning with its fewer perennial streams and more intermittent flow patterns. This layout underscores the distinct physiographic and hydro-climatic differences between the Tyrrhenian and Adriatic/Ionian slopes, ensuring comprehensive coverage of mountain, valley, and lowland systems for robust regional Flow Duration Curve (FDC) analyses

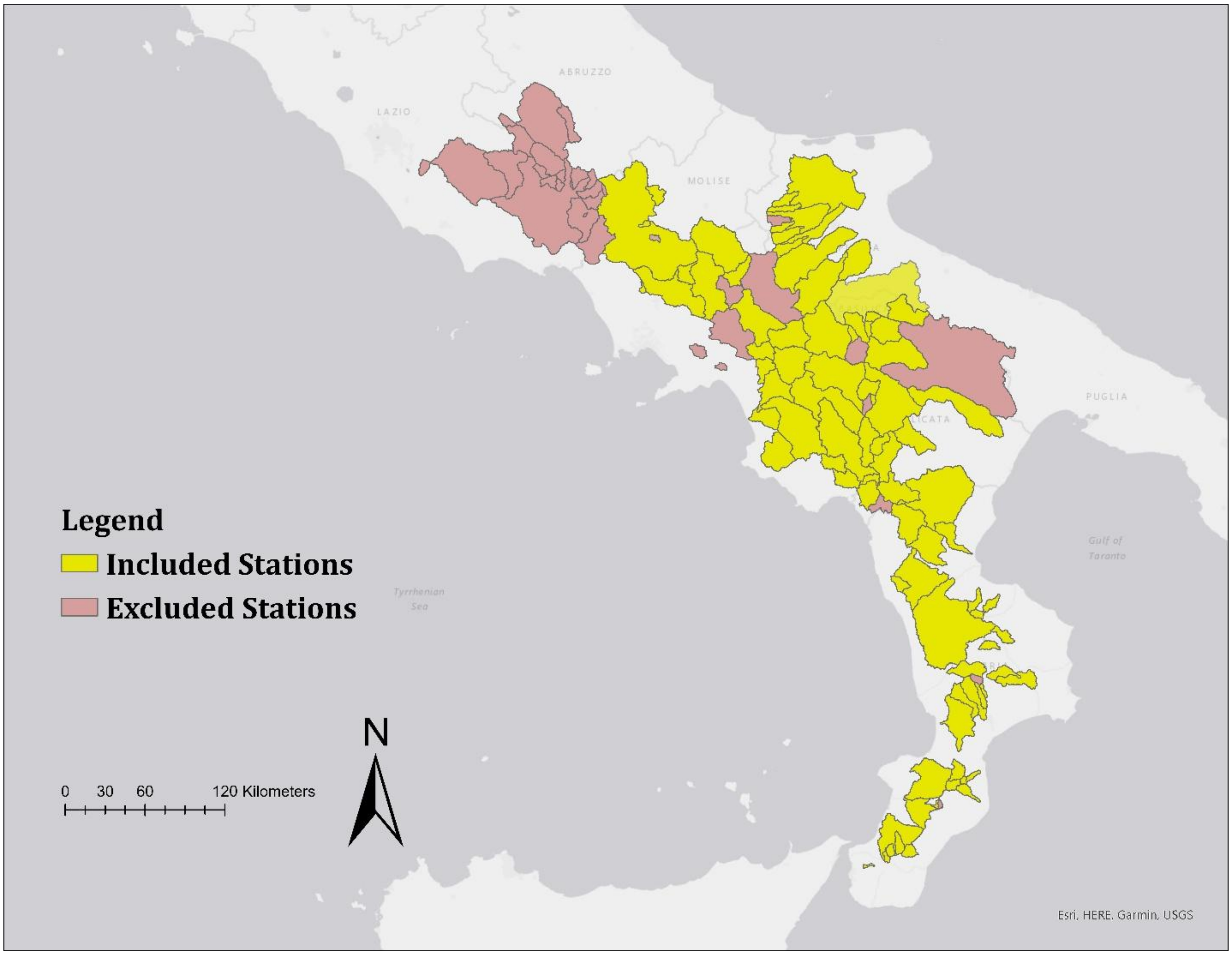

Figure 2.4: Spatial distribution of the 127 gauging stations collected from ISPRA

Table 2.5: Final dataset under investigation

No.	Station Code	Station Name	Catchment Name	Catchment Area (km^2)	Number of Recorded Years
1	B1	Ofanto a Samuele di Cafiero	Ofanto	2716	43
2	B2	Celone a Ponte Foggia .S. Severo	Candelaro	256	41
3	B3	Cervaro ad Incoronata	Cervaro	657	41
4	B4	Salsola a Ponte Foggia .S. Severo	Candelaro	463	40
5	B5	Arcidiaconata a Ponte Rappola-Lavello	Ofanto	124	40
6	B6	Ofanto a Monteverde	Ofanto	1028	39
7	B7	Ofanto a Cairano	Ofanto	272	31
8	B8	Vulgano a Ponte Troia Lucera	Candelaro	94	27
9	B9	Carapelle a Carapelle	Carapelle	720	26
10	B10	Celone a Vincenzo	Candelaro	85.8	25
11	B11	Salsola a Casanova	Candelaro	43.1	23
12	B12	Atella a Ponte sotte Atella2	Ofanto	175	22
13	B13	Triolo a Ponte Lucera Torremaggiore	Candelaro	53.8	22
14	B14	Lapilleso a Ponte S	Ofanto	29.5	22
15	B15	Venosa a Ponte Ferroviaro	Ofanto	201	21
16	B17	Canale S.Maria a Ponte Lucera Torremaggiore	Candelaro	59.8	20
17	B18	Venosa a Ponte S.Angelo	Ofanto	261	17
18	B19	Casanova a Ponte Lucera Motta1	Candelaro	55.8	15
19	B20	Locone a Ponte Brandi	Ofanto	219	12
20	B21	Carapelle a Ponte Vecchio Ordona	Carapelle	506	10
21	B22	Candelaro a STRADA DI Bonifica	Candelaro	1788	7
22	C1	Ancinale a Razzona	Ancinale	116	32
23	C2	Sinni a Pizzutello	Sini	233	15
24	C3	Alli a Orso	Alli	46	19
25	C4	Lese a Schiena Dasino	Lese	60	27
26	C5	Corase a Grascio	Corase	178	26
27	C6	Sini a Valsinni	Sini	1142	20
28	C7	Coscile a Camerata	Coscile	303	24
29	C8	Alaco a Pirrella	Alaco	38	24
30	C9	Garga a Torre Garga	Garga	43	20
31	C10	Lao a Pie di Borgo	Lao	279	19
32	C11	Agri a Le Tempe	Agri	174	20
33	C13	Basnto a Gallipoli	Basento	848	10
34	C14	Alaco a Mammone	Alaco	14.8	20
35	C15	Bradano a Ponte Colonna	Bradano	459	19

36	C16	Annunziata a Straorino	Annunziata	8.11	19
37	C17	Basnto a Menza	Basento	1405	19
38	C18	Tacina a Rivioto	Tacina	77	18
39	C19	Carti a Conca	Carti	1332	18
40	C20	Duverso a Giorgia	Duverso	28.68	18
41	C21	Noce a La Calda	Noce	44	17
42	C22	Amato a Marino	Amato	115	17
43	C23	Melito a Olivelia	Melito	41.2	17
44	C24	Trionto a Difesa	Trionto	31.7	16
45	C25	Agri a Grumento	Agri	278	17
46	C26	Basent a Ponte pignola2	Basento	57.6	15
47	C27	Vasi a Scifa	Vasi	19.4	13
48	C28	Assi a Botteria	Assi	52.8	12
49	C29	Ancinale a Spadola	Ancnale	42.5	12
50	C30	Colognati a Pizzuto	Colognati	48	12
51	C31	Amato a Licciardi	Amato	453	12
52	C32	Careri a Bosco	Careri	48	12
53	C33	Agri a Tarangelo	Agri	507	11
54	C34	Esaro a La Musica	Esaro	532	10
55	C35	Raganello a Terzeria	Raganello	143	11
56	C36	Esaro a Cameli	Esaro	55.4	10
57	C37	Metrano a Carmine	Metrano	233	10
58	C38	Savuto a Ponte Savuto	Savuto	141	10
59	C39	Metrano a Castagnara1	Metrano	19.7	9
60	C40	Noce a Le Fornaci	Noce	186	9
61	C41	Mesima a Sbarretta	Mesima	424	8
62	C42	Tacina a Serrarossa	Tacina	223	8
63	C43	Coriglianeto a Coriglinao	Coriglianeto	53	7
64	C44	Calabro a Puzzara	Calabro	54	6
65	C45	Basento a Ponte Vito	Basento	157	6
66	C46	Petrace a Gonia	Petrace	410	5
67	C48	Sauro a Acinello	Sauro	222	5
68	N1	Tanagro a Polla (Molino Maltempo)	Sele	659	70
69	N2	Calore Irpino a Montella	Volturno	123	60
70	N3	Sele ad Albanella	Sele	3235	59
71	N4	Volturno Cancello Arnone 1	Volturno	5558	53
72	N5	Calore Lucano a Persano	Sele	673	53
73	N6	Volturno ad Amorosi 1	Volturno	2015	52
74	N8	Sele a Contursi	Sele	329	47
75	N10	Calore Irpino a Apice	Volturno	533	39
76	N13	Alento a Casalvelino	Alento	284.6	25
77	N20	Calore Irpino a Solopaca	Volturno	2966	25
78	N21	Tammaro a Pago Veiano	Volturno	555.8	21
79	N25	Tammaro a Paduli	Volturno	672.8	18
80	N26	Volturno di Ponte Annibale	Volturno	5542	19
81	N27	Sele a Persano	Sele	2428	19

82	N32	Bussento a Caselle In Pittari1	Bussento	112.9	14
83	N33	Tusciano ad Olevano Tusciano	Tusciano	95.1	14
84	N40	Tanagro a Contursi	Sele	1863	10
85	N41	Sava a Gallo	Volturno	14.5	6
86	N42	Calore Irpino a Melizzano	Volturno	3057	7
87	N43	Platano a Romagnano	Sele	605	7
88	N44	Carpino a Carpinone	Volturno	72.3	7
89	N45	Bussento a Sicili	Bussento	228	5

2.3 Base Flow Index (*BFI*)

The Base Flow Index (*BFI*) is a hydrological metric that quantifies the proportion of total streamflow derived from baseflow, expressed as a ratio ranging from 0 to 1. Baseflow represents the stable, low-flow component of streamflow, primarily originating from groundwater discharge and delayed subsurface contributions, distinct from immediate surface runoff (Winter, 2007). This index is critical for water resource management, drought assessment, and watershed characterization, as it provides insights into aquifer recharge dynamics and low-flow conditions (Lee & Ajami, 2023). The *BFI* significantly influences the shape and position of Flow Duration Curves (FDCs), particularly in perennial river systems where baseflow constitutes a substantial portion of total streamflow.

Baseflow estimation employs various methodologies, with tracer-based techniques—utilizing isotopic or chemical markers—considered highly accurate but resource-intensive(Genereux, 1998; J. Wang et al., 2021) . To overcome the limitations of cost, time, and fieldwork demands, non-tracer-based methods have been developed, relying solely on streamflow records. These methods are categorized into graphical and digital filter approaches. Graphical methods involve manually connecting low-flow points on hydrographs (Sloto & Crouse, 1996), while digital filters employ algorithms to isolate the low-frequency baseflow signal from total streamflow (Chapman, 1991; Eckhardt, 2005; Lyne & Hollick, 1979). This study applies multiple baseflow separation techniques, including the Eckhardt filter, Lyne-Hollick filter, UKIH smoothed minima method, and the three HYSEP variants (Fixed Interval, Sliding Interval, and Local Minimum), each yielding distinct *BFI* values due to differences in computational frameworks and sensitivity to catchment characteristics.

2.3.1 Graphic Methods for Baseflow Separation

Graphical methods represent some of the earliest and most intuitive approaches to baseflow separation, relying on the visual identification and interpolation of low-flow points on a streamflow hydrograph. The process involves two primary steps: (i) identifying minimum streamflow values within specified time intervals, and (ii) interpolating these points to construct a baseflow hydrograph, constrained to remain below the total streamflow hydrograph. This study evaluates four graphical methods: the Smoothed Minima Method, developed by UK Institute of Hydrology (1980), and three variants of the Hydrograph Separation Program (HYSEP)—Fixed Interval, Sliding Interval, and Local Minimum—proposed by the United States Geological Survey.

2.3.1.1 UKIH Method

The UKIH method employs a smoothed minima technique to identify baseflow by locating local minima within specified intervals and constructing a baseflow hydrograph through linear interpolation. This method is robust for low-flow analysis but sensitive to the choice of interval length (Institute of Hydrology, 1980). The procedure is as follows:
The streamflow record is divided into non-overlapping 5-day blocks. The minimum streamflow, $Q_{min,i}$, is identified for each block, where i denotes the block index. Groups $\left(Q_{min,i}, Q_{min,i+1}, Q_{min,i+2}\right)$ of three consecutive minima are formed. The middle minimum, $Q_{min,i+1}$, is designated as a turning point if it satisfies the condition

$$0.9 \times Q_{min,i+1} \leq min\left(Q_{min,i}, Q_{min.i+2}\right) \quad (2.1)$$

All identified turning points are connected via linear interpolation to form a continuous baseflow line, constrained to remain below the total streamflow hydrograph.
This method provides a repeatable and straightforward approach to baseflow approximation, requiring only streamflow data without auxiliary inputs.

2.3.1.2 HYSEP Method

The HYSEP suite, developed by Sloto and Crouse (1996), comprises three algorithmic baseflow separation techniques—Fixed Interval, Sliding Interval, and Local Minimum—designed to systematically identify low-flow points in streamflow hydrographs. These methods are valued for their automated implementation and applicability across diverse hydrological settings. A key parameter, N, represents the duration of overland flow (in days) and is empirically estimated as:

$$N = A^{0.2} \quad (2.2)$$

Where A is the drainage area in square miles. For areas in square kilometers, conversion to square miles is performed using:

$$A[mi^2] = \frac{A[km^2]}{2.59} \quad (2.3)$$

The three HYSEP variants are described below, ordered by increasing methodological complexity.

Fixed Interval Method

The Fixed Interval Method segments the streamflow record into non-overlapping intervals of duration 2*N* days. The minimum daily streamflow within each interval is identified and used as a baseflow point. These minima are connected via linear interpolation to form the baseflow hydrograph, constrained to remain below the observed hydrograph. While computationally efficient, this method's reliance on fixed intervals may reduce its sensitivity to rapid streamflow fluctuations, particularly in dynamic catchments.

Sliding Interval Method

The Sliding Interval Method enhances temporal resolution by applying a moving window of length $2N$ days across the streamflow record. Within each window, the minimum streamflow is identified, and these values are interpolated to construct the baseflow hydrograph, constrained below the observed hydrograph. This approach improves upon the Fixed Interval Method by providing a more continuous identification of local minima, though its performance remains sensitive to window size selection.

Local Minimum Method

The Local Minimum Method employs a dynamic windowing strategy to enhance adaptability to varying hydrological regimes. The overland flow duration is estimated using Eq. 2.2, and a sliding window of length equal to the nearest odd integer approximating $2N$ is applied to ensure a distinct central day. Within each window, the streamflow of the central day is compared to all other values; if it is the minimum, it is designated as a local minimum. These local minima are connected via linear interpolation to form the baseflow hydrograph. This method is particularly suited to catchments with rapid hydrograph responses due to its adaptive window sizing.

2.3.1 Digital Filter Methods for Baseflow Separation

2.3.1.1 Lyne and Hollick (LH) Method

The method proposed by Lyne & Hollick (1979) is a one-parameter recursive digital filter designed to separate quick flow (surface runoff) from total streamflow, with baseflow derived by subtraction. The method conceptualizes hydrograph as a composite signal, where high-frequency components represent quick flow and low-frequency components represent baseflow. The filter is applied in multiple passes (forward and backward) to mitigate phase distortion.
The core equation calculates quick flow (q_k) at time step k:

$$q_k = \beta \cdot q_{k-1} + \frac{1+\beta}{2} \cdot (Q_k - Q_{k-1}) \tag{2.4}$$

where:
q_k: Quick flow at time step k
Q_k: Total streamflow at time step k
β: Filter parameter, set to 0.925.

The baseflow is:

$$b_k = Q_k - q_k \tag{2.5}$$

with the constraint $b_k \geq 0$. The fixed value of β may limit the method's precision in catchments with diverse hydrogeological characteristics.

2.3.1.2 Eckhardt Method

The Eckhardt method is a two-parameter recursive digital filter that directly computes baseflow, building on earlier one-parameter filters like Lyne-Hollick. It assumes a linear relationship between aquifer storage and discharge, leading to an exponential recession, and incorporates catchment-specific characteristics for improved physical basis. The filter equation is:

$$b_k = \frac{(1 - BFI_{max})\alpha b_{k-1} + (1 - \alpha)BFI_{max}Q_k}{1 - \alpha BFI_{max}} \quad (2.6)$$

where:
b_k: Baseflow at time step k
α: recession constant
BFI_{max}: Maximum baseflow index (a catchment-specific parameter, e.g., 0.80 for perennial streams with porous aquifers, 0.50 for ephemeral streams, or 0.25 for perennial streams with hard rock aquifers).
This method provides a more physically grounded approach to baseflow separation by accounting for hydrogeological variability.

2.3.2 Model Evaluation

The pairwise comparison among different *BFI* estimation methods (e.g., HYSEP variants, Eckhardt, Lyne-Hollick (LH), and UKIH) relies on fitting linear regression models of the form $y = mx + c$,
where:

- *y* represents the *BFI* estimates from one method.
- *x* represents the *BFI* estimates from another method.
- *m* (slope) indicates the scaling relationship between the two methods.
- *c* (intercept) captures any systematic bias.

The strength of the correlation between the *BFI* values computed by two different methods can be estimated with the well-known coefficient of determination R^2.

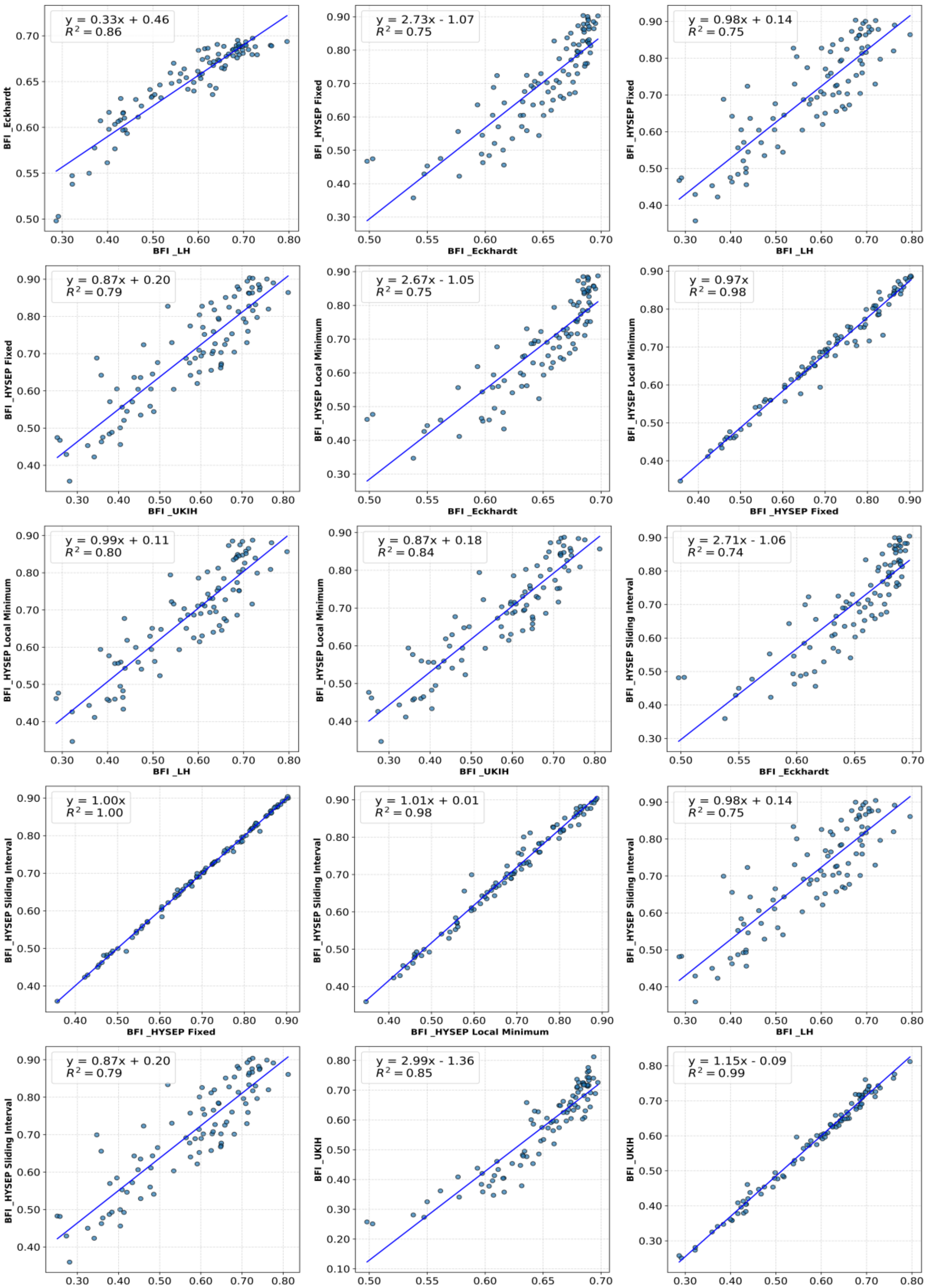

Figure 2.5: Scatter plots comparing BFI estimates from different methods, showing regression lines, equations, and R^2 values to illustrate their agreement.

As figure 2.5 shows that the HYSEP variants (Fixed Interval, Local Minimum, and Sliding Interval) exhibit exceptional consistency, with slopes near 1 and R^2 values ≥ 0.98. For instance, HYSEP Sliding Interval versus Fixed Interval achieves perfect equivalence ($y=x$, $R^2 = 1.00$) and Sliding Interval versus Local Minimum yields near-perfect agreement ($y=1.01x+0.01$, $R^2 = 0.98$). This high similarity stems from their shared reliance on minima-based detection, where base flow is identified as the lowest points within specified intervals, assuming these represent groundwater contributions. Minor differences, such as the slight intercept in the Local Minimum versus Sliding Interval comparison, likely arise from variations in interval selection or window size, which subtly affect minima identification. The strong correlations ($R^2 \geq 0.98$) and near 1:1 slope indicate that HYSEP variants are highly interchangeable, producing stable and consistent *BFI* estimates across similar datasets. This makes them ideal for standardized applications, particularly in large-scale studies where uniform data processing is prioritized. However, their empirical reliance on minima may lead to overestimation in catchments with frequent, transient flow peaks, such as urbanized or flashy systems, where short-lived minima could be misclassified as base flow.

The Eckhardt method shows significant differences from other approaches, with slopes ranging from 0.33 (vs. LH) to 2.99 (vs. UKIH) and R^2 values between 0.74 and 0.86. Comparisons with HYSEP variants reveal steep slopes and negative intercepts (e.g., $y=2.73x-1.07$ vs. Fixed Interval, $R^2 = 0.75$; $y=2.71x-1.06$ vs. Sliding Interval, $R^2 = 0.74$), indicating that Eckhardt overestimates BFI relative to graphical methods in low-BFI catchments (below ~0.62) but underestimates in high-BFI ones. This divergence arises from Eckhardt's sensitivity to recession dynamics, as it employs a two-parameter recursive digital filter assuming exponential decay in base flow, making it more conservative in catchments with rapid groundwater recession, such as karstic systems (Eckhardt, 2005). The comparison with LH ($y=0.33x+0.46$, $R^2 = 0.86$) suggests reversed scaling, where Eckhardt yields higher *BFI* values in lower ranges (below ~0.69), possibly due to LH's aggressive smoothing underestimating base flow. Against UKIH ($y=2.99x-1.36$, $R^2 = 0.85$), the exaggerated slope highlights significant scaling differences, reflecting Eckhardt's parametric complexity versus UKIH's reliance on smoothed minima.

The Lyne-Hollick (LH) and UK Institute of Hydrology (UKIH) methods for hydrograph separation demonstrate substantial similarity in estimating the Base Flow Index (*BFI*), as evidenced by a near-linear regression relationship ($y = 1.15x - 0.09$, where y represents UKIH-derived *BFI* and x denotes LH-derived *BFI*, with $R^2 = 0.99$). This close alignment reflects UKIH's tendency to yield slightly higher values, attributable to both methods' reliance on filtering techniques that emphasize temporal continuity in baseflow attribution—LH through a single-parameter recursive digital filter that dampens high-frequency quick flow components, and UKIH via a smoothed minima interpolation technique that connects hydrograph troughs linearly.

In contrast, both methods tend to produce conservatively lower *BFI* estimates compared to HYSEP variants. This is supported by regression slopes below unity (e.g., 0.87 for UKIH versus Fixed Interval HYSEP, $R^2 = 0.79$; 0.98 for LH versus Sliding Interval HYSEP, $R^2 = 0.75$) and positive intercepts. These outcomes are due to the smoothing algorithms employed, which attenuate hydrograph peaks and can potentially underestimate baseflow during transitional regimes, such as post-event recessions.

The high concordance between LH and UKIH highlights their near interchangeability in applications that prioritize continuous baseflow time series. Nonetheless, LH's parsimonious single-parameter structure offers a simplicity advantage over UKIH, which can be sensitive to interval selection. This sensitivity may introduce variability in catchments with irregular flow dynamics, thus informing method selection based on specific hydrological contexts and analytical objectives.

Determining the most accurate *BFI* estimation method is challenging due to the absence of observed base flow data for direct validation. Each method's performance depends on its algorithmic assumptions, which influence its behavior in different hydrological contexts. However, the pairwise comparisons reveal that all methods generally follow consistent trends, as evidenced by positive correlations ($R^2 \geq 0.74$), indicating that the calculated *BFI* values are reliable within the constraints of their respective approaches. Given the strong agreement between the LH and UKIH methods, the simplicity and robustness of the LH filter, and its widespread application in hydrological studies, the LH method was selected as the representative approach for future *BFI* calculations in this study.

3. Statistical Modelling of Flow Duration Curves

This chapter introduces the statistical framework for constructing Flow Duration Curves (FDCs) in intermittent Mediterranean rivers and for preparing them for regionalization. It explains how zero and non-zero flows are treated separately, how discharges are normalized for comparison across basins, and how statistical distributions are fitted to capture flow variability. The analysis is then expressed through a small set of dependent parameters — the mean (μ), standard deviation (σ), fraction of non-zero flow days (τ), and mean non-zero discharge (Q_{nz}). These parameters provide a compact way of describing the FDC and form the basis for transferring flow information to ungauged basins.

3.1 Construction of Flow Duration Curves (FDCs)

3.1.1 Hydrological Context: Mediterranean Intermittency

Hydrological regimes characteristic of Mediterranean climates is governed by pronounced seasonal variability, typified by extended dry periods—predominantly during summer—interspersed with high-magnitude runoff events during the wet season. This climatic pattern gives rise to intermittent or ephemeral streamflow behavior; wherein prolonged sequences of zero discharge are punctuated by episodic flow events. Under such conditions, the classical formulation of the FDC, which presupposes a continuous and unimodal discharge distribution, becomes methodologically inadequate (Croker et al., 2003). Specifically, the traditional approach fails to incorporate the discrete probability mass associated with zero-flow occurrences, leading to distortions in the representation of hydrological variability and extremes.

3.1.2 Probabilistic FDC Formulation

To accommodate zero-flow periods, we adopt a probabilistic decomposition rooted in the law of total probability. This approach splits the streamflow distribution into two mutually exclusive elements: (i) the probability of a zero-flow day, and (ii) the conditional distribution of flows on non-zero days (Jennings & Benson, 1969) .
Let Q represent daily discharge and let τ denote the fraction of days with non-zero discharge (i.e., days of active flow). This "duration of non-zero flow" is defined as:

$$\tau = \frac{N_{nz}}{N} \tag{3.1}$$

where N is the total number of daily observations, and N_{nz} is the number of days with Q>0. The complement, $1-\tau$, thus captures the probability of complete flow cessation (Q=0).
For any discharge value $Q \geq 0$, the cumulative distribution function (CDF) of discharge, $F(Q)$, takes the form:

$$F(Q) = (1 - \tau) + \tau \cdot \mathrm{F}(Q|Q > 0) \tag{3.2}$$

Here, $F\ (Q|Q > 0)$ is the conditional CDF of strictly positive flows. Equation (3.2) reveals a discrete jump of magnitude $1-\tau$ at zero discharge, reflecting the empirical likelihood of dry

conditions. Beyond that, the cumulative probability combines the fixed zero-flow mass with the scaled conditional probability of flows not exceeding Q on active days. This framework offers a comprehensive statistical view of the streamflow regime.
Notably, only the non-zero flow component, $F(Q|Q > 0)$ demands further modeling—the zero-flow aspect is fully encapsulated by the single parameter τ. The key hydrological variability, from low baseflows to flood peaks, arises solely during these active periods. Consequently, all subsequent FDC steps—such as ranking, normalization, and distribution fitting—are performed exclusively on the non-zero discharges. The influence of dry days, via τ, is then reintegrated during the final reconstruction of the full FDC.

3.1.3 Sorting and Ranking of non-zero Discharges

The first step in constructing the FDC is to separate non-zero flow observations from zero flows. Given a hydrological record of length N (daily flows over recorded years), let N_0 be the number of zero-flow observations:

$$N_0 = \sum_{j=1}^{N} I(Q_j = 0) \tag{3.3}$$

where $I(.)$is the indicator function, equaling 1 if the condition holds (i.e., flow is zero) and 0 otherwise. The count of strictly nonzero flows is then $N_{nz} = N - N_0$.
From the original series, extract the set of all non-zero discharges and order them in descending magnitude:

$$Q_{(1)} \geq Q_{(2)} \geq \cdots \geq Q_{(N_{nz})} \tag{3.4}$$

This ordering isolates the continuous component of the discharge regime, effectively removing the discontinuities introduced by zero flows. In this study, the threshold for zero flow is explicitly set at $Q = 0$, such that only strictly null discharge values are classified as zero-flow conditions. By treating the non-zero flow domain separately under this definition, the resulting FDC preserves the statistical integrity of the active flow periods and avoids distortion in curve shape that would otherwise arise from the inclusion of null values.

3.1.4-Dimensional Normalization using Mean of Non-Zero Flows

To facilitate inter-basin comparability across catchments of differing sizes, climatic conditions, and physiographic attributes, the non-zero discharge values are non-dimensionalized using the mean of non-zero flows, rather than the full-record mean which includes dry days. This adjustment ensures that normalization reflects only the active flow regime, thus preserving the hydrological signal while eliminating the dampening effect of prolonged zero-flow periods.
For each station, the mean of the non-zero discharge values is calculated as:

$$\bar{Q}_{nz} = \frac{1}{N_{nz}} \cdot \sum_{Q_j > 0} Q_j \tag{3.5}$$

Each ranked non-zero discharge $Q_{(j)}$ is then transformed into a dimensionless form:

$$q_{(j)} = \frac{Q_{(j)}}{\bar{Q}_{nz}} \tag{3.6}$$

This normalization yields a unit-free representation of flow magnitudes $q_{(j)}$, enabling consistent cross-comparison among basins exhibiting varying degrees of intermittency and runoff production. Crucially, it ensures that the resulting FDC reflects only the characteristics of the active flow regime, untainted by extended periods of hydrological inactivity.

3.1.5 Assignment of Exceedance Probabilities via Weibull Formula

Once sorted and normalized, each ranked discharge receives an exceedance probability, p_j, denoting the proportion of time the flow equals or exceeds that value. In hydrology, the Weibull plotting position serves as a robust, non-parametric estimator for these probabilities. For the *j-th* largest non-zero flow (where *j*=1corresponds to the maximum flow), the exceedance probability $p_j$is defined as:

$$p_j = \frac{j}{N_{nz} + 1} \tag{3.7}$$

This formulation ensures an unbiased estimate: the largest observation is assigned a probability just above zero, whereas the smallest non-zero observation tends toward unity. By convention, p_j denotes the exceedance probability of *Q*(*j*); accordingly, infrequent high-magnitude events are associated with small p_j, while recurrent low-magnitude flows correspond to large p_j.

The empirical conditional Flow Duration Curve (FDC) is then obtained by plotting each dimensionless discharge *q(j)*against its exceedance probability p_j. This corresponds to the inverse of the conditional cumulative distribution function (CDF) for non-zero flows:

$$q_{(j)} = F^{-1}_{Q|Q>0}\left(1 - p_j\right) \tag{3.8}$$

where $F^{-1}_{Q|Q>0}$ is the quantile function of non-zero flows, and 1−*p* is the non-exceedance probability used in the CDF. In simpler terms, the conditional FDC illustrates the relationship between flow magnitude and the frequency with which that flow (or a higher one) occurs, focusing solely on periods when the stream is flowing. By excluding zero-flow days, this approach yields a curve that accurately captures the variability and frequency of active streamflow events, unaffected by the presence of dry periods. This empirical conditional FDC forms the foundation for subsequent statistical modeling of the flow regime.

3.2 Choice of Distribution

Flow Duration Curves (FDCs) represent a foundational analytical tool for quantifying the long-term variability of streamflow regimes. Their utility is particularly pronounced in Mediterranean catchments, where hydrological patterns are characterized by strong seasonality, extended dry periods with zero or near-zero flows, and intermittent but intense high-flow events. These hydrological signatures introduce considerable complexity in cross-catchment analyses, especially when catchments differ significantly in size, climatic input, and topographic context. To mitigate scale effects and facilitate meaningful inter-basin comparisons, discharge values are commonly normalized. In this study, normalization was performed by dividing each daily discharge value by the corresponding mean of non-zero discharges. This procedure yields dimensionless FDCs, which preserve the relative structure of flow variability while removing the influence of absolute magnitude, thus enabling a clearer assessment of hydrological behavior across contrasting basins. Within this normalized framework, the log-normal distribution has emerged as a suitable model for representing the statistical behavior of streamflow values(Claps & Fiorentino, 1997). The preference for this distribution is rooted in its capacity to accommodate the positively skewed nature of hydrological data, which typically includes frequent occurrences of low discharge values interspersed with infrequent, high-magnitude flood events. The application of a logarithmic transformation to the normalized non-zero discharge data serves multiple purposes: it reduces skewness, stabilizes variance, and maps the data distribution closer to Gaussian form, thereby fulfilling key assumptions required for parametric statistical modeling. However, to handle prevalent zero flows in intermittent Mediterranean catchments—where log (0) is undefined and biases can arise in capturing the lower tail of the FDC—zero-flow periods were separated using the theory of total probability(Croker et al., 2003).The probability of zero flow was modeled empirically based on climate and catchment characteristics, with the log-normal applied only to the non-zero portion.

The adoption of the log-normal distribution, with these adjustments, effectively addresses scale dependence. By transforming non-zero discharge values into a log-normal space, both inter- and intra-catchment variability are retained in a form that is analytically tractable, allowing the use of standard inferential techniques for further analysis and model fitting. Moreover, this approach captures essential hydrological patterns—including intermittency, variability structure, and flow regime classification—without introducing bias from differences in catchment size or mean annual runoff.

Empirical support for the suitability of the log-normal model, particularly with log-transformed data, is provided by numerous studies. Notably, Vogel and Fennessey (1994) demonstrated that normalized FDCs derived from a wide range of US catchments could be modeled using log-transformed data to construct empirical densities and fit forms like logarithmic regression, Similarly, Castellarin et al. (2004a) validated parametric frameworks, including log-normal, for northern and eastern-central Italian catchments, reinforcing its applicability for regionalization.

3.2.1 Normalization

Leveraging the preparatory steps outlined in Sections 3.1.3 and 3.1.4, daily discharge records from each gauging station are refined for log-normal modeling. This entails segregating zero- from non-zero-flow values, normalizing the latter by their mean (yielding dimensionless data attuned to active flows), and applying a base-10 logarithmic transformation to each normalized non-zero flow.

$$Y_j = log_{10} q_{(j)} \tag{3.9}$$

This logarithmic step reshapes the y distribution toward Gaussian normality, reducing skewness and symmetrizing spread—as confirmed empirically across stations—to underpin the log-normal model's assumptions in original units. It is vital for subsequent normal-distribution fitting in log-space.

The refined dataset per station thus comprises $(Y_j)_{j=1}^{N_{nz}}$, a dimensionless array of active-flow magnitudes free from dry-period distortions. These ensembles provide the empirical foundation for log-normal fitting, facilitating precise streamflow analysis.

3.2.2 Maximum Likelihood Estimation (MLE)

Fitting the log-normal model to the non-zero flow data involves estimating the parameters of the underlying normal distribution for the log-transformed values. For a given station, denote these transformed observations as $Y_1, Y_2, \dots, Y_{N_{nz}}$. The Y_j are assumed to be independent and identically distributed, samples from a normal distribution $\mathcal{N}(\mu, \sigma^2)$, with mean μ and standard deviation σ. Maximum Likelihood Estimation (MLE) is employed to derive the best-fitting μ and σ for each station's dataset.

The log-likelihood function $\mathcal{L}(\mu, \sigma \middle| \{Y_j\})$,for these parameters given the sample is:

$$\mathcal{L}(\mu, \sigma) = -\frac{N_{nz}}{2} log(2\pi) - N_{nz} log(\sigma) - \frac{1}{2\sigma^2} \sum_{j=1}^{N_{nz}} (Y_j - \mu)^2 \tag{3.10}$$

This expression stems directly from the normal distribution's probability density function, log-transformed for optimization. The maximum likelihood estimates emerge by taking partial derivatives of $\mathcal{L}$ with respect to μ and σ, setting them to zero, and solving—yielding the values that maximize the likelihood:

$$\hat{\mu} = \frac{1}{N_{nz}} \sum_{j=1}^{N_{nz}} Y_j \tag{3.11}$$

$$\hat{\sigma} = \sqrt{\frac{1}{N_{nz}} \sum_{j=1}^{N_{nz}} (Y_j - \mu)^2} \tag{3.12}$$

Here, $\hat{\mu}$ corresponds to the sample mean of the Y_j values, and $\hat{\sigma}$ corresponds to the square root of the sample variance. In practice, these values are equivalent to the mean and standard deviation of log-transformed series.

Model adequacy for non-zero flows is evaluated in log-space via quantile-quantile (*Q-Q*) analysis, which contrasts observed quantiles Y_j (from the sorted *j-th* value) with their theoretical counterparts derived from the fitted normal distribution:

$$Y_j^{Theoretical} = \hat{\mu} + \hat{\sigma}\Phi^{-1}(F) \tag{3.13}$$

where Φ^{-1} is the standard normal inverse CDF, and F is the non-exceedance probability for the *j-th* ranked flow, $F = 1 - p_j = 1 - \frac{j}{N_{nz}+1}$.

Goodness of fit is assessed using a combination of visual and quantitative diagnostics. *Q–Q* plots provide a visual check by comparing the empirical quantiles (Y_j) with the theoretical quantiles ($Y_j^{Theoretical}$). A close alignment along the 1:1 reference line indicates a strong agreement between the observed data and the model, whereas systematic deviations, especially in the lower tail, highlight potential difficulties in representing small but positive discharges. This issue is particularly relevant in Mediterranean catchments, where frequent low-flow conditions are a defining hydrological characteristic.

To complement the visual inspection, five statistical indices are computed on the log-transformed discharges and their theoretical values. These include *RMSE, MAE,* R^2*, MAPE*, and *PBIAS*, which collectively quantify accuracy, error magnitude, explained variance, and overall bias. Evaluating the fit in the same transformed space ensures consistency with the log-normal modeling framework.

3.3 Model Evaluation and Validation

Root Mean Square Error (*RMSE*): Quantifies the standard deviation of the residuals, reflecting the average error in the log-transformed space:

$$RMSE = \sqrt{\frac{1}{N_{nz}}\sum_{j=1}^{N_{nz}}\left(Y_j^{Theoretical} - Y_j\right)^2} \tag{3.14}$$

Mean Absolute Percentage Error (*MAPE*): Expresses the average error as a percentage of the observed values, useful for assessing relative accuracy:

$$MAPE = \frac{1}{N_{nz}}\sum_{j=1}^{N_{nz}}\frac{\left|Y_j^{Theoretical} - Y_j\right|}{\left|Y_j\right|} \times 100 \tag{3.15}$$

Mean Absolute Error (*MAE*): Calculates the average absolute difference, providing a robust measure of error magnitude:

$$MAE = \frac{1}{N_{nz}} \sum_{j=1}^{N_{nz}} \left| Y_j^{Theoretical} - Y_j \right| \tag{3.16}$$

Coefficient of Determination (R^2): Indicates the proportion of variance in the observed log-transformed discharges explained by the model:

$$R^2 = 1 - \frac{\sum_{j=1}^{N_{nz}} \left(Y_j^{Theoretical} - Y_j \right)^2}{\sum_{j=1}^{N_{nz}} \left(Y_j - \bar{Y} \right)^2} \tag{3.17}$$

Percent Bias (*PBIAS*): Measures the average tendency of the predicted values to overestimate or underestimate the observed values:

$$PBIAS = \frac{\sum_{j=1}^{N_{nz}} \left(Y_j^{Theoretical} - Y_j \right)}{\sum_{j=1}^{N_{nz}} Y_j} \times 100 \tag{3.18}$$

Figure 3.1 presents *Q–Q* plots for a representative subset of nine stations drawn at random from the network. For most basins the points closely follow the 1:1 line across the central quantiles, confirming that the model reproduces the bulk of the log-transformed non-zero flows. The visible departures are concentrated in the tails. At the lower tail, several panels show "steps" or lateral spread, indicating heaping of very small values near measurement thresholds (e.g., B17, C20, C30). At the upper tail, a few stations bend above the line, suggesting heavier-than-log-normal extremes (e.g., N8). These tail effects explain the occasional *RMSE/MAPE* outliers, whereas the tight central alignment is consistent with the near-zero *PBIAS* and high R^2, supporting the adequacy of the log-normal fit for the range most relevant to regionalization.

The distribution of goodness-of-fit metrics is illustrated by histograms in Figure 3.2. (a,b,c,d,e). The *MAE* ranged from 0.015 to 0.136, with 73% of the values concentrated between 0.030 and 0.070. The mode occurred near 0.048, indicating that, on average, the absolute deviation between the observed and fitted quantiles was relatively low. This confirms a close alignment between the empirical and modeled distributions in the central range. The *MAPE* values displayed substantial dispersion, ranging from 7.403% to 1835.864%. Despite this wide range, 73.5% of the stations had *MAPE* values below 100%, and 41.2% fell between 10% and 50%. This suggests that, in most cases, the relative error remained within acceptable bounds. The extreme outliers (*MAPE* > 1000%) can be attributed to near-zero discharge values in the denominator of the *MAPE* formula, which inflate percentage errors disproportionately. This well-known limitation makes *MAPE* less informative in low-flow regimes and should be interpreted cautiously in hydrological applications. The *PBIAS* values were tightly distributed around zero, ranging from -4.551×10^{-14} to $+3.814 \times 10^{-14}$, with more than 95% of observations confined within $\pm 1.000 \times 10^{-14}$. This result confirms the absence of systematic bias in the fitted model, demonstrating that it neither consistently overestimates nor underestimates discharge quantiles. The *RMSE*, which places greater emphasis on larger errors, ranged from 0.028 to 0.157, with 76.5% of values falling between 0.040 and 0.090. The median value of 0.063 and the modal value near 0.065 suggest that significant deviations were rare, reinforcing the overall consistency and reliability of the log-normal fit, even in the tails of the distribution. The R^2 values exhibited a strong skew toward unity, ranging from 0.845 to 0.997, with a median of 0.980. Notably, 88.2% of the stations had R^2 values exceeding 0.960, and 61.8% exceeded 0.980, indicating a consistently high degree of linear correspondence between the modeled and observed quantiles. This provides robust statistical evidence for the explanatory power of the log-normal model in the log-transformed space.

Collectively, the metrics and *Q–Q* diagnostics indicate that the log-normal model is reliable for the central quantiles that underpin regionalization, while tail departures warrant caution when interpreting extremes.

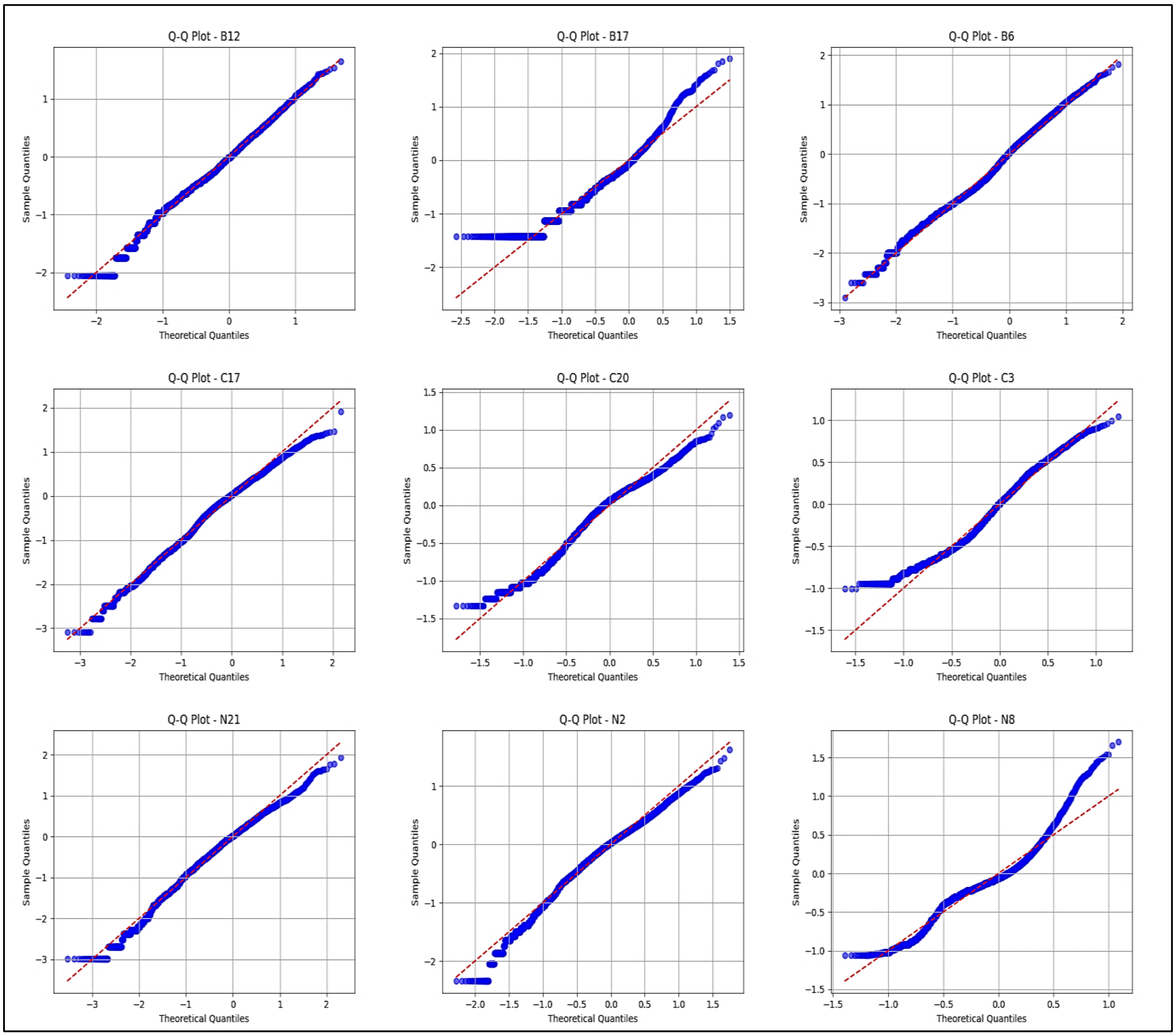

Figure 3.1: Q–Q plots of log-normal fit for nine representative stations

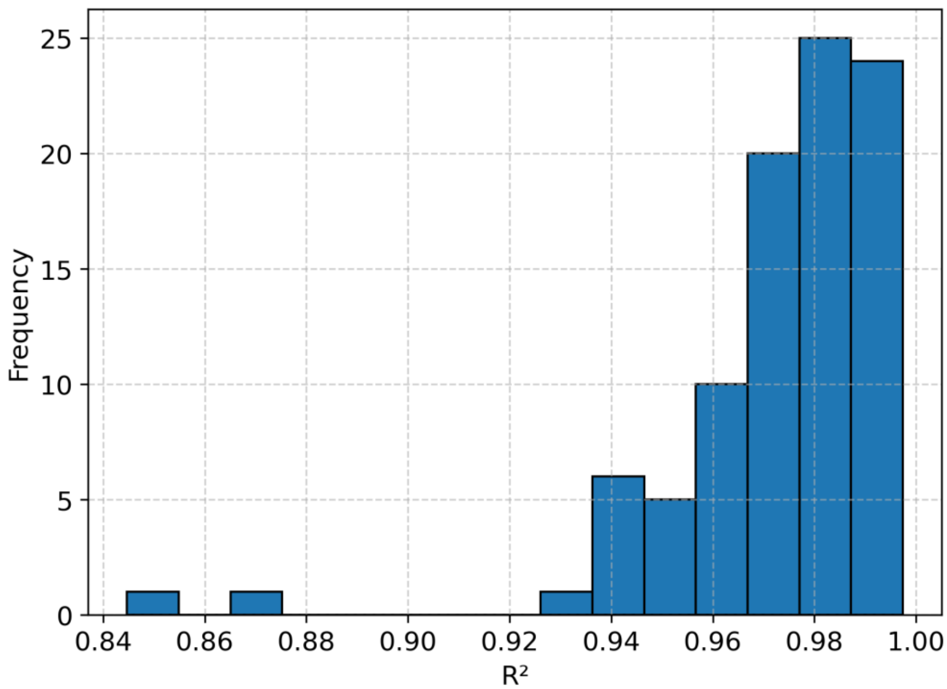

Figure 3.2.a: Distribution of statistical metrics (R^2) used to evaluate the log-normal fit to log-transformed non-zero daily streamflow across 89 stations.

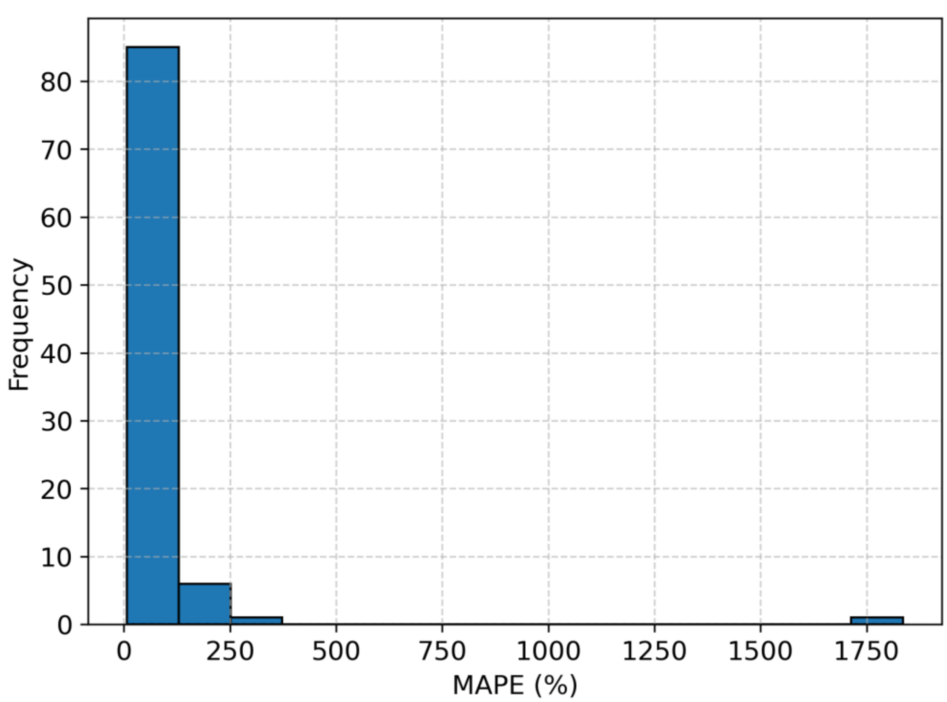

Figure 3.2.b: Distribution of statistical metrics (MAPE) used to evaluate the log-normal fit to log-transformed non-zero daily streamflow across 89 stations.

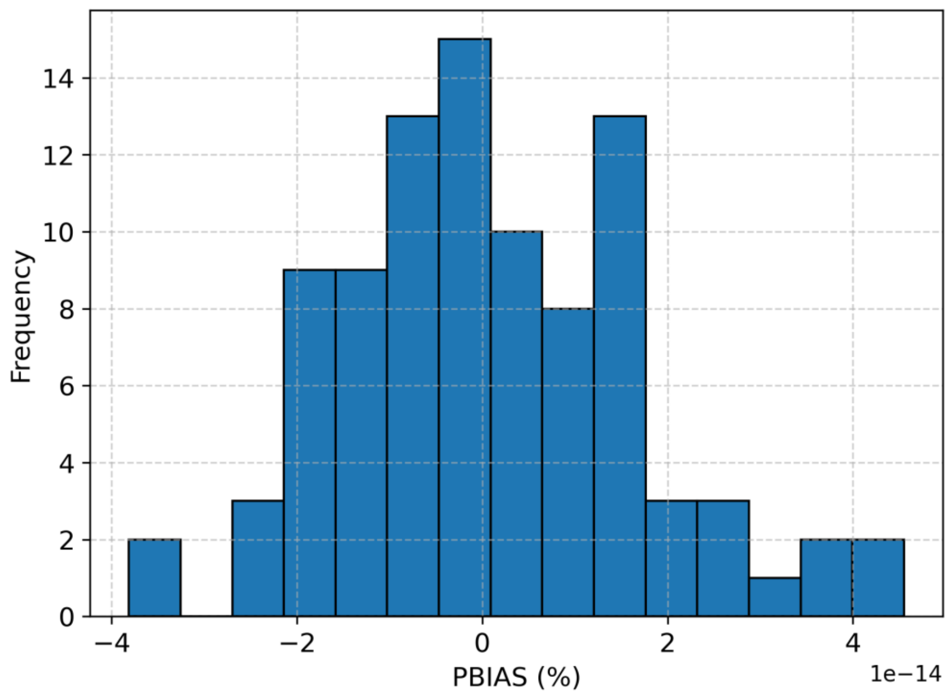

Figure 3.2.c: Distribution of statistical metrics (PBIAS) used to evaluate the log-normal fit to log-transformed non-zero daily streamflow across 89 stations.

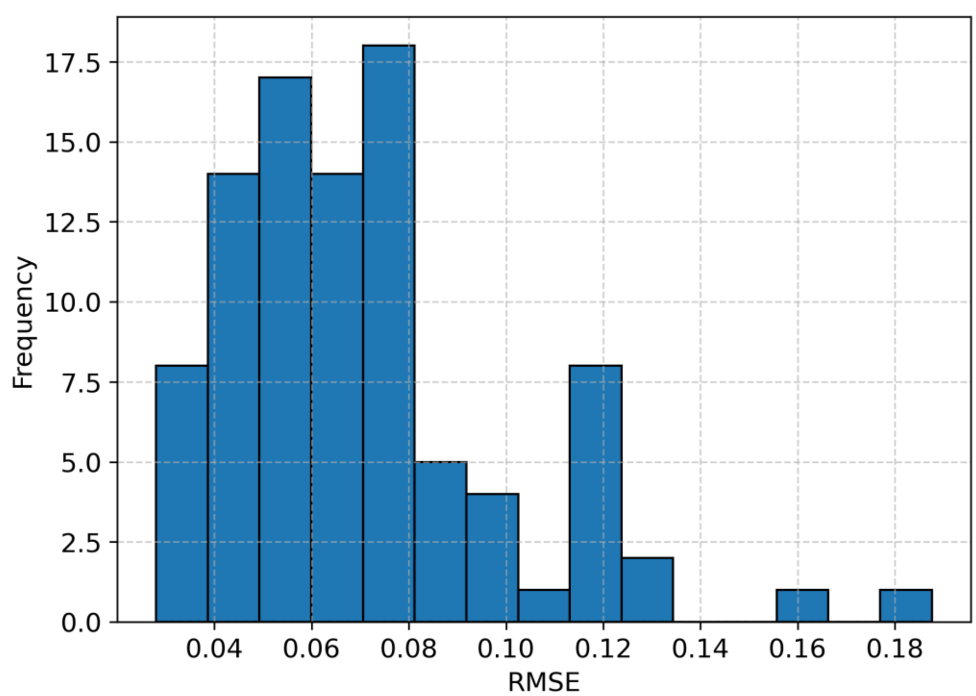

Figure 3.2.d: Distribution of statistical metrics (RMSE) used to evaluate the log-normal fit to log-transformed non-zero daily streamflow across 89 stations.

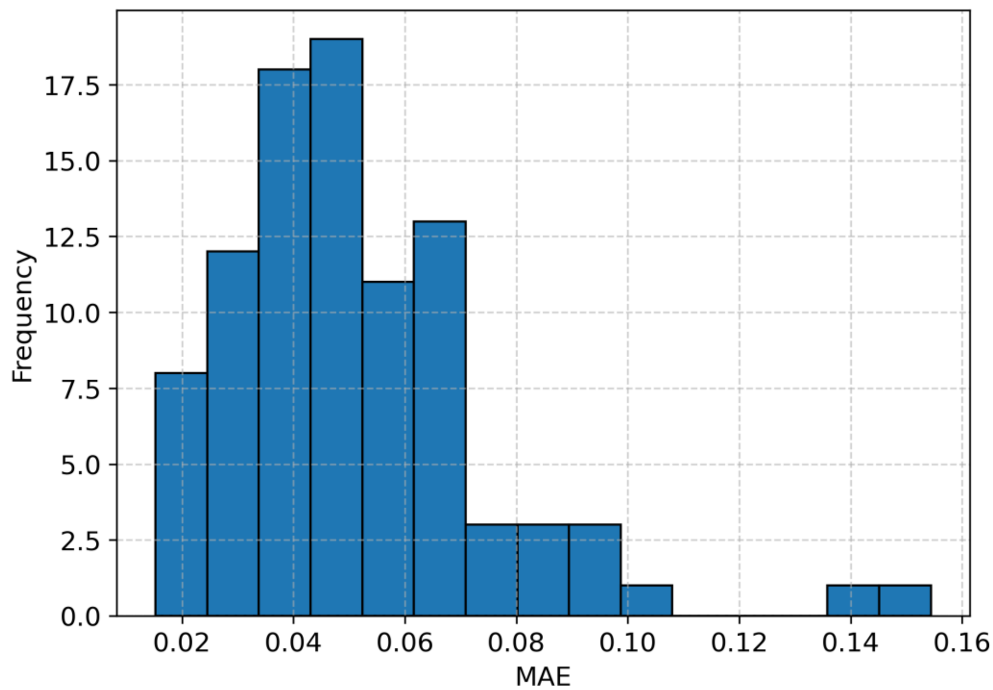

Figure 3.2.e: Distribution of statistical metrics (MAE) used to evaluate the log-normal fit to log-transformed non-zero daily streamflow across 89 stations.

3.3.1 Capturing the Full Flow Duration Curve (FDC)

The complete Flow Duration Curve can be fully described using four key parameters: the duration of non-zero flow (τ), the mean of non-zero discharges ($\bar{Q}_{nz}$), and the parameters of the log-normal distribution fitted to normalized flows ($\hat{\mu}$, $\hat{\sigma}$). Together, these quantities capture both the frequency of flow cessation and the statistical characteristics of active discharge variability. By integrating the probabilistic decomposition in Equations (3.2) with the log-normal model for strictly positive flows, the entire cumulative distribution function (CDF) of daily discharge is obtained.

$$\mathrm{F}(Q) = (1-\tau) + \tau \cdot \Phi\left(\frac{log_{10}(Q|Q>0) - \hat{\mu}}{\hat{\sigma}}\right) \tag{3.19}$$

where $\Phi\,(\cdot)$ denotes the standard normal cumulative distribution function.

3.3.2 Normalized Cumulative Distribution Function (CDF)

The Flow Duration Curve is obtained by considering the exceedance probability, which is the complement of the CDF. From Equation (3.20), the probability that nondimensional daily flow exceeds a given value q is:

$$p(q) = 1 - \mathrm{F}(q) = \tau \cdot \left[1 - \Phi\left(\frac{log_{10}(q|q > 0) - \hat{\mu}}{\hat{\sigma}}\right)\right] \tag{3.20}$$

At q=0, the exceedance probability equals τ, which reflects the proportion of time that flow occurs. For q>0, the exceedance probability is given by τ multiplied by the upper tail of the log-normal distribution. This structure indicates that positive discharges are only possible during the active fraction of time (τ), and within that fraction they are distributed according to the fitted log-normal law.
Hydrologically, this means that the probability of exceeding any flow threshold is reduced by the factor τ, representing the intermittency of the system. Large values of q correspond to small exceedance probabilities, while as q approaches zero from above, $p(q)$ approaches τ. For exceedance probabilities greater than τ, the corresponding nondimensional discharge is identically zero, reflecting the fact that flow cannot be sustained more frequently than the fraction of active days. Thus, the FDC displays a flat segment at zero discharge, extending from $p=\tau$ to p=1.

3.3.3 Cumulative Distribution Function (CDF)

According to Equation (3.6), the normalized formulation of 3.3.2 is transformed back into dimensional form by replacing the nondimensional variable q with the ratio $Q/\bar{Q}_{nz}$. This yields:

$$p(Q) = 1 - \mathrm{F}(Q) = \tau \cdot \left[1 - \Phi\left(\frac{log_{10}(Q/\bar{Q}_{nz}|Q/\bar{Q}_{nz} > 0) - \hat{\mu}}{\hat{\sigma}}\right)\right] \tag{3.21}$$

This expression preserves the same probabilistic structure as in the normalized case, while rescaling the log-normal distribution to physical discharge units.

3.3.4 Inverse Quantile Function

The FDC is often represented by the inverse quantile function, which expresses discharge as a function of exceedance probability. Rearranging Equation (3.22), the discharge quantile at exceedance level p is:

$$Q_{(p)} = \begin{cases} \bar{Q}_{nz} 10^{\hat{\mu} + \hat{\sigma}.\Phi^{-1}\left(1 - \frac{p}{\tau}\right)} & 0 < p \le \tau \\ 0 & \tau < p \le 1 \end{cases} \tag{3.22}$$

where $\Phi^{-1}(\cdot)$ is the inverse standard normal CDF.

These formulations provide the complete theoretical FDC. For exceedance probabilities $p>\tau$, the discharge is identically zero, representing dry days. For $p \le \tau$, flow values are determined by the quantiles of the log-normal distribution, scaled by the mean of non-zero discharges.

3.4 Hydrological Interpretation of FDC Parameters

The regionalization of Flow Duration Curves (FDCs) in ungauged catchments, where direct streamflow measurements are unavailable, is a critical process for hydrological analysis and water resource management. Four key parameters underpin the construction and regionalization of FDCs: the mean (μ) and standard deviation (σ) of the log-transformed normalized discharges, the Duration of non-zero flow (τ), and the mean non-zero discharge $\bar{Q}_{nz}$. These parameters collectively define the shape, scale, and intermittency of the FDC, enabling its application across diverse hydrological regimes. This section elucidates the relationships between these parameters and catchment characteristics as identified in the hydrological literature, detailing how each parameter contributes to the regionalization process and supports the estimation of FDCs in ungauged catchments.

Table 3.1. Summary of mean non-zero discharge ($\bar{Q}_{nz}$), duration of non-zero flow (τ), standard deviation (σ), and mean (μ) of log-transformed normalized discharges—calculated for 89 catchments.

Station's Code	τ	μ	σ	$\bar{Q}_{nz}$
B1	0.97	-0.48	0.68	12.85
B2	0.74	-0.45	0.66	1.05
B3	0.73	-0.67	0.90	3.72
B4	0.93	-0.50	0.65	1.44
B5	0.97	-0.26	0.45	0.71
B6	0.99	-0.49	0.64	7.91
B7	0.95	-0.63	0.77	3.02
B8	0.57	-0.44	0.61	0.57
B9	0.82	-0.64	0.80	3.17
B10	0.61	-0.45	0.69	0.80
B11	0.80	-0.39	0.52	0.19
B12	0.93	-0.37	0.57	1.13
B13	0.66	-0.59	0.64	0.33
B14	0.59	-0.31	0.49	0.18
B15	0.97	-0.27	0.47	0.97
B17	0.63	-0.54	0.58	0.27
B18	1.00	-0.23	0.40	1.19
B19	0.67	-0.51	0.62	0.25
B20	0.99	-0.18	0.39	0.36
B21	0.81	-0.47	0.68	1.13
B22	0.89	-0.51	0.69	3.79
C1	1.00	-0.17	0.36	3.67
C2	1.00	-0.34	0.54	7.77
C3	1.00	-0.19	0.39	1.32
C4	1.00	-0.22	0.42	1.39
C5	1.00	-0.32	0.54	3.65
C6	1.00	-0.31	0.51	20.76
C7	1.00	-0.11	0.32	5.86
C8	1.00	-0.16	0.35	1.25
C9	1.00	-0.15	0.35	0.99
C10	1.00	-0.09	0.25	7.97
C11	1.00	-0.17	0.35	4.54
C13	1.00	-0.52	0.72	9.33
C14	1.00	-0.23	0.45	0.56
C15	0.85	-0.63	0.78	2.31
C16	1.00	-0.26	0.51	0.21
C17	1.00	-0.55	0.75	12.25
C18	1.00	-0.13	0.32	2.14
C19	1.00	-0.20	0.47	25.67

C20	1.00	-0.19	0.44	0.86
C21	1.00	-0.19	0.40	2.02
C22	1.00	-0.34	0.59	2.49
C23	1.00	-0.32	0.54	0.81
C24	1.00	-0.20	0.43	0.59
C25	1.00	-0.14	0.31	6.73
C26	1.00	-0.28	0.50	0.76
C27	1.00	-0.22	0.45	0.93
C28	0.82	-0.25	0.54	1.34
C29	1.00	-0.23	0.40	1.76
C30	0.52	-0.26	0.54	0.96
C31	1.00	-0.34	0.64	7.39
C32	0.99	-0.37	0.60	0.89
C33	1.00	-0.14	0.33	9.31
C34	1.00	-0.27	0.48	10.89
C35	0.82	-0.32	0.60	1.78
C36	1.00	-0.17	0.36	1.59
C37	1.00	-0.18	0.43	4.33
C38	1.00	-0.21	0.44	3.83
C39	1.00	-0.15	0.35	0.73
C40	1.00	-0.18	0.37	7.10
C41	1.00	-0.19	0.43	4.73
C42	1.00	-0.17	0.36	4.43
C43	1.00	-0.23	0.47	0.75
C44	1.00	-0.27	0.48	2.12
C45	1.00	-0.25	0.49	1.64
C46	1.00	-0.16	0.38	8.38
C48	0.97	-0.52	0.75	1.57
N1	1.00	-0.22	0.39	10.20
N2	0.99	-0.26	0.52	2.22
N3	1.00	-0.21	0.41	63.42
N4	1.00	-0.17	0.35	90.75
N5	1.00	-0.36	0.49	24.68
N6	1.00	-0.22	0.42	35.87
N8	1.00	-0.15	0.32	10.06
N10	1.00	-0.25	0.50	11.69
N13	1.00	-0.49	0.64	4.34
N20	1.00	-0.34	0.54	34.15
N21	0.95	-0.61	0.80	9.75
N25	1.00	-0.65	0.93	8.01
N26	1.00	-0.13	0.29	96.85
N27	1.00	-0.17	0.35	48.06
N32	1.00	-0.10	0.29	4.90
N33	1.00	-0.07	0.22	3.60
N40	1.00	-0.13	0.30	39.83
N41	0.77	-0.53	0.73	0.99
N42	1.00	-0.15	0.33	51.32
N43	1.00	-0.44	0.59	6.55
N44	1.00	-0.09	0.28	1.71
N45	1.00	-0.06	0.20	6.67

3.4.1 Interpretation of Mean (μ) and Standard Deviation (σ)

This study employs the log-normal distribution to model normalized non-zero Flow Duration Curves (FDCs), using two key parameters: the mean μ and standard deviation σ of the logarithmically transformed discharge values. It is important to emphasize that the analysis focuses exclusively on normalized FDCs, where discharge values are expressed relative to their mean, thereby removing scale effects and enabling consistent cross-catchment comparison. A comprehensive understanding of both the statistical characteristics and hydrological interpretations of these parameters is essential for analyzing FDC behavior and for developing robust regionalization models applicable to ungauged basins.

The mean parameter μ reflects the central tendency of normalized flows and is strongly influenced by both climatic inputs and hydrogeological controls. Claps & Fiorentino (1997) demonstrated a positive association between μ and the Base Flow Index (*BFI*), suggesting that catchments with persistent groundwater contributions exhibit more stable and elevated flow regimes. Castellarin et al. (2004) showed that the parameters μ and σ of the log-normal distribution can be regionalized using catchment descriptors such as area, elevation range, mean annual net precipitation, and the proportion of permeable surfaces, reflecting controls on both flow magnitude and variability

Complementary evidence from Li et al. (2010) highlighted the dominant role of mean annual precipitation in shaping μ, with positive correlations to rainfall and negative correlations to potential evapotranspiration . However, their findings underscored precipitation as the primary driver, especially in arid and semi-arid climates, where water availability is predominantly governed by rainfall rather than atmospheric demand.

The standard deviation σ of the log-transformed discharges represents the variability of flow regimes and is similarly governed by climatic and catchment characteristics. According to Li et al. (2010), rainfall variability (i.e., the standard deviation of annual rainfall) emerged as a significant predictor of streamflow variability, with larger fluctuations in precipitation corresponding to broader flow distributions. Evapotranspiration further amplifies this variability by intensifying temporal flow discontinuities, particularly in dry environments. Conversely, vegetation cover, quantified through metrics such as the Leaf Area Index, exerts a dampening effect by enhancing infiltration, interception, and soil water retention, thus narrowing flow distributions and producing steeper FDC slopes.

These relationships were corroborated by Longobardi & Villani (2013), who employed multiple linear regression to demonstrate that both μ and σ are significantly modulated by an integrated set of physiographic and climatic variables. Key predictors included catchment permeability, mean elevation, average slope, forested area percentage, mean annual precipitation, and *BFI*.

Boscarello et al.(2016) showed that the mean and standard deviation parameters of flow duration curves can be effectively regionalized using catchment classification based on streamflow signatures and physiographic–climatic indices. Their study highlighted that these statistical parameters are closely linked to key catchment descriptors such as elevation, land cover, precipitation patterns, and soil characteristics, which collectively shape the hydrological response across different regions.

By linking the statistical properties of normalized FDCs to observable catchment attributes, the log-normal framework provides a practical basis for regional hydrological analysis and supports model transferability to data-scarce environments. This is particularly valuable in Mediterranean or semi-arid contexts, where flow intermittency is pronounced and conventional hydrological modeling approaches face limitations.

3.4.1.1 Parameter Interdependence

A critical aspect of modeling Flow Duration Curves (FDCs) is the interrelationship between the parameters of the log-normal distribution. Specifically, an empirical interdependence between the mean (μ) and standard deviation (σ) of the log-transformed, normalized non-zero discharges has been consistently observed across a wide range of catchments. This relationship is statistically validated through linear regression analysis(Claps & Fiorentino, 1997).

As shown in Figure 3.3, a strong negative linear correlation exists between μ and σ, with a coefficient of determination of $R^2 = 0.93$. The regression line, described by the equation $\sigma = -0.945\mu + 0.214$, suggests that catchments characterized by lower central flow tendencies (lower μ) tend to exhibit greater variability (higher σ). This phenomenon may be attributed to factors such as intermittent hydrological inputs which amplify discharge variability in low-flow environments.

The results summarized in Table 3.1 further substantiate the robustness of this empirical relationship, highlighting its potential utility in regionalization studies. Rather than treating μ and σ as independent parameters, the high degree of correlation supports the approach of expressing σ as a function of μ. This not only simplifies the parameterization process by reducing redundancy but also enhances the interpretability and predictive capability of models aimed at ungauged basins.

By leveraging this parameter interdependence, it becomes possible to estimate the full FDC using a single parameter (μ) and its relationship to σ, thereby facilitating the transfer of hydrological information across data-scarce regions. This approach improves the robustness of synthetic FDC construction and supports the development of regional models grounded in physiographic or climatic descriptors.

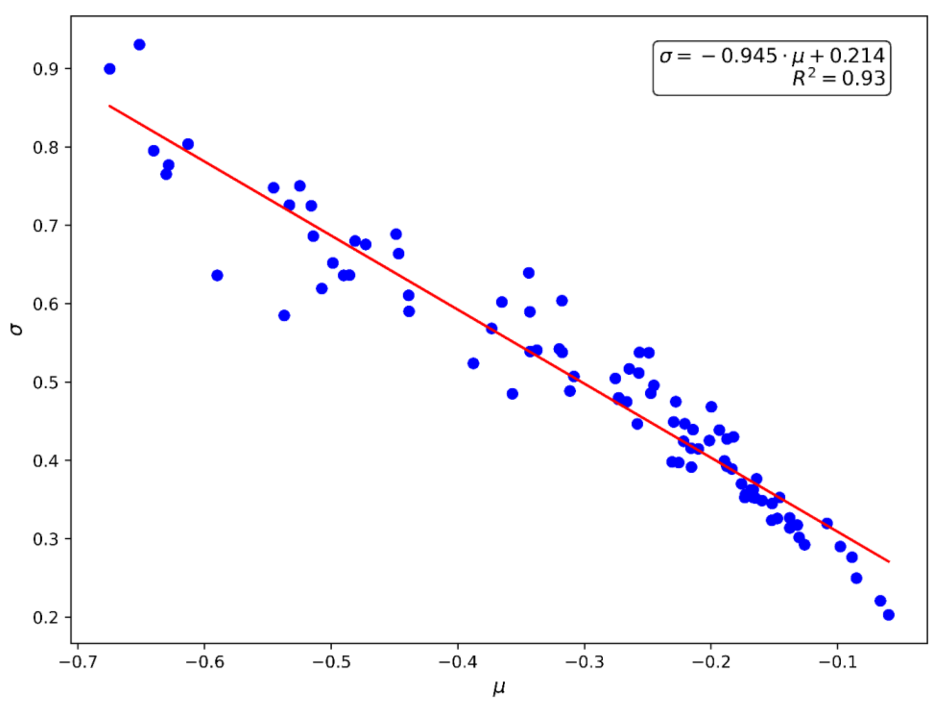

Figure 3.3: Empirical relationship between the log-normal distribution parameters μ and σ derived from normalized Flow Duration Curves (FDCs).

3.4.2 Interpretation of Duration of non-zero flow (τ)

In the present study, normalized Flow Duration Curves (FDCs) were derived exclusively from non-zero daily discharge values. By omitting zero-flow days during normalization, the analysis isolates periods of active streamflow, thereby provides a more accurate depiction of hydrological dynamics during active streamflow.

While normalization focuses on non-zero values, the inclusion of the Duration of non-zero flow τ remains essential for characterizing the broader hydrological regime. As a metric quantifying the frequency of active flow, τ is instrumental in evaluating drought susceptibility, stream connectivity, and hydrological persistence—particularly in arid and semi-arid environments. Within regionalization frameworks, τ provides a critical basis for distinguishing perennial streams from ephemeral systems, supporting the classification and comparative analysis of flow regimes

The variability in τ is largely governed by climatic, topographic, and ecological drivers. Higher mean annual precipitation and lower potential evapotranspiration are generally associated with more persistent flows and reduced zero-flow frequency(Brown et al., 2005). In contrast, steep-gradient catchments often exhibit greater flow intermittency due to limited groundwater retention and rapid surface runoff (Lane et al., 2005). Vegetation characteristics further influence flow persistence; dense woody cover can intensify evapotranspiration losses, depleting baseflow and increasing intermittency(Brown et al., 2007).

At the catchment scale, multiple physical characteristics act in concert to shape τ Mendicino & Senatore (2013) highlighted that the frequency of non -zero-flow days is strongly influenced by drainage area, elevation range, lithological composition, and soil texture. Smaller basins with steep slopes, low-permeability substrates, and poorly infiltrating soils are particularly prone to flow cessation. These findings underscore the combined role of geomorphology, substrate permeability, and infiltration potential in controlling flow continuity. Similarly, Croker et al. (2003) identified mean annual precipitation as the dominant predictor of non-zero flow occurrence, reaffirming the primary role of climatic forcing in sustaining streamflow.

3.4.3 Interpretation of $\bar{Q}_{nz}$

This study focuses on normalized FDCs, but deriving actual FDCs for ungauged basins requires rescaling with an appropriate flow magnitude. The mean non-zero discharge ($\bar{Q}_{nz}$) serves as a pivotal scaling factor, converting dimensionless curves into real discharge units. For ungauged contexts, ($\bar{Q}_{nz}$) must be regionalized using physiographic and climatic descriptors, highlighting its centrality in predictive frameworks (Table 3.1).

Fundamentally, mean river flow, often represented by mean annual discharge, is governed by essential catchment properties, chiefly catchment area and mean annual precipitation. Precipitation acts as the dominant climatic input to the hydrological system, while catchment area defines the spatial domain over which this input is accumulated and transformed into runoff (Smakhtin, 2001; Mohamoud, 2008; Mendicino & Senatore, 2013).

4. GIS-Based Catchment and River Network Reconstruction

This chapter presents the processing of spatial datasets necessary for the reconstruction of catchments and river networks, with the aim of establishing a consistent georeferenced framework for all basins under study. Through DEM-based hydrological conditioning, integration of historical gauging records, and the extraction of morphometric, hydrogeological, and land cover descriptors, each catchment is systematically associated with its physical and environmental attributes, providing the spatial foundation for subsequent analyses.

4.1 Digital Elevation Model (DEM)

The reliability of GIS-based catchment and river network delineation is fundamentally governed by the resolution and integrity of the underlying elevation data, which directly influence the accuracy of hydrological simulations (Z. Li, 2014). In this study, a Digital Elevation Model (DEM) with a spatial resolution of 20 meters[2] was employed to capture the fine-scale topographic variability essential for accurately representing hydrological processes such as flow direction, watershed boundaries, and drainage network morphology. This resolution offers a notable enhancement over commonly adopted datasets in regional-scale applications, such as the 30-meter Shuttle Radar Topography Mission (SRTM)[3], particularly in the complex orography of southern Italy, where subtle elevation gradients critically affect flow accumulation patterns. Although a finer-resolution national DEM (TINITALY, 10 m)[4] is available, it was not utilized due to spatial inconsistencies introduced by its construction as a mosaic of regionally produced DEMs, which results in discontinuities across administrative borders (Claps et al., 2023). Given these constraints, the 20 m DEM was identified as the most suitable and spatially coherent elevation dataset for ensuring consistent and robust hydrological analysis across the study domain.
All spatial analyses were performed using the WGS 1984 UTM Zone 33N coordinate reference system, ensuring spatial consistency, metric accuracy, and interoperability with ancillary geospatial datasets across the study area.

4.2 GIS-Based Delineation of Catchments and River Networks

4.2.1 DEM Reconditioning and Hydrological Alignment

The delineation of catchments and river networks forms a foundational component of hydrological and geomorphological studies. In this work, all spatial analyses were carried out using ArcGIS Pro, a high-precision GIS software platform widely used for hydrological modeling and spatial analysis.
The study area, located in southern Italy, is characterized by physiographic complexity, particularly in low-relief coastal regions where natural drainage features have been substantially modified through land reclamation, artificial channels, culverts. These anthropogenic changes often obscure or sever natural hydrological pathways, leading to challenges in catchment delineation and stream network extraction (Lindsay & Dhun, 2015). As such, a robust, multi-stage methodology was

[2] https://inspire-geoportal.ec.europa.eu/srv/api/records/m_amte:299FN3:eba41113-4141-4d46-9cdf-b0848deec44d
[3] https://www.earthdata.nasa.gov/data/instruments/srtm
[4] https://tinitaly.pi.ingv.it/

designed and implemented to ensure the accuracy, consistency, and hydrological reliability of the derived spatial products.

The workflow commenced with DEM reconditioning, a critical preprocessing stage designed to ensure that modeled flow paths closely reflect the actual hydrographic network. This step integrated into two fundamental datasets: (i) a raw Digital Elevation Model (DEM) representing the regional topographic surface, and (ii) the official ISPRA (Istituto Superiore per la Protezione e la Ricerca Ambientale) stream network shapefile[5], which incorporates both natural watercourses and anthropogenic features such as artificial channels and culverts.

Hydrological coherence was established through two sequential operations within ArcGIS Pro's ArcHydro toolset:

- Stream Burning (DEM Reconditioning Tool). The ISPRA stream network was embedded into the DEM by artificially lowering elevations along stream paths. This "burning" process forces modeled flows to follow the known channel network and eliminates erroneous divergence caused by subtle elevation errors, DEM interpolation artifacts, or flat terrain. The procedure is particularly indispensable in low-relief coastal areas, where very small gradients can lead to unrealistic flow routing and disconnected networks (Callow et al., 2007; Merwade, 2012). The operation was executed using the DEM Reconditioning tool, which applies the AGREE algorithm to systematically adjust cell values along the streamlines and taper the modifications laterally within a defined buffer to preserve geomorphic realism.
- Catchment Boundary Enforcement (Build Walls Tool). In a complementary step, the official ISPRA catchment perimeters[6] were imposed as hydrological divides. This was accomplished by raising DEM elevations along the catchment boundaries, thereby establishing topographic barriers that prevent modeled flow from spilling into adjacent basins. The enforcement of these boundaries is particularly critical in anthropogenically modified landscapes, where natural divides may be absent, subdued, or masked by drainage works such as reclamation channels or culverts. Arc Hydro's Build Walls tool was employed for this operation, which raises elevation values along polygonal or linear features and incorporates specified breach lines (e.g., outlets or river crossings) to maintain correct hydrological connectivity.

Together, these two operations produced a hydrologically conditioned DEM in which modeled streams align precisely with the ISPRA hydrographic network and delineated watersheds conform rigorously to authoritative boundaries (Fig. 4.1).

[5] https://inspire-geoportal.ec.europa.eu/srv/api/records/ispra_rm:001Idrografia250N_SVD
[6] https://inspire-geoportal.ec.europa.eu/srv/api/records/ispra_rm:02Idro250N_DT

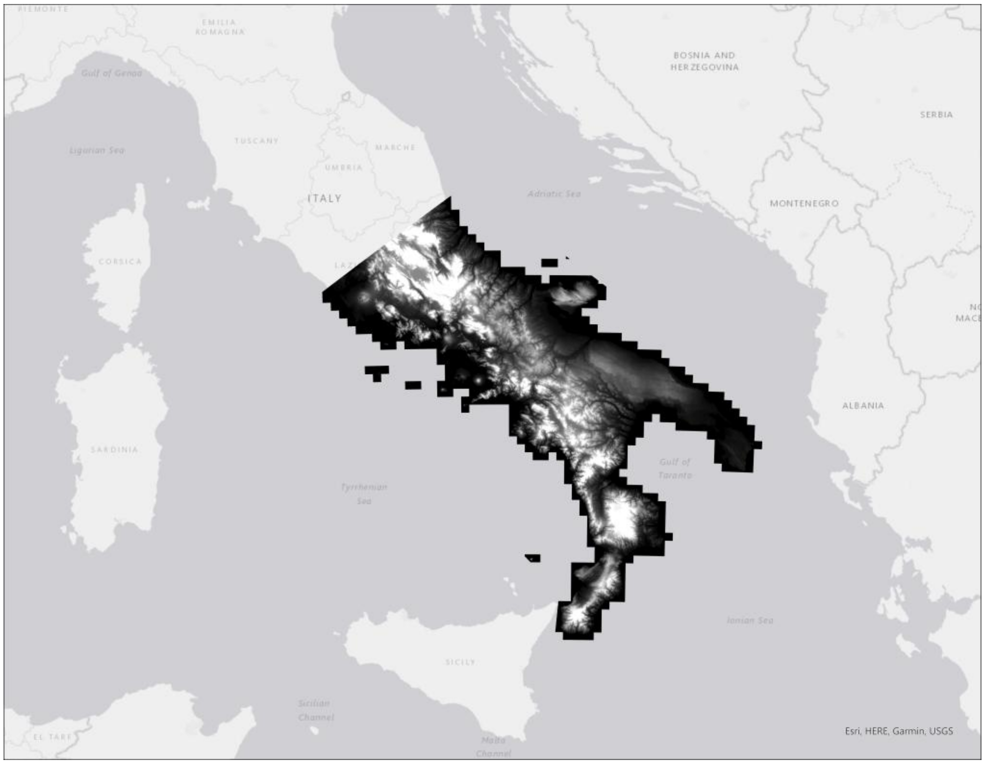

Figure. 4.1: Reconditioned DEM of southern Italy after stream burning

4.2.2 Flow Direction, Accumulation, and Catchment Delineation

After DEM reconditioning, a sink-filling algorithm was applied to remove artificial depressions in the elevation grid. These depressions—common in flat or low-relief regions due to data limitations—can incorrectly trap surface flow. The filling process elevated these cells just enough to allow continuous downstream routing, preserving hydrological realism.

Next, flow direction was calculated using the D8 algorithm, which assigns each cell a direction of steepest descent to one of its eight neighbors (Fig. 4.2). This was followed by flow accumulation (Fig. 4.3), wherein the number of upstream contributing cells was tallied for each cell in the grid. High accumulation values indicate potential stream channels; low values correspond to upland or ridge areas (Seibert & McGlynn, 2007).

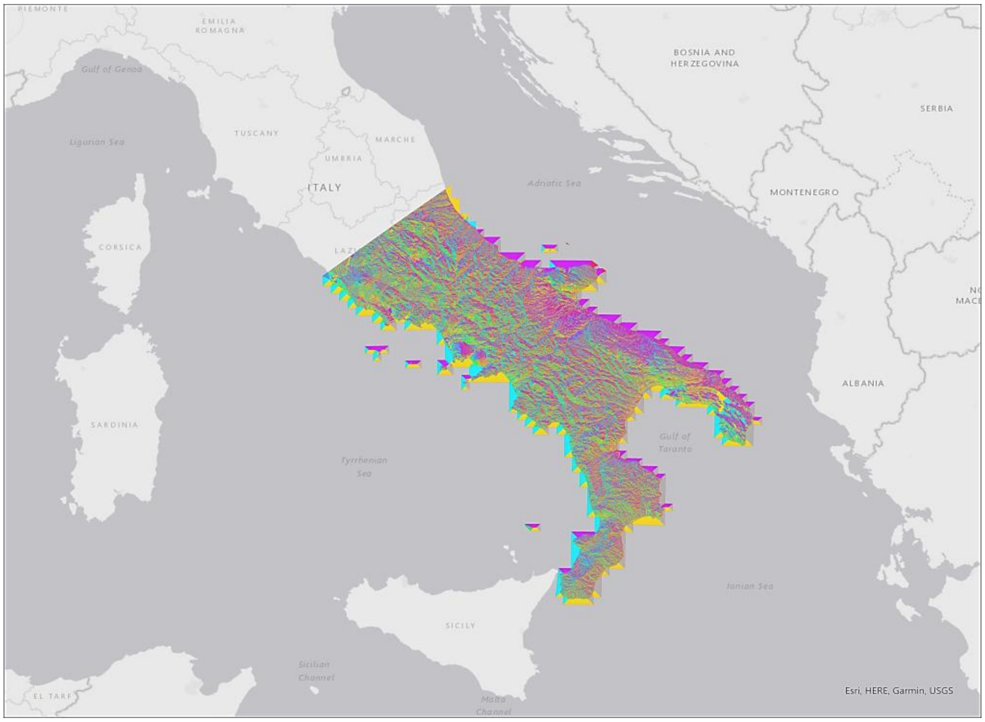

Figure. 4.2: Flow direction grid generated using the D8 algorithm, representing the steepest descent pathways across the terrain

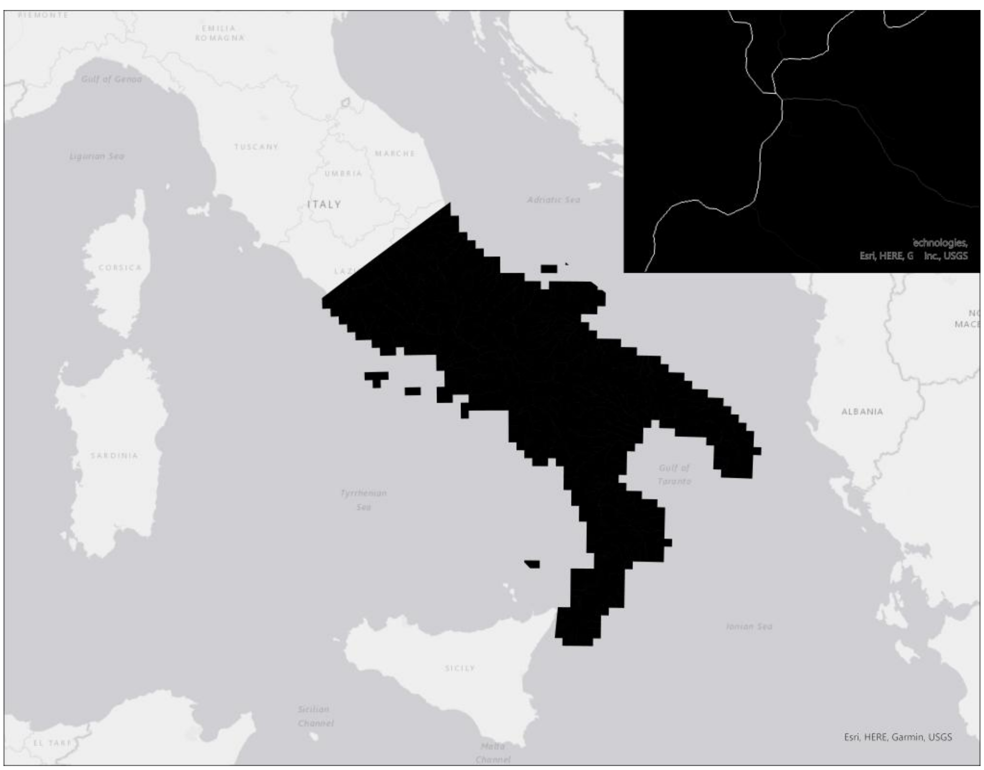

Figure. 4.3: Flow accumulation raster highlighting drainage concentration zones across the DEM.

Stream definition was then carried out by applying a threshold to the flow accumulation grid. In this study, a threshold equivalent to a drainage area of 1 km² was selected. This value represents a balance between capturing detailed channel networks and avoiding the inclusion of insignificant or ephemeral flow paths. The stream network was then segmented at confluences, enabling segment-level hydrological and morphometric analysis, as seen in Figure 4.4).
The catchment delineation step allocated each DEM cell to a contributing drainage area based on flow direction and accumulation, resulting in a raster-based representation of individual catchments (Fig. 4.5). These were subsequently converted into vector polygons (Fig. 4.6), providing clearly defined watershed boundaries. This format facilitates integration with additional spatial datasets and supports the calculation of geomorphological descriptors.
To refine and validate the stream geometry, the Drainage Line Processing tool was used to convert the raster-derived stream network into vector streamlines (Fig. 4.7). Within ArcGIS Pro, this step included smoothing and snapping operations. The resulting vector network was then systematically compared with the official ISPRA polylines to verify spatial alignment. This overlay analysis confirmed that the modeled streamlines closely matched known hydrological features, particularly in complex, low-relief coastal areas, where modeling errors are more likely. This comparison served as a key validation step in confirming the effectiveness and accuracy of the delineation procedure.
Adjoint catchment processing was then applied to aggregate all upstream sub-catchments for each outlet or stream segment. This hierarchical structuring enables the analysis of upstream-downstream relationships and supports hydrological characterization at various spatial scales.

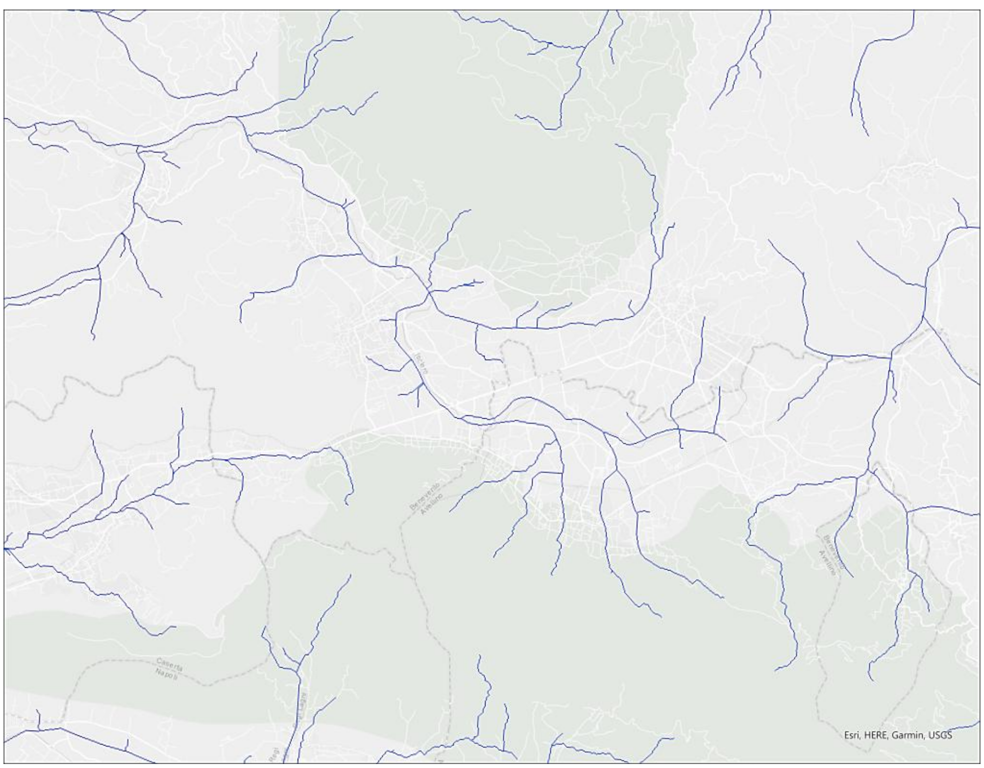

Figure. 4.4: Stream network obtained by applying a threshold to the flow accumulation raster.

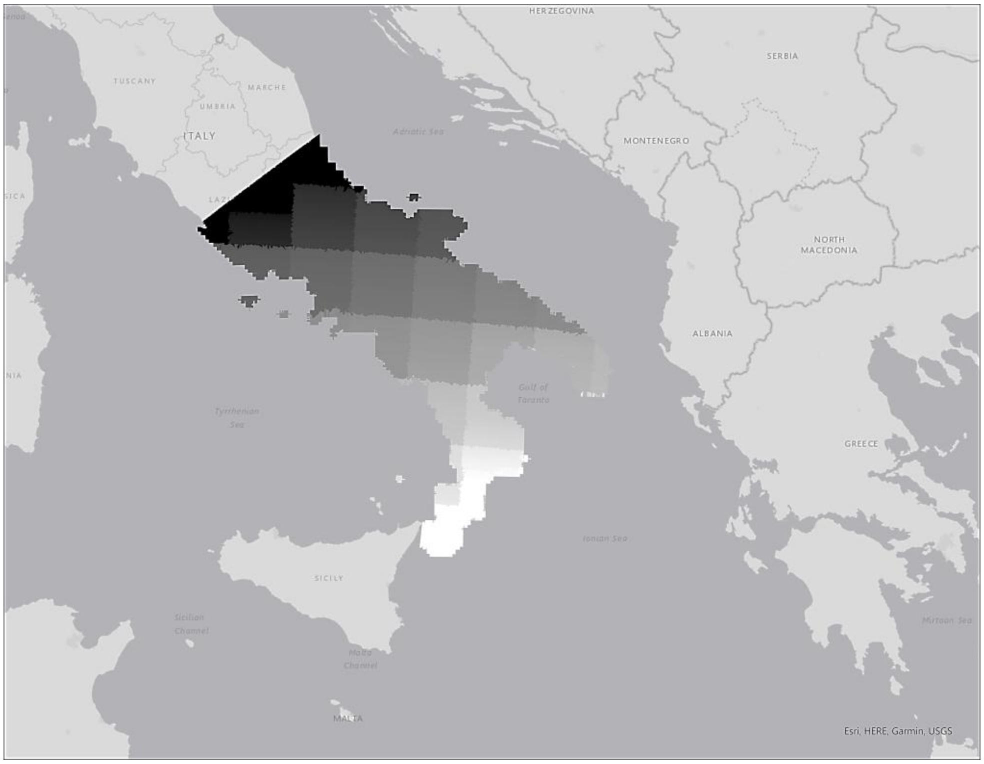

Figure. 4.5: Raster-based delineation of catchments, with each cell assigned to a drainage basin.

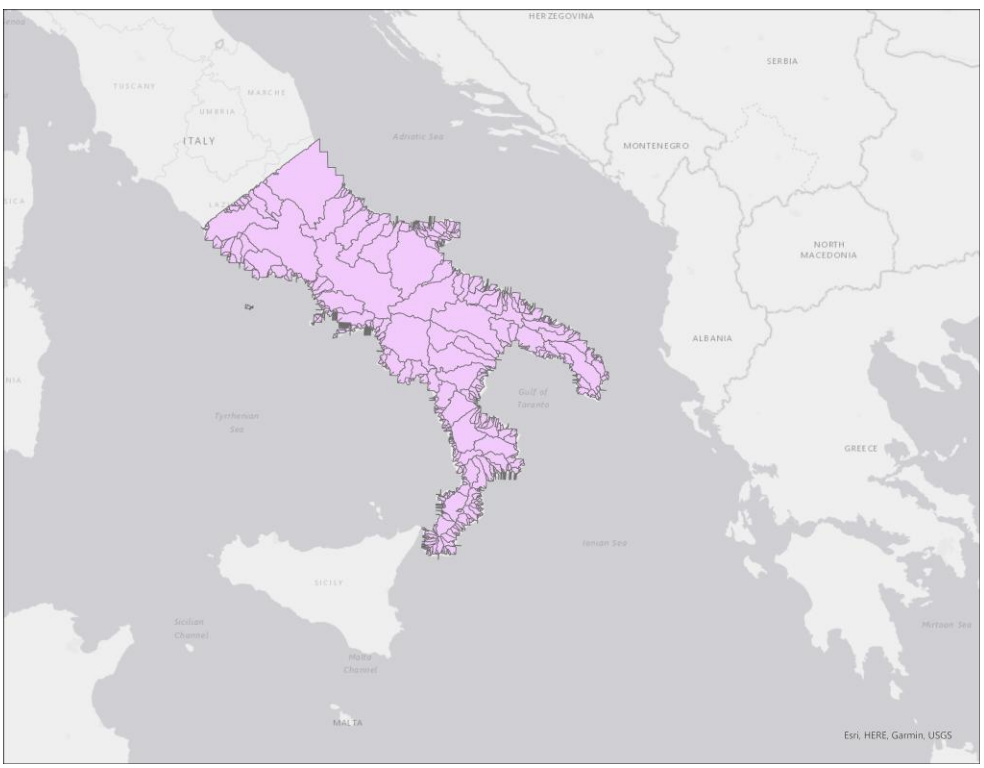

Figure. 4.6: Adjoint catchment polygons showing aggregated upstream drainage areas.

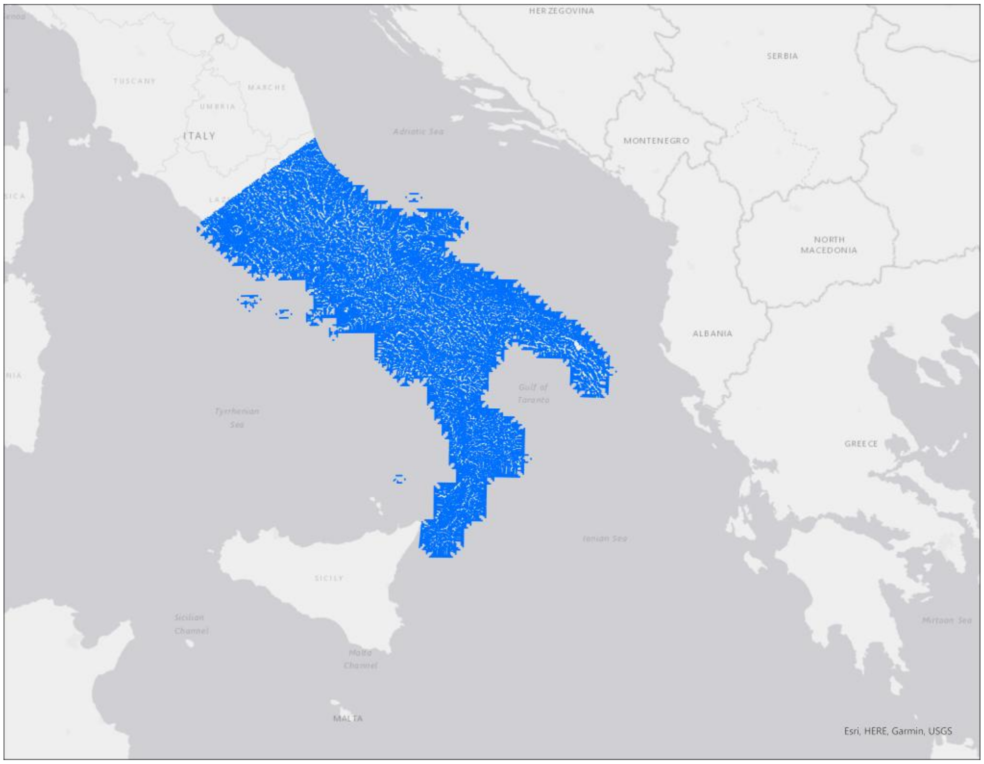

Figure. 4.7: Drainage lines extracted from flow accumulation, representing the modeled hydrographic network of the study area.

4.2.3 Outlet Identification and Station Georeferencing

The final step involved pour point delineation, which is essential for identifying key hydrological features such as catchment outlets and historical gauging stations. These points act as spatial anchors for linking hydrological observations to delineated watersheds. In this study, outlet points were manually positioned along the validated stream network within ArcGIS Pro. However, the precise geolocation of historical gauging stations proved challenging due to the lack of coordinate data in legacy hydrological records—a limitation discussed in detail in the subsequent section. The figure (4.8) shows the schematic station map from the historical Annali Idrologici*,* which depicts station locations without providing precise coordinate information.

CARTA DELLE STAZIONI DI MISURA

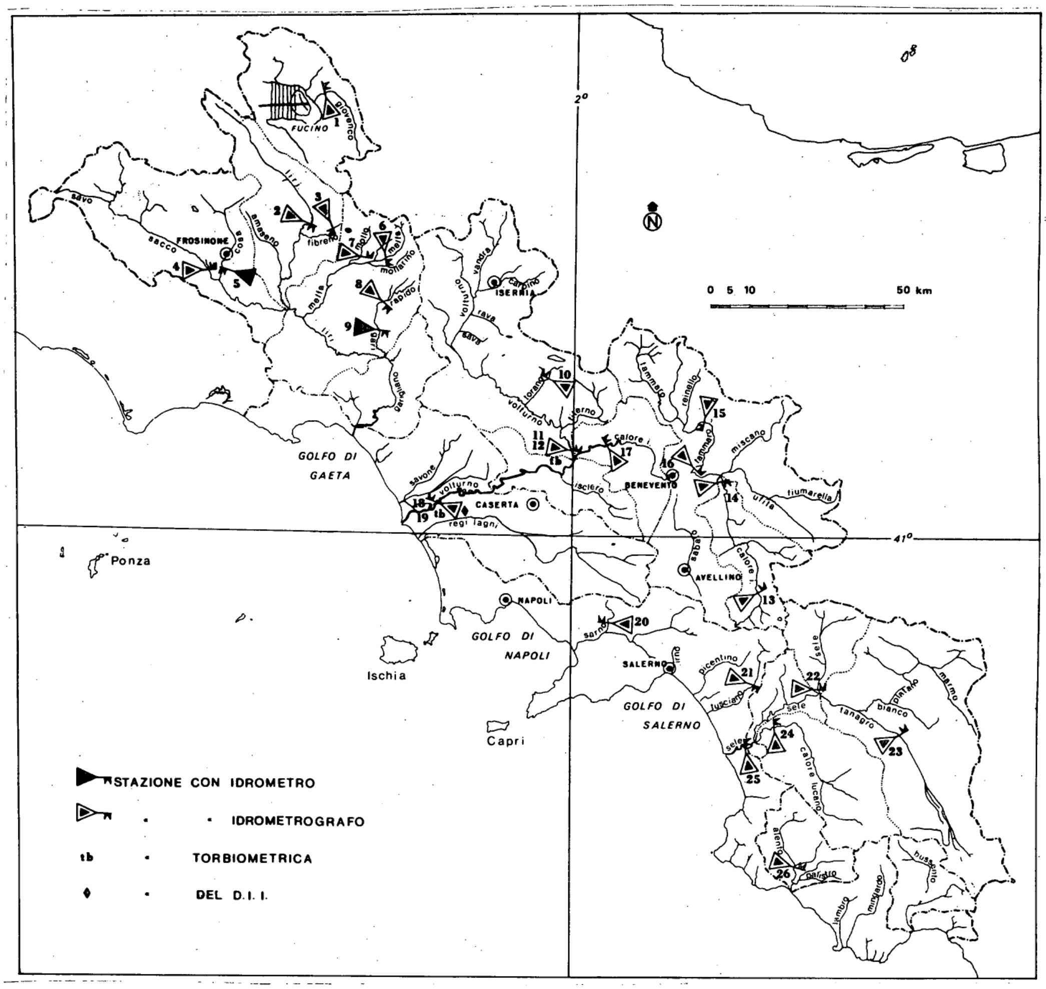

ELENCO DELLE STAZIONI

I – GIOVENCO a Pescina
II – LIRI a Sora
III – FIBRENO a Broccostella
IV – SACCO a Ceccano
V – COSA a Ceccano
VI – MELFA a Picinisco (Ponte Ascanio)
VII – RIO MOLLO a Settignano
VIII – RAPIDO a S.Elia Fiumerapido
IX – SORG.GARI a Cassino (Cerasola)
X – VOLTURNO ad Amorosi
XI – VOLTURNO ad Amorosi (con derivazione)
XII – CALORE IRPINO a Montella
XIII – CALORE IRPINO ad Apice
XIV – TAMMARO a Pago Veiano
XV – TAMMARO a Paduli
XVI – CALORE IRPINO a Solopaca
XVII – VOLTURNO a Cancello ed Arnone
XVIII – VOLTURNO a Cancello ed Arnone ■
XIX – SARNO a S.Valentino Torio
XX – SELE a Contursi
XXI – TANAGRO a Polla (Molino Maltempo)
XXII – CALORE LUCANO a Persano
XXIII – SELE ad Albanella
XXIV – ALENTO a Casalvelino

Figure 4.8: Schematic map of historical gauging stations from the Annali Idrologici

4.3 Integration of Historical Hydrological Data

A critical aspect of this study concerns the integration of historical hydrological data, which is notably complicated by significant gaps and ambiguities in spatial referencing. Unlike modern datasets, the historical records available for southern Italy—most notably those published in the Annali Idrologici by the Italian Hydrographic Service—do not provide explicit geographic coordinates for gauging stations or catchment outlets. Instead, these datasets typically include only qualitative descriptors, such as the names of catchments, symbolic markers on historical maps, or references to river reaches, making precise geospatial integration inherently challenging.

To address this limitation, a multifaceted approach was adopted. First, all available ancillary sources were compiled and cross-referenced, including both historical and current shapefiles of gauging station locations obtained from ISPRA, as well as legacy cartographic materials featured in the Annali Idrologici. These maps, while often lacking modern geodetic precision, provide invaluable clues regarding the relative positioning of stations within river networks.

Furthermore, the Annali Idrologici reports often include quantitative parameters, most importantly, the officially reported drainage area for each station—which serve as a critical reference for validation. By systematically comparing the reported drainage areas with those derived from the newly delineated catchment polygons in GIS, it was possible to iteratively adjust and confirm the most likely positions of historical stations. This process involved a combination of GIS-based spatial analysis, manual inspection, and trial-and-error matching, thereby compensating for the absence of direct coordinate information.

The reconstructed locations and boundaries of the gauged catchments are illustrated in Figure 4.9, which shows the spatial distribution of all delineated watersheds and their associated monitoring stations across the study area.

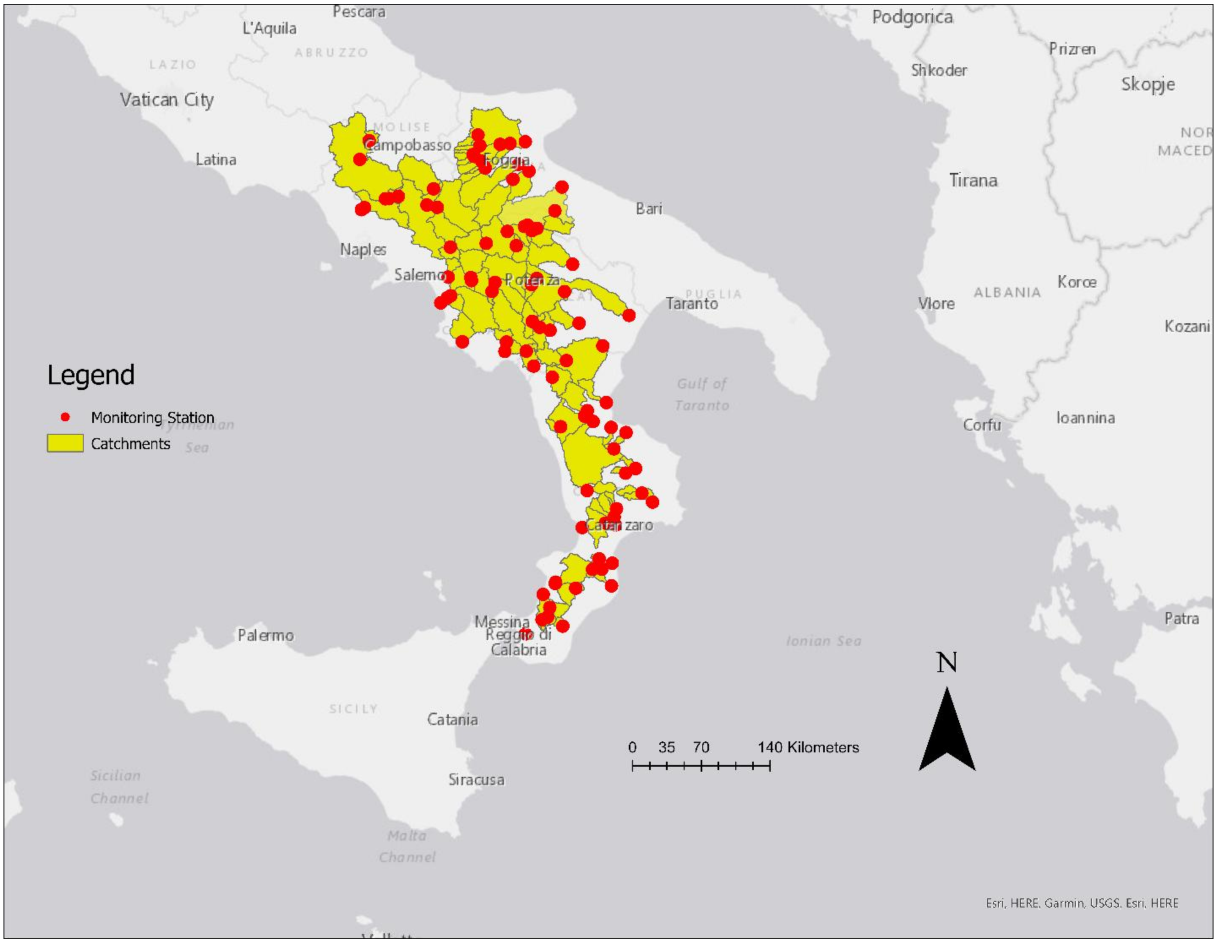

Figure 4.9: Location of Monitoring Stations and Delineated Catchments

Following the reconstruction of plausible spatial locations for the historical gauging stations, a critical next step was to validate the accuracy of the delineated catchment boundaries. This was accomplished by comparing the officially reported drainage areas (as published in the Annali Idrologici) with those derived from the *GIS*-based delineation process. These reported values, which served as a key reference during the spatial alignment phase, also provided an independent benchmark for validation.

The results of this comparison are illustrated in Figure 4.10 (see scatter plot), where each point represents a gauging station. The figure reveals a nearly perfect 1:1 relationship ($R^2 = 1$) between reported and delineated catchment areas, confirming that the georeferencing of stations and the subsequent delineation of their drainage basins were highly accurate. This strong agreement not only validates the reconstruction methodology but also ensures the spatial integrity of the catchments used for morphometric analysis. It is to note that this validation was performed for all 127 stations originally digitized, including those later excluded from the Flow Duration Curve (FDC) analysis in Chapter 2. The complete set of catchment areas was required to compute the Hydrological Consistency Ratio (*HCR*) used to assess potential damage. Thus, while only 89 stations were retained for FDC-based regionalization, the delineation of all catchments remained a necessary step in the overall workflow.

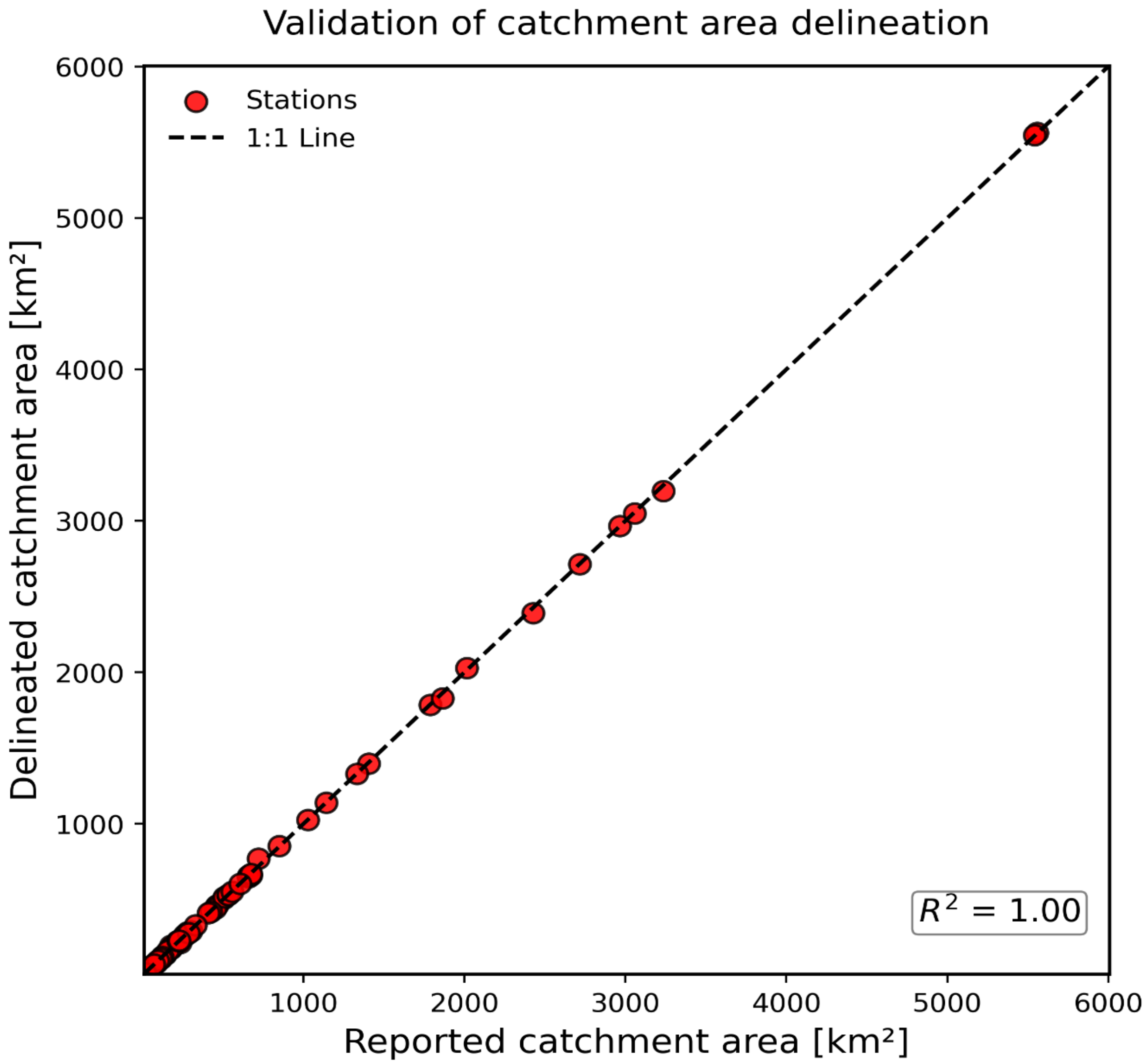

Figure 4.10: Validation of Catchment Area Delineation

4.4 Derivation of Catchment Morphometric and Topographic Descriptors

Physical parameters such as catchment area, elevation, slope, and drainage length are widely used in regionalization of flow duration curves to represent key aspects of watershed form and function. These descriptors are essential for analyzing spatial variability in hydrological behavior and have been consistently applied in various studies to support modeling efforts. In this study, a comprehensive set of morphometric and topographic indices was extracted for each delineated catchment using GIS (Wood et al., 1990; Gaviria & Carvajal-Serna, 2022).

Catchment Area and Perimeter (A, P)

Catchment area (*A*), expressed in square kilometers (km²), and perimeter (*P*), in kilometers (km), were computed from the geometry of watershed polygons generated during the delineation process. These measurements were obtained using *ArcGIS Pro*'s Field Calculator, which applies built-in geometry functions to ensure accurate and standardized calculations.

Elevation Parameters (*HMIN, HMAX, HMEAN, HRANGE*)
To characterize altitudinal variability, key elevation statistics were extracted from a high-resolution DEM using Zonal Statistics as Table tool, which treats each basin as an independent analysis unit. The following parameters were computed:

- Minimum elevation (*HMIN*)
- Maximum elevation (*HMAX*)
- Mean elevation (*HMEAN*)
- Elevation range (*HRANGE* = *HMAX* − *HMIN*)

These metrics provide insight into the topographic relief and vertical heterogeneity of each catchment.

Mean Catchment Slope (SMEAN)
General steepness was quantified by first applying the Slope tool from the Spatial Analyst toolbox to the DEM, generating a raster of slope values (*in degrees*). These values were then averaged within each basin using Zonal Statistics, yielding the mean catchment slope (*SMEAN*) a crucial factor in runoff production and erosion processes.

Length of the Longest Flow Path (L)
The principal drainage length, or the longest flow path (*L*), was derived using the Longest Flow Path tool. This procedure identifies the maximum flow distance from the catchment outlet to the most remote upstream point, based on the flow direction raster. The output polyline was then measured in kilometers and represents the dominant hydrological axis for each catchment.

Mean Slope of the Main Channel (SL)
To quantify the slope along the primary drainage line, the extracted flow path (*L*) was intersected with the slope raster derived from the DEM. The Extract Values to Points and subsequent Zonal Statistics tools were used to compute the average slope along the flow path (*SL*), maintaining angular units (*degrees*) for direct interpretability.

Shape Factor (SF)
The shape factor (*SF*) is a dimensionless indicator of basin elongation and was calculated using the formula:

$$SF = \frac{A}{L^2} \tag{4.1}$$

where A is the catchment area and L is the length of the longest flow path. Lower *SF* values indicate more elongated catchments, which typically exhibit delayed and attenuated runoff responses, while higher *SF* values are associated with more compact basins and potentially quicker runoff concentration (Soni, 2017).

Circularity Ratio (CR)
The circularity ratio (*CR*) measures the compactness of a catchment, defined as:

$$CR = \frac{4\pi A}{P^2} \tag{4.2}$$

where A is the area and P is the perimeter. Values approaching 1 suggest a circular, compact shape with more efficient runoff concentration, while lower values indicate elongated or irregular geometries (Apaydin et al., 2006).

All descriptors were derived using a standardized, automated workflow to ensure consistency and reduce operator-induced variability.

4.4.1 Summary Statistics and Spatial Variability

To explore the spatial heterogeneity of the catchments, key morphometric parameters were statistically summarized. Table 4.1 presents the minimum, maximum, mean, median, and standard deviation for each index, while Figure 4.11(a,b,c,d,e,f,g,h,i,j,k) illustrates their frequency distributions.

The statistical evaluation reveals notable patterns:

- Catchment area (*A*) and perimeter (*P*) exhibit strong right-skewed distributions, with 70% of areas under 500 km^2 and most perimeters under 150 km.
- Elevation metrics (*HMAX, HMEAN, HRANGE*) show broader and more symmetric patterns, with mean elevations (*HMEAN*) generally centered around 700–800 m.
- Flow path lengths (*L*) and slopes (*SMEAN, SL*) are positively skewed, with 75% of *L* values below 60 km and *SMEAN* values typically between 10° and 16°.
- Shape factor (*SF*) and circularity ratio (*CR*) display near-symmetric distributions, reflecting a consistent catchment geometry across the study area.

These patterns underscore the morphological diversity of the analyzed basins and provide a Type equation here.foundation for subsequent correlation analyses and hydrological modeling efforts.

Table 4.1 – Descriptive statistics of catchment characteristic

Parameter	Minimum	Maximum	Mean	Median	Std Dev
A (km^2)	8.8	5562.6	592.3	213.8	1043.2
P (km)	18.3	586.9	118.9	85.1	112.4
HMIN (m)	1.0	1223.0	252.1	170.0	259.0
HMAX (m)	618.0	2266.0	1559.2	1534.0	384.6
HRANGE (m)	309.0	2252.0	1307.1	1290.0	458.3
HMEAN (m)	196.4	1435.1	724.4	723.3	262.2
L (km)	5.7	161.7	45.2	33.1	37.5
SMEAN (°)	3.4	24.3	13.3	13.6	4.9
SL (°)	1.7	20.3	7.9	6.4	4.7
SF	0.1	0.5	0.2	0.2	0.1
CR	0.2	0.7	0.4	0.4	0.1

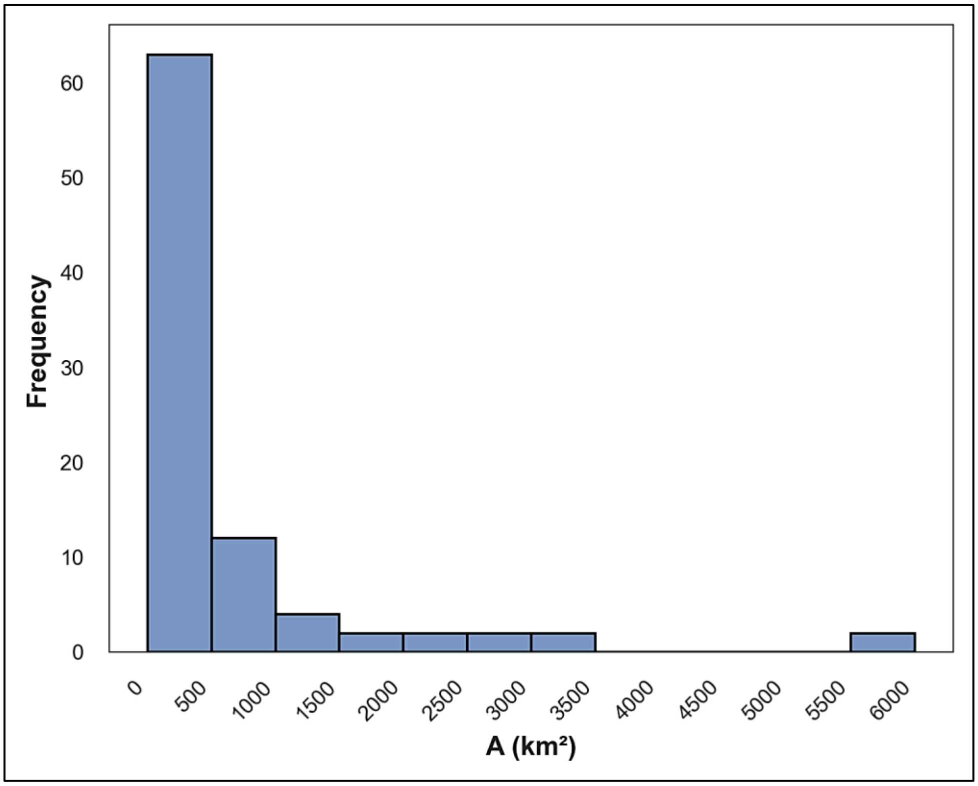

Figure 4.11.a: Frequency distributions of catchment properties (Catchment Area)

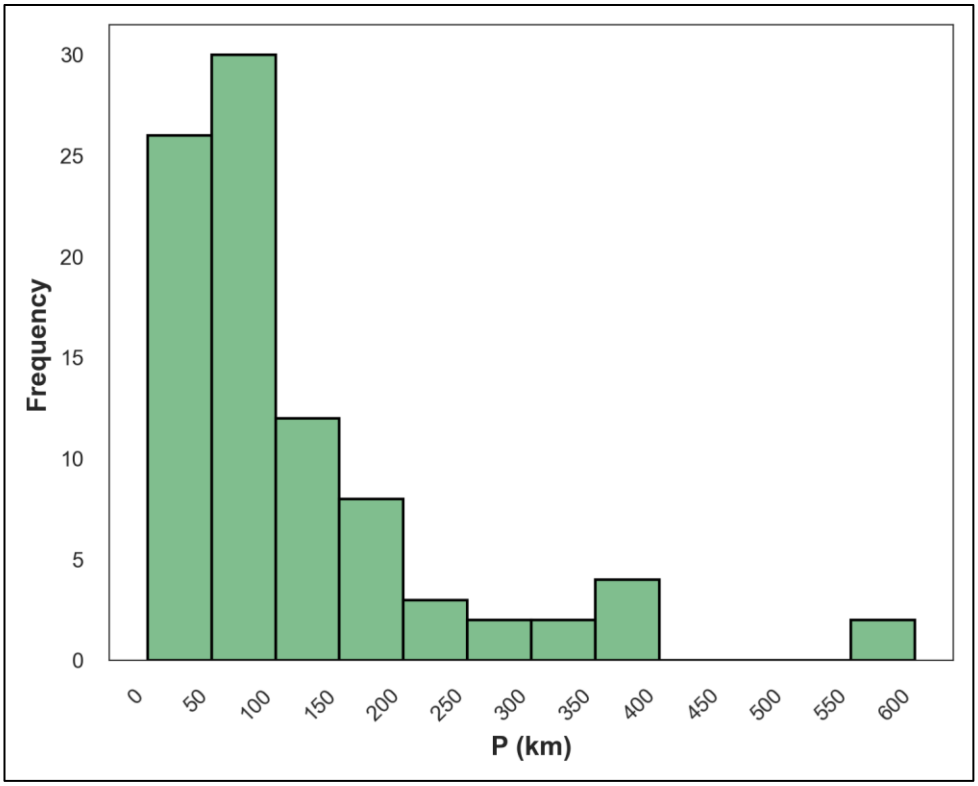

Figure 4.11.b: Frequency distributions of catchment properties (Catchment Perimeter)

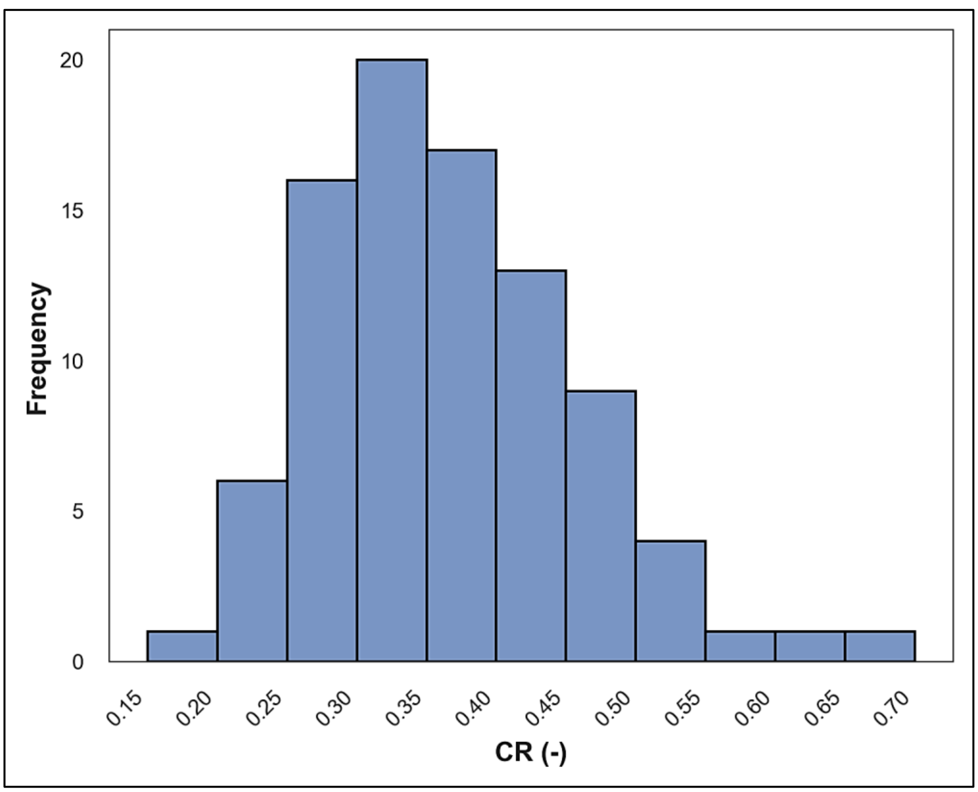

Figure 4.11.c: Frequency distributions of catchment properties (Circularity Ratio)

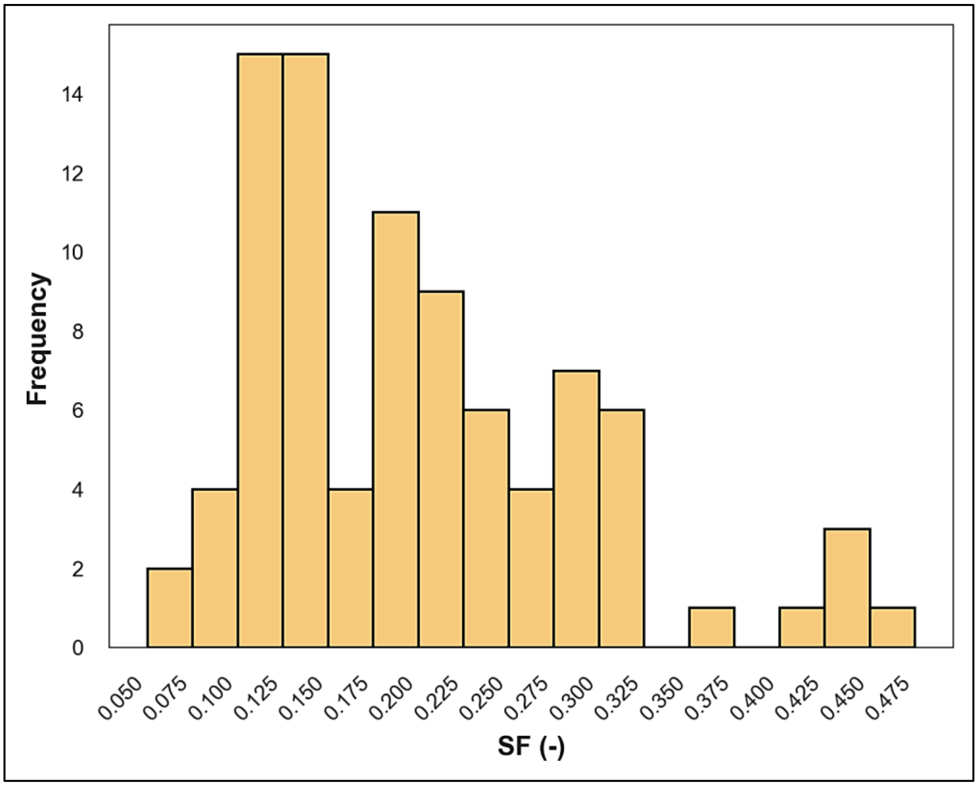

Figure 4.11.d: Frequency distributions of catchment properties (Shape Factor)

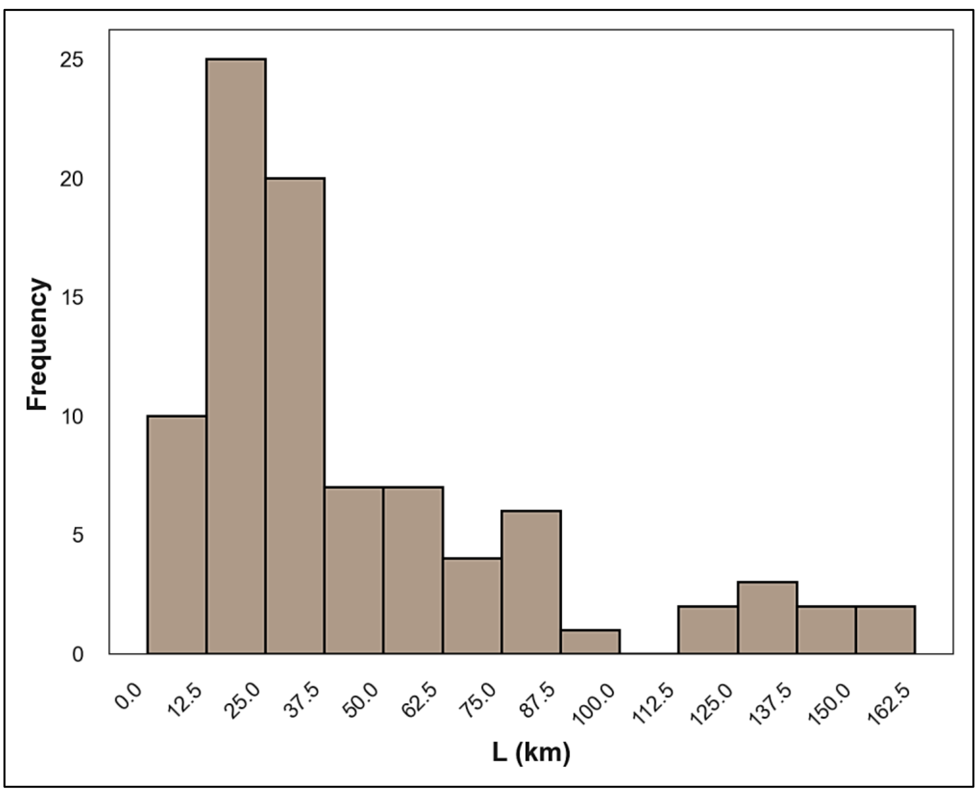

Figure 4.11.e: Frequency distributions of catchment properties (Longest flow path)

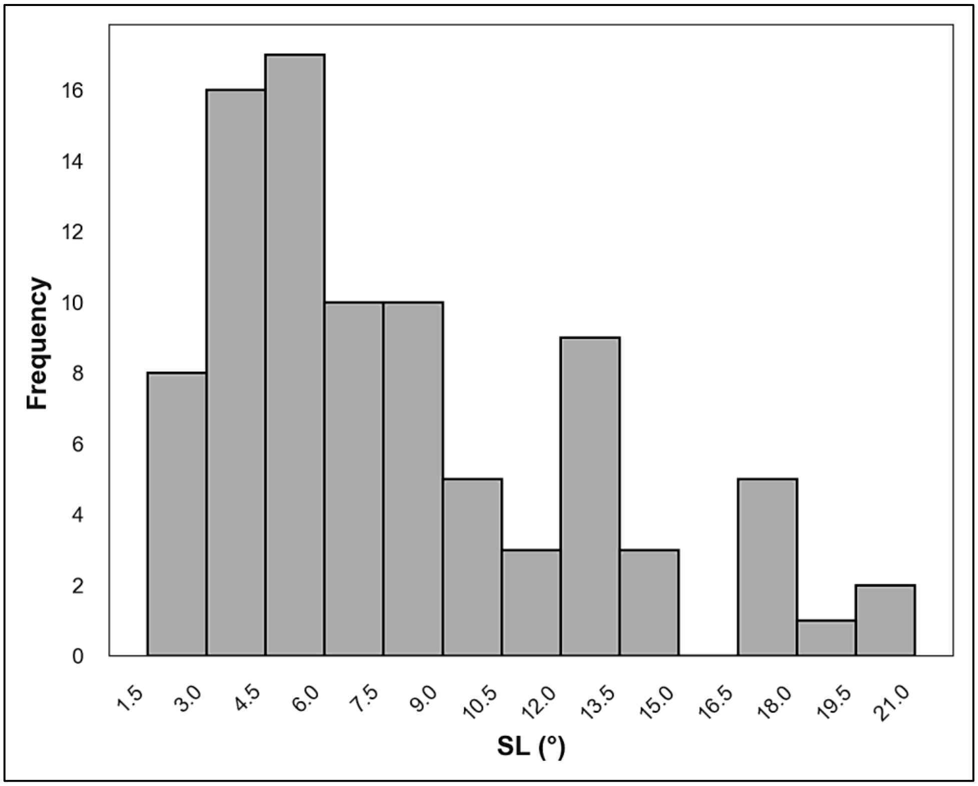

Figure 4.11.f: Frequency distributions of catchment properties (Mean Slope of the Main Channel)

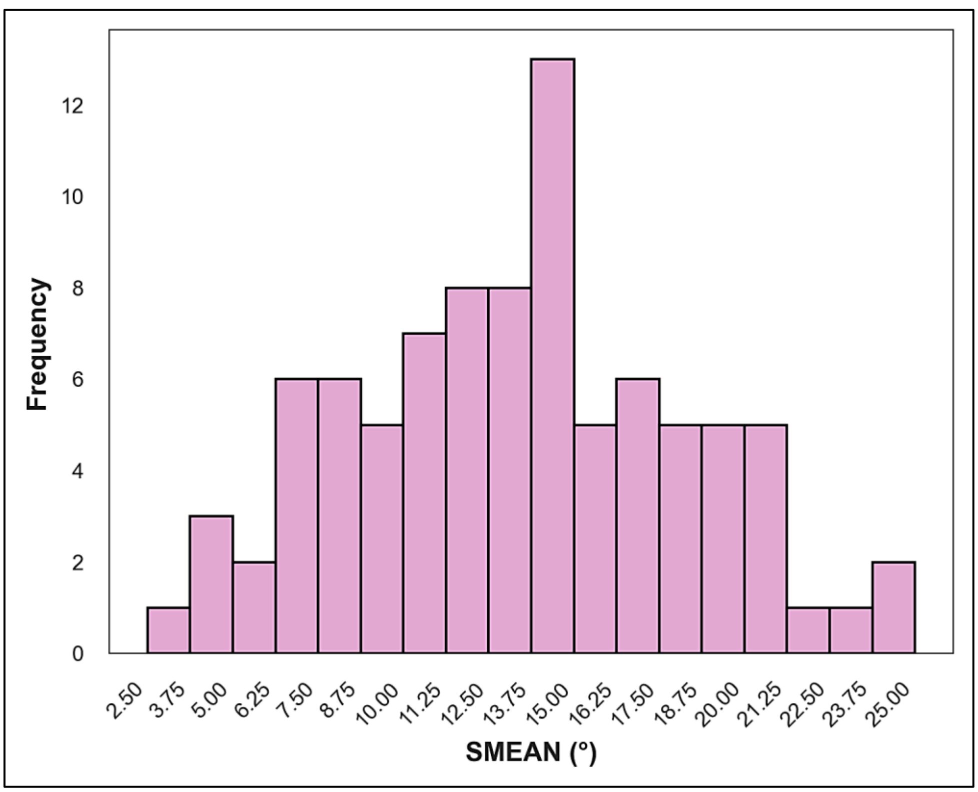

Figure 4.11.g: Frequency distributions of catchment properties(Mean Catchment Slope)

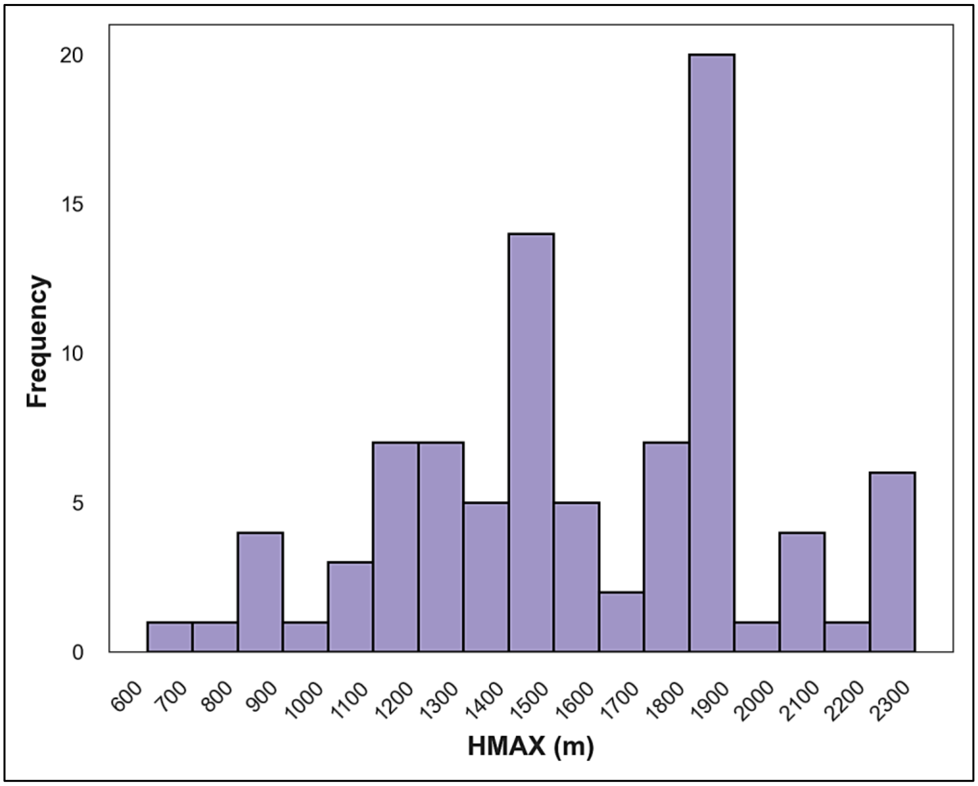

Figure 4.11.h: Frequency distributions of catchment properties (Maximum elevation)

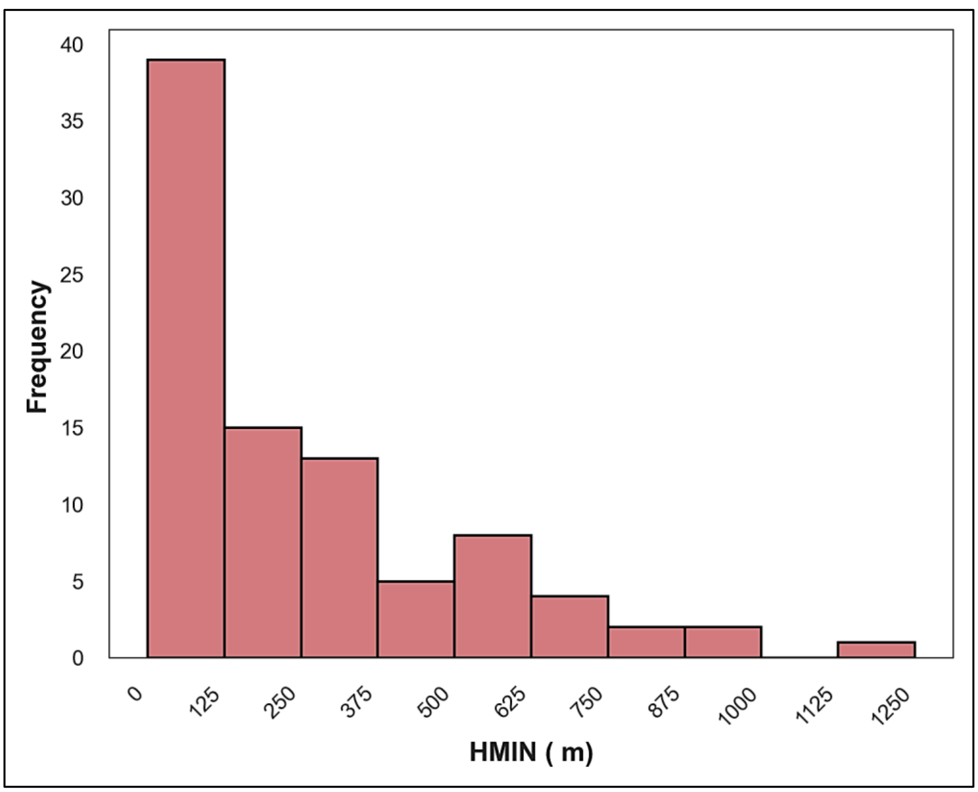

Figure 4.11.i: Frequency distributions of catchment properties (Minimum elevation)

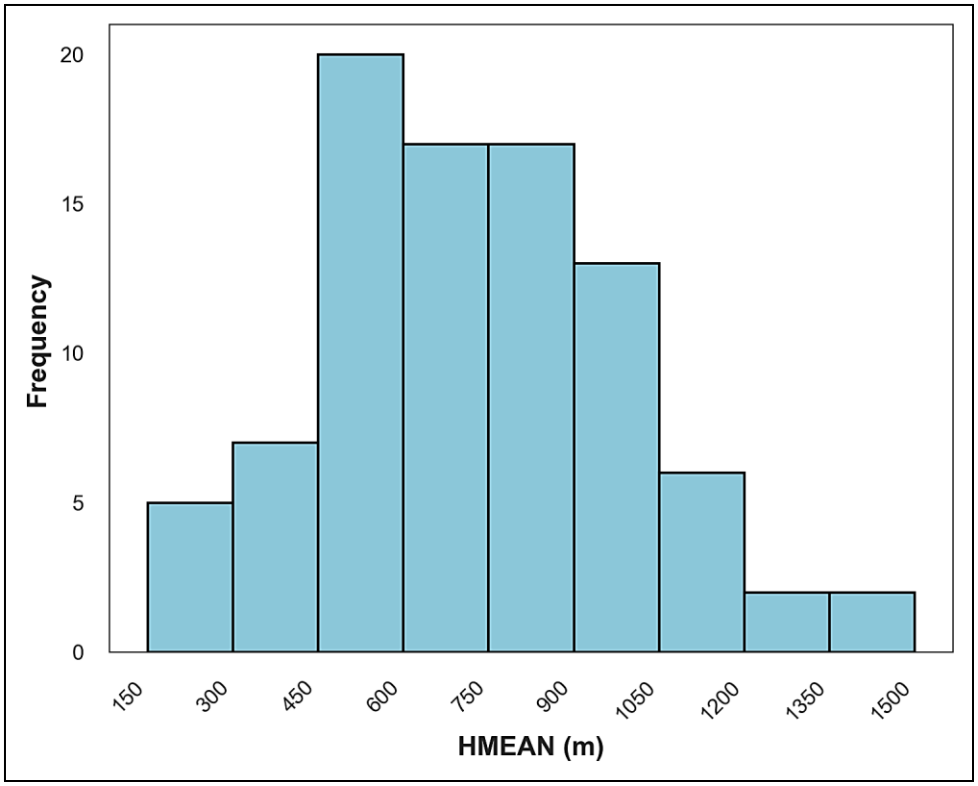

Figure 4.11.j: Frequency distributions of catchment properties (Mean elevation)

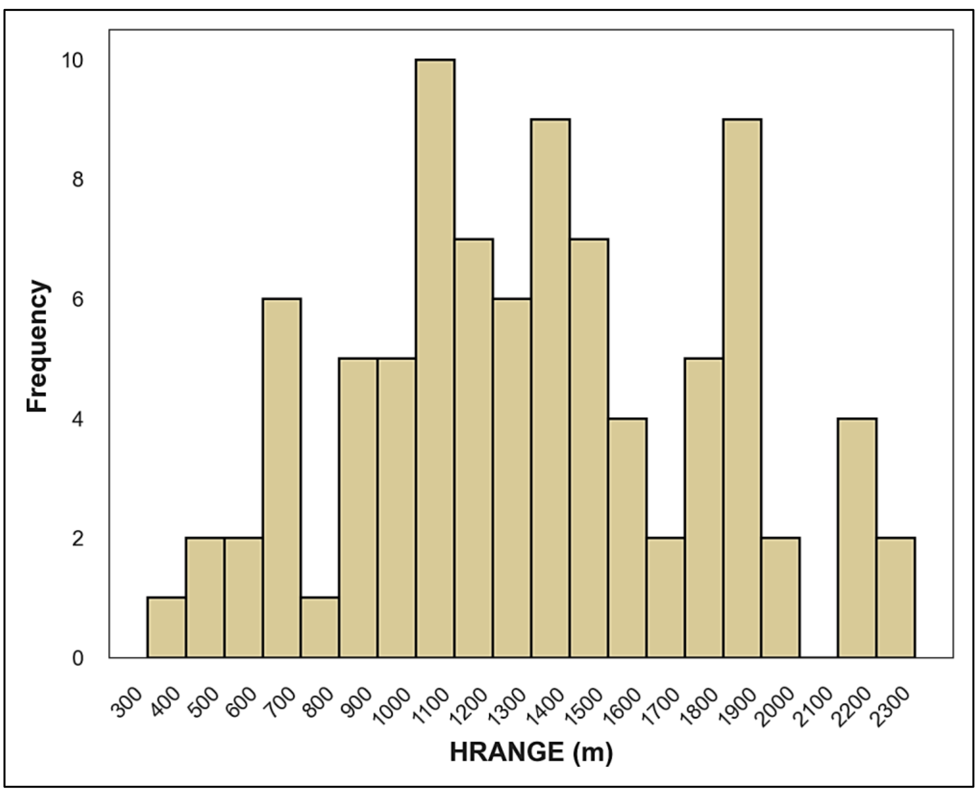

Figure 4.11.k: Frequency distributions of catchment properties(Elevation range)

4.5 Hydrogeological Classification and Soil Permeability Analysis

Numerous studies have contributed to advancing the geological and hydrogeological understanding of southern Italy, a region characterized by complex lithological compositions and tectonic settings (Celico, 1986; Bonardi et al., 1992). Building upon this foundational work, Allocca et al. (2007) developed a regional hydrogeological classification by delineating nine distinct hydrogeological complexes, derived through the integration of lithological, structural, and groundwater flow characteristics.

In the Soil Conservation Service (SCS) method (SCS, 1972), soils are grouped into four Hydrological Soil Groups (HSG: *A, B, C, D*), with permeability decreasing from *A* (high) to D (very low). In analogy, Allocca et al. (2007) later updated the regional framework, consolidating the nine hydrogeological complexes into four permeability classes for large-scale spatial and statistical applications: Class *A* (high permeability), Class *B* (moderate permeability), Class *C* (low permeability), and Class *D* (impermeable) (as shown figure 4.12). This simplified scheme provided a standardized, GIS-compatible framework that enables consistent hydrogeological analyses across the region.

Del Giudice et al. (2014) also employed this hydrogeological map to predict runoff coefficients in Southern Peninsular Italy for index-flood estimation. In their study, morphological features were described using the SCS permeability classification, highlighting its applicability for hydrological modeling and flood regionalization.

The spatial distribution of these four permeability classes across the study area is shown in Figure 4.12. The map clearly illustrates the regional heterogeneity in subsurface permeability, with high-permeability formations (Class *A*) mainly concentrated in karst domains, and impermeable units (Class *D*) associated with clay-rich or crystalline lithologies.

To quantify the distribution of these permeability classes within each catchment, the Tabulate Area tool in ArcGIS Pro was utilized. This geospatial tool calculates the area of each permeability class intersecting with catchment boundaries, producing a matrix of class-specific areas per catchment. These values were normalized by the total catchment area to compute the relative proportion of each class. The resulting ratios served as standardized indicators of catchment-scale permeability and were incorporated into subsequent regionalization and statistical modeling efforts.

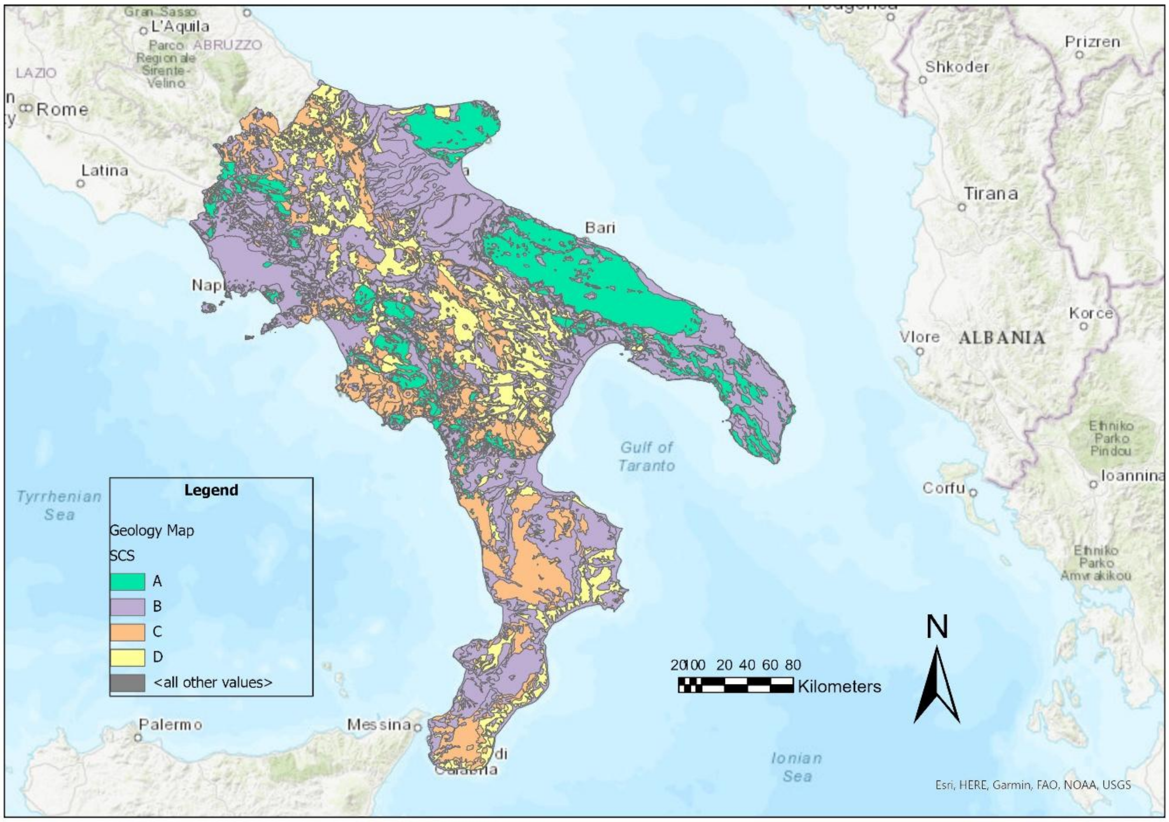

Figure 4.12: Spatial Distribution of Permeability Classes in Southern Italy

Beyond the individual class proportions, this study introduced a set of composite permeability indices aimed at capturing transitional hydrogeological conditions. Specifically, the combinations *A+B, B+C*, and *A+B+C* were computed by summing the normalized areas of adjacent classes. These aggregated indices are intended to reflect gradational permeability environments that may not be fully represented by single classes. For instance, the *A+B* index characterizes zones with predominantly permeable substrata, potentially associated with enhanced recharge and subsurface flow. The *B+C* combination highlights transitional settings with moderate-to-low permeability, while *A+B+C* represents the total extent of all permeable substrates, excluding only impermeable formations (Class *D*). These composite metrics provide a more integrative view of hydrogeological variability and may enhance the robustness of models seeking to relate physical catchment properties to hydrological response patterns.

Table 4.2. Descriptive statistics of soil-permeability class fractions (A–D) across catchments.

Parameter	Minimum	Maximum	Mean	Median	Std. Dev
SoilA	0.00	0.62	0.08	0.00	0.14
SoilB	0.00	1.00	0.52	0.53	0.27
SoilC	0.00	1.00	0.27	0.19	0.24
SoilD	0.00	0.69	0.13	0.06	0.16

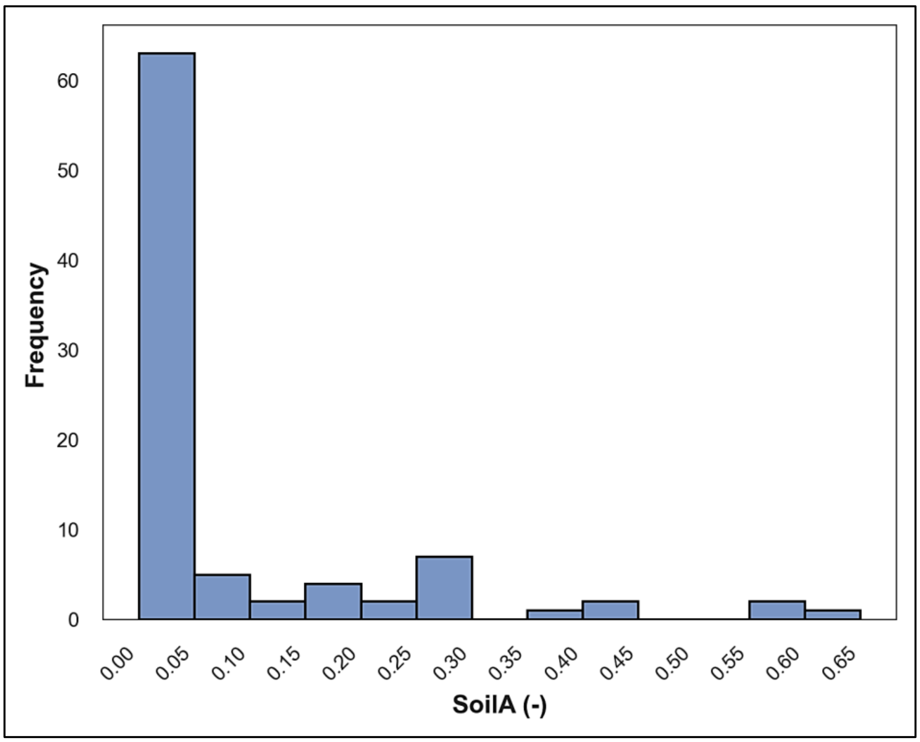

Figure 4.13.a : Histograms of soil-permeability class fractions (A) across the study catchments.

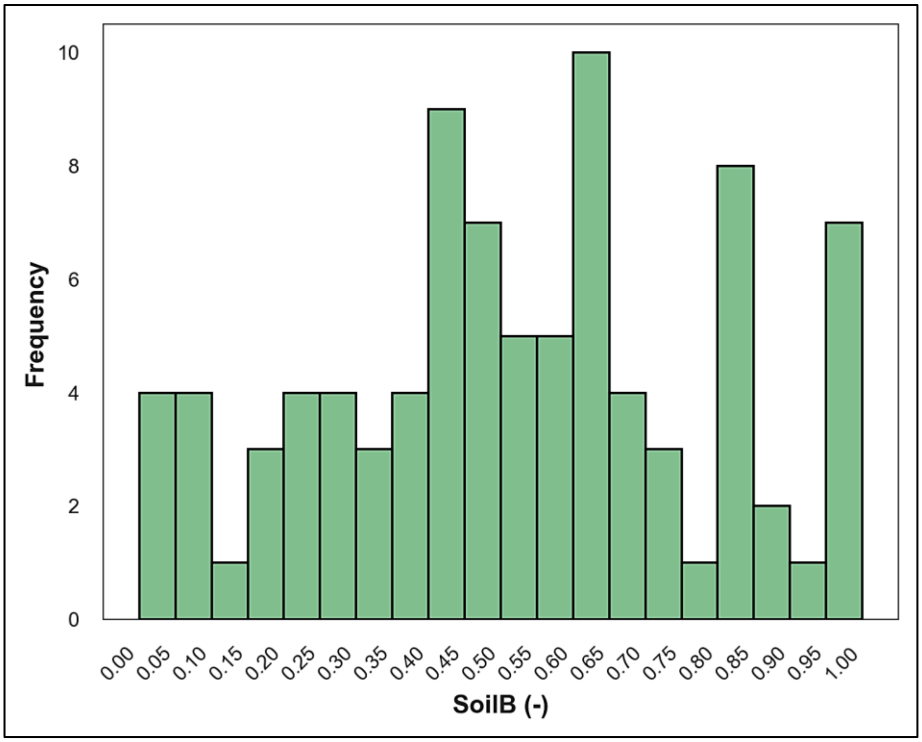

Figure 4.13.b: Histograms of soil-permeability class fractions (B) across the study catchments.

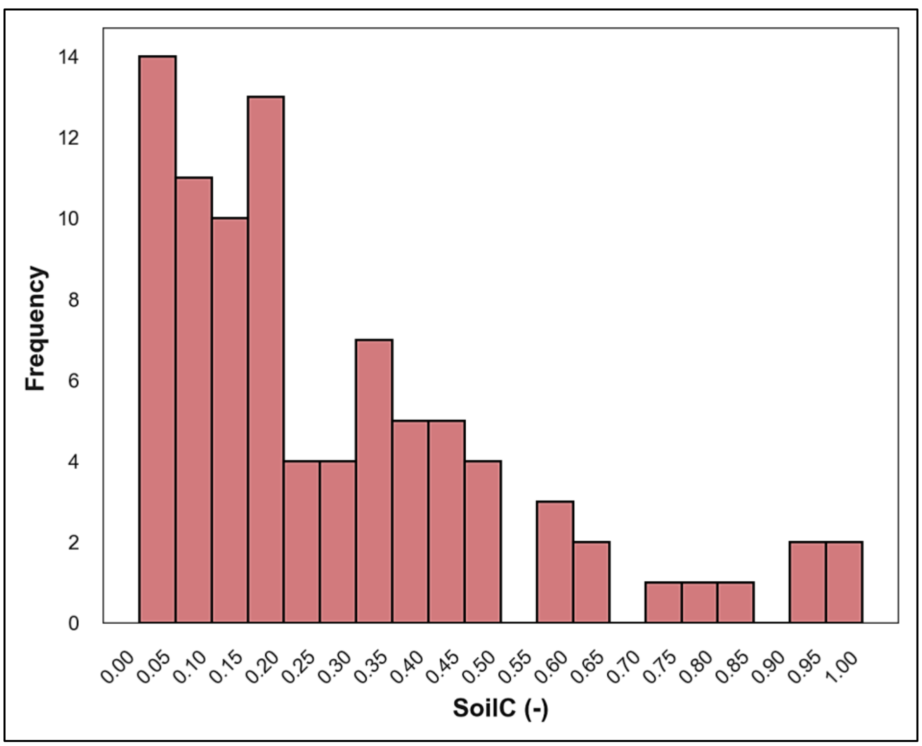

Figure 4.13.c: Histograms of soil-permeability class fractions (C) across the study catchments.

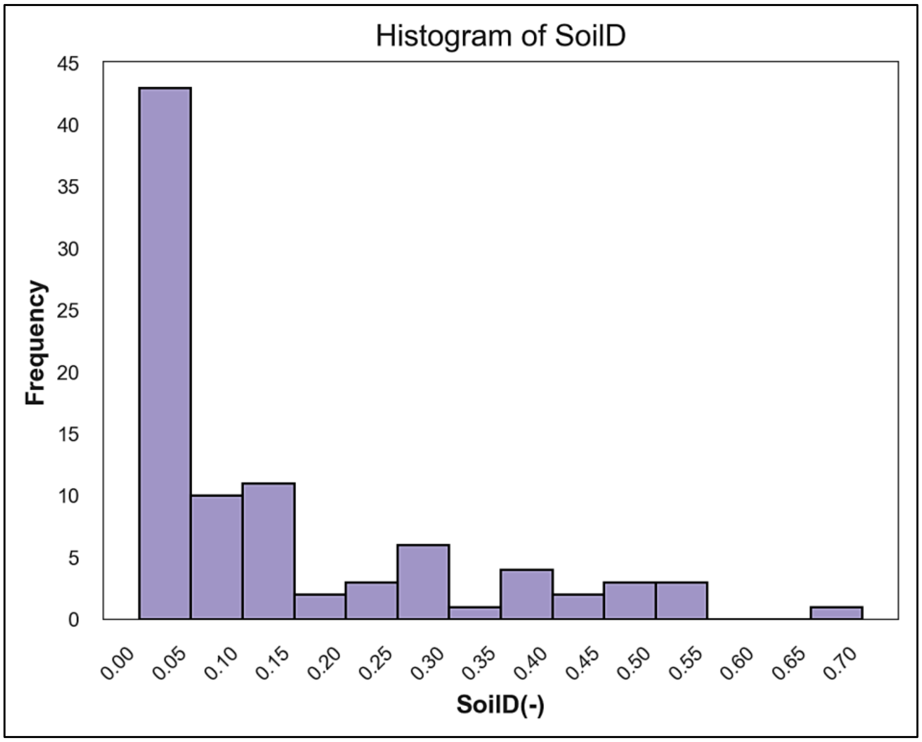

Figure 4.13.d: Histograms of soil-permeability class fractions (D) across the study catchments.

As summarized in Table 4.2 and visualized in Figure 4.13(a,b,c,d), the four classes show distinct distributional patterns. *SoilA* (high permeability) is strongly right skewed: more than half of the catchments lie near zero, with a thin tail up to 0.62 (mean = 0.08; median = 0.00), indicating that highly permeable substrates are generally scarce. *SoilD* (very low permeability) likewise peaks near zero and remains limited in extent (range 0–0.69; mean = 0.13; median = 0.06). In contrast, *SoilB* (moderate permeability) spans nearly the full 0–1 range and exhibits the largest spread (*SD* = 0.27), with mean and median around 0.52–0.53, pointing to widespread yet spatially variable moderate-permeability soils. *SoilC* (low permeability) shows a milder right skew: most fractions are < 0.4 (mean = 0.27; median = 0.19), implying an appreciable but non-dominant presence. Overall, the landscape is dominated by moderate to generally permeable formations (driven by *SoilB*, with contributions from *SoilC*), while both the most permeable (*SoilA*) and the most impermeable (Soil*D*) classes are typically restricted.

4.6 Land Cover Classification and Hydrological Implications

Land cover plays a critical role in hydrological analysis and the regionalization of Flow Duration Curves (FDCs), as it directly influences key processes such as surface runoff generation, infiltration, and evapotranspiration(Achugbu et al., 2022; Costa et al., 2014). To ensure temporal consistency with the streamflow records used in this study, land cover characterization was based on the CORINE Land Cover (CLC) 1990 dataset, developed by the European Environment Agency (EEA). This pan-European dataset provides harmonized land use information with a spatial resolution of 100 meters, making it suitable for catchment-scale hydrological analysis. As this study is based on historical data**,** the CLC 1990 dataset—the earliest available version of CORINE

Land Cover—was selected to ensure alignment between land cover conditions and the streamflow observation period.
For the purposes of this study, land cover types were aggregated into two broad categories of hydrological relevance: agricultural areas and forest and semi-natural areas. This classification was derived from the hierarchical structure of the CORINE system, which organizes land cover data into three levels of increasing thematic detail (Feranec et al., 2010). Table 4.3 presents the sub-classes included under each aggregated category, following the CORINE Level 1, Level 2, and Level 3 structure.

Table 4.3: Aggregated CORINE Land Cover Classes Used in the Study

Level 1	Level 2	Level 3
1. Agricultural areas	*1.1 Arable land*	1.1.1 Non-irrigated arable land
		1.1.2 Permanently irrigated land
	1.2 Permanent crops	1.2.1 Vineyards
		1.2.2 Fruit trees and berry plantations
		1.2.3 Olive groves
	1.3 Pastures	1.3.1 Pastures
	1.4 Heterogeneous agricultural areas	1.4.1 Annual crops with permanent crops
		1.4.2 Complex cultivation patterns
		1.4.3 Agriculture with natural vegetation
		1.4.4 Agro-forestry areas
2. Forest and semi-natural areas	*2.1 Forests*	2.1.1 Broad-leaved forests
		2.1.2 Coniferous forests
		2.1.3 Mixed forests
	2.2 Scrub/herbaceous vegetation	2.2.1 Natural grasslands
		2.2.2 Moors and heathland
		2.2.3 Sclerophyllous vegetation
		2.2.4 Transitional woodland-scrub

The spatial distribution of the two dominant land cover types across the study area is illustrated in Figure 4.14, which shows the extent of agricultural (light green) and forest/semi-natural (dark green) coverage. The map highlights the heterogeneity of land cover conditions: agricultural land is predominant in lowland areas, especially in Puglia and parts of Campania, while forest and semi-natural vegetation dominate the mountainous regions of Calabria and Basilicata.

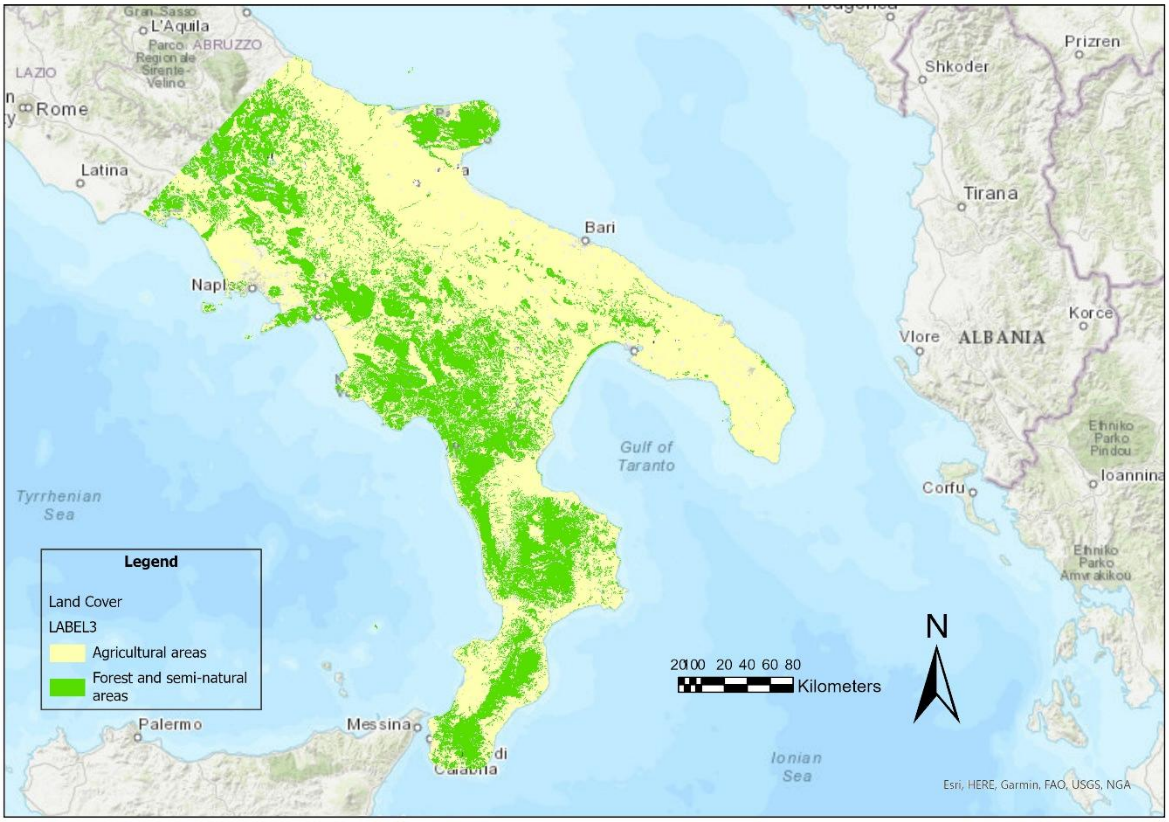

Figure 4.14: Spatial Distribution of Dominant Land Cover Classes

Statistical Overview of Land Cover Proportions

Descriptive statistics of the calculated land cover ratios are reported in Table 4.4, summarizing the range and central tendency for both agricultural and forest cover across all catchments.

Table 4.4 — Descriptive statistics of land-cover fractions (agriculture, forest).

Parameter	Min	Max	Mean	Median	Std. Dev
Agriculture	0.00	0.99	0.46	0.42	0.28
Forest	0.01	1.00	0.53	0.56	0.28

As reported in Table 4.4 and shown in Figure 4.15(a,b), agricultural cover spans the full 0–1 range with a clear mode around 0.4–0.5; its mean (0.46) slightly exceeds the median (0.42), indicating a mild positive (right) skew and substantial heterogeneity among basins. Forest cover is shifted toward higher values, with many catchments between 0.6 and 0.9; the mean (0.53) is slightly below the median (0.56), consistent with a slight negative (left) skew. Together, these patterns highlight marked spatial variability in land use and the largely complementary nature of the two fractions in this study: basins with higher forest shares typically show lower agricultural shares, and vice versa.

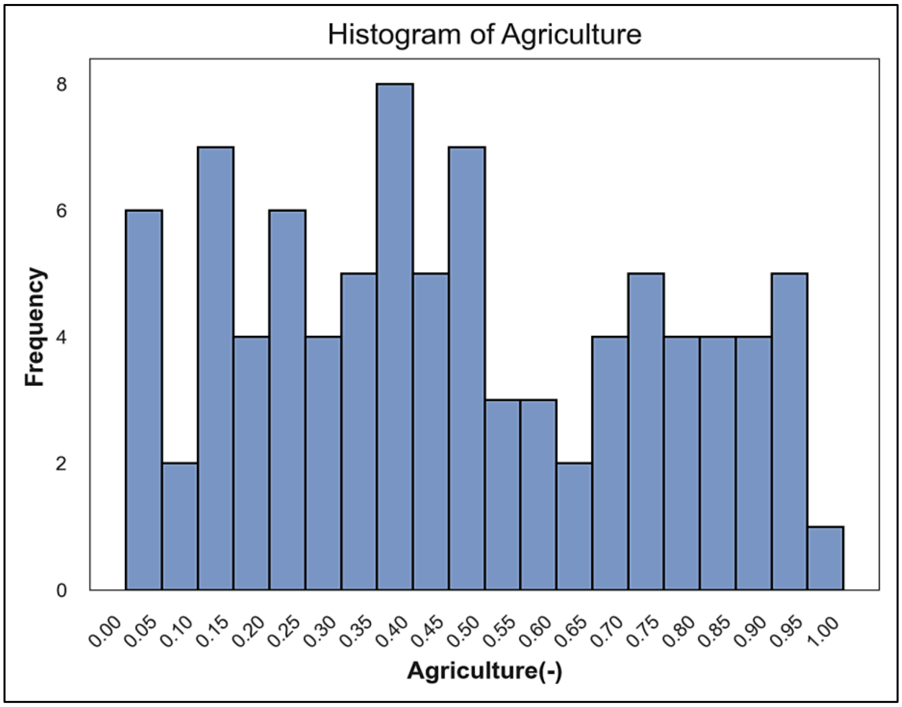

Figure 4.15.a: Histograms of agricultural cover fractions across the catchments.

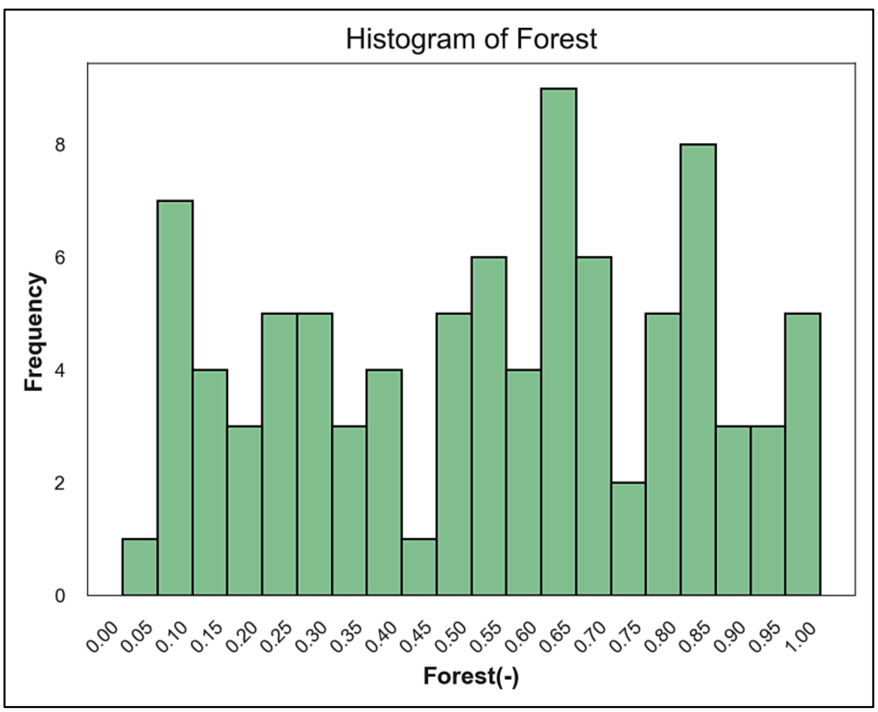

Figure 4.15.b: Histograms of forest cover fractions across the catchments.

5. Regionalization of FDC Parameters

Chapter 5 introduces the regionalization of Flow Duration Curve (FDC) parameters as a means of predicting streamflow characteristics in ungauged basins. The analysis focuses on linking key FDC metrics—such as the mean of the log-normal distribution (μ), the mean non-zero flow (Q_{nz}), and the duration of non-zero flow (τ)—to measurable catchment descriptors. Both linear and nonlinear regression approaches are applied, supported by exploratory correlation analysis and stepwise variable selection, to ensure parsimonious yet hydrologically meaningful models. Special attention is given to the effects of record length, validation through jackknife testing, and the complementary role of the Base Flow Index (*BFI*). Together, these methods establish a framework for developing robust and transferable regional models across the diverse hydrological settings of southern Italy.

5.1 Introduction to Regionalization Approach

Regionalization is a fundamental hydrological approach that supports streamflow prediction in ungauged basins by transferring knowledge from gauged sites through relationships built on observable catchment attributes. In this study, the regionalization of FDCs is carried out for large and hydrologically diverse regions of Southern Italy, an area characterized by marked climatic variability, complex geomorphology, and heterogeneous geology, as well as sparse monitoring networks. The focus is placed on estimating key FDC parameters essential for water resources assessment in data-scarce contexts, namely: the mean (μ) of the log-normal distribution, the average of non-zero flows (Q_{nz}), and the duration of non-zero flow (τ).

To link these hydrological parameters with catchment descriptors, a wide range of explanatory variables are considered, reflecting climatic (e.g., mean annual precipitation), geomorphological (e.g., area, slope, elevation), and geological (e.g., permeability) controls. The aim is to establish simple, empirical regression models that provide transparent and operational relationships between catchment attributes and FDC characteristics.

A regression-based framework was adopted for the regionalization analysis, owing to its methodological transparency and established effectiveness in hydrological prediction. Linear regression was selected as the primary modeling approach because of its simplicity, computational efficiency, and suitability for large-scale regional studies, where interpretability and operational applicability are of particular importance. In parallel, nonlinear formulations, especially power-law relationships, were investigated to capture potential multiplicative interactions and threshold-driven dynamics among catchment descriptors that cannot be adequately represented by linear structures. This combined strategy ensures a balance between parsimony and flexibility, thereby enhancing the robustness and practical relevance of the proposed regionalization models.

In this study, 56 streamflow stations were used from an initial dataset of 89, applying a minimum record length of 15 years of daily discharge data as the selection criterion. Although the series is not fully continuous, the retained records are sufficiently long to allow reliable estimation of FDCs parameters. The selected stations also cover a wide range of climatic, geological, and physiographic conditions across Southern Italy, ensuring that the regionalization models are representative of the hydrological diversity of the study area.

5.1.1 Linear and Nonlinear Regression: Formulation

Linear regression represents a fundamental statistical approach for describing the relationship between a dependent variable y and a set of explanatory variables x_i . Its general form is:

$$y = \beta_0 + \sum_{i=1}^{p} \beta_i x_i + \varepsilon \tag{5.1}$$

here β_0 is the intercept, β_i are the regression coefficients quantifying the contribution of each predictor, and ε is the random error term. Parameters are commonly estimated using the ordinary least squares (*OLS*) method, which minimizes the sum of squared residuals and, under standard statistical assumptions, yields unbiased and efficient estimators(Zdaniuk, 2023).
In contrast, nonlinear regression encompasses a broader class of functional forms that can capture the complex, often non-additive interactions typical of hydrological systems. A widely used formulation in regionalization studies is the power-law model**:**

$$y = a \prod_{i=1}^{p} {x_i}^{b_i} . \varepsilon \tag{5.2}$$

where *a* and b_i are model parameters to be estimated, and the product operator reflects the multiplicative nature of the predictors. This formulation is especially relevant for hydrological processes exhibiting nonlinear scaling relationships.
For ease of estimation and interpretability, the power-law model is frequently linearized via logarithmic transformation:

$$\log(y) = \log(a) + \sum_{i=1}^{p} b_i \log(x_i) + \varepsilon \tag{5.3}$$

This transformation allows the use of OLS in the log-transformed space, facilitating direct parameter estimation and enabling straightforward comparison with linear models. Moreover, it highlights multiplicative effects and scaling behaviors that are not adequately represented in purely additive frameworks (Lacombe et al., 2014).
By employing both linear and nonlinear regression approaches, the analysis accommodates a wide spectrum of empirical relationships between FDC parameters and catchment descriptors, ranging from simple additive effects to more complex scaling patterns, thereby strengthening the robustness of regionalization models.

5.2 Exploratory Data Analysis

The development of reliable regionalization models requires a systematic and transparent process of variable screening to ensure that the final set of predictors is both parsimonious and hydrologically meaningful. In the first step, attention was directed exclusively toward the relationships among the independent variables, with the objective of detecting strong correlations and diagnosing multicollinearity. This assessment is critical because high interdependence among catchment descriptors can inflate variance, obscure the unique contribution of individual predictors, and ultimately reduce the stability of regression models(Dou et al., 2024).

5.2.1 Correlation Structure and Collinearity

Morphometric and physiographic descriptors obtained from GIS were examined for collinearity using pairwise Pearson correlation coefficients. The results were displayed as heatmaps, which helped to identify groups of variables that were strongly related and therefore potentially redundant. Variables showing correlations of $|R| \geq 0.70$ were considered too closely related, and in such cases one descriptor was removed to reduce multicollinearity. As shown in Figure 5.1, the heatmap illustrates the full matrix of Pearson correlation coefficients, with colors ranging from blue (negative correlations) to red (positive correlations). As shown in the figure 5.1, the catchment descriptors include catchment area (*A,* km²), perimeter (*P,* km), maximum elevation (*HMAX,* m), mean elevation (*HMEAN,* m), elevation range (*HRANGE,* m), flow path length (*L,* km), mean slope (*SMEAN,* °), slope length (*SL,* °), shape factor (*SF,* –), and circularity ratio (*CR,* –).

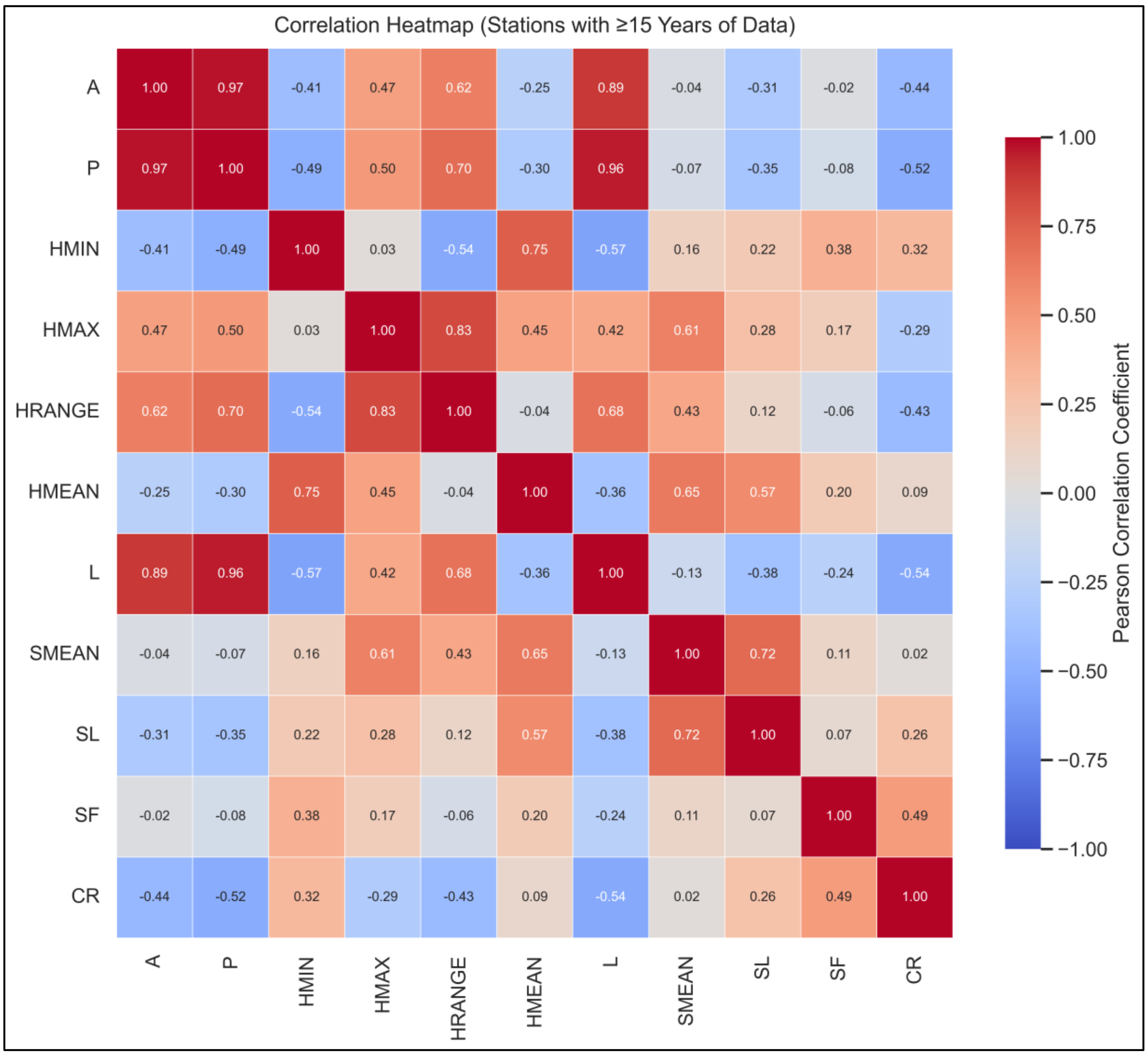

Figure 5.1: Heatmap of pairwise Pearson correlation coefficients among morphometric and physiographic descriptors

Within the set of size-related descriptors, catchment area (*A*) exhibited very strong correlations with both perimeter (*P*) (R=0.97) and longest flow path (*L*) (R=0.89), indicating a high degree of statistical dependence among these metrics. Such associations are consistent with geometric scaling laws of watershed morphology, whereby increases in basin extent are systematically accompanied by larger perimeters and longer drainage paths. To minimize redundancy while preserving hydrological interpretability, A was retained as the primary descriptor of basin scale. Conversely, *P* and *L* were excluded due to their secondary and derivative nature, ensuring a more parsimonious set of predictors for subsequent analyses.

Within the set of elevation-related descriptors, maximum elevation (*HMAX*) was strongly correlated with elevation range (*HRANGE*) (R=0.83), while mean elevation (*HMEAN*) was moderately correlated with minimum elevation (*HMIN*) (R=0.75). *HRANGE* was excluded because it does not provide independent information beyond *HMAX* and *HMIN*, being a simple derivative of the two. *HMIN* was also discarded since its explanatory contribution is largely captured by *HMEAN*. By contrast, *HMAX* was retained as an indicator of absolute relief, and *HMEAN* as a descriptor of overall altitude conditions with direct climatic and orographic implications. Together, *HMAX* and *HMEAN* offer complementary and non-redundant information on catchment elevation characteristics in this dataset.

Regarding terrain gradient, mean catchment slope (*SMEAN*) and slope of the main channel (*SL*) displayed collinearity (R=0.72), which was expected given their topographic basis. However, *SMEAN* was retained due to its integrative nature—it captures the average steepness across the entire basin, whereas *SL* is confined to the main drainage path and thus offers a more localized perspective.

For shape-related descriptors, shape factor (*SF*) and circularity ratio (*CR*) exhibited moderate correlation (R= 0.49), suggesting partial statistical dependence. However, both were retained, as they provide complementary geometric insights: *SF* reflects elongation, while *CR* captures compactness. These shape attributes influence hydrological response, particularly the concentration time and peak discharge behavior. For example, in a compact basin (low *SF*, high *CR*), water from all areas reaches the outlet more simultaneously because flow paths are shorter and more uniform. This shortens concentration time, leading to faster overall response to rainfall.

To maintain parsimony without reducing explanatory power, six descriptors—*A*, *HMEAN*, *HMAX*, *SMEAN*, *SF*, and *CR*—were selected for retention. These variables subsequently served as the principal physiographic and morphometric predictors in the regionalization and hydrological modeling framework.

5.2.2 Selection of Regionalization Descriptors for FDC Modeling

The identification of explanatory variables for regionalization was carried out through a sequential procedure that integrated statistical assessment with hydrological reasoning. In the first stage, bivariate Pearson correlation coefficients were calculated between 14 candidate descriptors, covering physiographic, geological, land cover, and climatic characteristics, and the target FDC indices (τ, μ, Q_{nz}). This analysis served as a screening tool to identify descriptors exhibiting strong and consistent associations with the flow metrics.

In the second stage, stepwise regression analysis was applied—both in raw and logarithmic space—to explore linear and potential multiplicative (power-law) relationships between descriptors and FDC metrics. This method iteratively selected the most informative subset of variables based on model performance, allowing for a more parsimonious representation of hydrological behavior.

In the final stage, hydrological reasoning and expert judgment were incorporated to refine the descriptor set. This ensured that the selected variables were not only statistically significant but also physically meaningful and interpretable within a hydrological framework.
By combining statistical correlation, data-driven regression modeling, and domain expertise, a robust and interpretable set of regionalization descriptors was established for subsequent FDC modeling and transferability across ungauged basins.

5.2.2.2 Correlation Analysis Between Q_{nz} and Catchment Descriptors

Pearson's R was computed between Q_{nz} and fourteen climatic, topographic, morphometric, land-cover, and soil descriptors for all catchments. Figure 5.2 summarizes the resulting correlation pattern, highlighting the descriptors with the largest absolute correlations with Q_{nz} , which are subsequently prioritized for regression analysis.
Among all predictors, catchment area (*A*) exhibits the strongest positive correlation with Q_{nz} (R = 0.95), confirming the fundamental hydrological principle that larger catchments generally yield greater discharge due to increased contributing surface and precipitation accumulation. Similarly, maximum elevation (*HMAX*) shows a moderate positive correlation (R = 0.55), indicating that catchments with higher elevation ranges tend to support greater discharge, likely reflecting orographic effects and enhanced runoff. For instance, basins located along the southern slopes of the Apennines, such as those in the Cilento and Irpinia areas, exhibit elevated *HMAX* values and correspondingly higher precipitation inputs, which intensify flow response. In contrast, lower-lying coastal basins near the Tyrrhenian margin, with more limited *HMAX*, receive less orographic rainfall and show comparatively reduced runoff. This gradient highlights the role of *HMAX* as both a geomorphic and hydro-climatic control across the region.
The circularity ratio (*CR*) exhibits a moderate negative correlation with Q_{nz} (R = –0.41). Regarding soil descriptors**,** *SoilBC* (R = –0.27), *SoilC* (R = –0.18), and *SoilABC* (R = –0.08) show negative associations, whereas *SoilA* (R = 0.35) and *SoilAB* (R = 0.13) exhibit modest positive correlations. Other topographic and shape-related descriptors mean elevation (*HMEAN*) (R = –0.16), mean slope (*SMEAN*) (R = 0.08), and shape factor (*SF*) (R = 0.01) exhibit weak correlations. Forest cover (R = –0.01) and mean annual precipitation (*MAP*) (R = 0.14) also show minimal linear association with Q_{nz}.
The results highlight catchment area as the dominant predictor of Q_{nz}, supported by secondary contributions from elevation-related parameters. Soil and shape descriptors display weaker and more variable correlations, whereas climatic and land-cover variables demonstrate only limited explanatory influence.

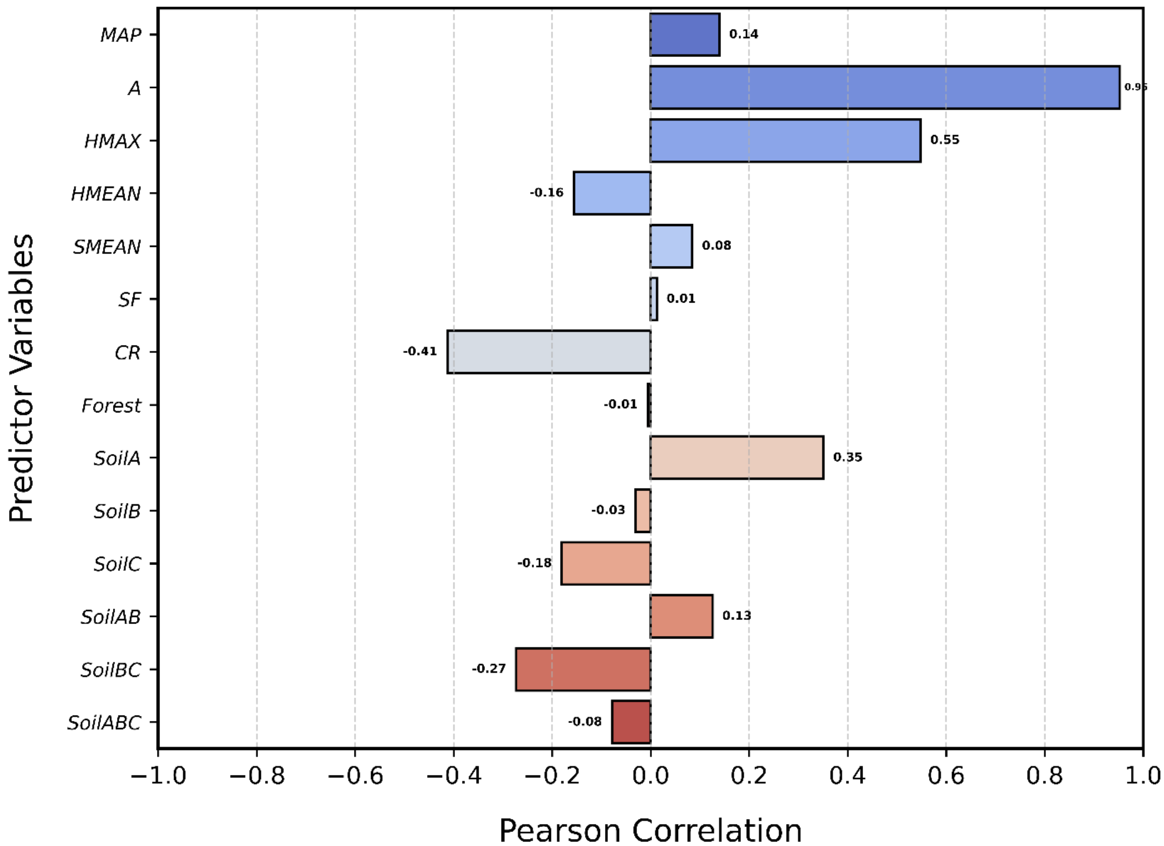

Figure 5.2: Pearson correlation coefficients between Q_{nz} and catchment descriptors.

5.2.2.1 Correlation Analysis between μ and Catchment Descriptors

Linear associations (Pearson's R) between μ and 14 catchment descriptors—covering climate, topography, morphometry, land cover, and soils—are quantified to indicate the direction and magnitude of potential controls. Figure 5.3 reports these coefficients as an initial statistical screen, informing the specification of models for μ.

As shown in the figure, forest cover exhibits the strongest positive correlation with μ (R = 0.63), closely followed by mean annual precipitation (*MAP*) (R = 0.63). These two variables emerge as the most influential drivers of μ. The strong association with forest cover suggests that vegetated catchments exhibit enhanced hydrological functioning through mechanisms such as increased infiltration capacity, delayed runoff generation, and greater groundwater recharge. Likewise, the correlation with *MAP* reflects the fundamental role of precipitation as the primary climatic input controlling water availability and long-term discharge generation.

Among topographic parameters, mean catchment slope (*SMEAN*) and mean elevation (*HMEAN*) show substantial positive correlations (R = 0.60), indicating that steeper and higher catchments are associated with μ. Maximum elevation (*HMAX*) also correlates moderately with μ (R = 0.55), further supporting the role of topography in enhancing discharge potential in elevated basins. This relationship is partly explained by the fact that precipitation generally increases with elevation (orographic effect), so catchments with higher *HMAX* typically receive greater *MAP*, which in turn sustains higher discharge levels.

In contrast, catchment area (*A*) shows a weak positive correlation (R = 0.13), while shape factor (*SF*) presents a low-to-moderate correlation (R = 0.29), and circularity ratio (*CR*) appears uncorrelated (R = 0.00). These results indicate that, once streamflow is normalized, the influence of basin size and shape becomes secondary, and geometric metrics contribute little explanatory power to the prediction of mean of the lognormal transformation.

The analysis of soil descriptors reveals a more heterogeneous behavior. The composite class *SoilABC*, representing catchments with a mixture of soil textures (types *A*, *B*, and *C*), exhibits the strongest correlation with μ (R = 0.44), suggesting that soil heterogeneity enhances hydrological response by combining infiltration and storage properties across different soil types. Among the individual classes, *SoilA* (R = 0.39) shows the highest positive correlation, reflecting its generally higher permeability and capacity to promote infiltration and subsurface storage. *SoilB* (R = 0.00) and *SoilC* (R = 0.11) display weaker associations, consistent with their lower permeability and more limited role in facilitating water retention. Intermediate classes, such as *SoilAB* (R = 0.18) and *SoilBC* (R = 0.15), follow the expected gradient between their constituent soils. Taken together, these results indicate that while *SoilA* exerts the strongest individual influence, the combined presence of *A, B*, and *C* textures within *SoilABC* captures the full spectrum of storage contributions, thereby explaining its higher correlation with μ compared to single soil classes.

In summary, Figure 5.3 demonstrates that μ is primarily governed by climatic (*MAP*), land cover (*forest*), topographic (slope and elevation), and soil properties—particularly soil heterogeneity (*SoilABC*) and permeability (*SoilA*). In contrast, morphometric descriptors exhibit considerably lower predictive relevance.

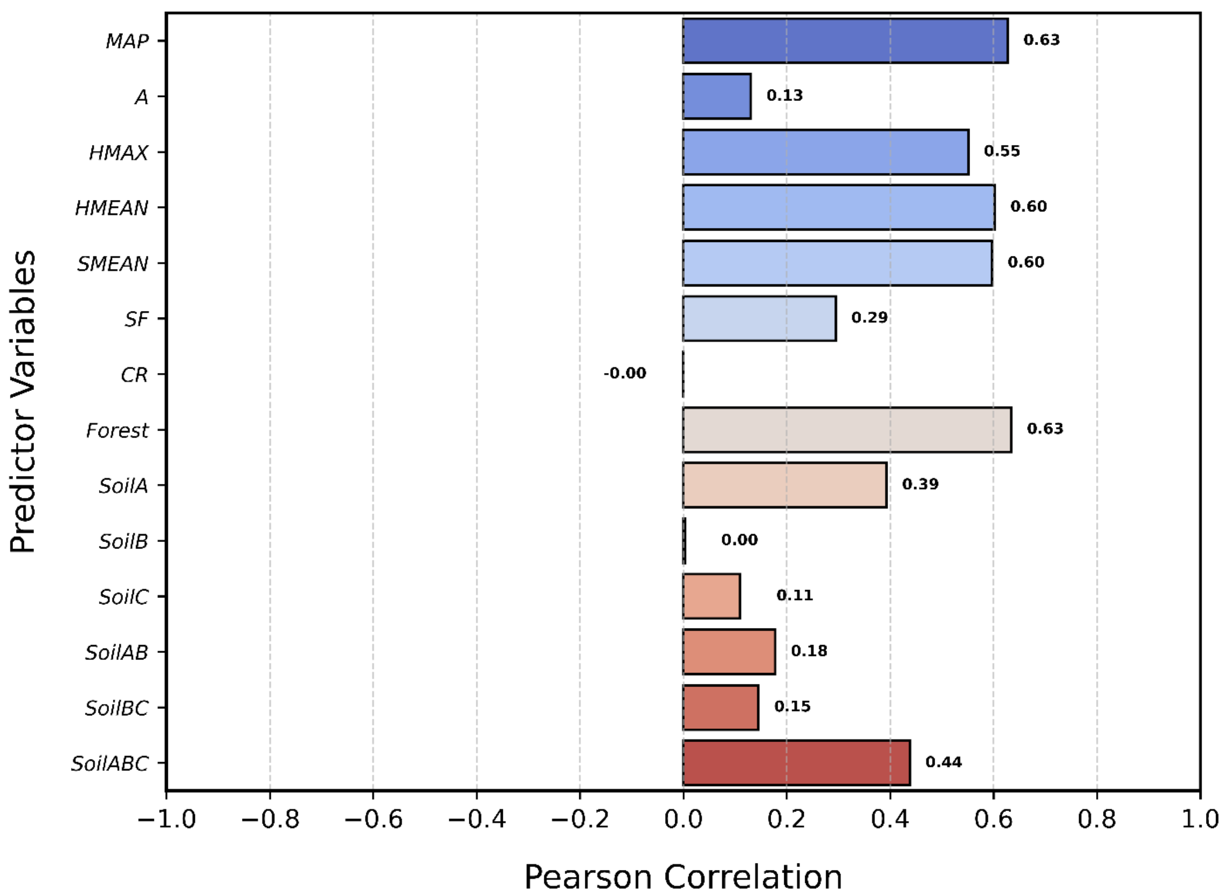

Figure 5.3: Pearson correlation coefficients between μ and catchment descriptors.

5.2.2.3 Correlation Analysis between τ and Catchment Descriptors

Flow persistence is assessed via Pearson correlations between τ and climatic, topographic, morphometric, land-cover, and soil descriptors. The correlation profile in Figure 5.4 identifies attributes systematically associated with τ, providing an initial appraisal of the climatic forcing, terrain configuration, and subsurface properties that regulate hydrological continuity.

Among climatic and topographic variables, maximum elevation (*HMAX*) shows the strongest positive correlation with τ ($R = 0.71$), indicating that more elevated basins tend to sustain flow for longer durations. Mean annual precipitation (*MAP*) exhibits a moderate positive correlation ($R = 0.48$), suggesting higher precipitation associates with prolonged non-zero discharge. Catchment area (*A*) and mean elevation (*HMEAN*) also demonstrate moderate positive correlations ($R = 0.41$ and 0.47, respectively), reinforcing the role of terrain in supporting hydrological continuity through greater water accumulation and enhanced groundwater recharge.

Mean catchment slope (*SMEAN*) ($R = 0.41$) and shape factor (*SF*) ($R = 0.50$) exhibit moderate positive associations, indicating more elongated basins may facilitate sustained runoff. The circularity ratio (*CR*) shows a low-moderate positive correlation ($R = 0.33$), suggesting more circular shapes can promote longer flow durations.

Land cover, particularly forest, displays a moderate positive correlation (R = 0.41), implying vegetated catchments contribute to sustained streamflow through improved infiltration, soil moisture retention.

Soil characteristics show contrasting patterns. *SoilA* (R = 0.37) displays a moderate positive correlation with τ, while *SoilC* (R = −0.46), *SoilBC* (R = −0.38), and *SoilABC* (R = −0.27) show notable negative correlations. *SoilB* (R = −0.10) and *SoilAB* (R = 0.02) exhibit weak or negligible associations.

The results emphasize that τ governed by a complex interplay of climatic input (*MAP*), terrain configuration (elevation, slope), morphology (shape factors), and subsurface properties (soil permeability).

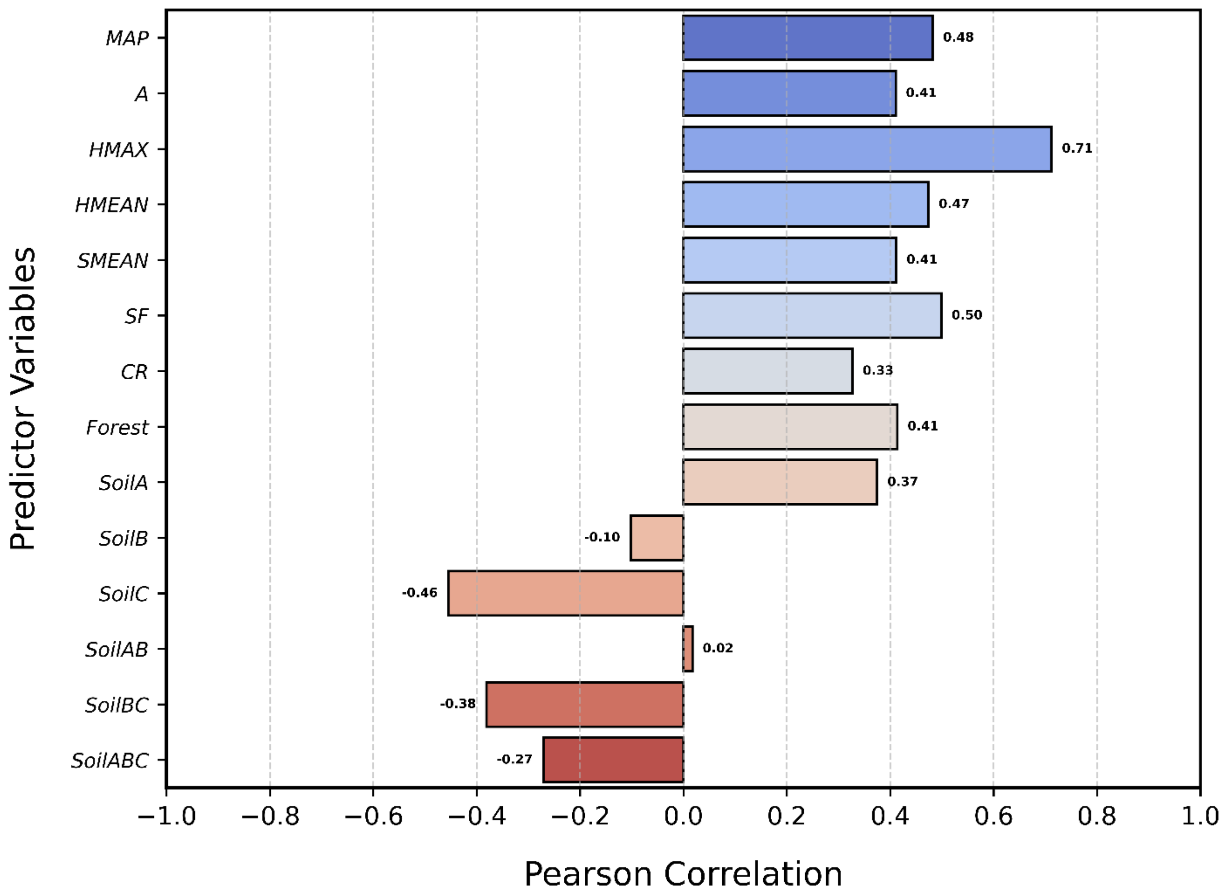

Figure 5.4: Pearson correlation coefficients between τ and catchment descriptors.

5.2.3 Stepwise Regression in Raw and Log Space

In the present study, stepwise regression was adopted as a methodological framework for the identification of the most influential catchment descriptors, with the objective of constructing parsimonious yet robust predictive models. Given its capacity to iteratively select explanatory variables based on statistical criteria, stepwise regression provides an efficient means of reducing model complexity while retaining explanatory power.

Stepwise regression has become a widely adopted technique in hydrological modelling, offering an efficient framework for identifying influential predictors and constructing parsimonious models. Its application spans several domains, from flood forecasting (. Kim et al., 2012) to groundwater studies (Sahoo & Jha, 2015) and water quality analysis (Yang et al., 2017; J. Wang et al., 2021), where it aids in isolating the dominant environmental drivers of variability.

Stepwise regression has often served as a central tool in regionalization methods, enabling the systematic selection of key physiographic and climatic predictors. For example, Ochoa-Tocachi et al.(2016) demonstrated the capacity of paired catchment networks to deliver statistically robust predictions of land-use change impacts on streamflow, while Nega & Seleshi(2021) applied stepwise regression to derive empirical equations for estimating mean annual flows in ungauged catchments of the Abbay River Basin in Ethiopia. Similarly, Cupak & Michalec (2022) explored regionalization through grouping techniques based on low-flow similarities, where stepwise regression supports the identification of dominant descriptors among potential alternatives. Visessri & McIntyre (2016) further incorporated adaptive regionalization strategies to account for land-use change and variable data quality, highlighting the role of stepwise regression in refining donor–receptor catchment transfers. Together, these studies highlight how stepwise regression enables researchers to distil complex sets of catchment descriptors into robust predictive models, strengthening the statistical and hydrological foundations of basin-scale analysis.

Recognizing that conventional stepwise regression operates under the assumption of linearity between predictors and the dependent variable, an initial analysis was conducted using raw (untransformed) physiographic descriptors to establish a baseline linear model. However, given the nonlinear and multiplicative nature of many hydrological processes, the analysis was subsequently extended to the logarithmic space. In this formulation, both the dependent and independent variables were log-transformed, thereby enabling the detection of power-law relationships that are commonly observed in hydrological systems. This two-pronged approach combining linear and log-space model structures allowed for a more comprehensive assessment of the functional relationships between catchment characteristics and hydrological response.

Stepwise regression is a data-driven variable–selection procedure that iteratively adds or removes predictors to balance explanatory power and parsimony. Two complementary moves are used: forward selection, which starts from the intercept-only model and adds the single predictor that most improves a selection criterion; and backward elimination, which starts from a multivariate model and deletes the single predictor whose removal most improves the same criterion. A bidirectional (forward–backward) routine alternates these moves so that, after any addition, currently included terms are re-tested for possible removal. Iteration stops when no single add/drop operation yields a better model under the chosen criterion, producing a transparent and reproducible subset of predictors.

Selection objective (AIC)

The Akaike Information Criterion (*AIC*) is defined as

$$AIC=2k-2lnL \tag{5.4}$$

where k is the number of estimated parameters (including the intercept), and L is the maximized Gaussian likelihood of the candidate linear model. This criterion balances fit and complexity: the likelihood term rewards better fit (smaller RSS), while the penalty $2k$ discourages over-parameterization. The model with the lowest *AIC* is preferred.

For normally distributed residuals with variance σ^2, the likelihood of observing a sample of size n with residual sum of squares RSS is

$$L = \left(\frac{1}{\sqrt{2\pi\sigma^2}}\right) exp\left(-\frac{RRS}{2\sigma^2}\right) \tag{5.5}$$

In stepwise selection, *AIC* guides the search process. At each iteration, the algorithm evaluates possible add/drop operations and selects the one that yields the largest reduction in *AIC*. No tolerance window is applied, and if multiple operations achieve the same improvement, the choice is made based on the smallest resulting *AIC*. Once the selection process terminates, the final subset of predictors is refitted using ordinary least squares (OLS), and the results are reported in full.

Companion parsimony metric (BIC)

For completeness, the Bayesian Information Criterion,

$$BIC = k\ ln(n) - 2lnL \tag{5.6}$$

with sample size n, is computed for fitted models. Because its penalty increases with ln n, *BIC* typically favors models that are the same size as—or smaller than—those preferred by *AIC*. In this workflow, *BIC* is presented as a descriptive parsimony benchmark and does not govern inclusion/exclusion during stepwise selection (the routine can be rerun with *BIC* as the objective by substituting it for *AIC* throughout).
While stepwise forward regression primarily relies on information-theoretic criteria such as the *AIC* and *BIC* for model selection, a comprehensive statistical assessment also necessitates evaluating the significance and explanatory power of each candidate model. In this context, coefficient of determination (R^2), and R^2_{adj} serve as complementary indicators of model quality and variable importance.

Coefficient of Determination ($\mathbf{R^2_{adj}}$)

The coefficient of determination (R^2) was already defined in Chapter 3.3 as a measure of explained variance. However, a limitation of R^2 is that it always increases with the addition of predictors, even if they do not improve model quality. To account for this, the adjusted R^2 provides a more conservative measure by incorporating both the number of predictors (k) and the sample size (n):

$$R^2_{adj} = 1 - \left(\frac{(1 - R^2)(n - 1)}{n - k - 1}\right) \tag{5.7}$$

This adjustment penalizes model complexity, ensuring that R^2_{adj} only increases when additional variables contribute genuine explanatory power.

p-Values

For each coefficient β_j in a linear (or log-linear/power-law) regression, the p-value tests the null hypothesis H_0: $\beta_j=0$ (no association) against H1: $\beta_j \neq 0$. Under standard assumptions (linearity, independent errors, homoscedasticity, approximate normality of residuals), the test statistic

$$t_j = \frac{\hat{\beta}_j}{SE(\hat{\beta}_j)} \tag{5.8}$$

follows a t-distribution with $n-k-1$ degrees of freedom, and the p-value is the probability of observing $|t_j|$ as large as (or larger than) the one computed if H_0 were true. Small p-values ($p<0.05$) indicate evidence that predictor j contributes explanatory signal beyond noise, conditional on the other variables in the model.

Model selection employed *AIC/BIC*–guided stepwise regression. Final models are evaluated using R^2, R^2_{adj}, *AIC/BIC*, and coefficient-level p-values, with coefficient estimates $\hat{\beta}$ also reported for interpretability.

5.2.3.1 Analysis of Stepwise Regression Models for μ

The stepwise linear regression models for the hydrological parameter μ, selected using *BIC* and *AIC* criteria, highlight key topographic and soil-related predictors with moderate explanatory power. The *BIC* model, which emphasizes parsimony, retained four variables—*SoilAB, SMEAN*, *HMEAN*, and *A*—achieving $R^2 = 0.60$ and $R^2_{adj} = 0.57$ (Table 5.1). All coefficients are positive, with slope (*SMEAN* = 0.084, $p < 0.001$) and moderately permeable soils (*SoilAB* = 0.059, p = 0.001) exerting the strongest influence, while elevation (*HMEAN* = 0.057, $p = 0.009$) shows consistent effects, but catchment area ($A = 0.031$, $p = 0.054$) exhibits marginal significance, implying a potentially inconsistent or weak link to μ. The *AIC* model expanded the predictor set to six variables, adding *SoilABC* (0.040, $p = 0.025$) and *SF* (0.028, $p = 0.063$), which increased the fit to $R^2 = 0.65$ ($R^2_{adj} = 0.61$). While these additions raise R^2, their independent contribution is limited: *SF* is not statistically significant ($p = 0.063$) and overlap between *SoilAB* and *SoilABC* reduces the significance of *SoilAB* (0.033, $p = 0.081$), indicating collinearity. Given that A is already marginal in the *BIC* model ($p = 0.054$), the small gain in fit comes at the expense of interpretability and stability. This outcome is fully consistent with the theoretical distinction between the two selection criteria: *AIC*, being more relaxed than *BIC*, tends to retain additional predictors such as *SoilAB* and *SoilABC*, even when their explanatory power is partly redundant.

Table 5.1: Stepwise linear regression models for μ selected by BIC and AIC.

Model Type	Criterion	Selected Variables	Coefficient	*P*-value	R^2	R^2_{adj}	*AIC*	*BIC*
Linear Regression	*BIC*	*Intercept*	–0.862	<0.001	0.6	0.57		-73.55
		SoilAB	0.059	0.001				
		SMEAN	0.084	<0.001				
		HMEAN	0.057	0.009				
		A	0.031	0.054				
Linear Regression	*AIC*	*Intercept*	–1.015	<0.001	0.65	0.61	-87.52	
		SoilAB	0.033	0.081				
		SMEAN	0.068	0.003				
		HMEAN	0.05	0.016				
		A	0.039	0.014				
		SoilABC	0.04	0.025				
		SF	0.028	0.063				

The *AIC* and *BIC* procedures converge on the same parsimonious linear model for Q_{nz} with three predictors—catchment area (*A*), *SoilA,* and mean annual precipitation (*MAP*)—delivering excellent fit ($R^2 = 0.92$; $R^2_{adj} = 0.91$, see table 5.2). All coefficients are positive and statistically significant at the 1% level or better ($A = 18.6689$, $p < 0.001$; $SoilA = 2.2102$, $p = 0.005$; $MAP = 2.1375$, $p = 0.006$), indicating that larger contributing area, a higher proportion of *SoilA*, and greater precipitation are each associated with higher Q_{nz}. The intercept is -8.226 ($p < 0.001$). Although coefficient magnitudes are not directly comparable due to differing units and scales, the *p*-values indicate the strongest statistical support for *A*, with *SoilA* and *MAP* providing additional, independent signals. Information criteria are *AIC* = 350.5 and *BIC* **=** 358.6**,** further confirming that no additional complexity is warranted.

Table 5.2: Stepwise linear regression models for Qnz selected by AIC and BIC.

Criterion	Variable	Coefficient	*P-value*	*R²*	R^2_{adj}	*AIC*	*BIC*
AIC	*Intercept*	-8.226	<0.001	0.92	0.91	350.5	
	A	18.668	<0.001				
	SoilA	2.2102	0.005				
	MAP	2.1375	0.006				
BIC	*Intercept*	-8.226	<0.001	0.92	0.91		358.6
	A	18.6689	<0.001				
	SoilA	2.2102	0.005				
	MAP	2.1375	0.006				

As reported in Table 5.3, in log-transformed (power-law) space with Q_{nz} as the output, the *BIC* model retains catchment area, mean elevation, and *SoilBC* and explains a moderate share of variance (R^2 = 0.55; R^2_{adj}= 0.53). All three effects are positive and statistically supported—area 0.3677 (p < 0.001), mean elevation 0.2354 (p < 0.001), *SoilBC* 0.1127 (p = 0.021)—yielding a compact, internally consistent specification. Compared to raw space, precipitation is no longer selected as a key driver in the log-transformed setting, suggesting that the effect of climatic forcing is partly absorbed by topographic descriptors (elevation) when the multiplicative structure of the power-law is imposed.

The *AIC* model increases the apparent fit to R^2 = 0.99 (R^2_{adj}= 0.98) by adding precipitation, maximum elevation, and *CR*; area and precipitation remain strongly positive (p < 0.001) and maximum elevation is positive (p = 0.009), but *SoilBC* becomes negative at −0.0786 (p = 0.014) and *CR* is not supported (p = 0.154). Although R^2 increases, these inconsistencies—especially the non-significant *CR*—introduce uncertainty and weaken the reliability of the combined *AIC* model for inference on Q_{nz}, making the leaner *BIC* specification the more interpretable choice. A further distinction emerges when comparing the raw and log-transformed models. In raw space, *SoilA* appeared as an effective predictor of Q_{nz}. However, this effect cannot be reproduced in log-transformed regression because many catchments have no coverage of *SoilA*, yielding zero values. Taking logarithms of zero is undefined, which forces stepwise regression in log space to exclude *SoilA*. In this context, *SoilBC* is preferred instead.

Table 5.3: Power-law regression models for Q_{nz} in log-transformed space selected by BIC and AIC.

Criterion	Variable	Coefficient	P-value	R^2	R^2_{adj}	AIC	BIC
BIC	*Intercept*	–20.437	<0.001	0.55	0.53		43.45
	A	0.3677	<0.001				
	HMEAN	0.2354	<0.001				
	SoilBC	0.1127	0.021				
AIC	*Intercept*	-20.397	<0.001	0.99	0.98	–13.51	
	A	1.3963	<0.001				
	MAP	0.5973	<0.001				
	HMAX	0.1457	0.009				
	SoilBC	–0.0786	0.014				
	CR	–0.0455	0.154				

5.2.3.3 Analysis of Stepwise Regression Models for Duration of non-zero flow

The *AIC*-selected model retains *HMAX, CR, SoilC*, and *MAP*, with an intercept of 0.19. It explains a large share of the variance (R^2=0.81, R^2_{adj}=0.76) and achieves an *AIC* of −42.89 (see Table 5.4). All predictors are statistically significant at the 0.01 level, substantially lower than the usual significance constraint of 0.05, providing strong evidence for their relevance. Among them, *HMAX* exerts the strongest positive influence (coefficient = 0.1673, $p < 0.001$), underscoring the effect of maximum elevation on prolonging flow occurrence. *CR* also contributes positively (0.0695, p = 0.002), indicating that more compact basins sustain longer non-zero flow durations. In contrast, *SoilC* carries a negative coefficient (−0.0575, p = 0.006), suggesting that poorly permeable soils reduce flow persistence. This is physically reasonable, as impermeable catchments exhibit an impulsive hydrological response—water is present essentially only during rainfall events, with little capacity for storage or delayed release. *MAP* also enters with a negative coefficient (−0.0997, p = 0.006), indicating that higher precipitation enhances direct runoff and reduces the stability of non-zero discharge. At first sight, one might expect a positive correlation with *MAP*, since greater rainfall should support more perennial flows (higher τ). However, the effect of *MAP* cannot be interpreted in isolation: its influence depends strongly on catchment permeability. In basins with poorly permeable soils, high rainfall intensifies flashy runoff rather than sustaining baseflow, leading to shorter flow durations. Thus, *MAP* and soil properties act in an intertwined manner, with their combined interaction ultimately determining the persistence of non-zero flow.

The *BIC*-selected specification favors parsimony, retaining only three predictors: *HMAX, CR*, and *HMEAN*, with an intercept of −0.062 (Table 5.4). This model achieves an R^2 of 0.71 and an adjusted R^2 of 0.65, with a *BIC* of −32.09, indicating a strong and efficient fit. Among the retained variables, *HMAX* emerges as the dominant contributor (0.1668, $p < 0.001$), underscoring the critical role of maximum elevation. *CR* also exerts a significant positive influence (0.0779, p = 0.005), highlighting the importance of basin compactness. This result is physically meaningful, since compact basins tend to have shorter lag times, enabling more rapid concentration and release of runoff. In contrast, *HMEAN* enters with a negative coefficient (−0.0841, p = 0.034), suggesting that catchments with higher mean elevations are associated with shorter durations of non-zero flow.

Table 5.4: Stepwise linear regression models for τ in raw space selected by AIC and BIC.

Criterion	Variable	Coefficient	P-value	R^2	R^2_{adj}	*AIC*	*BIC*
AIC	*Intercept*	0.19	<0.001	0.81	0.76	–42.89	
	HMAX	0.1673	<0.001				
	CR	0.0695	0.002				
	SoilC	–0.0575	0.006				
	MAP	–0.0997	0.006				
BIC	*Intercept*	-0.062	<0.001	0.71	0.65		–32.09
	HMAX	0.1668	<0.001				
	CR	0.0779	0.005				
	HMEAN	–0.0841	0.034				

According to the results summarized in Table 5.5, the *AIC*-selected model (Table 5.5) includes *CR, A, SoilA*, and *SoilC*, with an intercept of –0.2190. It explains a substantial portion of the variance with R^2= 0.75 and R^2_{adj}=0.69, achieving an *AIC* of –27.55. *CR* enters with a positive coefficient of 0.0645 (p = 0.024), indicating that catchment compactness increases τ under the power-law formulation. Drainage area also exerts a strong positive effect (0.1002, p = 0.002), highlighting its role in sustaining longer non-zero flow durations. *SoilA* is positive as well (0.0689, p = 0.027), consistent with permeable soils supporting storage and infiltration that increase τ. *SoilC* enters with a negative coefficient (–0.0345) and a relatively high p-value (0.227), indicating an uncertain and statistically unsupported effect. *AIC* combination incorporating *SoilC* is not reliable because the p-value of *SoilC* exceeds 0.2, which increases uncertainty in its estimated effect and potentially undermines the model's inferential robustness.

The *BIC*-selected model emphasizes parsimony, retaining three predictors: *HMAX, CR*, and *A,* again with an intercept of –0.2190 (Table 5.5). This model attains R^2=0.70 and R^2_{adj}=0.65, with *BIC* = –21.99. *HMAX* enters with a positive coefficient (0.0848, p = 0.016), underscoring the influence of relief on prolonging flow duration. *CR* also remains a consistent positive predictor (0.0726, p = 0.015), while *A* continues to demonstrate a strong positive effect (0.0861, p = 0.016). Collectively, this reduced specification balances explanatory capacity with parsimony, focusing on three dominant physiographic descriptors.

Table 5.5: Power-law regression models for τ in log-transformed space selected by AIC and BIC.

Criterion	Variable	Coefficient	P-value	R^2	R^2_{adj}	AIC	BIC
AIC	*Intercept*	–0.332	<0.001	0.759	0.69	–27.55	
	CR	0.0645	0.024				
	A	0.1002	0.002				
	SoilA	0.0689	0.027				
	SoilC	–0.0345	0.227				
BIC	*Intercept*	–2.997	<0.001	0.71	0.65		–21.99
	HMAX	0.0848	0.016				
	CR	0.0726	0.015				
	A	0.0861	0.016				

5.2.4 Hydrological Relevance and Physical Process Insight

Pearson correlation provides a direct measure of association between individual variables; however, its simplicity limits its capacity to identify the most appropriate set of predictors within a multivariate framework. Stepwise regression seeks to extend this analysis by algorithmically selecting combinations of predictors that maximize statistical fit, thereby producing what appears to be the "best" model. The appeal of this method lies in its computational efficiency and its integration into standard statistical software. Nevertheless, the central challenge does not concern the calculation itself but rather the decision-making process regarding which predictors ought to be retained and how the resulting specification should be interpreted. Problems such as multicollinearity, inflated significance levels, and the preference for models with artificially high R^2 or seemingly favorable *AIC/BIC* values often yield results that are statistically attractive yet theoretically unconvincing.

Accordingly, the critical task of the researcher is not to rely uncritically on the automated outcome of stepwise procedures, but instead to exercise judgment in determining whether the selected predictors are meaningful, theoretically grounded, and empirically defensible. This requires careful selection of variables, the formulation of multiple plausible regression specifications, and the evaluation of their validity in light of both statistical performance and substantive reasoning. In this study, the approach adopted was to identify the most plausible set of parameters and to construct several regression models that reflect different possible structures of association. In this way, regression techniques were employed as computational tools, while the responsibility for ensuring the validity and interpretability of the models rested on informed analytical decisions rather than on mechanical routines.

Based on the results of Pearson correlation analysis and stepwise regression, several catchment descriptors emerged as promising candidates for establishing statistically and hydrologically meaningful relationships. Under these premises, in the following multiple regression paths are evaluated by combining different sets of these descriptors, to provide a final version of the regression equations for the regionalization parameters. The performance of each model is assessed using a comprehensive suite of statistical metrics, including the coefficient of determination (R^2), root mean square error (*RMSE*), mean absolute error (*MAE*), mean absolute percentage error (*MAPE*), Percent Bias (*PBIAS*). For a model to be considered robust and statistically valid, all predictors are required to have p-values less than 0.05. The final selected models thus achieves a balance between statistical strength and physical interpretability, providing a reliable basis for the regionalization of FDC parameters.

5.2.5 Jackknife (Leave-One-Out) Validation

The jackknife (leave-one-out) cross-validation method was employed to rigorously assess the predictive performance of the hydrological model. For a dataset comprising (n) basins, the procedure iteratively excluded one basin at a time, recalibrated the regression model using the remaining (n-1) basins, and generated a prediction for the excluded basin's streamflow. This process was repeated (n) times, ensuring each basin was omitted exactly once, resulting in a complete set of out-of-sample predictions. These predictions were compared against observed streamflow values to evaluate the model's ability to generalize to ungauged basins, thereby providing a more robust measure of predictive accuracy than in-sample goodness-of-fit statistics, which may be inflated due to overfitting. The model's performance was evaluated using a suite of established hydrological metrics, R^2, *RMSE, MAE, MAPE, PBIAS*. These metrics were applied to both in-sample fits (derived from the full dataset) and out-of-sample jackknife predictions to facilitate a direct comparison of model performance under fitted and predictive conditions.

5.2.6 Outlier Detection

Outlier detection techniques are broadly divided into parametric and nonparametric approaches. Parametric methods assume the data follows a specific probability distribution, identifying outliers as points generated by a distinct process (Hawkins, 1980). Conversely, nonparametric methods make no distributional assumptions, offering greater flexibility (Huang et al., 2016). Parametric approaches can struggle in high-dimensional datasets or when the true distribution is unknown, as they depend on accurate model specification. In such cases, nonparametric methods often perform better (Hussain, 2020).
Nonparametric techniques include distance-based methods, which evaluate how far an observation deviates from a central point, and clustering-based methods, which flag outliers as members of small or isolated clusters(Subramaniam et al., 2006; Padulano et al., 2018). Distance-based approaches often use local distance metrics, with medians preferred over means for centering due to their robustness against extreme values(Padulano & Del Giudice, 2020).

A widely used distance metric is the Median Absolute Deviation (*MAD*). An observation x_i is flagged when

$$|x_i - median(x)| > \delta cMAD \tag{5.9}$$

with *MAD*=median(|x_i−median(x)|). This rule works best when the underlying distribution is approximately symmetric. The constant c rescales *MAD* to be consistent with the target scale parameter: under a Gaussian reference (ignoring the influence of anomalies), c=1.4826. For other reference distributions, one may set $c=1/Q_{0.75}$, where $Q_{0.75}$ is the 75th percentile of that distribution. The threshold δ reflects how aggressively to reject points; (Miller, 1991) suggests δ=3 (very

conservative), 2.5 (moderately conservative), or 2 (more tolerant). The *MAD* method was applied with a threshold of δ=2 to detect outliers, balancing sensitivity and robustness.
In real-world scenarios, detecting and handling outliers is challenging due to limited knowledge about the data's probability distribution or the processes producing outliers. This lack of information can make standard detection methods, like those in Equation (5.9), unreliable, often because they assume data symmetry or rely on an arbitrary scaling factor c.
To tackle this core issue in outlier detection, (Cousineau & Chartier, 2010) recommend transforming the data to achieve a more Gaussian-like distribution. Their approach builds on the square root transformation with the following formula:

Here, x_{min} and x_{max} denote the dataset's minimum and maximum values, respectively. Dividing by (x_{max}−x_{min}) normalizes the data to a [0, 1] range, and the square root function then stretches smaller values, pulling the lower tail closer to the center. This results in a distribution that is more symmetric than the original.

5.3 Model Development and Validation

In the previous section, both Pearson correlation and stepwise regression were applied to examine the relationships between catchment descriptors and the parameters of the FDC. Pearson correlation offers only a simple measure of pairwise linear association, which fails to capture the multivariate interactions that characterize hydrological systems. Stepwise regression extends this analysis by producing explicit multivariate formulas; however, such models come with important caveats. In some cases, predictors with *p*-values above 0.05 are retained, raising concerns about statistical consistency and the robustness of the inferred relationships. Equally problematic is the issue of multicollinearity among descriptors, which can inflate standard errors, obscure the relative contribution of individual variables, and lead to unstable model specifications. Furthermore, even when a regression yields seemingly acceptable performance, it may still lack physical interpretability, thereby offering limited hydrological insight.
To address these limitations, in this step, different formulations were systematically tested with the aim of identifying models that satisfied both statistical and hydrological requirements. Preference was given to specifications where all predictors exhibited p-values below the 0.05 threshold, ensuring statistical consistency, and where the coefficient of determination (R^2) remained sufficiently high. At the same time, emphasis was placed on whether the selected descriptors carried clear hydrological meaning, since a statistically acceptable regression may still be of limited value if it lacks process-based interpretability. By combining these criteria, the retained models achieve a balance between robust statistical performance and meaningful physical representation.

5.3.1 Model for μ

The parameter μ provides a concise description of the mean of log-transformed normalized discharges, reflecting the typical magnitude of the non-zero flow regime. Explaining its variability across basins is crucial for regionalization, as μ embodies the hydrological signature of catchment functioning. Several regression formulations were explored, each combining different climatic, topographic, and morphometric descriptors. Although stepwise selection generated multiple statistically acceptable specifications, preference was given to models that combined strong coefficient of determination (R^2) with predictors carrying clear hydrological meaning. On this basis, the following model was identified as the most suitable, offering a balance between statistical robustness and process-based interpretability.

$$\mu = -0.738 + 1.111 \times 10^{-4}. H_{max} + 0.305. Forest + 0.165. SoilAB \qquad (5.10)$$

The coefficient signs and magnitudes are hydrologically coherent: higher maximum elevation, greater forest cover, and a larger proportion of *SoilAB* are associated with higher (less negative) μ, corresponding to more sustained relative flows. In quantitative terms, *Hmax* exerts a modest influence at landscape scales (≈ +0.011 per +100 m), likely reflecting orographic precipitation effects in regions like the Apennines. Forest cover emerges as the strongest driver, with a 0.10 increase in forest fraction raising μ by about 0.0305. *SoilAB* provides a moderate contribution, adding roughly 0.0165 for each 0.10 increase in area fraction.
In hydrological studies, μ represents the mean of the log-normal distribution fitted to a normalized flow duration curve (FDC), where normalization is performed with respect to the mean discharge. Consequently, μ does not reflect absolute flow values; rather, it describes the internal structure of a basin's flow regime, capturing the distribution of relative flows across hydrological conditions. A higher μ corresponds to a distribution shifted toward larger relative flows, indicating that the basin more consistently sustains discharges above its mean. Such behavior is often associated with catchments characterized by dense forest cover, permeable soils, or subdued topography, where infiltration dominates over rapid runoff, supporting more stable and sustained flows. In addition, higher maximum elevations can enhance precipitation through orographic effects, particularly in mountainous areas such as the Apennines, where moist air masses are forced to rise and release rainfall. This additional water input increases recharge and baseflow contributions, thereby reinforcing more sustained relative discharges.
The coefficient of determination (R^2 = 0.52) indicates that the model explains about half of the observed variance in μ across 56 sites. This represents a moderate fit—sufficient to capture regional patterns but not precise enough for site-specific prediction. Such performance is expected in large-scale applications, particularly within regions characterized by strong variability in topography, climate, and catchment morphology, where descriptor–response relationships are inherently more diffuse.
RMSE (0.114) effectively averages how much predictions deviate from observations while penalizing larger errors more heavily due to squaring. Complementing this, the mean absolute error (*MAE* = 0.088) offers a straightforward average of absolute differences, indicating that, on average, predicted μ deviates by ±0.088 from observed values. The *MAPE* is 32.81%, indicating the absolute error is about one-third of the observed μ value on average. This confirms that, although the model captures general patterns, individual site predictions may still diverge noticeably from observations. The *PBIAS* of the model is 0, indicating no systematic bias—the positive and negative errors balance out perfectly when aggregated.
Figure 5.5. Predicted versus observed μ across 56 basins. The plot shows the alignment of predicted and observed μ along the 1:1 diagonal line, with labeled basin points. The scatter indicates moderate fit, with systematic departures for very negative and moderately negative observed values.
Two systematic departures are evident. Basins with very negative observed μ (strongly intermittent regimes) tend to plot above the diagonal, meaning the model yields less negative (higher) μ than observed and thus overestimates flow persistence. By contrast, basins with moderately negative

observed μ often fall below the line, indicating more negative predictions than measurements and hence underestimation of baseflow.

Using the median absolute deviation method (δ=2), five basins—B3 (Cervaro ad Incoronata), B7 (Ofanto a Cairano), B14 (Lapilleso a Ponte S), B18 (Venosa a Ponte S. Angelo), and N25 (Tammaro a Paduli)—were identified as clear outliers in the model residuals. Interestingly, four of the five outliers (B3, B7, B14, B18) are in the Puglia region, and the fifth (N25) is in Campania. Outlier basins B3, B7, and N25 all have positive residuals, meaning the model over-predicted their μ. In plain terms, the model expected these basins to have a more sustained flow regime than they actually do. Basins B14 and B18 are the opposite—negative residuals, meaning the model under-predicted their μ (the real basins have more stable flow than the model anticipated).

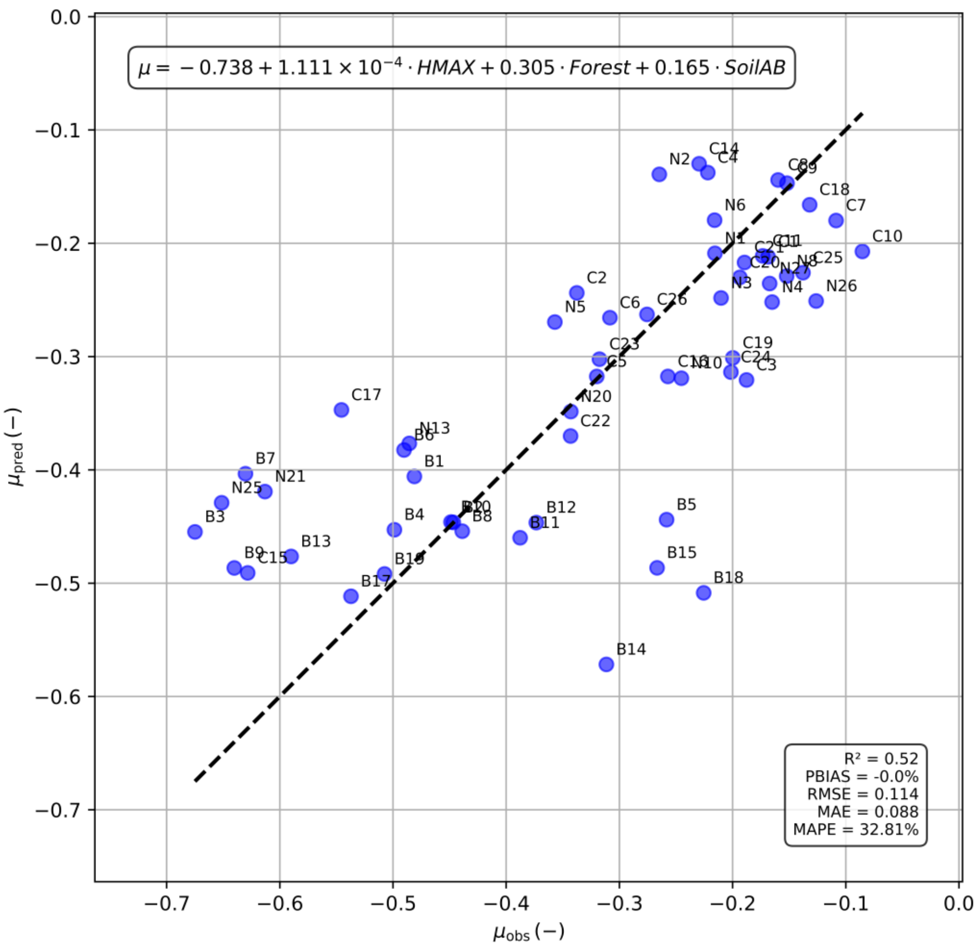

Figure 5.5: Predicted versus observed μ across 56 basins. Station codes: ***B*** *– Bari,* ***C*** *– Catanzaro,* ***N*** *– Napoli.*

Residuals were examined against each predictor (Figures 5.6.a-5.6.c). No strong systematic patterns were evident: for the bulk of basins, residuals did not increase or decrease monotonically with *HMAX*, *Forest*, or *SoilAB*. This behavior supports the adequacy of a first-order linear specification; neither pronounced curvature nor funnel-shaped spread—signatures of strong nonlinearity or heteroscedasticity—was observed. The scatter with *HMAX* (Figure 5.6.a), the distribution with *SoilAB* (Figure 5.6.b), and the residual cloud with Forest (Figure 5.6.c) all remain centered close to zero without systematic structure, confirming that model assumptions are not evidently violated.

B14 (*HMAX*: 817 m, *Forest*: 0.20, *SoilAB*: 0.08) and B18 (*HMAX*: 890 m, *Forest*: 0.085, *SoilAB*: 0.64) differ notably: both feature low relief and minimal forest cover, with B14 having an exceptionally low *SoilAB* fraction (~0.08, well below the median 0.49), suggesting poor infiltration. Nonetheless, their observed μ exceeds predictions (negative residuals of -0.26 and -0.28), implying lower-than-expected baseflow sustainment. This anomaly aligns with dynamics environment in Apulian ,rivers like the Ofanto, which exhibit semi-perennial patterns—dry summers followed by storm floods((Verri et al., 2017)). Consequently, the model, reliant solely on *Hmax*, *Forest*, and *SoilAB*, underestimates the baseflow component. It is to be noted that Iacobellis et al.(1999) also identified B18 as an outlier without elaborating on the cause.

B3, B7, and N25 have moderate-to-high *Hmax* (1109–1484 m) and large *SoilAB* fractions (0.48–0.70), with moderate *Forest* cover (~0.15–0.24). All three have lower-than-predicted μ (≈ –0.63 to –0.67).

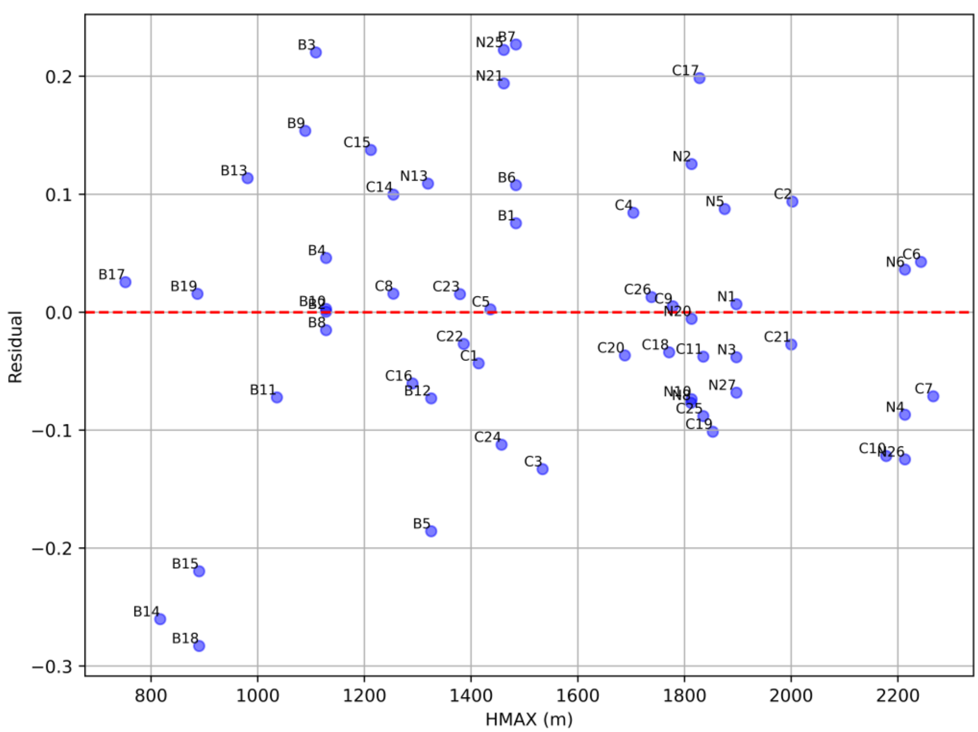

Figure 5.6.a: Residuals plotted against maximum elevation (HMAX).

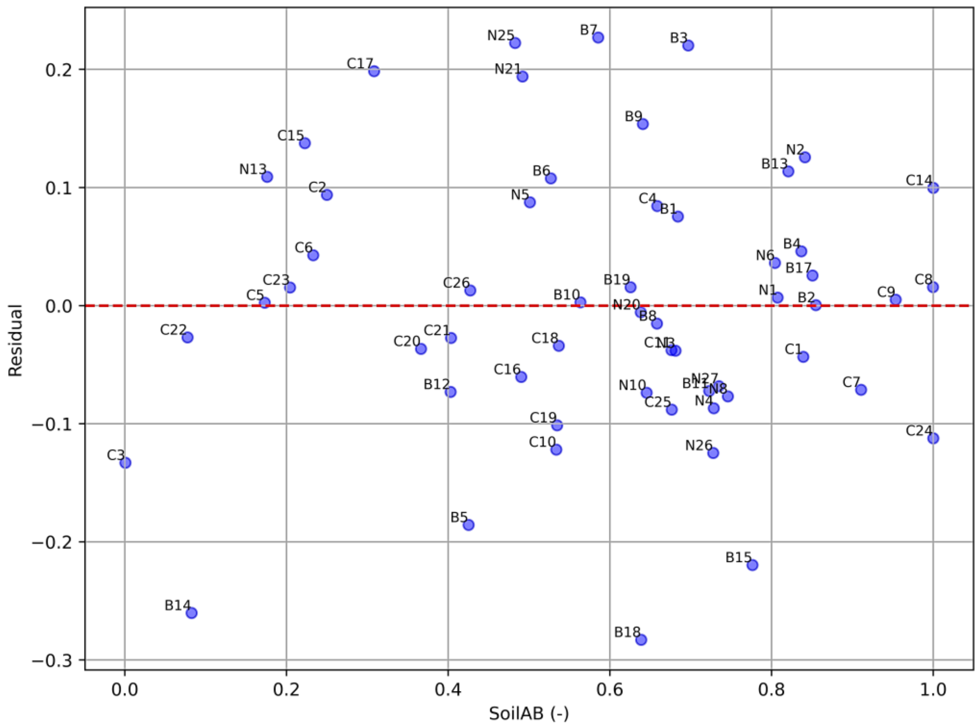

Figure 5.6.b: Residuals plotted against soil class AB fraction (SoilAB).

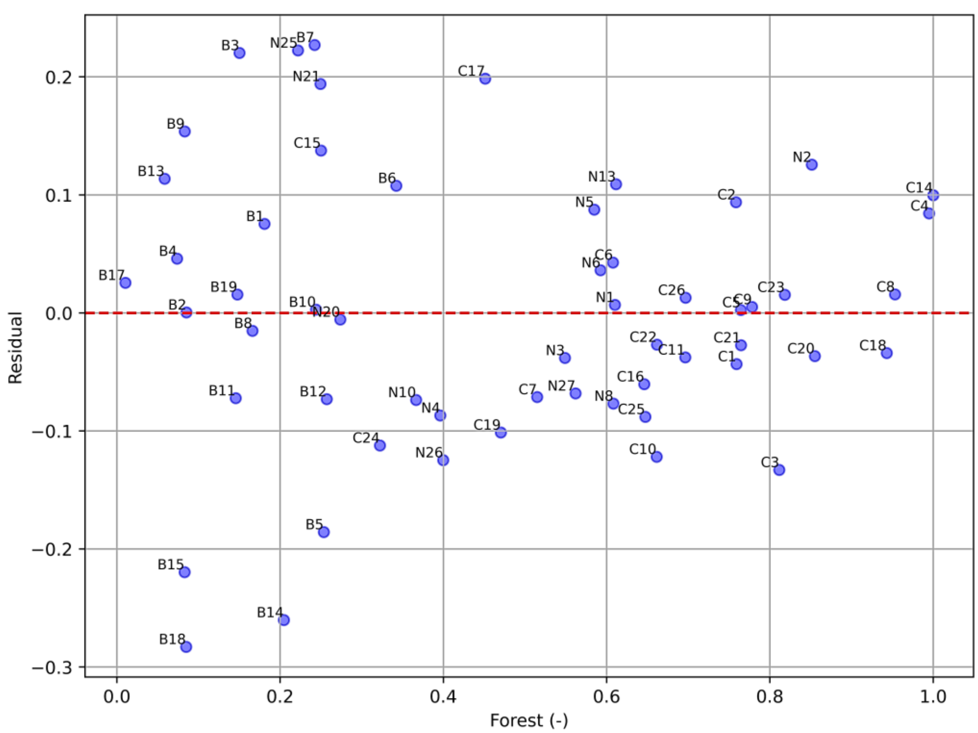

Figure 5.6.c: Residuals plotted against forest cover (Forest).

Leave-one-out cross-validation (jackknife) was applied to evaluate the model's predictive capability for the μ in ungauged basins. In each iteration, one of the 56 basins was omitted, the regression refitted on the remaining 55, and the excluded basin's μ predicted. Compared to full calibration, jackknife performance (Table 5.6) exhibited modest degradation: R^2 declined from 0.52 to 0.45, *RMSE* rose from 0.114 to 0.123 (≈8% increase), and *MAE* from 0.088 to 0.095 (≈7% increase). The increase in *MAPE* from 32.81% to 35.57% in jackknife validation reflects the model's sensitivity to the omission of individual basins, particularly those with extreme predictor values.
Notably, *PBIAS* stayed near zero (0.0% full vs. -0.17% jackknife), which is classified as very good under standard hydrological criteria that rate *PBIAS* within ±10% as excellent.

Table 5.6: Model vs. jackknife validation metrics for μ (R², RMSE, MAE, MAPE, PBIAS).

Metric	Model	Jackknife
R^2	0.52	0.45
RMSE	0.114	0.123
MAE	0.088	0.095
MAPE	32.81	35.57
PBIAS	0	0.173

Figure 5.7 shows the results of the jackknife cross-validation. The model stability is evaluated using the error metric $\Delta=|y_{jack}-y_{model}|$ between the full-model predictions (blue) and the leave-one-out predictions (red rings). The distribution of Δ is tightly concentrated near zero (median $\Delta\approx0.0035$), indicating that the regression is generally stable, yet a handful of sites exert disproportionate leverage because they occupy the extremes of the predictor space. The largest adjustment is for B14 (Δ=0.046), which lies in the joint lower tail of all three drivers—*HMAX* = 817 m (P_5), *Forest* = 0.205 (P_{25}), *SoilAB* = 0.082 (P_5)—well below the dataset's low percentile. The second largest is C14 (Δ=0.03), positioned at the opposite end for land cover and soils—Forest = 1.00 m (P_{100}) and *SoilAB* = 1.00 m (P_{100}) with *HMAX* = 1254 m (P_{25})—pushing the fit toward the upper envelope. Additionally, Moderate leverage arises at B18 ($\Delta\approx0.021$), C3 ($\Delta\approx0.021$), and B15 ($\Delta\approx0.019$); these ~0.02 jackknife shifts are not negligible, indicating localized sensitivity of the fit, though they do not overturn the overall elasticity structure. These configurations—either jointly low relief/forest/permeable soils (e.g., B14, B15) or extreme forest/soil fractions (e.g., C14) and unusual mixes (e.g., C3 with near-zero *soil AB* but high *forest*)—are hydrologically atypical and likely reflect processes (e.g., localized geology, storage, soil interactions) that a single linear specification cannot fully capture. Crucially, aside from the leverage points, 95% of sites have $\Delta \leq 0.010$, so dropping any single site barely affects predictions or the elasticity structure—underscoring the model's robustness.

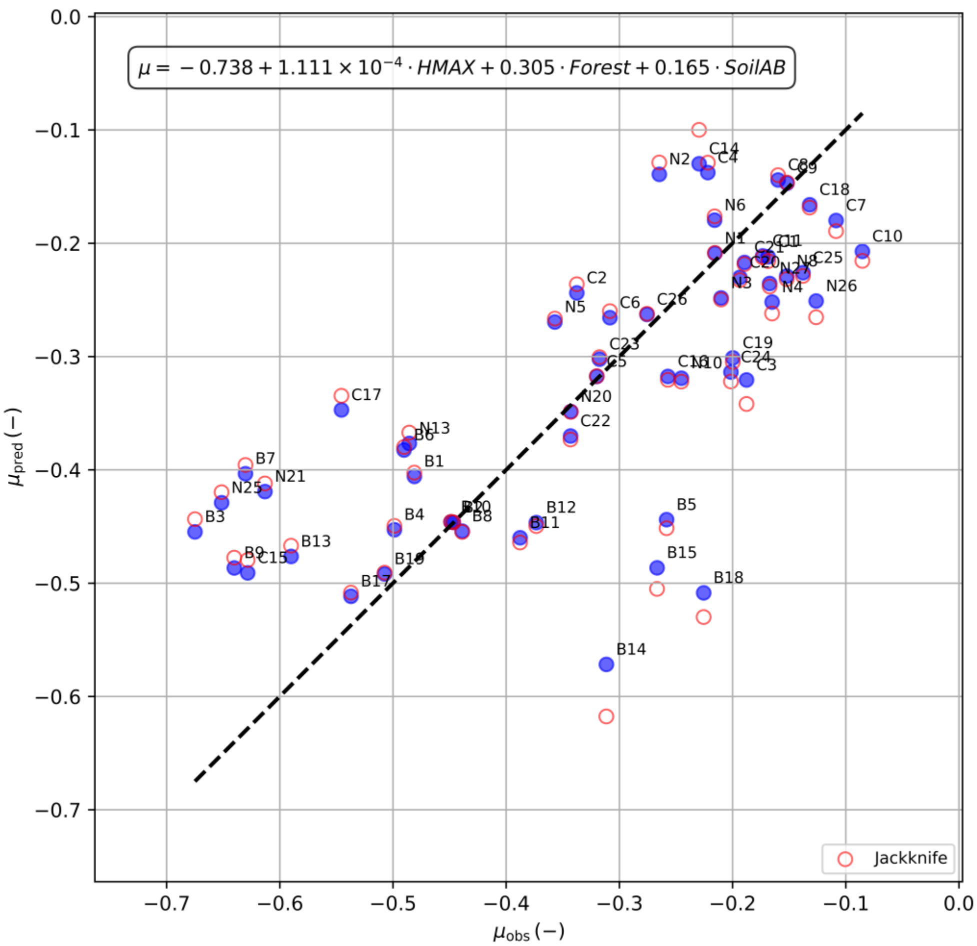

Figure 5.7: Observed versus predicted μ under jackknife validation. Station codes: ***B*** *– Bari,* ***C*** *– Catanzaro,* ***N*** *– Napoli.*

5.3.2 Model for Duration of non-zero flow (τ)

The parameter τ represents the duration of non-zero flow, describing the persistence of streamflow within the year. Several regression formulations were explored to relate τ to catchment descriptors, including both multivariate models derived from stepwise regression and simpler morphological relationships. While stepwise regression initially suggested more complex combinations, these formulations were often affected by multicollinearity among predictors and achieved lower coefficients of determination (R^2), limiting their robustness and interpretability.

In light of these considerations, the most suitable formulation was identified as a parsimonious model that relies only on two morphometric descriptors, catchment area (A) and shape factor (SF). This relationship is expressed as:

$$\tau = 0.675 A^{0.111} . SF^{0.23} \tag{5.11}$$

Most points cluster around the 1:1 line, and the performance metrics confirm a reasonable fit. The general model achieves an R^2 of about 0.72, meaning that the two simple morphological descriptors

explain roughly three quarters of the variation in flow duration across the 20 catchments (Figure 5.8). *PBIAS* is only about –1 %, indicating little systematic under-estimation. The *RMSE* (≈ 0.078) and *MAE* (≈ 0.067) are small relative to the range of τ (0.55–1), and the *MAPE* (≈ 8.8 %) suggests that predicted τ values deviate from observations by less than 10 % on average.
The estimated exponents on catchment area (A) and shape factor (SF) are both positive, reflecting that larger or more "compact" catchments tend to have more persistent flow (higher τ). Specifically, $\tau \propto A^{0.111}$ implies that doubling the catchment area increases τ by a factor of $2^{0.111} \approx 1.08$ (an 8 % increase). Similarly, $\tau \propto SF^{0.230}$ means that doubling SF increases τ by $2^{0.230} \approx 1.17$ (17 % increase). Catchment area represents the contributing surface and, by integrating rainfall over a larger space, generally supports greater storage and more persistent flow. The shape factor, instead, captures the compactness of the basin: higher *SF* values (more rounded basins) typically correspond to stronger hydraulic connectivity and simultaneous tributary inflows, which help sustain non-zero flows. In contrast, elongated basins with low *SF* are more prone to transmission losses and asynchronous runoff, making flow interruptions more likely. The scaling exponent for *SF* (0.230) thus indicates that basin shape exerts a stronger influence than size in determining the persistence of streamflow.

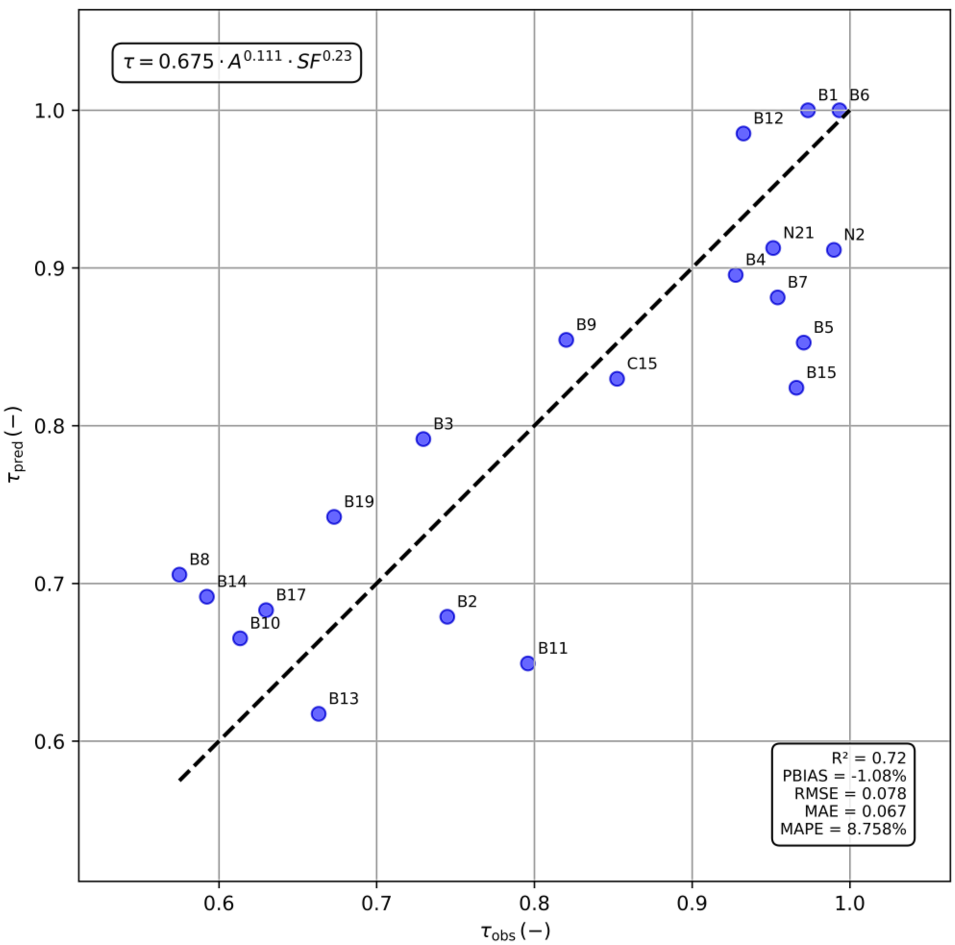

Figure 5.8: Observed versus predicted τ values. Station codes: ***B*** *– Bari,* ***C*** *– Catanzaro,* ***N*** *– Napoli.*

Visual inspection of the scatterplot (figure 5.8) suggests that several stations deviate markedly from the 1:1 line. Notably, the majority of stations originate from the Bari source, which encompasses Puglia and a part of Basilicata. In these regions, the durations of no-flow periods tend to be lower because of the underlying geological characteristics.

To move beyond subjective assessment, the residuals were analyzed using the Median Absolute Deviation (MAD) method with a $\delta = 2$. This robust procedure confirmed that stations B8 (Vulgano a Ponte Troia – Lucera) and B11 (Salsola a Casanova) constitute genuine outliers. The numerical evidence supports this classification: for B8, the observed value of τ is approximately 0.57, whereas the model predicts 0.71, yielding a residual of about 0.13; for B11, the observed τ is approximately 0.80 compared to a prediction of 0.65, producing a residual of about -0.15.

Residual plots were employed to diagnose potential model bias, with two complementary views relating prediction errors to independent variables. In the A–Residual plot (Figure 5.9.a), most points are concentrated near the zero-reference line (red dashed), indicating no evident systematic bias with respect to catchment area. Only a few stations, most notably B11 and B8, exceed the ±0.10 threshold, suggesting the presence of outliers or localized misfit. The SF–Residual plot (Figure 5.9.b) reveals an even tighter clustering of residuals around zero, with fewer pronounced deviations. Exceptions include station B8 (residual ≈ 0.13), which shows a positive residual at low SF values, and station B11 (residual ≈ -0.146), which exhibits a negative residual. These cases indicate localized discrepancies, whereas the overall distribution supports the absence of systematic bias across the full range of shape factor values.

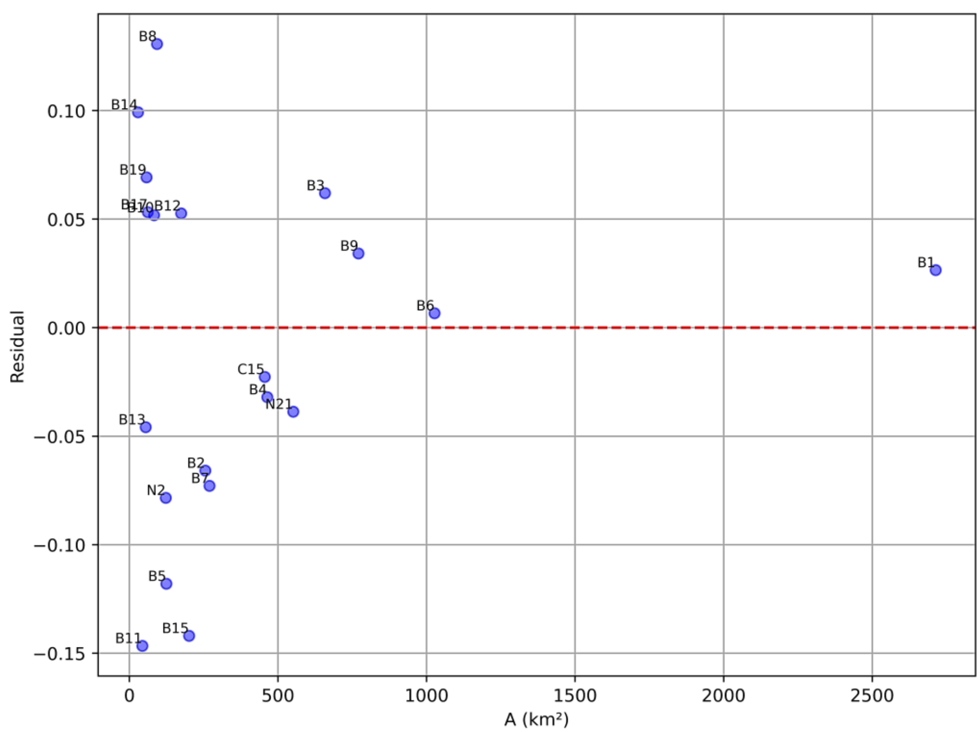

Figure 5.9.a: Residuals versus catchment area (A) for the τ regression model.

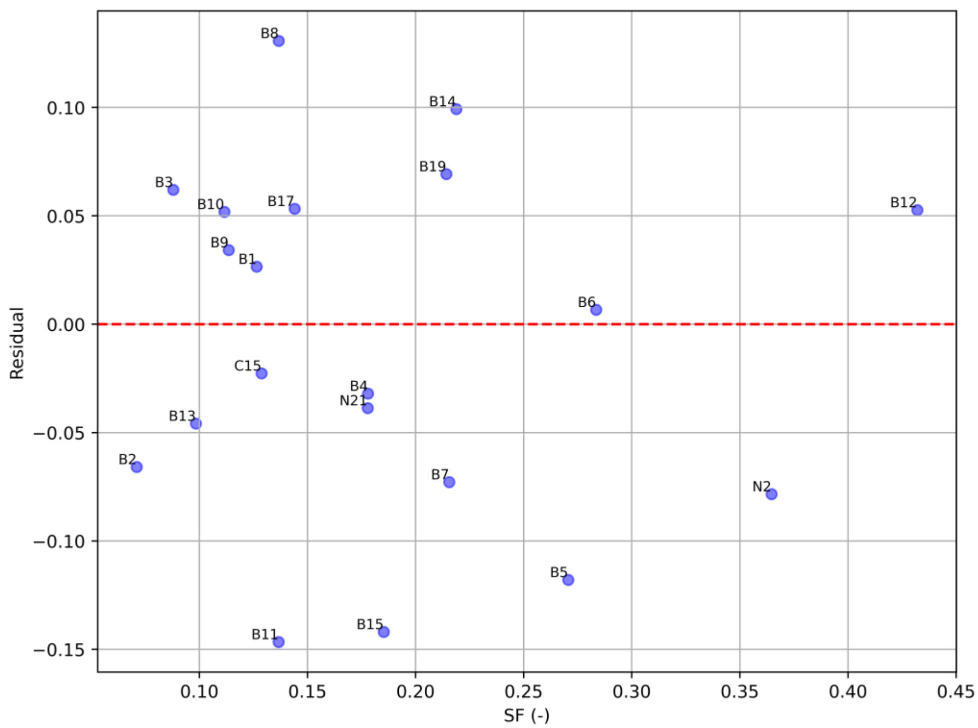

Figure 5.9.b: Residuals versus shape factor (SF) for the τ regression model.

Leave-one-out cross-validation (jackknife) was applied to assess the robustness of the regional model for the Duration of non-zero flow τ. In each iteration, one catchment was excluded, the regression recalibrated on the remaining 19, and the omitted basin predicted. Compared to the full calibration, jackknife performance showed moderate deterioration: R^2 declined from 0.72 to 0.63, *RMSE* increased from 0.078 to 0.090 (≈15 % rise), and *MAE* from 0.067 to 0.078 (≈16 % rise). Despite this reduction in accuracy, the overall predictive capability remained acceptable, indicating that the model structure captures the main controls on τ, though sensitivity to individual basins is evident (Table 5.7).

Table 5.7: Performance statistics of the τ regression model and jackknife validation.

Metric	General Regression	Jackknife (Leave-One-Out)
R^2	0.72	0.63
RMSE	0.078	0.090
MAE	0.067	0.078
MAPE (%)	8.76	10.11
PBIAS (%)	-1.08	-1.12

As Figure 5.10 shows, the jackknife analysis assesses how omitting each basin affects its predicted τ under the model $\tau = c\, A^a\, SF^b$. For basin i, influence is quantified as $\Delta_i = |y_{jack} - y_{model}|$. The distribution of Δ is tightly centered (mean ≈0.010, median ≈0.008): about 80% of basins have

$\Delta \leq 0.015$ and 90% have $\Delta \leq 0.020$, indicating that predictions for most sites remain virtually unchanged when they are omitted. A small subset exerts stronger leverage—most notably B14 (Δ=0.026; 0.6916→0.7177, +3.8%) and B11 (0.023; 0.6493→0.6263, −3.5%)—with additional but more moderate shifts for N2 (0.019; −2.0%), B2 (0.018; −2.6%), and B12 (0.015; +1.5%); only B14 and B11 exceed twice the mean Δ. The comparison plots (Fig. 5.9.a and 5.9.b) clarify why these cases are influential: B14 and B11 are among the smallest catchments (29–44 km²; ~10th percentile of A), anchoring the low-area edge; B2 has the lowest shape factor (SF = 0.071; highly elongated), while B12 (SF = 0.432) and N2 (SF = 0.365) lie toward the compact, high-SF end. Including or excluding these extremes slightly tilts the exponents a and b, but the multiplicative form $\tau = c\, A^a SF^b$ and the overall performance remain robust

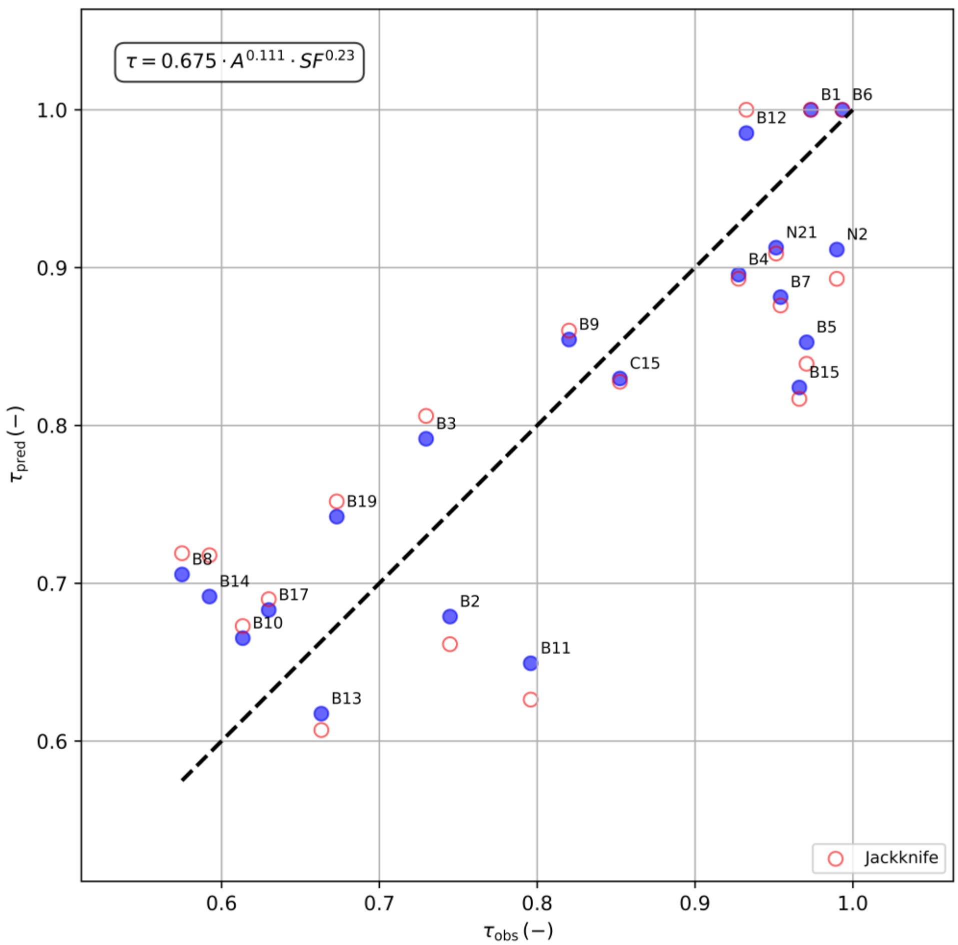

*Figure 5.10: Observed versus predicted τ values under the jackknife validation. Station codes: **B** – Bari, **C** – Catanzaro, **N** – Napoli.*

.

5.3.3 Model for Q_{nz}

The parameter Q_{nz} , representing the mean non-zero discharge, was analyzed through regional regression against climatic and morphometric descriptors. Among the different formulations tested, the most robust and physically meaningful relationship was obtained using mean annual precipitation (*MAP*) and catchment area (*A*). The resulting power-law model is expressed as:

$$Q_{nz} = 5.833 \times 10^{-9}. MAP^{2.110}. A^{0.992} \quad (5.12)$$

The estimated exponents underscore the dominant role of precipitation: the *MAP* term is approximately quadratic (exponent ≈ 2.11), whereas the drainage-area term is nearly linear (exponent ≈ 0.99). In another words, the *MAP* exponent exceeds unity, indicating a super-linear response of discharge to precipitation, whereas the exponent for *A* is close to one, reflecting a nearly linear scaling between catchment area and Q_{nz}. The observed versus predicted Q_{nz} values are shown in Figure 5.11, where points are tightly clustered around the 1:1 line, confirming strong agreement between model and data.
The model's goodness-of-fit metrics are very high. For the general fit (using all data), R^2= 0.96, meaning about 96% of the variance in observed runoff is explained by the model The *PBIAS* is only ≈+1.7%, indicating a very small systematic overestimation on average. The *RMSE* is about 4.18 (in the same units as *Q*), and the mean absolute error (*MAE*) is ~1.90. These imply that typical errors are moderate; because *RMSE* squares errors, it is more sensitive to large deviations. The mean absolute percentage error (*MAPE*) is ≈17.6%, indicating that on average the model's predictions deviate by roughly 18% from observed values.
Q_{nz} (m^3/s)

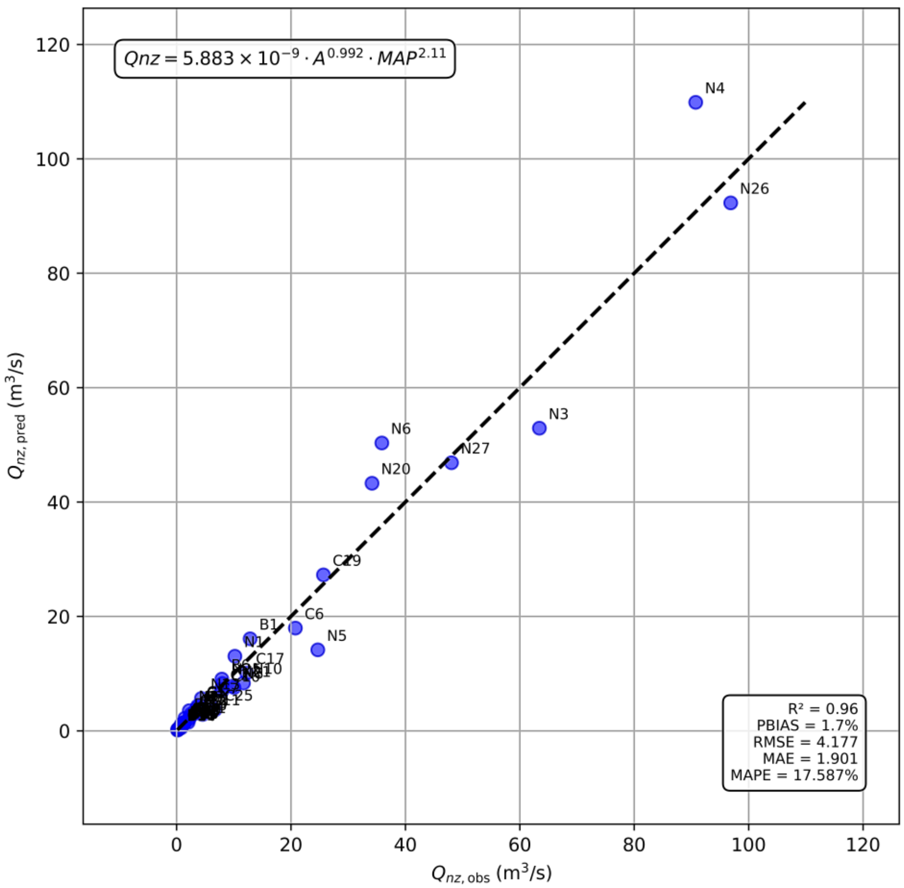

Figure 5.11: Observed versus predicted Q_{nz} values. Station codes: ***B*** *– Bari,* ***C*** *– Catanzaro,* ***N*** *– Napoli.*

Model performance was assessed using relative residuals, defined as (Predicted – Observed)/Observed. This metric was selected because the regression is based on dimensional predictors—mean annual precipitation (*MAP,* mm) and catchment area (*A*, km²)—whose values span wide and heterogeneous ranges across the study basins. When such dimensional variables are employed, absolute residuals can mask systematic deviations by disproportionately reflecting the scale of the predictors. By contrast, relative residuals provide a scale-independent measure of error, allowing deviations to be evaluated consistently and compared meaningfully across catchments that differ greatly in both climatic and geomorphic conditions.

In the plot of residuals against *MAP* (Figure 5.12a), most stations are distributed close to the zero line, showing no overall bias. A number of basins, however, stand out as outliers. Stations N2 (*MAP* ≈ 1512 mm) and B4 (*MAP* ≈ 645 mm) exhibit large positive residuals, indicating relative overprediction. By contrast, stations C25 (*MAP* ≈ 1056 mm) and N5 (*MAP* ≈ 1320 mm) show large negative residuals, marking relative underprediction. These points define the tails of the distribution, while the majority of catchments remain within a narrow band around zero.

A similar distribution is observed in the residuals plotted against catchment area (Figure 5.12b). Most basins are centered close to the reference line, but the spread of residuals increases with catchment size. Here again, N2 (*A* ≈ 122 km²) and B4 (*A* ≈ 464 km²) appear as positive outliers, while C25 (*A* ≈ 275 km²) and N5 (*A* ≈ 661 km²) emerge as negative outliers. These cases represent the most evident deviations, whereas the rest of the dataset remains more compactly distributed around zero.

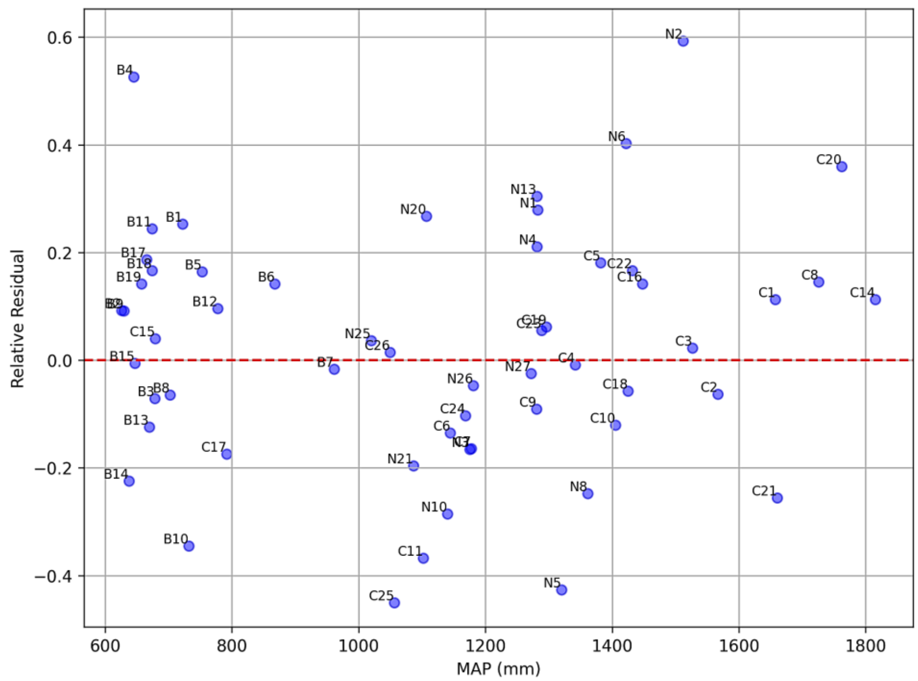

Figure 5.12.a: Relative residuals versus MAP for the Q_{nz} model.

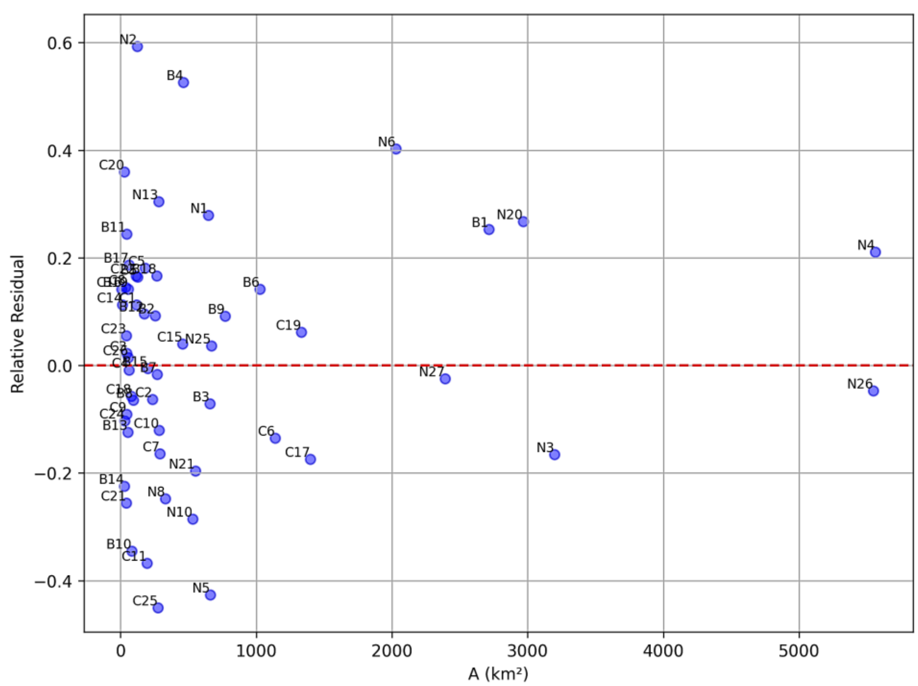

Figure 5.12.b: : Relative residuals versus catchment area (A) for the Q_{nz} model.

The leave-one-out approach estimates the model's bias, variance, and predictive stability without the need for a holdout set. In regression settings, it is used to detect influential points and diagnose overfitting by comparing predictions from the full model with those obtained from the jackknife refits. In this case, the jackknife validation (Table 5.8) shows a slight deterioration in performance: R^2 decreases to 0.95, *RMSE* increases to 4.575, *MAE* to 2.043, *MAPE* to 18.62%, and *PBIAS* to 2.26%. These shifts reflect the slight decline in accuracy under cross-validation, as each refit is based on reduced training data.

Table 5.8: Model vs. jackknife validation metrics for Qnz.

Metric	Model	Jackknife
R^2	0.96	0.95
RMSE	4.177	4.575
MAE	1.901	2.043
MAPE (%)	17.59	18.62
PBIAS (%)	1.70	2.26

To quantify the impact of single-point omission, Δ is defined as $|y_{modeli} - y_{jack,i}|$ that is, the absolute difference between the predicted value from the full model y_{modeli} and the jackknife predicted value from the refitted model excluding station $y_{jack,i}$. This metric captures how much the omission of a station perturbs its own prediction, serving as a proxy for influence or leverage. Across the dataset, the mean delta is approximately 0.141, with a median of 0.020, indicating that most omissions induce only minor shifts—half of them below 0.02 units—thus pointing to overall data homogeneity and model stability. The distribution, however, is skewed: a few stations exhibit large Δ values, highlighting their disproportionate influence on the fitted exponents and on prediction consistency, typically due to extreme values in *A*, or *MAP*. The strongest effects are concentrated in the *N*-series stations, generally representing larger basins with higher variability. N4 shows the maximum Δ=2.55, where the prediction of 109.88 increases to 112.43 under jackknife refitting, vast (*A*=5562.6 km²), and *MAP* of 1281 mm make it a high-leverage site, pulling the precipitation exponent upward and inflating predictions when retained. N6 follows with Δ=1.39 (50.32 → 51.71), reflecting sensitivity in mid-sized basins with high precipitation (*MAP* = 1422 mm). N3 shows Δ=0.78 (52.90 → 52.13), tied to its large area (3198.9 km²) and elevated (*MAP* =1300), again illustrating how omission of wet, large basins dampens the model's ability to reproduce high-end flow variability. Further cases include N20 (Δ=0.77) and N26 (Δ = 0.50), which similarly exhibit leverage due to large basins. Generally, these differences highlight how influential points (often stations with extreme size or climatic conditions) can distort regression estimates. The jackknife scatterplot (Figure 5.13) shows that while most points align closely to the 1:1 line, these high-leverage stations introduce visible perturbations, confirming the statistical sensitivity of the model to such extremes.

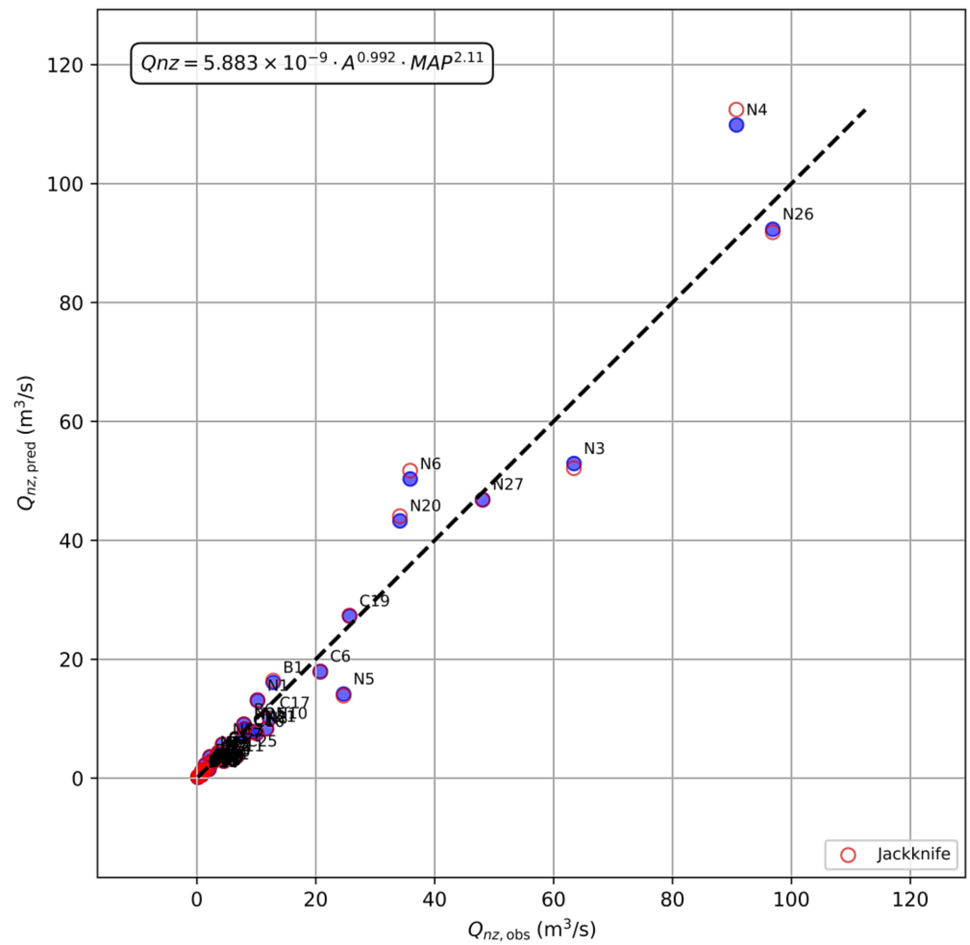

*Figure 5.13: Observed versus predicted τ values under the jackknife validation. Station codes: **B** – Bari, **C** – Catanzaro, **N** – Napoli.*

5.4 Sensitivity Analysis to Record Length

Hydrological regionalization seeks to predict flow statistics at ungauged sites by relating observed flow characteristics at gauged basins to their physical and climatic attributes. An implicit assumption in such models is that the target statistics computed from existing gauges are representative of the long-term behaviour of the basins. The reliability of these target statistics depends critically on the length of the underlying streamflow records. Short records may miss extreme wet or dry periods, leading to biased flow duration curves (FDCs), unstable regression coefficients and misleading inferences. Conversely, long records smooth out stochastic variability and better capture climate cycles, but they restrict the number of available stations, particularly in small or poorly monitored basins. This study therefore begins by examining how the record length threshold affects the performance of regional models for three flow metrics: the log normal mean (μ) of the dimensionless flow duration curve, the mean non zero discharge (Q_{nz}) and the duration of non-zero flow (τ).

To evaluate the sensitivity of regionalization outcomes to observational extent, the workflow was conducted under three record-length scenarios: a reference case of ≥15 years, and two truncated alternatives of ≥10 years and ≥5 years of continuous observations. All other steps were kept constant, ensuring that differences across the three scenarios reflect only the effect of record length. Model skill in each scenario is evaluated using standard statistical metrics, including the coefficient of determination (R^2), Root Mean Square Error (*RMSE*), Mean Absolute Error (*MAE*), and Mean Absolute Percentage Error (*MAPE*). Beyond overall fit, the analysis examines the stability of regression coefficients in terms of both sign and magnitude, the dispersion of residuals, and the incidence of influential or outlier stations. The objective is to identify the shortest defensible record length that preserves decision-relevant predictive accuracy while minimizing systematic bias and parameter instability.

5.4.1 The μ Model

The regional regression for μ, calculated on the longest and most reliable records (≥15 years, N=56), provides the *Eq.* (5.11). At this threshold, all predictors remain positive and hydrologically consistent. Model performance is strongest (R^2=0.52, *RMSE* = 0.114, *MAE* = 0.088, *MAPE* = 32.8%), and both the scatterplot (Figure 5.14.a) and the performance metrics in Table 5.9 confirm this stability. Most points lie close to the 1:1 line, residuals are balanced, and errors are comparatively low, underlining the robustness of the ≥15-year calibration.

When the threshold is relaxed to include 10–15-year records ($N=74$), coefficients evolve in a coherent way but with reduced stability. The slope for maximum elevation decreases by ~27%, while the effect of *soil AB* strengthens slightly. As shown in Table 5.9, *RMSE* and *MAE* reach their lowest values, yet *MAPE* increases by ~3 percentage points. The scatterplot (Figure 5.14.b) illustrates this: most of the additional stations (red squares) align reasonably with the regression, but some increase dispersion. For example, B20 is under-predicted and C13 over-predicted, deviations that visibly disrupt the otherwise compact point cloud. This explains why error statistics show mixed behavior—absolute errors improve slightly, while relative errors worsen due to the variability introduced by shorter records.

At the most permissive threshold (≥5 years, $N=89$), reliability declines further. The forest coefficient weakens by ~11.5% relative to the baseline, while other slopes remain broadly similar. Performance metrics in Table 5.9 show a sharp deterioration: R^2 drops to 0.45, *RMSE* rises to 0.118, *MAE* to 0.092, and *MAPE* to 38.4%. The scatterplot (Figure 5.14.c) reflects this instability: shorter records (yellow triangles) scatter widely around the 1:1 line, with strong over-prediction at stations such as N41 and N43, and clear under-prediction at B20, N42, C41, and N45. Although a fraction of shorter records follows the regression well, the overall dispersion is much larger than in the baseline case, inflating residuals and reducing explanatory power.

Table 5.9: Performance metrics of the linear regression models for μ under different minimum record-length thresholds (≥5, ≥10, and ≥15 years).

Years Filter	*N*	REGRESSION FORMULA	*R²*	*RMSE*	*MAE*	*MAPE* (%)
≥ 5 Years	89	$\mu = -0.712 + 0.00011 \cdot HMAX + 0.270 \cdot Forest + 0.163 \cdot SoilAB$	0.45	0.118	0.092	38.36
≥ 10 Years	74	$\mu = -0.699 + 0.00008 \cdot HMAX + 0.308 \cdot Forest + 0.177 \cdot SoilAB$	0.51	0.111	0.088	35.49
≥ 15 Years	56	$\mu = -0.738 + 0.00011 \cdot HMAX + 0.305 \cdot Forest + 0.165 \cdot SoilAB$	0.52	0.114	0.088	32.81

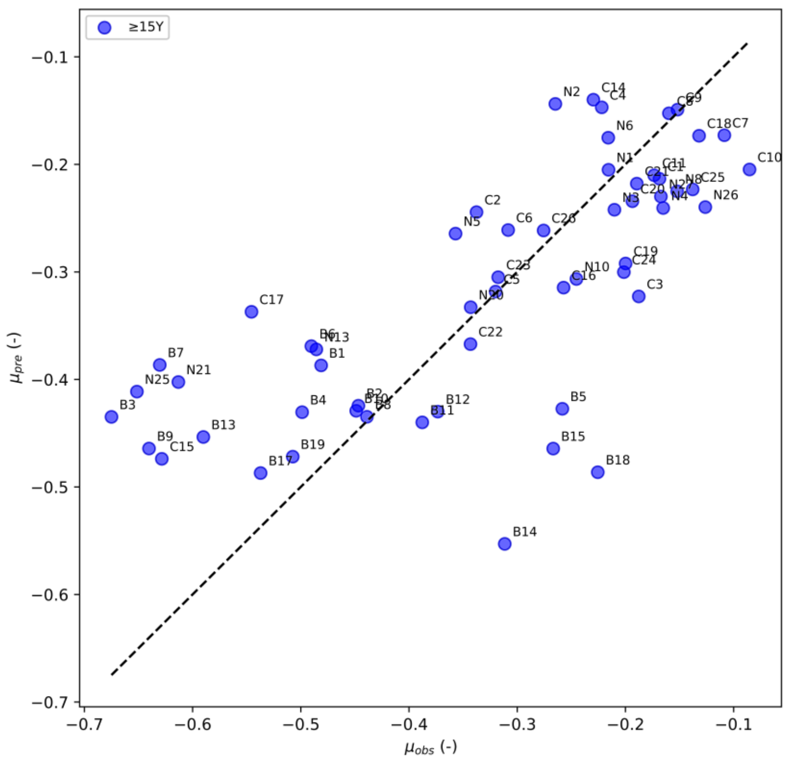

Figure 5.14.a: Observed vs predicted values of μ for for three record-length thresholds (≥15 years).

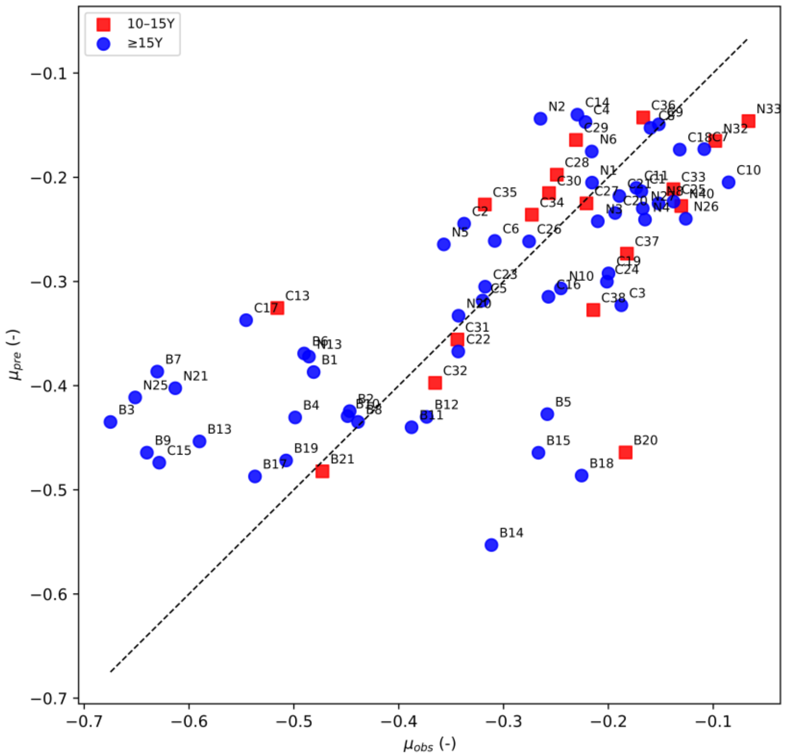

Figure 5.14.b: Observed vs predicted values of μ for for three record-length thresholds (≥10 years).

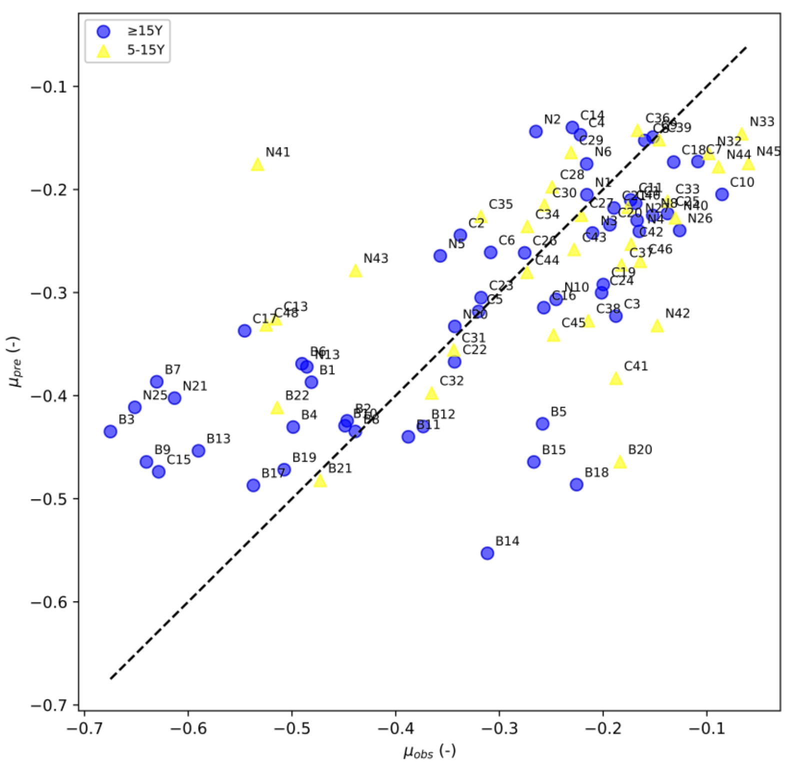

Figure 5.14.c: Observed vs predicted values of μ for for three record-length thresholds (≥5 years).

5.4.2 The τ Model

Re-estimating the regional power-law model $\tau = c\,A^a\,SF^b$ under progressively relaxed minimum record lengths (≥10, ≥5 years) highlights the decisive role of data series length in controlling model stability and explanatory power (Table 5.10). The strongest performance emerges when only the longest and most reliable records are retained (≥15 y*; N=20*). In this case, the regression explains 72% of the variance with markedly low errors (*RMSE/MAE* = 0.078/0.067; *MAPE* = 8.75%). The fitted coefficients are hydrologically coherent, with a=0.111and b=0.230; the relative weighting of b/a≈2.1confirms that planform compactness is roughly twice as influential as catchment area in sustaining non-zero flows. The diagnostic plot in Figure 5.15.a illustrates this robustness: blue circles cluster nearly around the 1:1 line.
When the threshold is lowered to include records of 10–15 years (N=26), model strength remains acceptable but visibly weaker. Explanatory power declines to R^2=0.57, with errors increasing modestly (*RMSE/MAE* = 0.092/0.078; *MAPE* = 10.44%). The coefficients evolve consistently, with a=0.106 and b=0.228, maintaining a physically plausible ratio b/a≈2.2. The scatterplot in Figure 5.15.b reflects this intermediate stability: compared to the compact distribution in Figure 5.15, the addition of the 10–15-year records (red squares) introduces a broader spread, particularly through a few stations that deviate systematically from the 1:1 line. For example, C28 and C35 lie noticeably below the identity line, indicating consistent under-prediction of their observed τ, while B21 falls slightly above the line, suggesting a modest over-prediction. These deviations, though moderate, explain the deterioration in fit reported in Table 5.10 and show that temporal truncation begins to weaken the signal.
The weakest performance appears when short records down to 5 years are admitted (*N=29*). Here, the model explains only half of the variance (R^2=0.50), and errors increase (*RMSE/MAE* = 0.095/0.082; *MAPE* = 10.75%). Coefficients remain hydrologically consistent (a=0.084, b=0.204), but the precision of their estimates diminish. The diagnostic plot in Figure 5.15.c confirms this: adding the 5–15 y sites (yellow triangles) produce the widest and most anisotropic scatter. Outliers such as C30 and B22 lie well above the 1:1 line (systematic over-prediction), while C28, C35, and N41 fall below (under-prediction). The broad spread of points corresponds directly to the weaker statistics in Table 5.10, demonstrating that short records inject noise into the calibration rather than revealing a structural weakness in the power-law form.

Table 5.10: Performance of the τ model under three record-length thresholds (≥15, ≥10, ≥5 years).

Record Length Threshold	*N*	Regression Formula	R^2	*RMSE*	*MAE*	*MAPE (%)*
Years ≥ 5	29	$0.7505 \cdot A^{0.084} \cdot SF^{0.204}$	0.5	0.095	0.082	10.75
Years ≥ 10	26	$0.6985 \cdot A^{0.106} \cdot SF^{0.228}$	0.57	0.092	0.078	10.44
Years ≥ 15	20	$0.675 \cdot A^{0.111} \cdot SF^{0.230}$	0.72	0.078	0.067	8.75

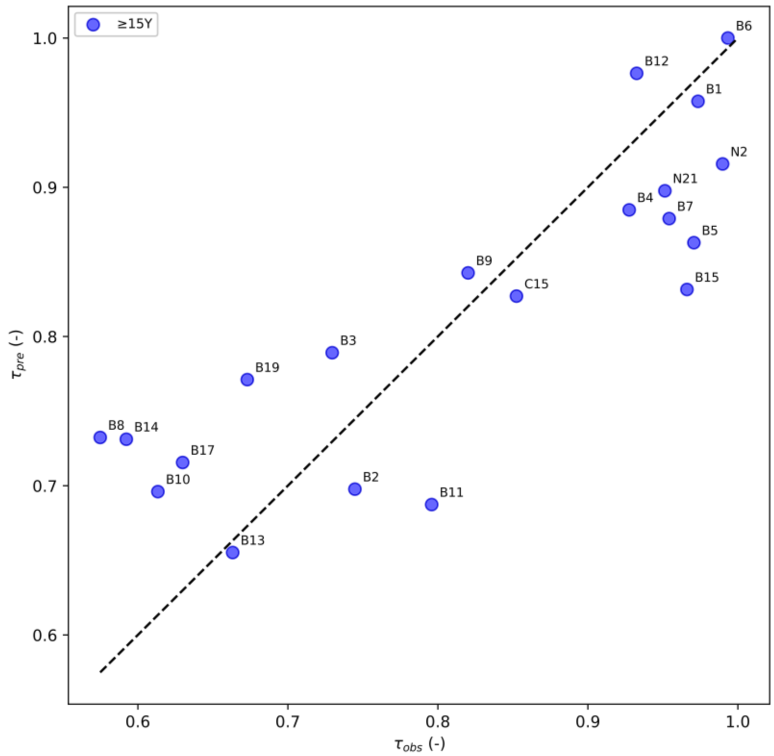

Figure 5.15.a: Observed versus predicted values of τ for three record-length thresholds (≥15 years).

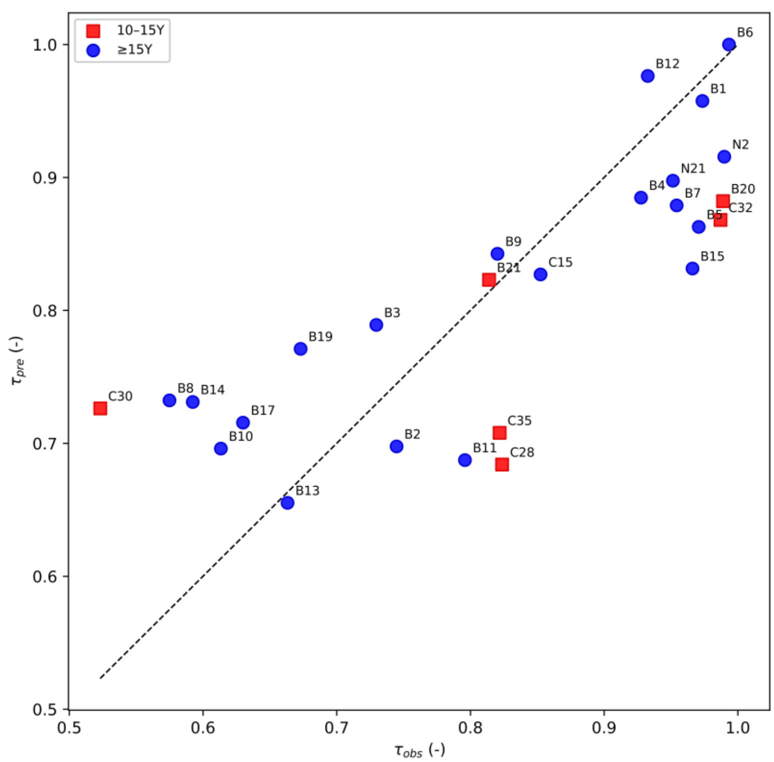

Figure 5.15.b: Observed versus predicted values of τ for three record-length thresholds (≥10 years).

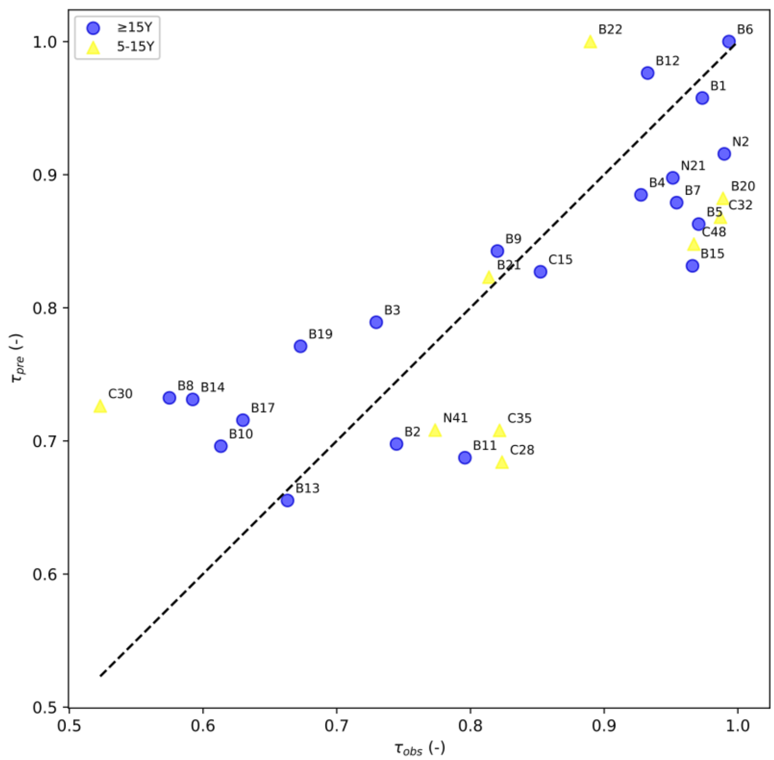

Figure 5.15.c: Observed versus predicted values of τ for three record-length thresholds (≥5 years).

5.4.3 The Q_{nz} Model

Across record-length thresholds, the model form remains consistent, but proportional accuracy declines as shorter records are incorporated (Table 5.11). With ≥15-year records (N = 56), the model shows the most balanced behavior: precipitation exponent ($b \approx 2.11$) and area exponent ($a \approx 0.99$) align with hydrological expectations, and the scatterplot in Figure 5.16.a shows blue points tightly clustered around the 1:1 line. Error metrics are correspondingly favorable ($RMSE$ = 4.177; MAE = 1.901; $MAPE$ = 17.6%).

Lowering the threshold to ≥10 years (N = 74) leaves the coefficients largely unchanged and slightly reduces absolute errors ($RMSE$ = 3.710; MAE = 1.699). However, $MAPE$ increases to 21.1% (Table 5.11). This apparent inconsistency reflects the differing sensitivities of the error metrics: most of the newly added basins belong to the lower-Q_{nz} domain ($Q_{nz} < 20$), where residuals are small in absolute terms (≈1 m³/s) and thus depress $RMSE$ and MAE, but appear large when expressed as a proportion of observed discharge ($MAPE$). In addition, station N40, with a residual of 3 m³/s in the upper domain, introduces a downward deviation in the scatterplot (Figure 5.16.b) that further inflates relative error.

Expanding to 5–10-year records (N = *89*) alter the calibration more markedly, amplifying rainfall elasticity ($b \approx 2.20$) while slightly reducing the area effect ($a \approx 0.97$). Again, most of the additional points cluster in the lower range of the scatterplot, reinforcing the increase in proportional error despite stable absolute errors. Figure 5.16.c illustrates the leverage of N42, which falls well below the 1:1 line with a residual of 10 m³/s, exerting a visible pull on the fit. In this case, *MAE* remains essentially unchanged (1.699), but *MAPE* escalates to 22.7% (Table 5.11), The rise in *MAPE* is not due to a general worsening of predictions across all basins, it is mainly driven by the leverage of a small number of anomalous stations with atypical behavior and large residuals, which distort proportional accuracy metrics.

Overall, Table 5.11 and Figure 5.16(a,b,c) show that R^2 remains high (~0.96) across all thresholds, but including shorter records systematically changes the regression coefficients and increases relative error. This demonstrates a trade-off: adding stations with short-period data expands coverage yet reduces the reliability of predictions in proportional terms.

Table 5.11: Performance of the Q_{nz} model under three record-length thresholds (≥15, ≥10, ≥5 years).

Record Length Threshold	*N*	Regression Formula	R^2	*RMSE*	*MAE*	*MAPE (%)*
Years ≥ 5	89	$3.4\times10^{-9}\cdot MAP^{2.199}\cdot A^{0.973}$	0.96	3.423	1.699	22.74
Years ≥ 10	74	$3.6\times10^{-9}\cdot MAP^{2.176}\cdot A^{0.995}$	0.96	3.710	1.699	21.12
Years ≥ 15	56	$5.9\times10^{-9}\cdot MAP^{2.110}\cdot A^{0.992}$	0.96	4.177	1.901	17.59

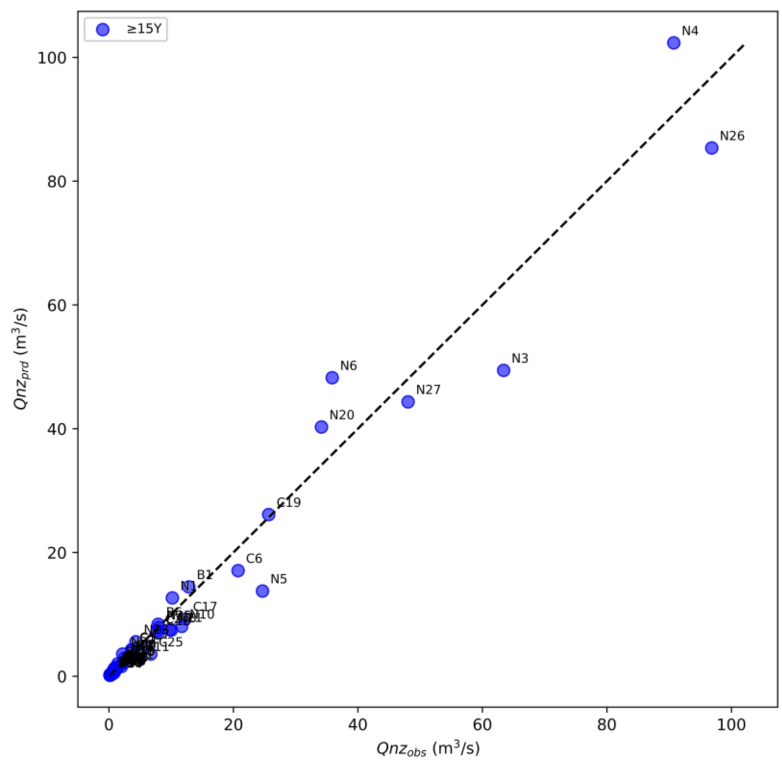

Figure 5.16.a: Observed vs predicted Q_{nz} for three record-length thresholds (≥15 years).

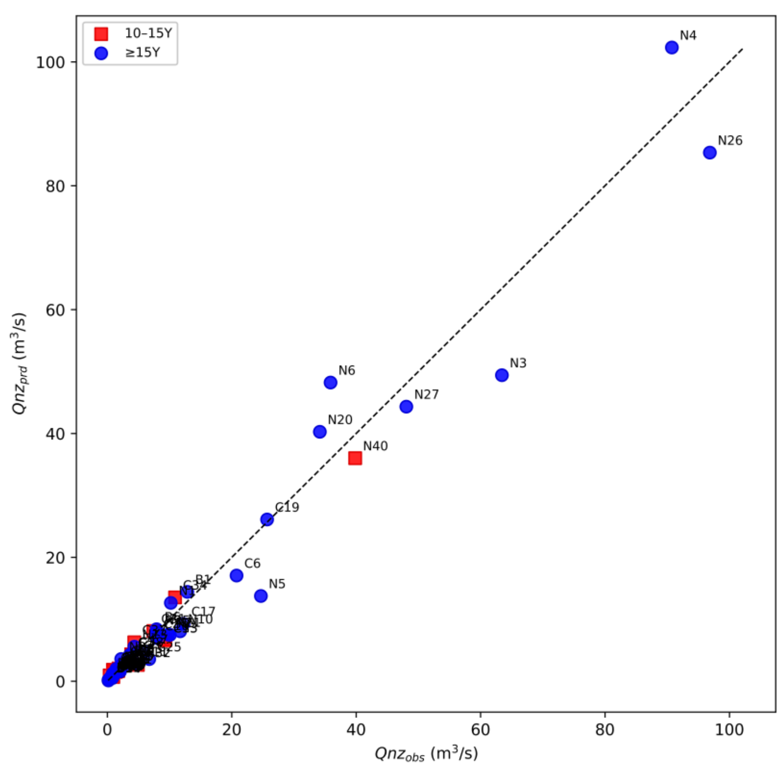

Figure 5.16.b: Observed vs predicted Q_{nz} for three record-length thresholds (≥10 years).

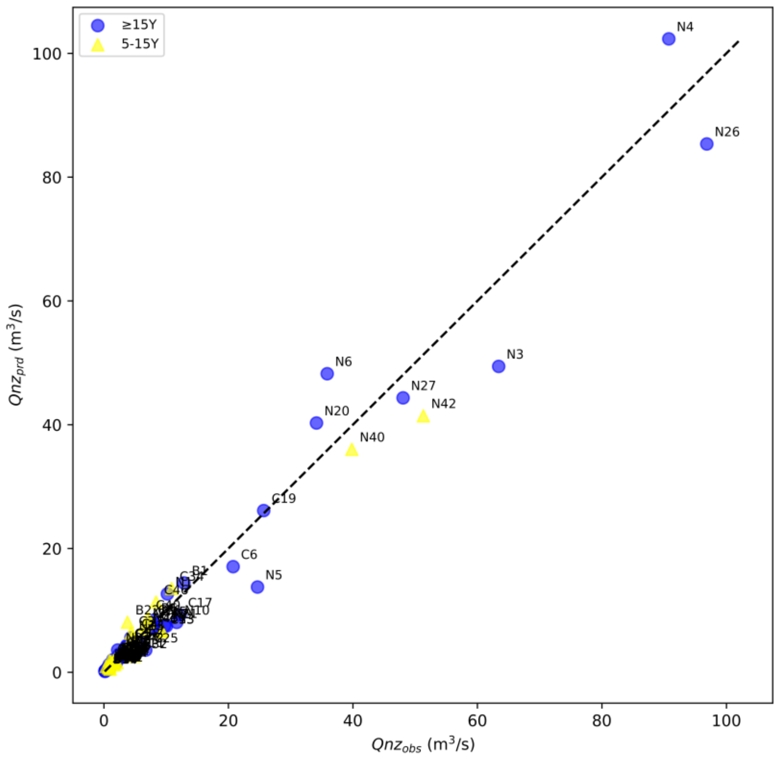

Figure 5.16: Observed vs predicted Q_{nz} for three record-length thresholds (≥5 years).

5.5 Base Flow Index (*BFI*) Analysis

Although the main objective of this study is the regionalization of Flow Duration Curves (FDCs), the Baseflow Index (*BFI*) was also included as a complementary component of the analysis. The rationale for this integration lies in the hydrological relationship between the two descriptors. The FDC provides a continuous representation of the entire flow regime, from high flows to extreme low flows, whereas the *BFI* condenses information specifically related to the contribution of groundwater and sustained baseflow. In this sense, *BFI* can be viewed as a scalar index that summarizes the behavior of the lower tail of the FDC.

5.5.1 Correlation Analysis between *BFI* and Catchment Descriptors

Pearson correlations between *BFI* and basin descriptors point to climate and vegetation as the dominant controls (Figure 5.17). The strongest positive relationships are with mean annual precipitation (*MAP*, $R = 0.65$) and *forest* cover ($R = 0.64$), consistent with higher infiltration and groundwater recharge sustaining baseflow. Relief variables are also positive—*SMEAN* ($R = 0.57$), *HMEAN* ($R = 0.53$), and *HMAX* ($R = 0.42$)—indicating that mountainous basins tend to maintain baseflow, likely due to orographic precipitation and extensive forest cover. The positive slope signal, which runs counter to the common expectation of flashier steep basins, likely reflects co-variation with *MAP* and elevation in this dataset.
Soil descriptors are weaker but generally positive: *SoilABC* ($R = 0.43$) is the largest, followed by *SoilBC* (0.22), *SoilA* (0.20), and *SoilAB* (0.17); *SoilB* (0.05) and *SoilC* (0.12) are negligible.

Catchment geometry shows little linear signal: *A* ($R = -0.03$) and *CR* (0.04) are near zero, while *SF* (0.20) is marginal.

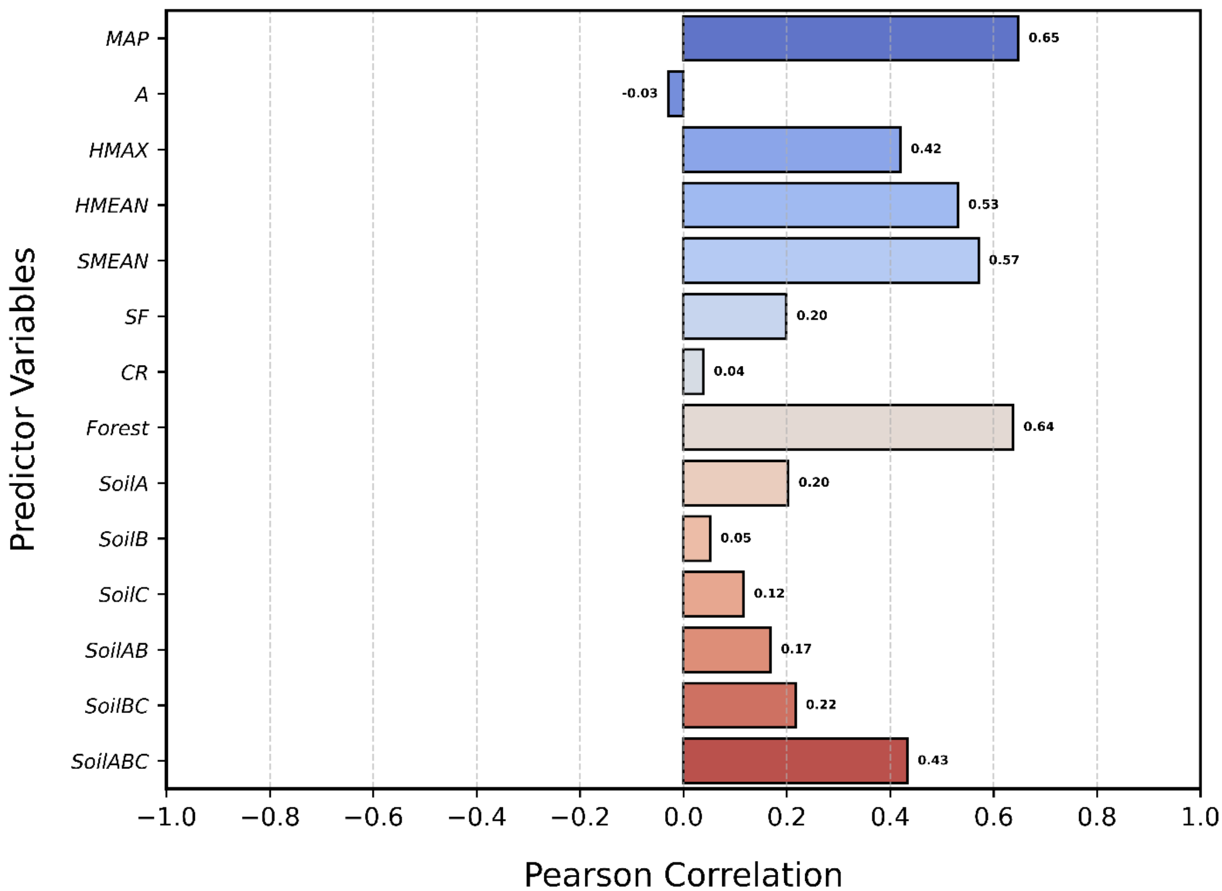

Figure 5.17: Pearson correlations between Baseflow Index (BFI) and candidate predictors.

5.5.2 Analysis of Stepwise Regression Models for *BFI*

The first, richer specification (Table 5.12) explains a large share of the variance ($R^2 = 0.74$; $R^2_{adj} = 0.70$) and attains the lowest *AIC* (−132.9). Within it, mean annual precipitation (*MAP*, 0.0547) and mean elevation (*HMEAN*, 0.0736) emerge as the strongest and highly significant predictors ($p < 0.05$). Slope (*SMEAN*, 0.0456), *SoilAB* (0.0187) and *SoilABC* (0.0255) also contribute significantly, though with smaller effects.Forest (−0.0626, $p = 0.054$), drainage area (*A*, 0.0203, $p = 0.057$) and *SoilC* (−0.0022, $p = 0.752$) are not significant. This pattern suggests the high fit partly reflects the inclusion of weak or redundant predictors—improving *AIC* but not necessarily robustness. The second, pared-down model retains only *MAP* (0.0598), *HMEAN* (0.0498) and *SoilAB* (0.023), all significant ($p < 0.05$). Although it explains slightly less variance ($R^2 = 0.67$; $R^2_{adj} = 0.65$), it achieves the lowest *BIC* (−118.7) and offers a more efficient balance between explanatory power and parsimony.

Table 5.12: Stepwise linear regression models for BFI in raw space.

Variable	Coefficient	P-value	R^2	R^2_{adj}	*AIC*	*BIC*
const	−0.0316	0.679	0.74	0.70	−132.9	—
MAP	0.0547	0.018				
HMEAN	0.0736	<0.001				
SoilAB	0.0187	0.005				
SMEAN	0.0456	0.022				
Forest	−0.0626	0.054				
SoilABC	0.0255	0.005				
A	0.0203	0.057				
SoilC	−0.0022	0.752				
const	0.1688	<0.001	0.67	0.65	—	−118.7
MAP	0.0598	<0.001				
HMEAN	0.0498	0.001				
SoilAB	0.023	0.027				

The log-space stepwise regression (Table 5.13) first yields a specification explaining 68% of the variance in *BFI* ($R^2 = 0.68$; $R^2_{adj} = 0.66$; $AIC = -49.38$). In this model, mean elevation (*HMEAN*, 0.137; $p < 0.001$) is the dominant control, and *SoilABC* (0.0611; $p = 0.010$) is also significant, highlighting the roles of catchment altitude and mixed soil permeability in sustaining low flows. By contrast, mean annual precipitation (*MAP*, 0.0656; $p = 0.054$) is only marginal, and drainage area (*A,* 0.0334; $p = 0.143$) is not significant. The coexistence of significant and non-significant terms, despite the good fit, signals a less stable formulation for regional use.

The streamlined alternative (Table 5.13) reduces complexity with only a small decrease in fit ($R^2 = 0.66$; $R^2_{adj} = 0.64$) and attains the lowest *BIC* (−40.90). *HMEAN* remains the strongest, highly significant descriptor (0.1181; $p < 0.001$), while *MAP* becomes clearly significant (0.0796; $p = 0.017$), and *SoilABC* stays significant (0.0503; $p = 0.027$). This parsimony—retaining only consistently informative predictors—improves statistical efficiency and interpretability, making the second specification the preferable choice for robust regionalization.

Table 5.13: Stepwise regression models for BFI in log-transformed space.

Variable	Coefficient	*P*-value	R^2	R^2_{adj}	*AIC*	*BIC*
const	−4.2787	<0.001	0.68	0.66	−49.38	—
MAP	0.0656	0.054				
HMEAN	0.137	<0.001				
SoilABC	0.0611	0.01				
A	0.0334	0.143				
const	−4.1614	<0.001	0.66	0.64	—	−40.90
MAP	0.0796	0.017				
HMEAN	0.1181	<0.001				
SoilABC	0.0503	0.027				

In this phase, the analysis centers on the Base Flow Index (*BFI*), a scalar indicator that expresses the relative contribution of groundwater to total streamflow. As a key descriptor in regionalization frameworks, *BFI* provides insight into the capacity of catchments to sustain flow during dry periods. Results from Pearson correlation and stepwise regression analyses reveal that *SoilABC*, mean annual precipitation (*MAP*), mean slope (*SMEAN*), and forest cover represent the most suitable catchment descriptors for explaining the spatial variability of *BFI*. At this stage, different combinations of input parameters were tested to obtain valid models that aligned with hydrological knowledge.

5.5.2 Regional Model for *BFI*

The regional model for the Base Flow Index (*BFI*) in southern Italy is a two-factor power law (Fig. 5.18):

$$BFI=0.676\ SoilABC^{0.298}\ Forest^{0.185} \tag{5.13}$$

The two predictors summarize land-surface controls on baseflow: the *SoilABC* fraction captures catchment-average permeability (infiltration/recharge potential), while Forest proxies vegetation effects promote infiltration and dampen rapid runoff. The exponents act as elasticities: a 1% rise in *SoilABC* increases *BFI* by ≈0.298%, and a 1% rise in *Forest* by ≈0.185%. In practical terms, doubling *SoilABC* raises *BFI* by $2^{0.298}$ ≈23%, while doubling *Forest* yields $2^{0.185}$≈14%. With just these two factors the calibration explains 59% of the variance ($R^2 = 0.59$), with *RMSE* =0.080 and *MAE* = 0.064 relative to an observed range ≈ 0.30–0.70; bias is small (*PBIAS* ≈ 1.20%, i.e., a slight overall over-prediction), and Mean Absolute Percentage Error is ≈ 12.8% (Figure 5.18). Residual diagnostics confirm no obvious misspecification. In Fig. 5.19.a (residuals vs *Forest*), the cloud is centered around zero without trends or fanning. In Fig. 5.19.b (residuals vs *SoilABC*), dispersion is broadly uniform with no funnel shape, indicating approximate homoscedasticity.

A robust MAD screen (δ = 2) flags three outliers: B18 (Venosa a Ponte S.Angelo), B15 (Venosa a Ponte Ferroviario), and N13 (Alento a Casalvelino). As figures (5.19.a and 5.19.b) shown B18 and B15 sit in the low-Forest/high-*SoilABC* corner (Forest ≈ 0.085 and 0.083; *SoilABC* ≈ 0.783 and 0.833). Their observed BFIs (0.590 and 0.577) exceed model predictions (0.398 and 0.404), giving large negative residuals (-0.192 and -0.173). In such sparsely vegetated yet highly permeable basins, infiltration and subsurface storage sustain baseflow more than the two-factor elasticity on

Forest permits, so the model under-predicts there. N13 lies at the opposite edge—very high *SoilABC* (~0.918) and substantial *Forest* (~0.611)—but its observed *BFI* (0.399) is far below the prediction (0.601), yielding a 0.202 residual (percentage error ≈ 50.6%). This points to limiting controls beyond land-surface descriptors (e.g., relief-driven quickflow or local hydrogeology/management). For the remaining basins, residuals align with the model structure.

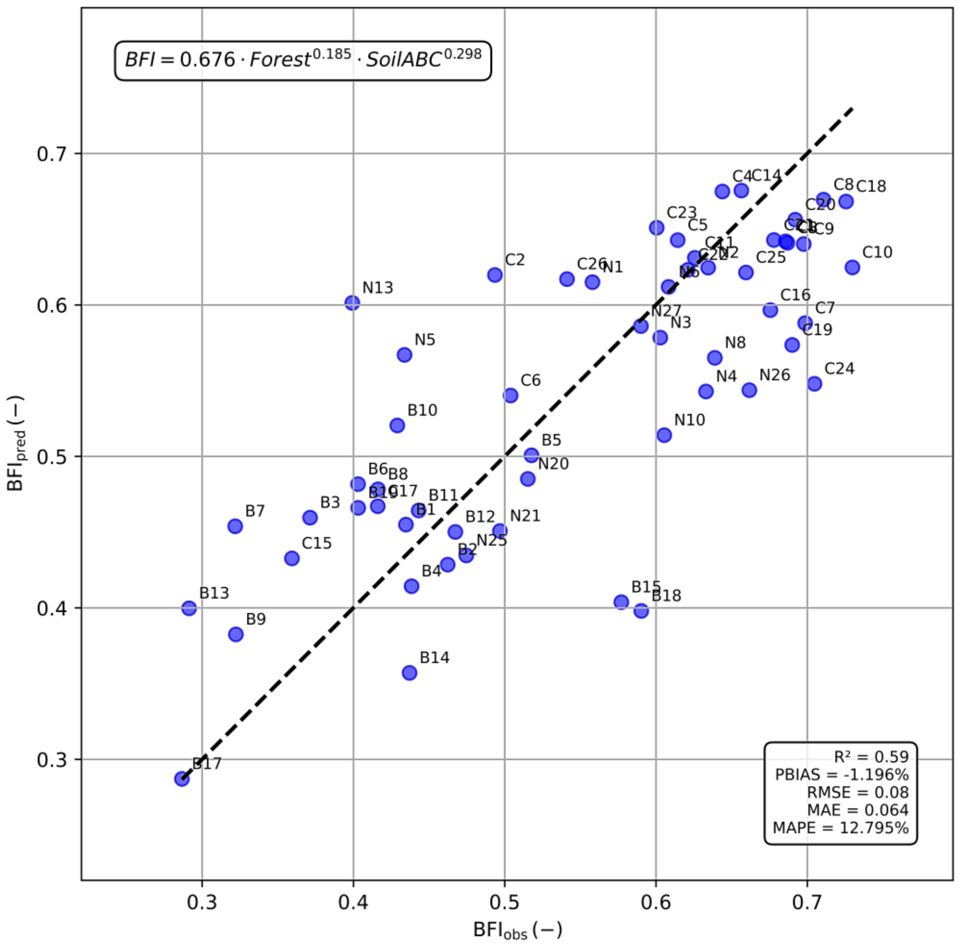

Figure 5.18: Predicted vs. observed for the BFI model. Station codes: ***B*** *– Bari,* ***C*** *– Catanzaro,* ***N*** *– Napoli.*

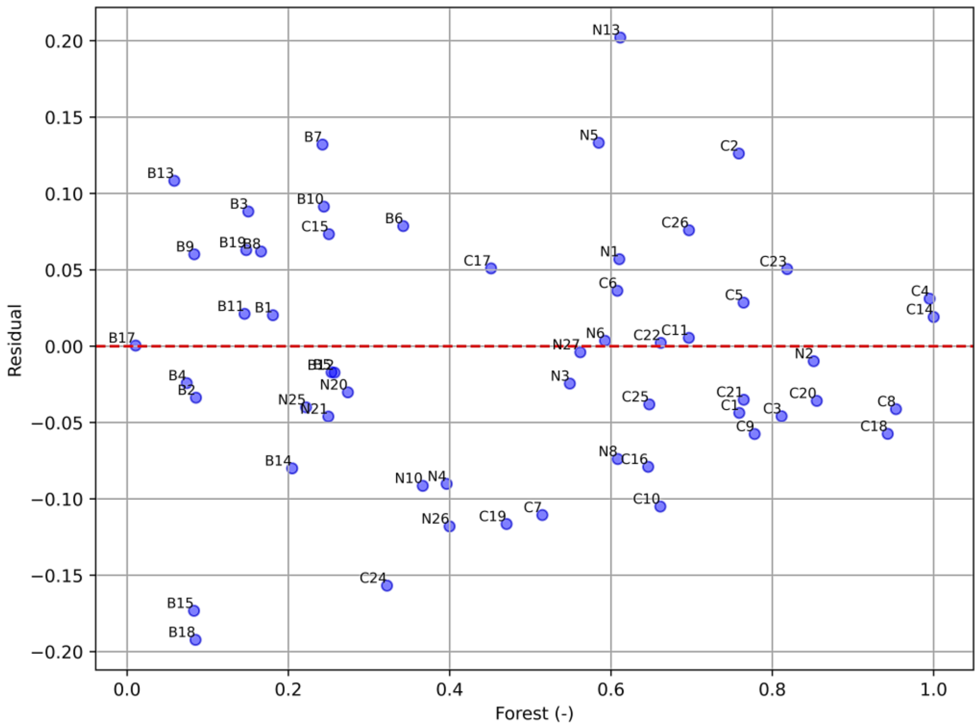

Figure 5.19.a: Residuals plotted against Forest for the BFI model.

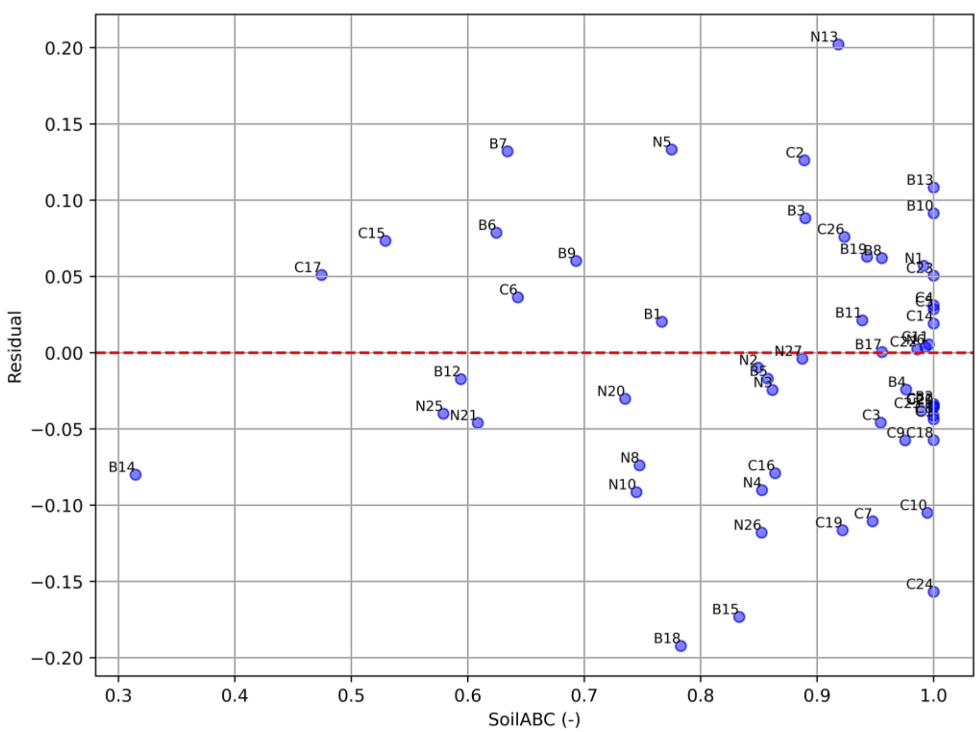

Figure 5.19.b: Residuals plotted against SoilABC for the BFI model

Leave-one-out (jackknife) validation confirms the stability of the *BFI* model (Figure 5.20; Table 5.14). Compared to the full calibration, the jackknife results show only a slight reduction in fit (R^2=0.54, i.e. ≈ 3–4% lower), while *RMSE* increases from 0.080 to 0.085 (≈ +2%) and *MAE* from 0.064 to 0.068, overall percentage error remains close to 13%.

Table 5.14: Calibration and jackknife performance metrics for BFI.

Metric	Model	Jackknife
R^2	0.59	0.54
RMSE	0.08	0.085
MAE	0.064	0.068
PBIAS (%)	1.196	1.238
MAPE (%)	12.8	13.6

Pointwise influence, measured as $\Delta=|y_{Jack}-y_{model}|$ is concentrated in two stations: B14 ($\Delta \approx 0.037$, the largest in the dataset) and B13 ($\Delta \approx 0.016$), both well above the median adjustment (< 0.005) and thus exerting clear leverage on the fitted elasticities. In contrast, stations such as B18 ($\Delta \approx$ 0.010), B15 ($\Delta \approx 0.010$), and N13 ($\Delta \approx 0.007$) display relatively large residuals in the full model but their exclusion produces only small parameter shifts, meaning they behave as response outliers rather than structurally influential observations. Across the network, the distribution of shifts is narrow: median $\Delta \approx 0.0022$, mean $\Delta \approx 0.0036$, 86% of sites with $\Delta \leq 0.005$, 95% with $\Delta \leq 0.010$, and maximum $\Delta = 0.0365$ at B14. This confirms that, apart from B14 (and to a lesser extent B13), case deletion has negligible impact on model form and predictions.

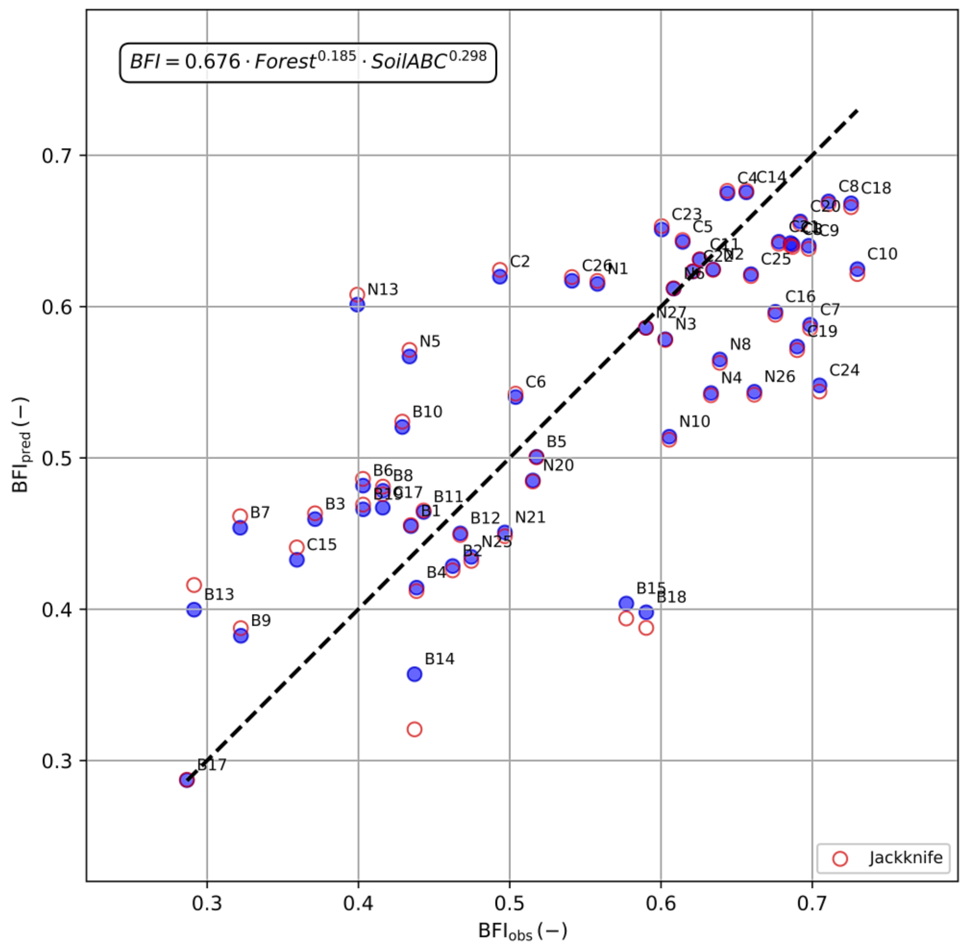

Figure 5.20: Jackknife validation of the BFI model. Station codes: ***B*** *– Bari,* ***C*** *– Catanzaro,* ***N*** *– Napoli.*

5.6 Performance of the FDC Regionalization Framework

In this study, the parameters of the Flow Duration Curve (FDC)—μ, τ, and Q_{nz}—were first estimated through regional regression models. Based on these predicted parameters, the FDC was subsequently regionalized. The procedure involves reconstructing the FDC at each site using the predicted parameters, thereby enabling the estimation of different flow quantiles. These predicted quantiles were then directly compared with the observed ones at each gauging station to evaluate the performance of the regionalization.

To assess the predictive accuracy, several statistical indicators were employed, including the root mean square error (*RMSE*), mean absolute error *(MAE*), coefficient of determination (R^2), and percent bias (*PBIAS*). These metrics provide complementary insights: RMSE emphasizes large deviations, *MAE* quantifies overall accuracy, R^2 measures explained variance, and *PBIAS* indicates whether the model systematically over- or underestimates flows.

As shown in Figure 5.21, the histograms of *RMSE* and *MAE* display a pronounced right-skewed distribution, with many stations concentrated at low error levels and only a few exhibiting substantial deviations. Most *RMSE* values fall below approximately 7, while a small fraction exceed 20 and reach up to nearly 60. A similar pattern is evident for *MAE*, where most stations remain below about 5, and only a few surpass 20–30. This pattern indicates generally reliable model performance across most catchments, while highlighting a limited number of sites with considerably larger errors.

The R^2 distribution offers additional perspective on model performance. More than half of the stations exhibit R^2 values above 0.9, with a dense concentration near 1.0. This demonstrates that, for most basins, the model successfully reproduces the observed flow variability, confirming its strong explanatory capacity. Nonetheless, a small subset of stations records markedly lower R^2 values, occasionally below 0.3, signifying weak agreement between observed and predicted flows. The bimodal shape of the distribution—with a major cluster near 1.0 and a trailing tail of low value suggests that the model performs very well in most basins but encounters difficulties in a few exceptional cases. These low-performing sites likely correspond to the outliers identified in the *RMSE* and *MAE* distributions.

The *PBIAS* distribution is more balanced and approximately symmetric around zero. Most stations fall within ±20%, a range generally regarded as acceptable, while only a small proportion exceed ±30–50%. Positive and negative biases occur with similar frequency, indicating the absence of systematic overestimation or underestimation at the regional scale. This near-symmetry suggests that opposite errors largely compensate for one another, confirming that the model does not exhibit a directional bias.

Overall, these results indicate that the model provides consistent and robust performance across most stations, while a small number of outliers contribute disproportionately to the overall error distribution. The extreme *RMSE* and *MAE* values observed in some basins are likely attributable to site-specific hydrological or geomorphological features not fully represented in the regional model.

Figure 5.22 illustrates nine representative stations, showing that the predicted FDCs generally follow the observed curves across the entire exceedance range. In most cases, the fit is very close, while only a few stations display noticeable departures at the high-flow or low-flow tails, corresponding to the same outliers identified in the statistical analyses.

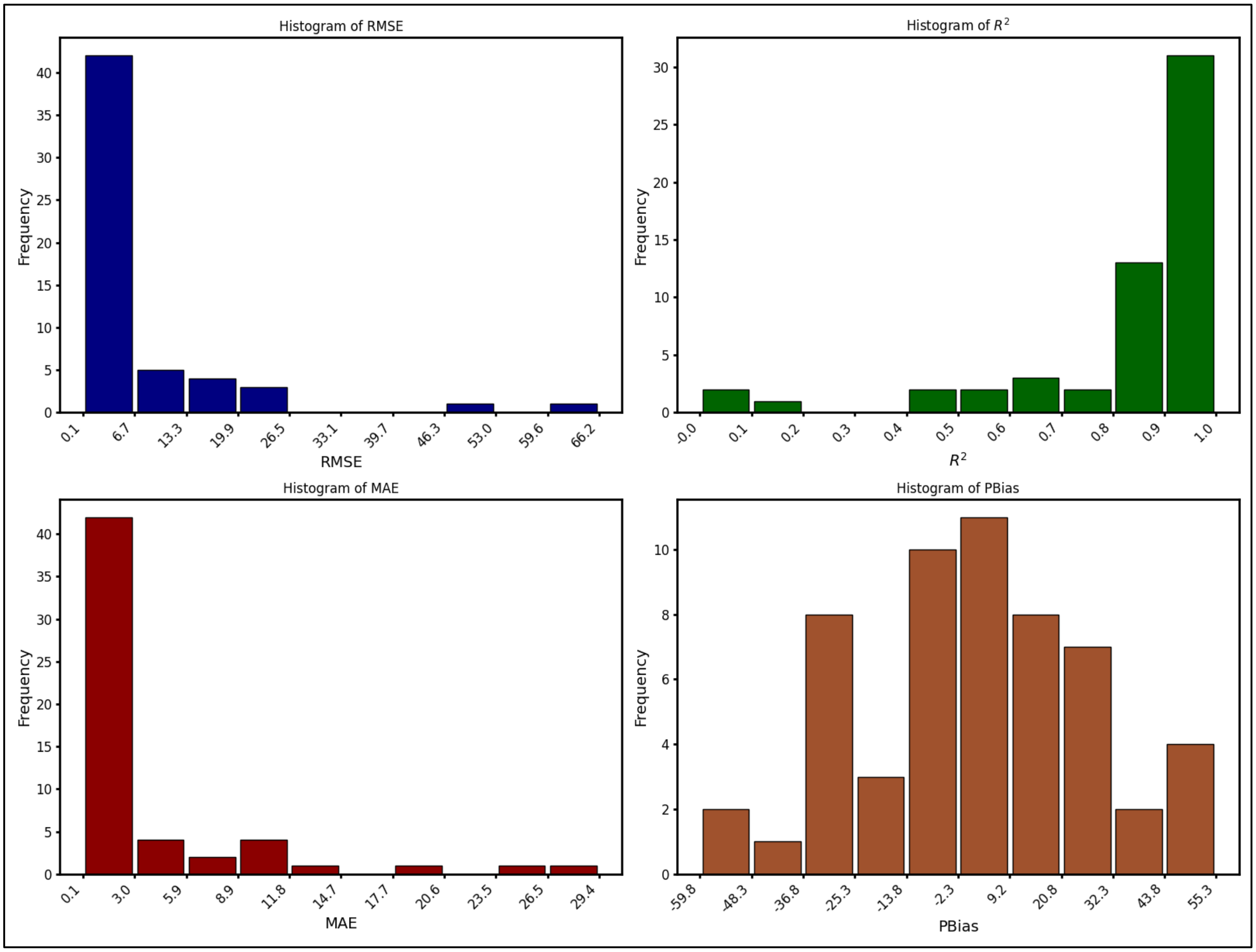

Figure.5.21: Histograms of performance metrics across all gauging stations: RMSE, R², MAE, and PBIAS

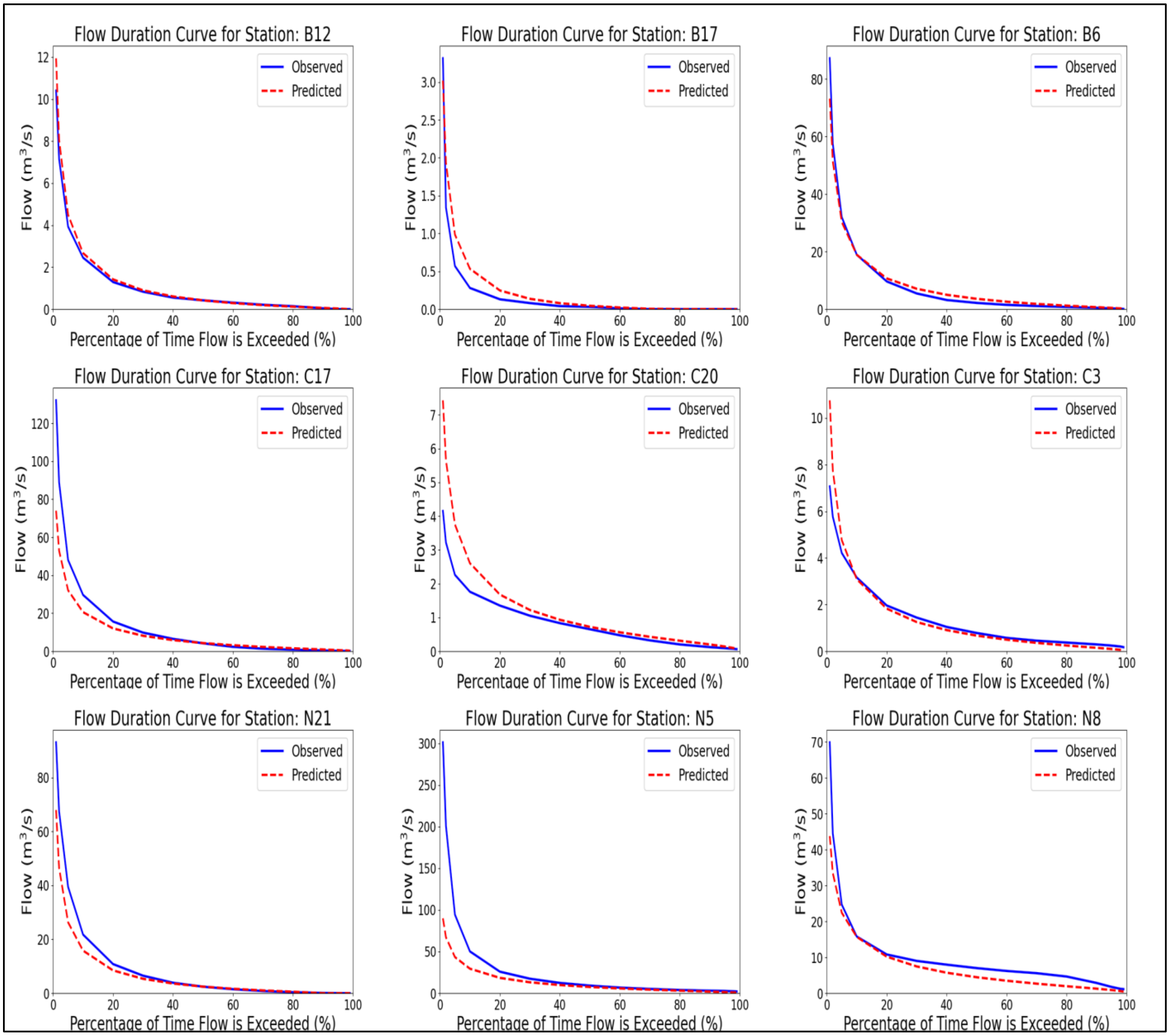

Figure 5.22: Flow Duration Curves (FDCs) at nine representative stations comparing observed (solid) and predicted (dashed)

In the framework of the Italian National Hydrological and Mareographic Service (Servizio Idrografico e Mareografico Nazionale), the FDC ordinates Q25 and Q75 are widely adopted as standard indicators of the upper-intermediate and low-mid flow regimes. Their clear hydrological meaning and consistency across gauging stations make them fundamental references for regional analysis and transferability to ungauged basins.

As illustrated in Figure 5.23, the Q25 plot (moderate–high flows) displays an excellent correspondence between observed and regionally predicted values ($R^2 = 0.96$, RMSE = 4.11, MAE = 1.93). Points (each representing a gauged catchment) are tightly clustered around the 1:1 line, with only a few high-flow outliers. This confirms that the selected regional predictors effectively reproduce the dominant controls of the upper FDC regime, capturing both magnitude and spatial variability of moderate–high flows.

Similarly, Figure 5.23 shows that the Q75 plot (frequent low–mid flows) also exhibits a strong and consistent relationship between observed and predicted values ($R^2 = 0.84$, RMSE = 3.26, MAE = 1.27). The distribution of points along the 1:1 line suggests that the regional model successfully captures the overall spatial pattern of the lower-flow regime. Although some dispersion is visible at higher magnitudes, this reflects natural hydrological variability. Overall, the Q75 results demonstrate that the regional relationships remain reliable across the low-to-intermediate range of the FDC, confirming their suitability for regional assessments and supporting the robustness of the overall model structure.

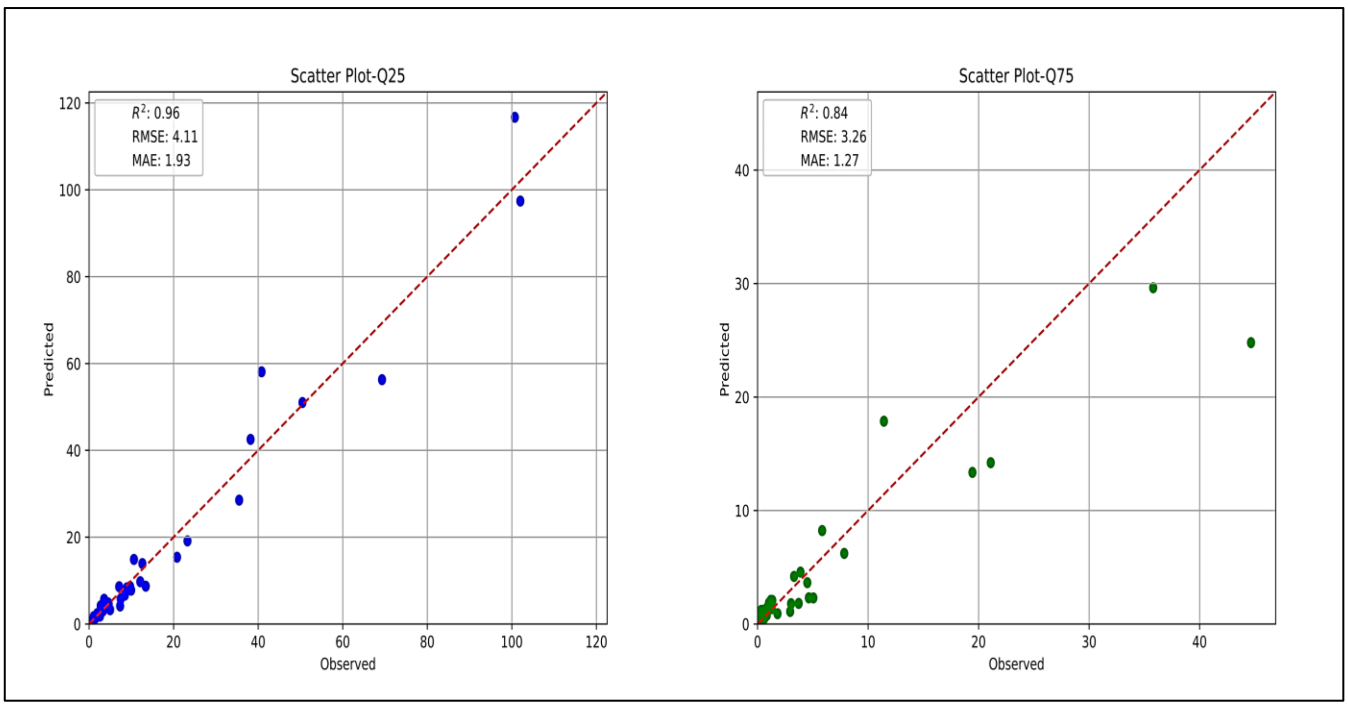

Figure 5.23: Comparison between observed and predicted discharges for Q_{25} and Q_{75}.

6.Conclusions and Future Work

This study has presented a comprehensive framework for the regionalization of Flow Duration Curves (FDCs) in ungauged basins of southern Italy, leveraging a combination of morphometric, physiographic, climatic, land cover, and soil descriptors to predict key hydrological parameters. By integrating statistical analyses, including Pearson correlations, stepwise regressions, and power-law models, with hydrological reasoning, the study aimed to develop robust, parsimonious models for the parameters μ (mean of log-transformed normalized discharges), τ (duration of non-zero flow), and Q_{nz} (mean non-zero discharge). These parameters were subsequently used to reconstruct FDCs and estimate flow quantiles, enabling reliable predictions in data-scarce regions. The inclusion of complementary analyses, such as sensitivity to record length and Base Flow Index (*BFI*) modeling, further strengthened the framework's applicability and interpretability.

The primary objectives of the research—to identify dominant catchment descriptors, mitigate multicollinearity, and validate regional models through cross-validation and outlier detection—were successfully achieved. Initial correlation analyses revealed strong associations between FDC parameters and descriptors like catchment area (*A*), maximum elevation (*HMAX*), mean annual precipitation (*MAP*), *forest* cover, and soil classes (e.g., *SoilAB, SoilABC*). Stepwise regressions in both raw and log-transformed spaces distilled these into parsimonious models, prioritizing BIC for efficiency while ensuring hydrological coherence. For μ, the selected model ($\mu = -0.738 + 0.00011 \cdot HMAX + 0.305 \cdot Forest + 0.165 \cdot SoilAB$) explained 52% of variance, highlighting the roles of elevation-driven precipitation, vegetation-enhanced infiltration, and permeable soils in sustaining relative flows. The τ model ($\tau = 0.675 \cdot A^{0.111} \cdot SF^{0.230}$) captured 72% of variance, emphasizing basin size and compactness in prolonging flow persistence. For Q_{nz}, the power-law form ($Q_{nz} = 5.9 \times 10^{-9} \cdot MAP^{2.110} \cdot A^{0.992}$) achieved an exceptional R^2 of 0.96, underscoring super-linear precipitation effects and near-linear area scaling. Jackknife validation confirmed model stability, with modest performance degradation (e.g., R^2 drops of 5–10%), while outlier detection via Median Absolute Deviation (*MAD*) identified site-specific anomalies attributable to unique geological or climatic conditions.

Sensitivity analyses to record length demonstrated a clear trade-off: stricter thresholds (≥15 years) yielded the most stable coefficients and lowest relative errors, whereas relaxing to ≥5 years increased sample size but amplified noise and *MAPE* (e.g., by 5–10%). This underscores the importance of long-term data for reliable regionalization, particularly in Mediterranean climates prone to intermittency. The BFI model ($BFI = 0.676 \cdot SoilABC^{0.298} \cdot Forest^{0.185}$), explaining 59% of variance, complemented the FDC framework by quantifying baseflow contributions and emphasizing the combined influence of soil permeability and vegetation cover in sustaining low flows.

The overall performance of the FDC regionalization was evaluated through quantile-specific metrics, revealing strong predictive accuracy. Histograms of *RMSE, MAE*, R^2, and *PBIAS* across stations indicated robust fits for most basins, with $R^2 > 0.9$ in over half and *PBIAS* within ±20% for the majority. Scatterplots for standard quantiles (Q_{25} and Q_{75}) confirmed excellent reproduction of moderate-high ($R^2 = 0.96$) and low-mid flows ($R^2 = 0.84$).

Future work will focus on developing annual Flow Duration Curves (AFDCs) to assess inter-annual variability and temporal stability in flow regimes. In addition, quantile-based regionalization approaches will be explored to directly relate specific FDC ordinates (e.g., Q_{10}, Q_{50}, Q_{90}) to catchment descriptors. This direction is expected to enhance model flexibility and improve predictive performance in ungauged basins.

Reference:

Achugbu, I. C., Olufayo, A. A., Balogun, I. A., Dudhia, J., McAllister, M., Adefisan, E. A., & Naabil, E. (2022). Potential effects of land use land cover change on streamflow over the Sokoto Rima River Basin. *Heliyon*, *8*(7), Article e09807. https://doi.org/10.1016/j.heliyon.2022.e09807

Acreman, M. (2005). Linking science and decision-making: Features and experience from environmental river flow setting. *Environmental Modelling & Software*, *20*(2), 99–109. https://doi.org/10.1016/j.envsoft.2003.08.019

Adongo, T. A. (2022). Effect of hydrologic soil groups on runoff generation in reservoir catchments in Northern Ghana. *Ghana Journal of Science, Technology and Development*, *8*(1), 32–47.

Allocca, V., Celico, F., Celico, P., De Vita, P., Fabbrocino, S., Mattia, S., Musilli, I., Piscopo, V., & Summa, G. (2007). *Note illustrative della Carta idrogeologica dell'Italia meridionale*. Istituto Poligrafico e Zecca dello Stato. https://www.iris.unina.it/handle/11588/122726

Apaydin, H., Ozturk, F., Merdun, H., & Aziz, N. M. (2006). Determination of the drainage basin characteristics using vector GIS. *Hydrology Research*, *37*(2), 129–142. https://doi.org/10.2166/nh.2006.0010

Archfield, S. A. (2009). *Estimation of continuous daily streamflow at ungaged locations in southern New England* [Doctoral dissertation, Tufts University].

Archfield, S. A., Steeves, P. A., Guthrie, J. D., & Ries, K. G., III. (2013). Towards a publicly available, map-based regional software tool to estimate unregulated daily streamflow at ungauged rivers. *Geoscientific Model Development*, *6*(1), 101–115. https://doi.org/10.5194/gmd-6-101-2013

Arnold, J. G., Muttiah, R. S., Srinivasan, R., & Allen, P. M. (2000). Regional estimation of base flow and groundwater recharge in the Upper Mississippi river basin. *Journal of Hydrology*, *227*(1–4), 21–40. https://doi.org/10.1016/S0022-1694(99)00139-0

Basso, S., & Botter, G. (2012). Streamflow variability and optimal capacity of run-of-river hydropower plants. *Water Resources Research*, *48*(10), Article W10530. https://doi.org/10.1029/2012WR012017

Blum, A. G., Archfield, S. A., & Vogel, R. M. (2017). On the probability distribution of daily streamflow in the United States. *Hydrology and Earth System Sciences*, *21*(6), 3093–3103. https://doi.org/10.5194/hess-21-3093-2017

Bonardi, G., Amore, F. O., Ciampo, G., De Capoa, P., Miconnet, P., & Perrone, V. (1992). Il Complesso Liguride Auct.: Stato delle conoscenze e problemi aperti sulla sua evoluzione preappenninica ed i suoi rapporti con l'arco calabro. *Memorie della Società Geologica Italiana*, *41*, 17–35.

Boscarello, L., Ravazzani, G., Cislaghi, A., & Mancini, M. (2016). Regionalization of flow-duration curves through catchment classification with streamflow signatures and physiographic–climate indices. *Journal of Hydrologic Engineering*, *21*(3), Article 05015027. https://doi.org/10.1061/(ASCE)HE.1943-5584.0001307

Botter, G., Zanardo, S., Porporato, A., Rodriguez-Iturbe, I., & Rinaldo, A. (2008). Ecohydrological model of flow duration curves and annual minima. *Water Resources Research*, *44*(8), Article W08418. https://doi.org/10.1029/2008WR006814

Braud, I., Breil, P., Thollet, F., Lagouy, M., Branger, F., Jacqueminet, C., Kermadi, S., & Michel, K. (2013). Evidence of the impact of urbanization on the hydrological regime of a medium-sized periurban catchment in France. *Journal of Hydrology*, *485*, 5–23. https://doi.org/10.1016/j.jhydrol.2012.04.049

Brown, A. E., Podger, G. M., Davidson, A. J., Dowling, T. I., & Zhang, L. (2007). Predicting the impact of plantation forestry on water users at local and regional scales: An example for the Murrumbidgee River Basin, Australia. *Forest Ecology and Management*, *251*(1–2), 82–93. https://doi.org/10.1016/j.foreco.2007.06.024

Brown, A. E., Western, A. W., McMahon, T. A., & Zhang, L. (2013). Impact of forest cover changes on annual streamflow and flow duration curves. *Journal of Hydrology*, *483*, 39–50. https://doi.org/10.1016/j.jhydrol.2012.12.031

Brown, A. E., Zhang, L., McMahon, T. A., Western, A. W., & Vertessy, R. A. (2005). A review of paired catchment studies for determining changes in water yield resulting from alterations in vegetation. *Journal of Hydrology*, *310*(1–4), 28–61. https://doi.org/10.1016/j.jhydrol.2004.12.010

Callow, J. N., Van Niel, K. P., & Boggs, G. S. (2007). How does modifying a DEM to reflect known hydrology affect subsequent terrain analysis? *Journal of Hydrology*, *332*(1–2), 30–39. https://doi.org/10.1016/j.jhydrol.2006.06.020

Castellarin, A. (2014). Regional prediction of flow-duration curves using a three-dimensional kriging. *Journal of Hydrology*, *513*, 179–191. https://doi.org/10.1016/j.jhydrol.2014.03.050

Castellarin, A., Camorani, G., & Brath, A. (2007). Predicting annual and long-term flow-duration curves in ungauged basins. *Advances in Water Resources*, *30*(4), 937–953. https://doi.org/10.1016/j.advwatres.2006.08.006

Castellarin, A., Galeati, G., Brandimarte, L., Montanari, A., & Brath, A. (2004). Regional flow-duration curves: Reliability for ungauged basins. *Advances in Water Resources*, *27*(10), 953–965. https://doi.org/10.1016/j.advwatres.2004.07.005

Castellarin, A., Vogel, R. M., & Brath, A. (2004). A stochastic index flow model of flow duration curves. *Water Resources Research*, *40*(3), Article W03105. https://doi.org/10.1029/2003WR002524

Celico, P. (1986). *Prospezioni idrogeologiche* (Vol. 1). Liguori.

Ceola, S., Pugliese, A., Ventura, M., Galeati, G., Montanari, A., & Castellarin, A. (2018). Hydropower production and fish habitat suitability: Assessing impact and effectiveness of ecological flows at regional scale. *Advances in Water Resources*, *116*, 29–39. https://doi.org/10.1016/j.advwatres.2018.04.002

Chapman, T. G. (1991). Comment on "Evaluation of automated techniques for base flow and recession analyses" by R. J. Nathan and T. A. McMahon. *Water Resources Research*, *27*(7), 1783–1784. https://doi.org/10.1029/91WR01007

Choubin, B., Solaimani, K., Rezanezhad, F., Roshan, M. H., Malekian, A., & Shamshirband, S. (2019). Streamflow regionalization using a similarity approach in ungauged basins: Application of the geo-environmental signatures in the Karkheh River Basin, Iran. *Catena*, *182*, Article 104128. https://doi.org/10.1016/j.catena.2019.104128

Claps, P., Evangelista, G., Ganora, D., Mazzoglio, P., & Monforte, I. (2023). FOCA: A new quality-controlled database of floods and catchment descriptors in Italy. *Earth System Science Data Discussions*, 1–22. (Advance online publication)

Claps, P., & Fiorentino, M. (1997). Probabilistic flow duration curves for use in environmental planning and management. In N. B. Harmancioglu, M. N. Alpaslan, S. D. Ozkul, & V. P. Singh (Eds.), *Integrated approach to environmental data management systems* (pp. 255–266). Springer. https://doi.org/10.1007/978-94-011-5616-5_22

Costa, V., Fernandes, W., & Naghettini, M. (2014). Regional models of flow-duration curves of perennial and intermittent streams and their use for calibrating the parameters of a rainfall–runoff model. *Hydrological Sciences Journal*, *59*(2), 262–277. https://doi.org/10.1080/02626667.2013.802093

Cousineau, D., & Chartier, S. (2010). Outliers detection and treatment: A review. *International Journal of Psychological Research*, *3*(1), 58–67. https://doi.org/10.21500/20112084.844

Creed, I. F., Sass, G. Z., Wolniewicz, M. B., & Devito, K. J. (2008). Incorporating hydrologic dynamics into buffer strip design on the sub-humid Boreal Plain of Alberta. *Forest Ecology and Management*, *256*(11), 1984–1994. https://doi.org/10.1016/j.foreco.2008.07.021

Croker, K. M., Young, A. R., Zaidman, M. D., & Rees, H. G. (2003). Flow duration curve estimation in ephemeral catchments in Portugal. *Hydrological Sciences Journal*, *48*(3), 427–439. https://doi.org/10.1623/hysj.48.3.427.45287

Cupak, A., & Michalec, B. (2022). Regionalisation of watersheds with respect to low flow. *Journal of Water and Land Development*, *55*, 47–55. https://doi.org/10.24425/jwld.2022.143709

Del Giudice, G., Padulano, R., & Rasulo, G. (2014). Spatial prediction of the runoff coefficient in Southern Peninsular Italy for the index flood estimation. *Hydrology Research*, *45*(2), 263–281. https://doi.org/10.2166/nh.2013.170

Dou, P., Tian, Y., Zhang, J., & Fan, Y. (2024). Multi-scale spatial relationship between runoff and landscape pattern in the Poyang Lake Basin of China. *Water*, *16*(23), Article 3501. https://doi.org/10.3390/w16233501

Eckhardt, K. (2005). How to construct recursive digital filters for baseflow separation. *Hydrological Processes*, *19*(2), 507–515. https://doi.org/10.1002/hyp.5675

Feranec, J., Jaffrain, G., Soukup, T., & Hazeu, G. (2010). Determining changes and flows in European landscapes 1990–2000 using CORINE land cover data. *Applied Geography*, *30*(1), 19–35. https://doi.org/10.1016/j.apgeog.2009.07.003

Franchini, M., & Suppo, M. (1996). Regional analysis of flow duration curves for a limestone region. *Water Resources Management*, *10*(3), 199–218. https://doi.org/10.1007/BF00424203

Ganora, D., Claps, P., Laio, F., & Viglione, A. (2009). An approach to estimate nonparametric flow duration curves in ungauged basins. *Water Resources Research*, *45*(10), Article W10418. https://doi.org/10.1029/2008WR007472

Gaviria, C., & Carvajal-Serna, F. (2022). Regionalization of flow duration curves in Colombia. *Hydrology Research*, *53*(8), 1075–1089. https://doi.org/10.2166/nh.2022.044

Genereux, D. (1998). Quantifying uncertainty in tracer-based hydrograph separations. *Water Resources Research*, *34*(4), 915–919. https://doi.org/10.1029/98WR00010

Haan, C. T. (1977). *Statistical methods in hydrology*. Iowa State University Press.

Hamel, P., Daly, E., & Fletcher, T. D. (2015). Which baseflow metrics should be used in assessing flow regimes of urban streams? *Hydrological Processes*, *29*(20), 4367–4378. https://doi.org/10.1002/hyp.10475

Hanafi, S., Mailhol, J. C., Poussin, J. C., & Zairi, A. (2012). Estimating water demand at irrigation scheme scales using various levels of knowledge: Applications in Northern Tunisia. *Irrigation and Drainage*, *61*(3), 341–347. https://doi.org/10.1002/ird.652

Hawkins, D. M. (1980). Multivariate outlier detection. In D. M. Hawkins (Ed.), *Identification of outliers* (pp. 104–114). Springer. https://doi.org/10.1007/978-94-015-3994-4_8

Hrachowitz, M., Soulsby, C., Tetzlaff, D., Dawson, J. J. C., Dunn, S. M., & Malcolm, I. A. (2009). Using long-term data sets to understand transit times in contrasting headwater catchments. *Journal of Hydrology*, *367*(3–4), 237–248. https://doi.org/10.1016/j.jhydrol.2009.01.001

Huang, J., Zhu, Q., Yang, L., & Feng, J. (2016). A non-parameter outlier detection algorithm based on natural neighbor. *Knowledge-Based Systems*, *92*, 71–77. https://doi.org/10.1016/j.knosys.2015.10.014

Hussain, I. (2020). Outlier detection using nonparametric depth-based techniques in hydrology. *International Journal of Advanced Computer Science and Applications*, *11*(9), 264–271. https://doi.org/10.14569/IJACSA.2020.0110933

Iacobellis, V., Claps, P., & Fiorentino, M. (1999). Climatic controls on the flood frequency distribution. In *Proceedings of the EGS Plinius Conference on Mediterranean Storms*, Maratea, Italy (pp. 341–351). http://www.idrologia.polito.it/~claps/pliniusonline/pdf_proceedings/Plinius/Iacobellis/IACOBELLIS.pdf

Jang, J.-Y., Kim, D.-W., Choi, Y.-J., & Jang, D.-W. (2021). Analysis of the water quality characteristics of urban streams using the flow–pollutant loading relationship and a load duration curve (LDC). *Applied Sciences*, *11*(20), Article 9694. https://doi.org/10.3390/app11209694

Jennings, M. E., & Benson, M. A. (1969). Frequency curves for annual flood series with some zero events or incomplete data. *Water Resources Research*, *5*(1), 276–280. https://doi.org/10.1029/WR005i001p00276

Kim, D., & Kaluarachchi, J. (2014). Predicting streamflows in snowmelt-driven watersheds using the flow duration curve method. *Hydrology and Earth System Sciences*, *18*(5), 1679–1693. https://doi.org/10.5194/hess-18-1679-2014

Kim, Y.-O., Seo, S. B., & Jang, O.-J. (2012). Flood risk assessment using regional regression analysis. *Natural Hazards*, *63*(2), 1203–1217. https://doi.org/10.1007/s11069-012-0221-6

Kinoshita, A. M., & Hogue, T. S. (2015). Increased dry season water yield in burned watersheds in Southern California. *Environmental Research Letters*, *10*(1), Article 014003. https://doi.org/10.1088/1748-9326/10/1/014003

Kjeldsen, T. R., Ahn, H., & Prosdocimi, I. (2017). On the use of a four-parameter kappa distribution in regional frequency analysis. *Hydrological Sciences Journal*, *62*(9), 1354–1363. https://doi.org/10.1080/02626667.2017.1335400

Kjeldsen, T. R., Lundorf, A., & Rosbjerg, D. (2000). Use of a two-component exponential distribution in partial duration modelling of hydrological droughts in Zimbabwean rivers. *Hydrological Sciences Journal*, *45*(2), 285–298. https://doi.org/10.1080/02626660009492325

Kresic, N. (2010). Types and classifications of springs. In *Groundwater hydrology of springs* (pp. 31–85). Elsevier. https://www.sciencedirect.com/science/article/pii/B9781856175029000025

Kroll, C. N., & Vogel, R. M. (2002). Probability distribution of low streamflow series in the United States. *Journal of Hydrologic Engineering*, *7*(2), 137–146. https://doi.org/10.1061/(ASCE)1084-0699(2002)7:2(137)

Kumar, A., Sung, M., Xu, J., & Wang, J. (2004). Data streaming algorithms for efficient and accurate estimation of flow size distribution. *ACM SIGMETRICS Performance Evaluation Review*, *32*(1), 177–188. https://doi.org/10.1145/1012888.1005709

Lacombe, G., Douangsavanh, S., Vogel, R. M., McCartney, M., Chemin, Y., Rebelo, L.-M., & Sotoukee, T. (2014). Multivariate power-law models for streamflow prediction in the Mekong Basin. *Journal of Hydrology: Regional Studies*, *2*, 35–48. https://doi.org/10.1016/j.ejrh.2014.08.002

Lane, P., Best, A., Hickel, K., & Zhang, L. (2005). The effect of afforestation on flow duration curves. *Journal of Hydrology*, *310*(1–4), 253–265. https://doi.org/10.1016/j.jhydrol.2005.01.005

Lang, M. M. (2005). *California Department of Transportation (Caltrans) District 1 pilot fish passage assessment study: Volume 1–Overall results* (Report No. FHWA-CA-EN-2005-02). California Department of Transportation.

LeBoutillier, D. W., & Waylen, P. R. (1993). A stochastic model of flow duration curves. *Water Resources Research*, *29*(10), 3535–3541. https://doi.org/10.1029/93WR01409

Lee, S., & Ajami, H. (2023). Comprehensive assessment of baseflow responses to long-term meteorological droughts across the United States. *Journal of Hydrology*, *626*, Article 130256. https://doi.org/10.1016/j.jhydrol.2023.130256

Li, M., Shao, Q., Zhang, L., & Chiew, F. H. (2010). A new regionalization approach and its application to predict flow duration curve in ungauged basins. *Journal of Hydrology*, *389*(1–2), 137–145. https://doi.org/10.1016/j.jhydrol.2010.05.039

Li, Z. (2014). Watershed modeling using arc hydro based on DEMs: A case study in Jackpine watershed. *Environmental Systems Research*, *3*(1), Article 11. https://doi.org/10.1186/2193-2697-3-11

Lindsay, J. B., & Dhun, K. (2015). Modelling surface drainage patterns in altered landscapes using LiDAR. *International Journal of Geographical Information Science*, *29*(3), 397–411. https://doi.org/10.1080/13658816.2014.975715

Liu, Y., Lu, M., Huo, X., Hao, Y., Gao, H., Liu, Y., Fan, Y., Cui, Y., & Metivier, F. (2016). A Bayesian analysis of Generalized Pareto Distribution of runoff minima. *Hydrological Processes*, *30*(3), 424–432. https://doi.org/10.1002/hyp.10606

Longobardi, A., & Villani, P. (2013). A statistical, parsimonious, empirical framework for regional flow duration curve shape prediction in high permeability Mediterranean region. *Journal of Hydrology*, *507*, 174–185. https://doi.org/10.1016/j.jhydrol.2013.10.029

Lyne, V., & Hollick, M. (1979). Stochastic time-variable rainfall-runoff modelling. *Institute of Engineers Australia National Conference*, *79*(10), 89–93. https://www.academia.edu/download/39814987/Stochastic_Time-Variable_Rainfall-Runoff20151108-28652-1m3nhta.pdf

Mailhot, A., Talbot, G., Ricard, S., Turcotte, R., & Guinard, K. (2018). Assessing the potential impacts of dam operation on daily flow at ungauged river reaches. *Journal of Hydrology: Regional Studies*, *18*, 156–167. https://doi.org/10.1016/j.ejrh.2018.06.006

Marcinkowski, P., & Grygoruk, M. (2017). Long-term downstream effects of a dam on a lowland river flow regime: Case study of the Upper Narew. *Water*, *9*(10), Article 783. https://doi.org/10.3390/w9100783

Mendicino, G., & Senatore, A. (2013). Evaluation of parametric and statistical approaches for the regionalization of flow duration curves in intermittent regimes. *Journal of Hydrology*, *480*, 19–32. https://doi.org/10.1016/j.jhydrol.2012.12.017

Merwade, V. (2012). *Watershed and stream network delineation using ArcHydro tools* [Tutorial]. School of Civil Engineering, Purdue University. https://web.ics.purdue.edu/~vmerwade/education/terrain_processing.pdf

Miller, J. (1991). Short report: Reaction time analysis with outlier exclusion: Bias varies with sample size. *The Quarterly Journal of Experimental Psychology Section A*, *43*(4), 907–912. https://doi.org/10.1080/14640749108400962

Mimikou, M., & Kaemaki, S. (1985). Regionalization of flow duration characteristics. *Journal of Hydrology*, *82*(1–2), 77–91. https://doi.org/10.1016/0022-1694(85)90048-3

Mohamoud, Y. M. (2008). Prediction of daily flow duration curves and streamflow for ungauged catchments using regional flow duration curves. *Hydrological Sciences Journal*, *53*(4), 706–724. https://doi.org/10.1623/hysj.53.4.706

Mohor, G. S., Rodriguez, D. A., Tomasella, J., & Júnior, J. L. S. (2015). Exploratory analyses for the assessment of climate change impacts on the energy production in an Amazon run-of-river hydropower plant. *Journal of Hydrology: Regional Studies*, *4*, 41–59. https://doi.org/10.1016/j.ejrh.2015.05.002

Mosley, M. P., & McKerchar, A. I. (1993). Streamflow. In D. R. Maidment (Ed.), *Handbook of hydrology* (pp. 8.1–8.39). McGraw-Hill.

Müller, M. F., Dralle, D. N., & Thompson, S. E. (2014). Analytical model for flow duration curves in seasonally dry climates. *Water Resources Research*, *50*(7), 5510–5531. https://doi.org/10.1002/2014WR015301

Müller, M. F., & Thompson, S. E. (2016). Comparing statistical and process-based flow duration curve models in ungauged basins and changing rain regimes. *Hydrology and Earth System Sciences*, *20*(2), 669–683. https://doi.org/10.5194/hess-20-669-2016

Nega, H., & Seleshi, Y. (2021). Regionalization of mean annual flow for ungauged catchments in case of Abbay River Basin, Ethiopia. *Modeling Earth Systems and Environment*, *7*(1), 341–350. https://doi.org/10.1007/s40808-020-01033-z

Ochoa-Tocachi, B. F., Buytaert, W., & De Bièvre, B. (2016). Regionalization of land-use impacts on streamflow using a network of paired catchments. *Water Resources Research*, *52*(9), 6710–6729. https://doi.org/10.1002/2016WR018596

O'Shea, D., Nathan, R., Sharma, A., & Wasko, C. (2023). Improved extreme rainfall frequency analysis using a two-step kappa approach. *Water Resources Research*, *59*(4), Article e2021WR031854. https://doi.org/10.1029/2021WR031854

Padulano, R., & Del Giudice, G. (2020). A nonparametric framework for water consumption data cleansing: An application to a smart water network in Naples (Italy). *Journal of Hydroinformatics*, *22*(4), 666–680. https://doi.org/10.2166/hydro.2020.124

Padulano, R., Giudice, G. D., Giugni, M., Fontana, N., & Uberti, G. S. D. (2018). Identification of annual water demand patterns in the City of Naples. *Proceedings*, *2*(11), Article 587. https://doi.org/10.3390/proceedings2110587

Pandey, D., Pandey, A., Ostrowski, M., & Pandey, R. P. (2012). Simulation and optimization for irrigation and crop planning. *Irrigation and Drainage*, *61*(2), 178–188. https://doi.org/10.1002/ird.633

Patil, S., & Stieglitz, M. (2011). Hydrologic similarity among catchments under variable flow conditions. *Hydrology and Earth System Sciences*, *15*(3), 989–997. https://doi.org/10.5194/hess-15-989-2011

Petrucci, G., Rodriguez, F., Deroubaix, J.-F., & Tassin, B. (2014). Linking the management of urban watersheds with the impacts on the receiving water bodies: The use of flow duration curves. *Water Science and Technology*, *70*(1), 127–135. https://doi.org/10.2166/wst.2014.185

Post, D. A. (2004). A new method for estimating flow duration curves: An application to the Burdekin River catchment, North Queensland, Australia. In *Proceedings of the 2nd International Environmental Modelling and Software Society Conference* (iEMSs 2004). https://scholarsarchive.byu.edu/iemssconference/2004/all/2/

Powell, D. M., Ockelford, A., Rice, S. P., Hillier, J. K., Nguyen, T., Reid, I., Tate, N. J., & Ackerley, D. (2016). Structural properties of mobile armors formed at different flow strengths in gravel-bed rivers. *Journal of Geophysical Research: Earth Surface*, *121*(8), 1494–1515. https://doi.org/10.1002/2015JF003794

Pumo, D., Viola, F., La Loggia, G., & Noto, L. V. (2014). Annual flow duration curves assessment in ephemeral small basins. *Journal of Hydrology*, *519*, 258–270. https://doi.org/10.1016/j.jhydrol.2014.07.024

Quimpo, R. G., Alejandrino, A. A., & McNally, T. A. (1983). Regionalized flow duration for Philippines. *Journal of Water Resources Planning and Management*, *109*(4), 320–330. https://doi.org/10.1061/(ASCE)0733-9496(1983)109:4(320)

Ranatunga, T., Tong, S. T. Y., & Yang, Y. J. (2016). An approach to measure parameter sensitivity in watershed hydrological modelling. *Hydrological Sciences Journal*, *61*(1), 76–92. https://doi.org/10.1080/02626667.2014.993987

Rianna, M., Efstratiadis, A., Russo, F., Napolitano, F., & Koutsoyiannis, D. (2013). A stochastic index method for calculating annual flow duration curves in intermittent rivers. *Irrigation and Drainage*, *62*(S2), 41–49. https://doi.org/10.1002/ird.1803

Rianna, M., Russo, F., & Napolitano, F. (2011). Stochastic index model for intermittent regimes: From preliminary analysis to regionalisation. *Natural Hazards and Earth System Sciences*, *11*(4), 1189–1203. https://doi.org/10.5194/nhess-11-1189-2011

Sahoo, S., & Jha, M. K. (2015). On the statistical forecasting of groundwater levels in unconfined aquifer systems. *Environmental Earth Sciences*, *73*(7), 3119–3136. https://doi.org/10.1007/s12665-014-3608-8

Searcy, J. K. (1959). *Flow-duration curves* (Manual of hydrology: Part 2. Low-flow techniques; Geological Survey Water-Supply Paper 1542-A). U.S. Government Printing Office. https://doi.org/10.3133/wsp1542A

Seibert, J., & McGlynn, B. L. (2007). A new triangular multiple flow direction algorithm for computing upslope areas from gridded digital elevation models. *Water Resources Research*, *43*(4), Article W04501. https://doi.org/10.1029/2006WR005128

Shabri, A., & JeMain, A. A. (2010). LQ-moments: Parameter estimation for kappa distribution. *Sains Malaysiana*, *39*(5), 845–850.

Shao, Q., Zhang, L., Chen, Y. D., & Singh, V. P. (2009). A new method for modelling flow duration curves and predicting streamflow regimes under altered land-use conditions. *Hydrological Sciences Journal*, *54*(3), 606–622. https://doi.org/10.1623/hysj.54.3.606

Singh, R. D., Mishra, S. K., & Chowdhary, H. (2001). Regional flow-duration models for large number of ungauged Himalayan catchments for planning microhydro projects. *Journal of Hydrologic Engineering*, *6*(4), 310–316. https://doi.org/10.1061/(ASCE)1084-0699(2001)6:4(310)

Sivakumar, B. (2000). Chaos theory in hydrology: Important issues and interpretations. *Journal of Hydrology*, *227*(1–4), 1–20. https://doi.org/10.1016/S0022-1694(99)00186-9

Sloto, R. A., & Crouse, M. Y. (1996). *HYSEP: A computer program for streamflow hydrograph separation and analysis* (U.S. Geological Survey Water-Resources Investigations Report 96-4040). U.S. Geological Survey. https://pubs.usgs.gov/wri/1996/4040/report.pdf

Smakhtin, V. U. (2001). Low flow hydrology: A review. *Journal of Hydrology*, *240*(3–4), 147–186. https://doi.org/10.1016/S0022-1694(00)00340-1

Smakhtin, V. U., & Batchelor, A. L. (2005). Evaluating wetland flow regulating functions using discharge time-series. *Hydrological Processes*, *19*(6), 1293–1305. https://doi.org/10.1002/hyp.5555

Soni, S. (2017). Assessment of morphometric characteristics of Chakrar watershed in Madhya Pradesh India using geospatial technique. *Applied Water Science*, *7*(5), 2089–2102. https://doi.org/10.1007/s13201-016-0395-2

Subramaniam, S., Palpanas, T., Papadopoulos, D., Kalogeraki, V., & Gunopulos, D. (2006). Online outlier detection in sensor data using non-parametric models. In *Proceedings of the 32nd international conference on Very large data bases* (pp. 187–198). VLDB Endowment. http://vldb.org/conf/2006/p187-subramaniam.pdf

Tasker, G. D. (1987). A comparison of methods for estimating low flow characteristics of streams. *Journal of the American Water Resources Association*, *23*(6), 1077–1083. https://doi.org/10.1111/j.1752-1688.1987.tb00858.x

Verri, G., Pinardi, N., Gochis, D., Tribbia, J., Navarra, A., Coppini, G., & Vukicevic, T. (2017). A meteo-hydrological modelling system for the reconstruction of river runoff: The case of the Ofanto river catchment. *Natural Hazards and Earth System Sciences*, *17*(10), 1741–1761. https://doi.org/10.5194/nhess-17-1741-2017

Viola, F., Noto, L. V., Cannarozzo, M., & La Loggia, G. (2011). Regional flow duration curves for ungauged sites in Sicily. *Hydrology and Earth System Sciences*, *15*(1), 323–331. https://doi.org/10.5194/hess-15-323-2011

Visessri, S., & McIntyre, N. (2016). Regionalisation of hydrological responses under land-use change and variable data quality. *Hydrological Sciences Journal*, *61*(2), 302–320. https://doi.org/10.1080/02626667.2015.1006226

Vogel, R. M., & Fennessey, N. M. (1994). Flow-duration curves. I: New interpretation and confidence intervals. *Journal of Water Resources Planning and Management*, *120*(4), 485–504. https://doi.org/10.1061/(ASCE)0733-9496(1994)120:4(485)

Vogel, R. M., & Fennessey, N. M. (1995). Flow duration curves II: A review of applications in water resources planning. *Journal of the American Water Resources Association*, *31*(6), 1029–1039. https://doi.org/10.1111/j.1752-1688.1995.tb03419.x

Vrugt, J. A., & Sadegh, M. (2013). Toward diagnostic model calibration and evaluation: Approximate Bayesian computation for hydrologic models. *Water Resources Research*, *49*(7), 4335–4352. https://doi.org/10.1002/wrcr.20354

Wang, J., Liang, X., Ma, B., Liu, Y., Jin, M., Knappett, P. S., & Liu, Y. (2021). Using isotopes and hydrogeochemistry to characterize groundwater flow systems within intensively pumped aquifers in an arid inland basin, Northwest China. *Journal of Hydrology*, *595*, Article 126048. https://doi.org/10.1016/j.jhydrol.2021.126048

Wang, S. X., & Singh, V. P. (1995). Frequency estimation for hydrological samples with zero values. *Journal of Water Resources Planning and Management*, *121*(1), 98–108. https://doi.org/10.1061/(ASCE)0733-9496(1995)121:1(98)

Westerberg, I. K., Guerrero, J.-L., Younger, P. M., Beven, K. J., Seibert, J., Halldin, S., Freer, J. E., & Xu, C.-Y. (2011). Calibration of hydrological models using flow-duration curves. *Hydrology and Earth System Sciences*, *15*(7), 2205–2227. https://doi.org/10.5194/hess-15-2205-2011

Winter, T. C. (2007). The role of ground water in generating streamflow in headwater areas and in maintaining base flow. *Journal of the American Water Resources Association*, *43*(1), 15–25. https://doi.org/10.1111/j.1752-1688.2007.00003.x

Wood, E. F., Sivapalan, M., & Beven, K. (1990). Similarity and scale in catchment storm response. *Reviews of Geophysics*, *28*(1), 1–18. https://doi.org/10.1029/RG028i001p00001

Yang, X., Liu, Q., Luo, X., & Zheng, Z. (2017). Spatial regression and prediction of water quality in a watershed with complex pollution sources. *Scientific Reports*, *7*(1), Article 8318. https://doi.org/10.1038/s41598-017-08254-w

Yokoo, Y., & Sivapalan, M. (2011). Towards reconstruction of the flow duration curve: Development of a conceptual framework with a physical basis. *Hydrology and Earth System Sciences*, *15*(9), 2805–2819. https://doi.org/10.5194/hess-15-2805-2011

Yu, P.-S., Yang, T.-C., & Wang, Y.-C. (2002). Uncertainty analysis of regional flow duration curves. *Journal of Water Resources Planning and Management*, *128*(6), 424–430. https://doi.org/10.1061/(ASCE)0733-9496(2002)128:6(424)

Zdaniuk, B. (2023). Ordinary least-squares (OLS) model. In F. Maggino (Ed.), *Encyclopedia of quality of life and well-being research* (pp. 4867–4869). Springer. https://doi.org/10.1007/978-3-031-17299-1_2008